HAL
open science

Study of J/ψ polarization in proton-proton collisions with the ALICE detector at the LHC

Arianna Batista Camejo

▶ **To cite this version:**

Arianna Batista Camejo. Study of J/ψ polarization in proton-proton collisions with the ALICE detector at the LHC. Accelerator Physics [physics.acc-ph]. Université Clermont Auvergne [2017-2020], 2017. English. NNT : 2017CLFAC004 . tel-01610078

HAL Id: tel-01610078

https://theses.hal.science/tel-01610078

Submitted on 4 Oct 2017

HAL is a multi-disciplinary open access archive for the deposit and dissemination of scientific research documents, whether they are published or not. The documents may come from teaching and research institutions in France or abroad, or from public or private research centers.

L'archive ouverte pluridisciplinaire **HAL**, est destinée au dépôt et à la diffusion de documents scientifiques de niveau recherche, publiés ou non, émanant des établissements d'enseignement et de recherche français ou étrangers, des laboratoires publics ou privés.

N^0 d'ordre : D. U. 2790 PCCF T 1701

UNIVERSITÉ CLERMONT AUVERGNE

U.F.R. Sciences et Technologies

ÉCOLE DOCTORALE DES SCIENCES FONDAMENTALES

N^0 d'ordre : 904

THÈSE

présentée pour obtenir le grade de

DOCTEUR D'UNIVERSITÉ

Spécialité : Physique des particules

par : **Arianna Batista Camejo**

Master on Nuclear Physics

Study of J/ψ polarization in proton-proton collisions with the ALICE detector at the LHC

Thèse soutenue le 20 janvier 2017, devant le jury d'examen :

Président	M. P. Dupieux	LPC (Clermont-Ferrand)
Rapporteurs	Mme R. Arnaldi	INFN (Turin, Italie)
	M. I. Laktineh	IPNL (Lyon)
Examinateurs	M. J. E. Castillo Castellanos	CEA/Irfu (Saclay)
	Mme K. Shtejer Diaz	CEADEN (La Havane, Cuba)
Directeurs de thèse	Mme V. Ramillien	LPC (Clermont-Ferrand)
	M. P. Rosnet	LPC (Clermont-Ferrand)

Contents

Abstract

The main purpose of the ALICE experiment is the study and characterization of the Quark Gluon Plasma (QGP), a state of nuclear matter in which quarks and gluons are deconfined. Quarkonia (bound states of a heavy quark Q and its anti-quark $\bar{Q}$) constitute one of the most interesting probes of the QGP. Besides this motivation, the study of quarkonium production is very interesting since it can contribute to our understanding of Quantum Chromodynamics, the theory of strong interactions.
The formation of quarkonium states in hadronic collisions is not yet completely understood. The two main theoretical approaches to describe the production of quarkonium states, the Color Singlet Model and the Non-Relativistic QCD framework (NRQCD), have historically presented problems to simultaneously describe the production cross section and polarization of such states. On the experimental side, quarkonium polarization measurements have not always been complete and consistent between them. So, neither from the theoretical nor from the experimental point of view the situation was clear.
Improved methods for the measurement of quarkonium polarization have been recently proposed, highlighting the necessity to perform the measurements of all polarization parameters with respect to different reference axes. In this context, new measurements could help to improve and set new constraints to the calculations. ALICE has measured the J/ψ polarization in pp collisions at $\sqrt{s}$= 7 TeV. The higher statistics of the 8 TeV data with respect to the 7 TeV data allows to extend the p_{T} range of the measurements. This thesis presents a complete measurement of J/ψ polarization, i.e. the three polarization parameters, in two polarization frames: the Collins-Soper and Helicity frames.
The results show no significant J/ψ polarization in the kinematic domain studied: $2.5 < y < 4.0$ and $2 < p_{\mathrm{T}} < 15$ GeV/c. The measurement of a frame invariant parameter $\tilde{\lambda}$, was also performed to ensure that no bias was present in the analysis procedure. The comparison with different theoretical predictions shows that there is not yet a satisfactory description of quarkonium production. None of the present theoretical approaches is able to describe both, the cross section and polarization measurements.

Chapter 1

Introduction to quarkonia

In this chapter a general introduction to heavy quarkonium systems is given, with emphasis on charmonia (and specifically J/ψ). The main characteristics of such systems, the theoretical considerations in the description of their production, and the motivations for their study in hadron and heavy ions collisions will be covered.

1.1 Standard Model and the strong interaction

1.1.1 Standard Model of Particle Physics

The Standard Model (SM) is the theory that describes the properties of elementary particles and their electromagnetic, weak and strong interactions. It was established in the 1960s and it has been confirmed by a large number of experimental results (historical and recent results are highlighted in [1]).
In the SM, particles are of two kind: fermions, which are the matter particles and bosons, responsible of interactions. According to their mass hierarchy, the matter particles are grouped in three generations, their properties are summarized in Table 1.1 for quarks (*left*) and leptons (*right*).

Table 1.1: Quarks and leptons of the Standard Model. From [2].

Flavour	Mass	Charge (e)
u	$2.2^{+0.6}_{-0.4}$ MeV/c^2	2/3
d	$4.7^{+0.5}_{-0.4}$ MeV/c^2	-1/3
c	1.27 ± 0.03 GeV/c^2	2/3
s	96^{+8}_{-4} MeV/c^2	-1/3
t	173.5 ± 0.6 GeV/c^2	2/3
b	$4.18^{+0.04}_{-0.03}$ GeV/c^2	-1/3

Flavour	Mass (MeV/c^2)	Charge (e)
e	0.51 ± 0.31	-1
ν_e	$< 2 \times 10^{-3}$	0
μ	105.7 ± 2.4	-1
ν_μ	$< 2 \times 10^{-3}$	0
τ	1776.86 ± 0.12	-1
ν_τ	$< 2 \times 10^{-3}$	0

The force carriers (vector bosons) are: the photon which mediates the electromagnetic interactions, the $W^\pm$ and Z^0 bosons responsible for the weak interaction and gluons which

carry the strong force, whose properties are summarized in Table 1.2.

Table 1.2: Vector bosons in the Standard Model. From [2].

Boson	Force	Mass (GeV/c^2)	Charge (e)
γ	Electromagnetic	0	0
$W^{\pm}$	Weak	80.385 ± 0.015	$\pm$ 1
Z^0	Weak	91.1876 ± 0.0021	0
g	Strong	0	0

A last (scalar) boson, the Brout-Englert-Higgs (usually called Higgs) is introduced in the Standard Model. The Higgs boson is associated to the mechanism by which the $W^{\pm}$ and Z^0 bosons and fermions acquire their masses in the electroweak sector of the SM. Figure 1.1 summarizes all particles and possible interactions of the SM.

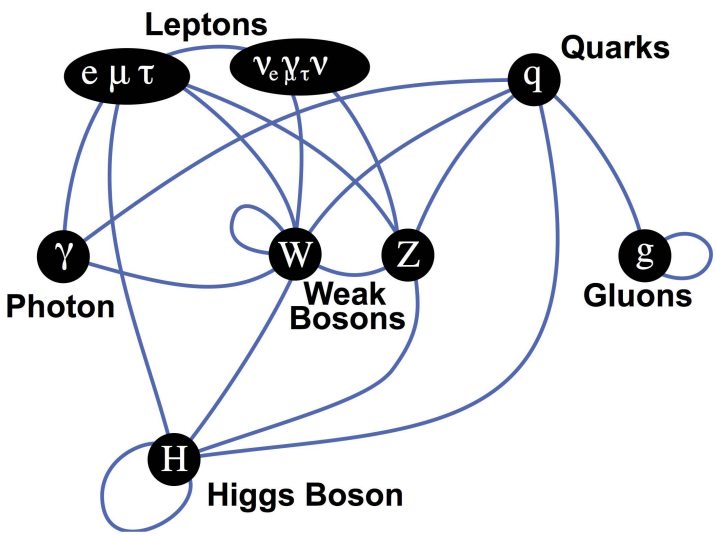

Figure 1.1: Particles of the Standard Model and possible interactions among them (represented by lines).

The SM is based on gauge theories with:

- the electroweak interaction invariant under the weak isospin $SU(2)_L$ and the weak hypercharge $U(1)_Y$ transformations,
- the strong interaction invariant under the color charge $SU(3)_C$ transformations.

To each symmetry groups are associated interaction propagators (vector bosons). The Higgs boson appears in the spontaneous symmetry breaking mechanism of the electroweak interaction.

1.1.2 Characteristics of the strong interaction

Quantum Chromodynamics (QCD) is the sector of the SM that describes the strong interactions. In QCD quarks can exist in one of three different color charges (red, blue and green). Gluons, the force mediators, also carry color charge and can therefore interact among each other; this property is a consequence of the non-Abelian nature of the SU(3) group. Due to the gluons self-interactions, the coupling constant α_s shows a large variation as a function of the scale at which it is measured. The α_s dependence of the transferred momentum in a given process (Q) can be written as:

$$\alpha_s(Q) = \frac{12\pi}{(11n_c - 2n_f)\ln\left(\frac{Q^2}{\Lambda^2_{QCD}}\right)} \tag{1.1}$$

where n_c and n_f are the number of colors and quark flavors respectively, and Λ_{QCD} is the non-perturbative QCD scale, i.e. the scale at which perturbative QCD is no longer applicable due to the large value of α_s. Figure 1.2 shows the α_s dependence given by Equation 1.1 as well as a set of experimental measurements confirming its Q dependency.

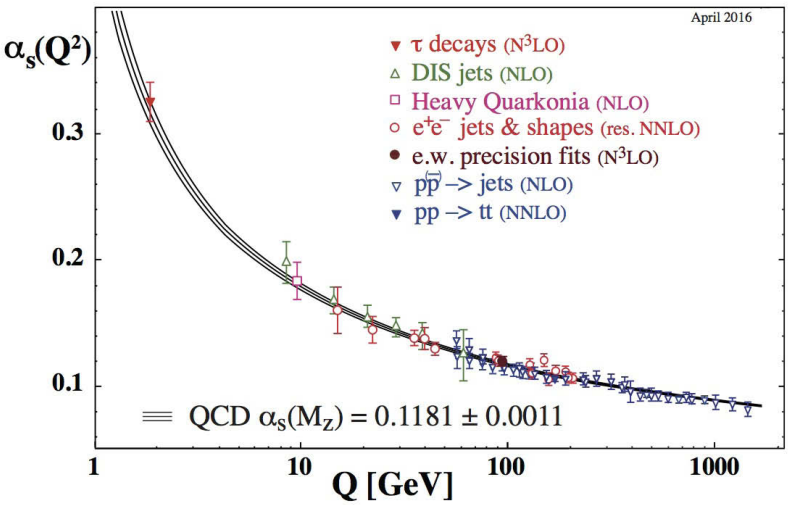

Figure 1.2: The running QCD coupling constant as a function of the momentum transfer Q. Different experimental results are also shown. From [2].

For small values of Q^2, $\alpha_s \to 1$, this explains the fact that quarks are confined in neutral color states, the baryons and mesons. This feature is called *color confinement*.
For high momentum transfer α_s tends to zero, the quarks behave as quasi-free particles, this regime is called *asymptotic freedom*, as predicted by D.J. Gross, H.D. Politzer and F. Wilczek [3, 4], who received the Nobel Price of Physics in 2004.
These features of QCD allow precise calculations only for processes occurring at very high momentum scales (with the use of perturbative QCD), while the description of hadron states, occurring at lower momentum scales, would require the use of effective theories, lattice QCD methods or phenomenological models.

The asymptotic freedom property of QCD suggests the existence of a state of nuclear matter in which quarks and gluons are deconfined, this state is called Quark-Gluon Plasma (QGP). The study of the QGP constitute the main physics motivation of the ALICE experiment at the CERN/LHC.

QCD phase diagram

The transition to this new state of matter can be reached by increasing the temperature of the system or by increasing the baryochemical potential, i. e. baryon density. Figure 1.3 shows the QCD phase diagram as a function of the temperature T and the baryochemical potential μ_B. The QGP is supposed to have existed in the first micro-seconds after the Big Bang, this situation corresponds to low baryochemical potential and high temperature [5]. Also in the core of neutron stars, where the μ_B is supposed to exceed the critical value, quarks are supposed to form a color superconducting state [6]. Experimentally, the QGP can be produced in high-energy heavy-ions collisions.

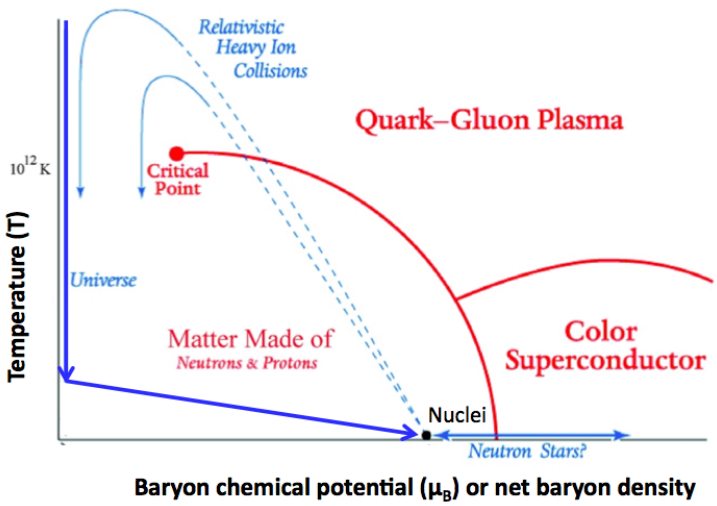

Figure 1.3: QCD phase diagram illustrating the different states of nuclear matter as a function of the temperature T and baryochemical potential μ_B. From [7].

Lattice QCD extrapolations to $\mu_B = 0$ gives for the transition temperature $T_{\mathrm{QCD}} = (154 \pm 9)$ MeV $\approx 1.8 \times 10^{12}$ K [8].

1.2 Heavy quarkonia

Heavy quarkonia are the bound state of a heavy quark and its anti-quark. They exist in two families: the charmonium (charm and anti-charm bound state $c\bar{c}$) and the bottomonium (bottom and anti-bottom $b\bar{b}$) families. Due to their simple composition, quarkonia are ideal systems to improve our understanding of hadron formation in QCD. The study of quarkonium systems is however challenging, since it involves both perturbative and non-perturbative aspects of QCD. In this sense, quarkonia also constitute an ideal labo-

ratory to test the interplay between both regimes of QCD.

1.2.1 Discovery of quarkonium states

The first observation of a quarkonium state occurred in the year 1974, when two groups simultaneously announced the observation of a resonance corresponding to a mass of $m = 3.1\,\mathrm{GeV}/c^2$.
At the time, the group led by Samuel C. C. Ting, at the Brookhaven National Laboratory (BNL) in the US, was studying the collision of protons from the Alternating Gradient Synchrotron (AGS), on a beryllium target to produce electron-positron pairs (pBe $\rightarrow$ e^+e^- + anything). They detected an unexpected narrow peak in the e^+e^- invariant mass spectrum (Figure 1.4 left) [9], the new observed particle was called "J" (the character for "Ting" in Chinese).
A second group, Richter *et al.*, from the Stanford Linear Accelerator Center (SLAC) in the US, reported the observation of an enhancement in the cross section for $e^+e^- \rightarrow$ hadrons, e^+e^- and $\mu^+\mu^-$ at the electron-positron storage ring SPEAR (Figure 1.4 right) [10]. They suggested to name the new particle ψ, motivated by the topology of the $e^+e^- \rightarrow \mu^+\mu^-$ channel.
Both announcements were submitted to the *Physical Review Letters* journal with only one day of difference, in November of 1974. Two years later, Ting and Richter were awarded the Nobel Price of Physics for their discovery of the new particle, which was consensually named J/ψ.
The discovery of J/ψ, followed by the shortly after announcement, by the SLAC group, of the observation of a second resonance, $\psi(2\mathrm{S})$, of mass $m = 3.7\,\mathrm{GeV}/c^2$, triggered a series of possible explanations for these new particles and its interactions, the so called "November revolution".
The fact that J/ψ is produced with such a large cross section in the e^+e^- channel suggested that its quantum numbers should be $J^{PC} = 1^{--}$, the same as the photon. Further studies on the total $e^+e^- \rightarrow \mu^+\mu^-$ cross section and forward-backward asymmetry in the angular distribution of the final μ established this assumption [11]. By studying the multiplicity of pion decays [12], it was concluded that J/ψ and $\psi(2\mathrm{S})$ were mesons of G-parity -1 and isospin $I = 0$.
Before the J/ψ discovery Glashow, Iliopoulos and Maiani had suggested the existence of a fourth quark (beyond u, d and s) to solve the disagreement between the predicted and observed decay rates of kaons [13]. It was suggested that, if a charm quark existed it should form a non-relativistic bound state $\mathrm{c\bar{c}}$ with an energy level spectrum similar to positronium, this system was called "charmonium" to emphasize such parallel.
A similar experimental scenario led the team of L.M. Lederman to the discovery of the $\Upsilon(1\mathrm{S})$ resonance in proton-nucleus collisions at the Fermi National Accelerator Laboratory (US) [14]. But contrary to the J/ψ, at the time no theoretical arguments were in favor of a fifth quark.

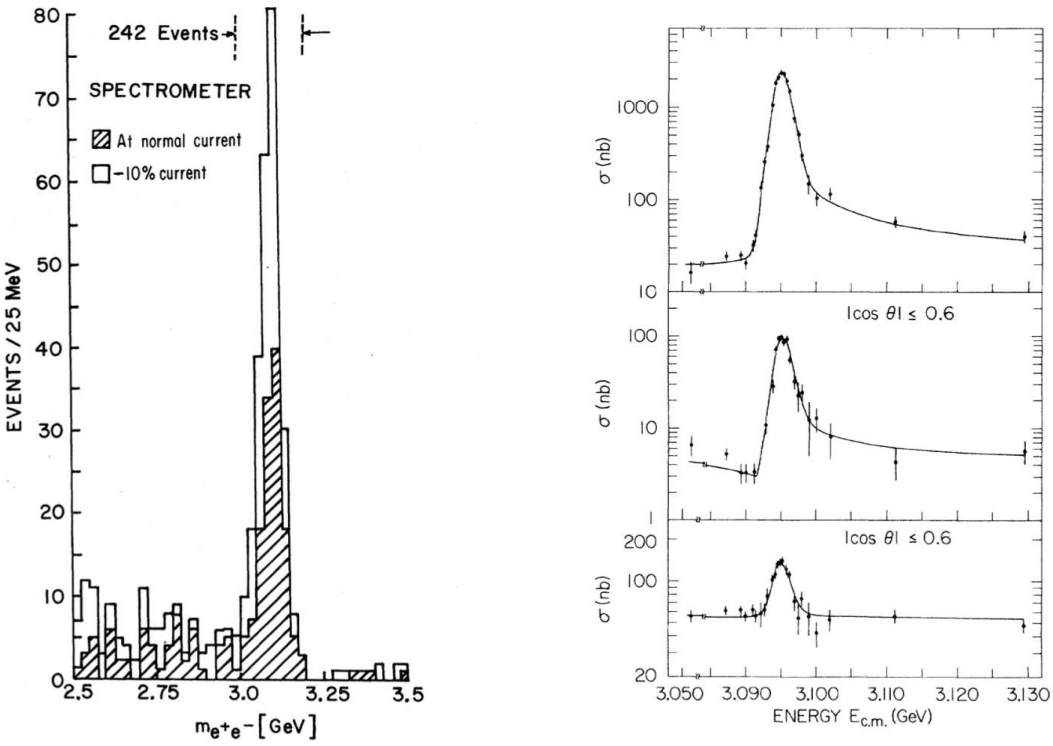

Figure 1.4: *Left*: Mass spectrum of e^+e^- pairs produced in the reaction p+Be from proton beams accelerated at the alternating gradient synchrotron of the BNL [9]. *Right*: Cross sections for the production of hadrons (*top*), e^+e^- (*middle*) and two collinear particles $\mu^+\mu^-$, $\pi^+\pi^-$ and K^+K^- (*bottom*) as final states in the e^+e^- annihilation [10].

1.2.2 Charmonium spectrum

The different quantum states of the $c\bar{c}$ system can be characterized by the quantum numbers L (for the orbital angular momentum), S (spin), J (total angular momentum) and the principal quantum number n, analogous to the spectroscopy of the hydrogen atom. Both, the spectroscopic notation ($n^{2S+1}L_J$) and the J^{PC} convention (with parity $P = (-1)^{(L+1)}$ and charge conjugation $C = (-1)^{(L+S)}$) are used in the literature. Figure 1.5 shows the charmonium spectrum for states under the open heavy-flavour pair production threshold.

The charmonium spectrum can be divided in two main categories, the S-wave ($L = 0$) and the P-wave ($L = 1$) states. The singlet S-wave states ($J = 0$) are called η_c's. The triplet S-wave states ($J = 1$) are the ψ's and the triplet P-wave states ($J = 0, 1, 2$) are named χ_{c0}, χ_{c1} and χ_{c2}.

1.2.3 J/ψ yields and decays

Some properties of J/ψ relevant to this work are presented in the following.

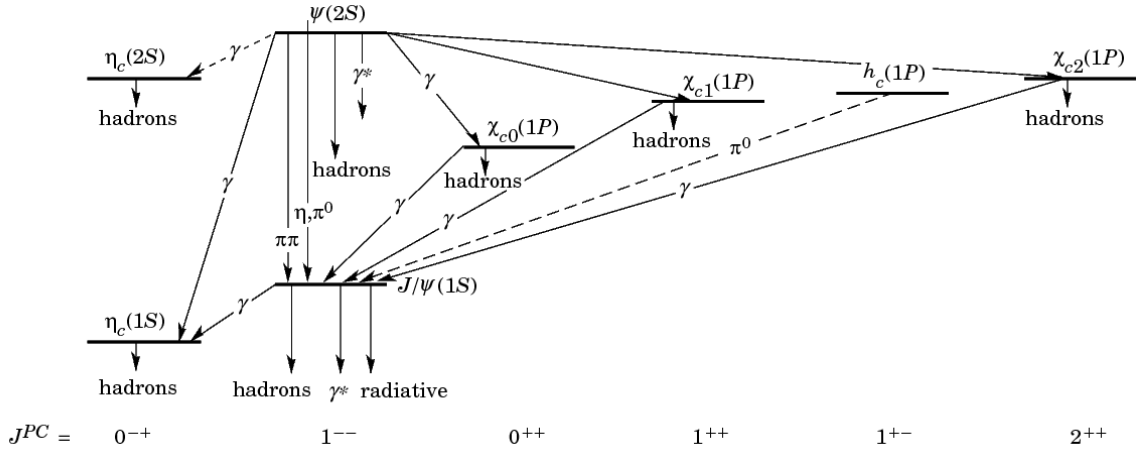

Figure 1.5: Spectrum and transitions of the charmonium family.

J/ψ production in hadron colliders

The J/ψ production in hadron collider experiments can be due to:

- Direct production: direct interactions of partons from the colliding hadrons, and further hadronization of a $c\bar{c}$ into J/ψ;
- Feed-down from excited states: direct hadronization of a $c\bar{c}$ into ψ(2S) or χ_{nJ} states and decay to J/ψ;
- Decay product of b-hadrons.

The first two processes contribute to the "prompt" J/ψ sample, the branching ratios from the charmonium excited states to J/ψ are shown in Table 1.3. The third process contributes to the "non-prompt" J/ψ (the branching ratios BR are reported in Table 1.4). This name comes from the fact that b-hadrons decay through weak processes so they have a relatively longer lifetime. Since b-hadrons travel away from the primary vertex before decaying, the J/ψ prompt and non-prompt components can be separated by a proper J/ψ vertex reconstruction.

Table 1.3: Feed-down from excited charmonium states. From [2].

Process	BR (%)
$\chi_{c0} \to J/\psi\gamma$	1.27 ± 0.06
$\chi_{c1} \to J/\psi\gamma$	33.9 ± 1.2
$\chi_{c2} \to J/\psi\gamma$	19.2 ± 0.7
ψ(2S) $\to J/\psi X$	61.0 ± 0.6

The results presented in this thesis corresponds to the measurement of inclusive J/ψ reconstructed in pp collisions at $\sqrt{s} = 8$ TeV with the ALICE Muon Spectrometer. The

Table 1.4: Contribution from b-hadrons decays.

Process	BR (%)
$B^{\pm}/B^{0} \to J/\psi X$	1.094 ± 0.032
$B_s \to J/\psi\phi$	0.13 ± 0.04
mixture of b-hadrons $\to J/\psi X$	1.16 ± 0.10

prompt-J/ψ results are also reported after the correction from b-hadrons decays, as it will be explained in Section 5.4.3.

J/ψ decay modes

Table 1.5 shows the J/ψ decay branching ratios. The $e^+e^-\gamma$ is shown in parenthesis since it contributes to the reported BR for the e^+e^- channel, shown in the table. The channel $\mu^+\mu^-\gamma$ is also present in J/ψ decays but its branching ratio has not been determined experimentally.

Table 1.5: J/ψ decay modes. From [2].

Decay Mode	BR (%)
hadrons	87.7 ± 0.5
e^+e^-	5.971 ± 0.032
$(e^+e^-\gamma)$	$(8.8 \pm 1.4)\times10^{-3}$
$\mu^+\mu^-$	5.961 ± 0.033

In this work, the J/ψ identification is performed in the dimuon decay channel, with muon tracks reconstructed in the ALICE Muon Spectrometer.

1.3 Theoretical description of quarkonium production

Due to the heavy quark masses and the small relative velocity v of the heavy quark/antiquark in the bound state ($v^2 \approx 0.3$ for the $c\bar{c}$ pair in the J/ψ and $v^2 \approx 0.1$ for the $b\bar{b}$ pair in the $\Upsilon(1S)$ state), quarkonia can be treated as non-relativistic systems and are thus characterized by the hierarchy of three intrinsic momentum scales:

- the heavy quark mass m_Q (hard scale),
- the relative momentum of the quark/antiquark in the quarkonium rest frame $p \sim m_Q v$ (soft scale)
- and the binding energy of the $Q\bar{Q}$ pair $E \sim m_Q v^2$ (ultra-soft scale).

All scales are involved in the description of quarkonium production observables, making difficult their theoretical understanding. Quarkonium production can be understood as a two-step process: the creation of an intermediate $Q\bar{Q}$ pair or pre-resonance, and its evolution towards the quarkonium bound state.
The creation of the heavy $Q\bar{Q}$ pair in the collision of light partons involves a momentum transfer of the order of m_Q, if the $Q\bar{Q}$ pair is produced with a transverse momentum p_{T} much larger than m_Q, then the momentum transfer is of the order of p_{T}. These scales are much larger than Λ_{QCD}, the QCD confinement scale, so $\alpha_{\mathrm{s}} \ll 1$ and such processes can be treated perturbatively. Processes involved in this intermediate step of quarkonium production are referred to as "short distance" effects.
On the other hand, the evolution of the $Q\bar{Q}$ system into a bound state, also called "long distance effects", involves the softer scales $m_Q v$ and $m_Q v^2$ and will thus require to be treated within non-perturbative QCD.
In hadronic collisions at the LHC energies, the dominant production mechanisms of heavy quarkonia are gluon fusion and gluon fragmentation. Figure 1.6 shows some representative diagrams for the production of quarkonia ($\mathcal{Q}$) via color-singlet and color-octet channels.

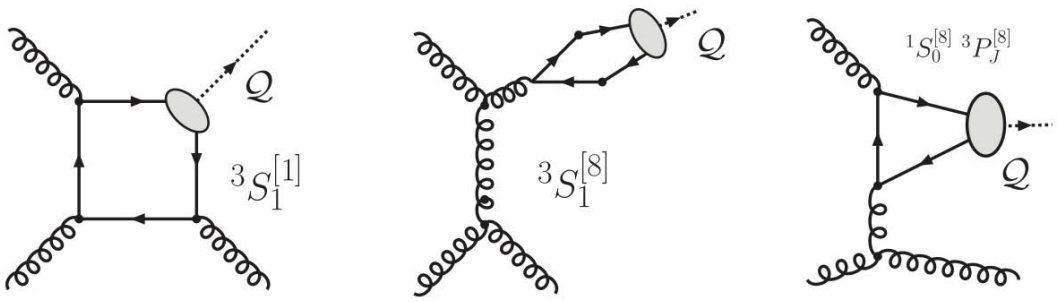

Figure 1.6: Leading-order Feynman diagrams for quarkonium hadro-production, in the $^3S_1^{[1]}$ (*left*), $^3S_1^{[8]}$ (*middle*) and $^1S_0^{[8]}$ and $^3P_J^{[8]}$ (*right*) channels.

Most current theoretical models introduce the concept of "factorization" between the hard and soft scale processes involved in quarkonium production. Such assumption is based on the fact that the timescales involved in those processes ($1/m_Q$ and $1/m_Q v^2$) are, in good approximation, well separated for all quarkonium states.
While full QCD calculations of the perturbative part of quarkonium production are available up to certain orders of α_{s}, the non-perturbative description relies on the framework of effective field theories (EFT) or pure phenomenological models. In principle lattice QCD calculations could be used in the description of the non-perturbative part, but they constitute still a challenge to the current computational power and have not been yet performed in this context. In the following sections the two effective frameworks approaches predicting the full production properties of quarkonia, differential cross sections and polarization, are described.

1.3.1 Nonrelativistic QCD factorization

In the case of heavy quarkonium, for processes involving momentum scales of the order of m_Q or smaller, the suitable EFT is Nonrelativistic QCD (NRQCD). Within this approach, the cross-section for the production of the bound state H from the collision of initial systems A and B can be expressed as the sum over the different spin, orbital angular momentum and color configuration of the cross section for the production of the $Q\bar{Q}$ pair in a given quantum state $n = {}^{2S+1}L_J^{[C]}$, multiplied by the long-distance matrix elements (LDME) $\mathcal{L}$, which express the probability the $Q\bar{Q}$ pair will evolve into the bound state $\mathcal{Q}$.

$$\sigma_{A+B\to\mathcal{Q}+X} = \sum_{i,j,n} \int dx_i dx_j f_i^A(x_i,\mu_F) f_j^B(x_j,\mu_F) \hat{\sigma}_{i+j\to Q\bar{Q}+X}(\mu_F,\mu_R) \mathcal{L}(Q\bar{Q}\to\mathcal{Q}),$$

where i and j represent partons with a relative momentum x_i and x_j of hadrons A and B, respectively. The parton distribution functions f_i^A and f_j^B give the density of partons i and j in hadrons A and B, respectively, at the factorization scale μ_F, while $\hat{\sigma}$ is the partonic cross section to produce a $Q\bar{Q}$ pair at energy μ_F and which depends on the strong coupling constant α_s evaluated at the renormalization scale μ_R. The μ_F and μ_R scales are chosen in the vicinity of the hard scale, and usually set to be equal ($\mu_F = \mu_R$). The individual n terms of this sum are called "partial cross sections" $\sigma(n)$. One peculiarity of the NRQCD factorization formula is that the LDMEs are assumed to be constant and universal, i.e. they do not depend on the kinematics of the $Q\bar{Q}$ pair, and are supposed to be the same for any collision system. The LDMEs scale with powers of the relative velocity v of the heavy quark/antiquark, depending on the quantum state of the intermediate $Q\bar{Q}$ pair; i.e. the relative importance of the different $Q\bar{Q}$ transitions into the quarkonium bound state will follow a certain hierarchy given by "velocity scaling rules".
The LDMEs are determined through a fitting procedure of measured cross sections by different groups [15–17].
The sum in the equation for $\sigma_{A+B\to\mathcal{Q}+X}$ can be interpreted as an expansion in powers of v, then, due to the small velocities v in heavy quarkonium states, the partial terms characterized by large powers of v are considered to be negligible. By truncating in v the predictive power of NRQCD calculations is limited, however the standard approach for S-wave states is to consider the terms scaled up to v^4, which in the case of J/ψ includes the contributions from the ${}^3S_1^{[1]}$, ${}^1S_0^{[8]}$, ${}^3S_1^{[8]}$ and ${}^3P_J^{[8]}$ intermediate states (Figure 1.6).

1.3.2 The Color-Singlet model

The Color-Singlet model (CSM) is one of the earliest approaches to describe quarkonium production, it was proposed shortly after the discovery of J/ψ [18–20]. It states that the quantum state of the $Q\bar{Q}$ pair produced in the high energy collision does not change between its production and its hadronization, i.e. the initial $Q\bar{Q}$ pair can only evolve into a quarkonium if it is in a color-singlet state and has the same spin and orbital angular momentum quantum numbers of the bound state. In the CSM, the production cross section of a given quarkonium state can be expressed as the product of the cross

section for the production of a $Q\bar{Q}$ pair with zero relative velocity and the square of the color-singlet $Q\bar{Q}$ wave function evaluated at zero $Q\bar{Q}$ separation:

$$\sigma_{A+B\to\mathcal{Q}+X} = \sum_{i,j} \int dx_i dx_j f_i^A(x_i,\mu_F) f_j^B(x_j,\mu_F) \hat{\sigma}_{i+j\to Q\bar{Q}+X}(\mu_F,\mu_R)|\Psi(0)|^2.$$

where i and j represent partons with a relative momentum x_i and x_j of hadrons A and B, respectively.
The CSM can be considered as a particular case of the NRQCD factorization approach at leading order in v, where all color-octet matrix elements are equal to zero, thus the only intermediate state that contributes to the production of S-wave quarkonia is ${}^3S_1^{[1]}$ while for P-wave quarkonia only ${}^3P_J^{[1]}$ is considered. The color-singlet LDME can be determined experimentally through the measurement of decay widths of the quarkonium state into a lepton pair, or phenomenologically by the application of potential models, apart from this, the model has no adjustable parameters thus having a high predictive power. It is known however that the CSM shows inconsistencies in the description of the production and decay of P-wave (and higher orbital momentum) states due to uncanceled infrared divergences. Furthermore, NLO and NNLO corrections to the quarkonium production cross sections have been found to be significant at mid and large-p_{T} and for the time being it is not clear that a perturbative expansion in α_{s} is convergent.

1.3.3 CDF results: ψ(2S) anomaly and polarization puzzle

By the mid 1990's, using the data collected during the Tevatron's Run I ($p\bar{p}$ at $\sqrt{s}$ = 1.8 TeV), the CDF experiment measured the production cross section of different quarkonium states: J/ψ, ψ(2S), χ_c and $\Upsilon(1S)$ [21–23]. Up to that moment, the CSM was believed to describe reasonably well the production of quarkonium, it was found however that the measured cross sections exceeded by large factors the theoretical predictions (Figure 1.7, left).
While for J/ψ the unknown feed-down fractions could eventually explain the discrepancy, the fact that the CSM predictions underestimated by about a factor 50 the ψ(2S) production cross-section was alarming at the time. The problem was known as the "ψ(2S) anomaly". This unexpected result lead to a re-visitation of the theory of the production of $Q\bar{Q}$ bound states. The basic assumption of the CSM was doubted and a new description of quarkonia, including the color-octet mechanism was proposed [24]. The CDF data were used to determine the color-octet matrix elements. Figure 1.7 right, shows the results of the fit of CDF prompt J/ψ production cross section.
The inclusion of the color-octet mechanism could satisfactorily describe the data, however the validity of the model was subject to its comparison with quarkonium production data from different reactions or with polarization measurements. In particular, the model predicted a strong transverse polarization of the J/ψ and ψ(2S) which had not been observed in previous fixed target experiments [25]. Higher p_{T} measurements, available from collider experiments, were expected to provide a more reliable test to the model. In the following years, the CDF and D0 collaborations reported the J/ψ, ψ(2S), Υ(1S) and Υ(2S) polarization measurements [26–29] (more details are given in Section 2.3.1).

The results were not compatible with the expected polarization degree predicted by the NRQCD models. This unclear situation is often referred as the "quarkonium polarization puzzle".

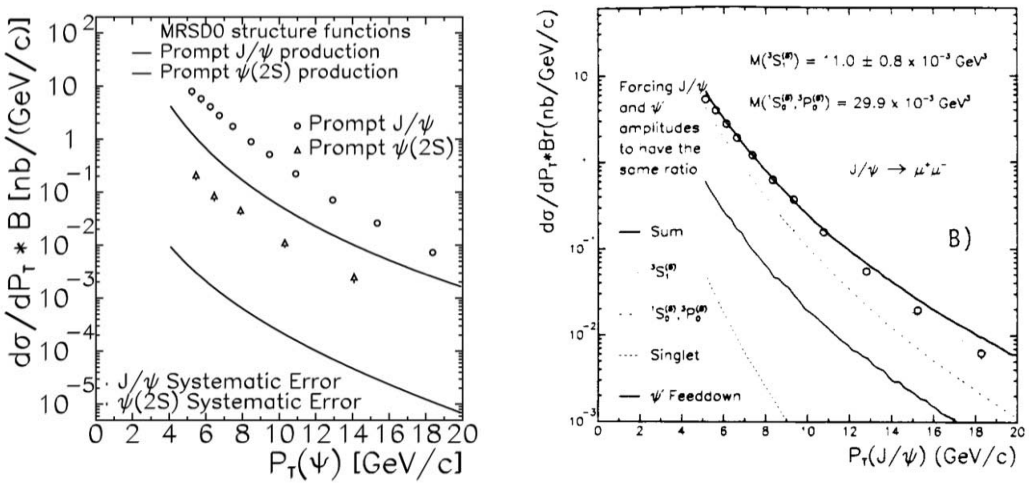

Figure 1.7: *Left*: Prompt J/ψ and ψ(2S) production cross section measured by CDF in $p\bar{p}$ collisions at $\sqrt{s} = 1.8\,\text{TeV}$. The data are compared to theoretical expectations based on LO CSM (from [21]). *Right*: Different contributions to the prompt J/ψ cross section: color singlet component, contribution from ψ(2S), color octet component and their sum (from [23]).

On the other side, the inclusion of higher order terms in the perturbative calculations of the CSM [30] showed an important increase of the predicted quarkonium production cross sections at high p_{T}, decreasing the importance of color-octet contributions.
Figure 1.8 shows the results from LO and NLO CSM compared to the CDF J/ψ [31] and ψ(2S) [32] cross section measurements in $p\bar{p}$ collisions at $\sqrt{s} = 1.96\,\text{TeV}$.
The NNLO* CSM [30] predicts a longitudinal polarization for ψ(2S).
By this time, the importance of polarization measurements was risen, as the tool that could discriminate among the different theoretical predictions. A review of experimental results on quarkonium polarization will be given in Section 2.3.

1.4 Quarkonia in heavy ions collisions

The study of quarkonium production is also interesting in the case of ultra-relativistic heavy ion collisions where the QGP can be produced. In fact, quarkonia have been suggested as a probe of the QGP, since quarkonium states are produced in the early stages of the collisions, they will experience the evolution of the system towards the QGP formation. If the QGP is formed, the confining potential of the quark-antiquark pair is screened due to interactions with quarks and gluons of the medium, leading to the dissociation of the state [33]. Such suppression depends on the medium temperature and occurs sequentially according to the increasing binding energy of different states [34]: due

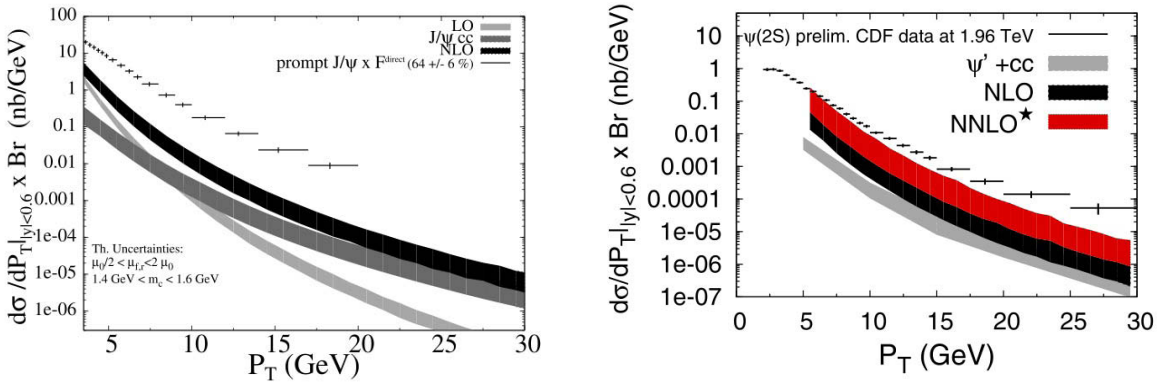

Figure 1.8: Prompt J/ψ (*left*) and ψ(2S) (*right*) production cross section measured by CDF in $p\bar{p}$ collisions at $\sqrt{s} = 1.96$ TeV [31,32]. The data are compared to CSM predictions from [30]. For ψ(2S), the NNLO* band corresponds to calculations with a truncation of NNLO expansions.

to this, quarkonium states are often called "QGP thermometer".
Quarkonium suppression has been confirmed by a number of experimental observations at SPS, RHIC and LHC [35–38]. On the other hand, in heavy ion collisions at LHC energies, where the number of binary collisions is important, quarkonia can be also produced by recombination of quark-antiquark pairs in the deconfined medium or at the phase boundary [39–41].
The medium effects are usually quantified by measuring the nuclear modification factor R_{AB}, defined as the ratio of quarkonium production yields in nucleus–nucleus and nucleon–nucleon collisions, scaled by the average number of binary collisions.
The nuclear modification factor R_{AB} of a given particle produced in the collision of nuclei A and B is defined as the ratio of their production yield N_{AB} and their production cross section σ_{pp} in pp collisions at the same energy, scaled by the average nuclear overlap function $\langle T_{\mathrm{AB}} \rangle$ obtained from a Glauber model [42]:

$$R_{\mathrm{AB}} = \frac{N_{\mathrm{AB}}}{\langle T_{\mathrm{AB}} \rangle \sigma_{\mathrm{pp}}}.$$

It should be taken into account, that the quarkonium yields are also affected by pure nuclear effects related to the difference between nucleon and nucleus parton distribution functions (nPDF) [43], parton saturation [44], energy losses [45], nuclear absorption [46] in the medium or dissociation by comoving particles [47]. Hence the interest to study the quarkonium production yields also in nucleon–nucleus collisions.
Some relevant ALICE results on charmonium production in p–Pb and Pb–Pb collisions at forward rapidities are presented in the following.

Results from p–Pb collisions at $\sqrt{s_{\rm NN}} = 5.02$ TeV

Figure 1.9 (left) shows the nuclear modification factor $R_{\rm pPb}$ for inclusive J/ψ in the transverse momentum interval $0 < p_{\rm T} < 15$ GeV/c as a function of rapidity [48]. The two center-of-mass (cms) rapidity domains correspond to p–Pb or Pb–p configurations, backward rapidity ($-4.46 < y_{\rm cms} < -2.96$) corresponds to the configuration in which the lead beam goes towards the muon spectrometer and forward rapidity ($2.03 < y_{\rm cms} < 3.53$) in the opposite case. J/ψ suppression has been observed at mid- and forward

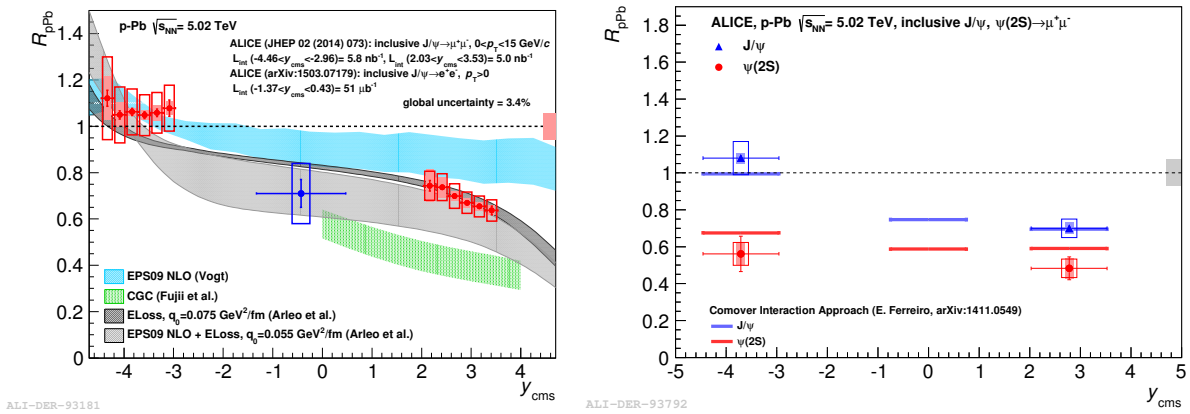

Figure 1.9: *Left:* inclusive J/ψ $R_{\rm pPb}$ as a function of rapidity. Several theoretical calculations are also shown: NLO CEM calculations including the EPS09 shadowing parameterization [49], predictions from the CGC framework [50] and from a model including energy loss processes with and without the inclusion of shadowing [51]. *Right:* inclusive J/ψ and $\psi(2S)$ $R_{\rm pPb}$ vs rapidity and predictions from the comover interaction model [52].

rapidity, while at backward rapidity $R_{\rm pPb}$ is compatible with unity within uncertainties. The data were compared with several models: a NLO CEM calculation that uses the EPS09 shadowing parameterization [49]; a prediction based on the Color Glass Condensate framework [50] and a calculation including coherent parton energy loss processes with and without shadowing effects [51]. It was observed that the models including coherent energy loss processes in the nuclear matter are able to describe the experimental results, however a better agreement was reached with the inclusion of nPDF effects.
Figure 1.9 right shows the results for ψ(2S) and J/ψ in two rapidity bins for $p_{\rm T} > 0$ [53]. As it can be seen, a stronger suppression is observed in the case of ψ(2S) compared to J/ψ in particular in the backward rapidity region. Effects like shadowing and coherent energy loss that can describe the J/ψ results are not expected to be sensitive to the final charmonium state, thus the theoretical predictions shown in the left panel of Figure 1.9 are the same for both resonances. Nuclear absorption is also not expected to affect differently the J/ψ and ψ(2S) yields at the LHC, however, other final state mechanisms may be at play. The predictions within the comover interaction approach are shown in the right panel of Figure 1.9 [52]. The dissociation by comovers is expected to have a stronger impact on the ψ(2S) yields due to its larger size (or smaller binding energy) compared to the J/ψ meson; additionally, the effect should be stronger in the Pb-going configuration (backward rapidity) due to the higher comover density. The inclusion of this effect results

in a good qualitative agreement with the experimental measurements for both resonances.

Results from Pb–Pb collisions at $\sqrt{s_{\mathrm{NN}}} = 2.76$ TeV

Figure 1.10 shows the inclusive J/ψ nuclear modification factor R_{PbPb} as a function of p_{T} in the centrality range 0–90%. The Pb–Pb data sample used for these results was collected at the end of 2011 [41]. The left panel shows the comparison with the product $R_{\mathrm{pPb}}^{\mathrm{forw}} \times R_{\mathrm{pPb}}^{\mathrm{backw}}$, which can be interpreted as an extrapolation of CNM effects to R_{PbPb} [54]. From the

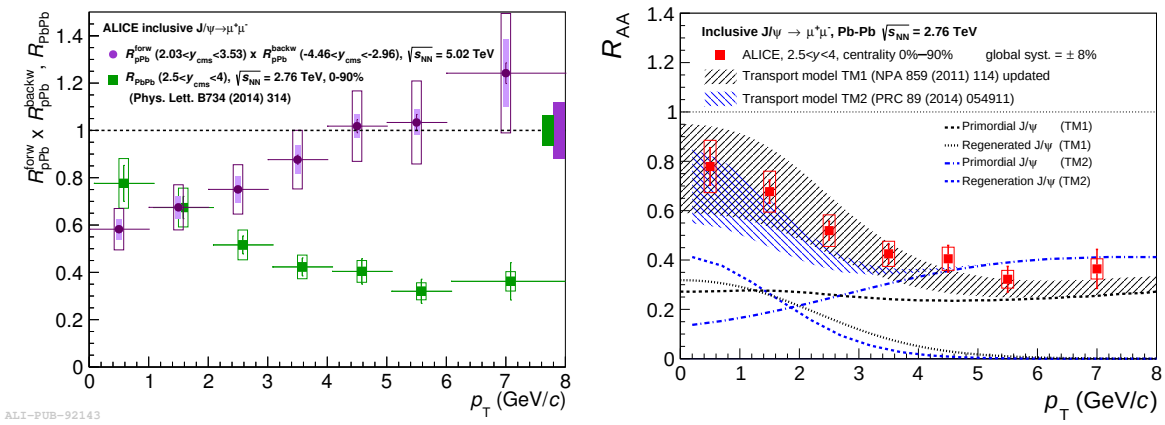

Figure 1.10: J/ψ R_{PbPb} as a function of p_{T} in the centrality range 0–90%. In the left panel a result from a CNM extrapolation is also shown. In the right panel the data are compared with two transport models [55, 56].

comparison, it can be inferred that CNM effects cannot explain the J/ψ suppression in Pb–Pb collisions. At low-p_{T}, one would expect a stronger J/ψ suppression just as a result of nucleus related effects; R_{PbPb} being greater than $R_{\mathrm{pPb}}^{\mathrm{forw}} \times R_{\mathrm{pPb}}^{\mathrm{backw}}$ constitutes a hint of J/ψ production enhancement in Pb–Pb collisions. The results in the high-p_{T} region suggests that the strong suppression observed in Pb–Pb collisions is associated to hot nuclear matter effects. Figure 1.10 right shows the comparison of data with two transport models [55,56], primordial and regenerated J/ψ contributions are shown separately as well. The calculations of the two models differ essentially in the rate equation that controls J/ψ dissociation and regeneration. The uncertainty bands are related to the inclusion of CNM effects and the $c\bar{c}$ cross section. Both predictions show a fair agreement with the data. The J/ψ R_{AA} centrality dependence [41] also confirmed the agreement with the models. ALICE also measured the J/ψ elliptic flow (v_2) in Pb–Pb collisions at forward rapidity in the range $0 < p_{\mathrm{T}} < 10$ GeV/c [57]: the observation constituted a further hint towards the occurrence of J/ψ regeneration in the hot medium.

1.4.1 Quarkonium polarization in a quark-gluon plasma

As discussed before, in ultra-relativistic heavy-ion collisions, a quark-gluon plasma (QGP) is formed when the temperature of the nuclear matter is higher than the critical temperature. The QGP corresponds to a deconfined medium with a high energy density, i.e.

characterized by a weak value of the strong coupling constant, and its theoretical description can be treated with the use of perturbative QCD. Within this hypothesis, if a quarkonium system is formed, the non perturbative effects must be negligible, contrary to its production in pp collisions. This means that the polarization parameters can be affected by the formation of QGP. The main polarization parameter, called λ_θ (the definition is given Chapter 2), is predicted to be 0.35-0.40 [58].
It is worth to recall, however, that these are not yet the conditions attained at the LHC energies, where data confirms the formation of a very strongly interacting QGP [59].

Chapter 2

Polarization concepts

Polarization is referred to the degree of alignment of a particle's total angular momentum J with respect to a characteristic quantization axis z. If J has no preferential orientation the particle is said to be unpolarized. If, on the contrary, it is most probably observed in one of the eigenstates of J_z, the particle is said to be polarized.
For spin-1 particles, like J/ψ, the quantum state in terms of angular momentum can be expressed as a superposition of the three J_z eigenstates:

$$|V\rangle = b_{+1}|+1\rangle + b_0|0\rangle + b_{-1}|-1\rangle \tag{2.1}$$

Two extreme situations can be distinguished: the amplitudes b_{+1} (or b_{-1}) $= 1$ and $b_0 = 0$, in this case we called it *transverse* polarization[1], and on the contrary, if $b_0 = 1$ and $b_{+1} = b_{-1} = 0$, *longitudinal* polarization.
In two-body decays (like $J/\psi \to \mu^+\mu^-$, the one studied in this work) a preferred spin alignment will be reflected in the angular distribution of the decay particles in the rest frame of the quarkonium. An isotropic distribution will indicate no quarkonium polarization, while an anisotropic distribution can signal different degrees of polarization.

2.1 Decay distribution

Let us start by considering a partial process $J/\psi(m) \to \ell^+\ell^-(l')$ in which the J/ψ is in an initial state $|J/\psi; 1, m\rangle$ expressed in the J_z basis and the dilepton system state $|\ell^+\ell^-; 1, l'\rangle$ in the $J_{z'}$ basis, where z' is defined as the axis parallel to the momentum of one of the decay leptons (usually in the direction of ℓ^+) in the quarkonium rest frame, as shown in Figure 2.1. Due to helicity conservation of massless fermions in QED, the leptons, coupled to a (helicity zero) virtual photon in the process $J/\psi \to \gamma^* \to \ell^+\ell^-$, should have their spins parallel to its own momentum direction (z') in the quarkonium rest frame (and thus opposite helicity), so the possible values for l' are ± 1.
The amplitude of this process is then:

$$B_{ml'} = \langle \ell^+\ell^-; 1, l'|\mathcal{B}|J/\psi; 1, m\rangle \tag{2.2}$$

[1] In analogy to the massless spin-1 photon for which the $J_z = 0$ is forbidden, leading to two independent transverse polarization states $J_z = 1$ or $J_z = -1$.

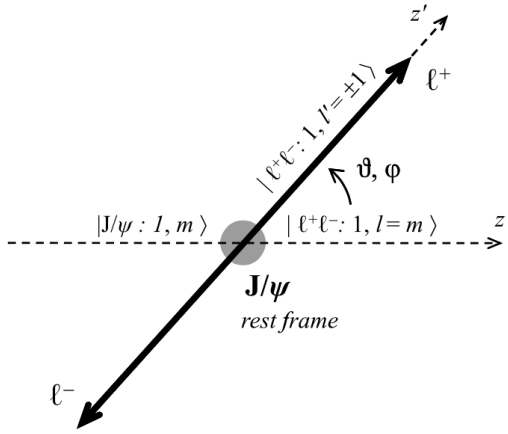

Figure 2.1: Schematic picture of the decay $J/\psi \to \ell^+\ell$, showing the notation for axes, rotation angles and angular momentum states of the initial and final systems (from [60]).

where $\mathcal{B}$ is the transition operator that embeds the dynamics of the decay.
If we want to express the dilepton state in the J_z basis we need to perform a rotation which brings the z axis to coincide with z'. In general, through a rotation $R(\alpha, \beta, \gamma)$, where α, β and γ are the Euler angles, an eigenstate $|J, M'\rangle$ can be expressed as a superposition of $|J, M\rangle$ eigenstates as:

$$|J, M'\rangle = \sum_{M=\ J}^{+J} \mathcal{D}^J_{MM'}(\alpha, \beta, \gamma)|J, M\rangle \tag{2.3}$$

The complex numbers $\mathcal{D}^J_{MM'}(\alpha, \beta, \gamma)$ are the rotation matrix elements defined as:

$$\mathcal{D}^J_{MM'}(\alpha, \beta, \gamma) = \mathrm{e}^{\ iM\alpha} d^J_{MM'}(\beta) \mathrm{e}^{\ iM\gamma} \tag{2.4}$$

where the $d^J_{MM'}(\beta)$ are the elements of the Wigner matrices:

$$\begin{aligned} d^J_{MM'}(\beta) = & \sum_{t=\max(0,M\ \ M')}^{t=\max(J+M,J\ \ M')} (\ \ 1)^t \cdot \frac{\sqrt{(J+M)!(J\ \ M)!(J+M')!(J\ \ M')!}}{(J+M\ \ t)!(J\ \ M'\ \ t)!(t\ \ M+M')!} \\ & \times \left(\cos\frac{\beta}{2}\right)^{2J+M\ \ M'\ \ 2t} \left(\sin\frac{\beta}{2}\right)^{2t\ \ M+M'} \end{aligned} \tag{2.5}$$

which in the case of spin-1 systems, take the form:

$$d^1(\beta) = \begin{pmatrix} \frac{1}{2}(1+\cos\beta) & \frac{1}{\sqrt{2}}\sin\beta & \frac{1}{2}(1\ \ \cos\beta) \\ \frac{1}{\sqrt{2}}\sin\beta & \cos\beta & \frac{1}{\sqrt{2}}\sin\beta \\ \frac{1}{2}(1\ \ \cos\beta) & \frac{1}{\sqrt{2}}\sin\beta & \frac{1}{2}(1+\cos\beta) \end{pmatrix} \tag{2.6}$$

In our case, we need a rotation in which $\alpha = \varphi$, $\beta = \theta$ and $\gamma = \ \ \varphi$ (θ and φ being the

zenithal and azimuthal angles in spherical coordinate systems), so

$$|\ell^+\ell^-;1,l'\rangle = \sum_{l=0,\pm1} \mathcal{D}^1_{ll'}(\varphi,\theta,-\varphi)|\ell^+\ell^-;1,l\rangle \tag{2.7}$$

The partial amplitudes $B_{ml'}$ take the form:

$$B_{ml'} = \sum_{l=0,\pm1} \mathcal{D}^{1*}_{ll'}(\varphi,\theta,-\varphi)\langle\ell^+\ell^-;1,l|\mathcal{B}|J/\psi;1,m\rangle \tag{2.8}$$

Because of total angular momentum conservation ($l = m$), the transition operation has the form $\langle\ell^+\ell^-;1,l|\mathcal{B}|J/\psi;1,m\rangle = B\delta_{ml}$ and:

$$B_{ml'} = B\mathcal{D}^{1*}_{ml'}(\varphi,\theta,-\varphi) \tag{2.9}$$

The amplitude of the process $J/\psi \to \ell^+\ell^-(l')$ can be obtained by summing 2.9 over all possible m values:

$$B_{l'} = \sum_{m=0,\pm1} b_m B\mathcal{D}^{1*}_{ml'}(\varphi,\theta,-\varphi) \tag{2.10}$$

where b_m are the amplitudes of the three J_z eigenstates, as in 2.1.
Or, in terms of the decay amplitudes $a_m = b_m B$:

$$B_{l'} = \sum_{m=0,\pm1} a_m\mathcal{D}^{1*}_{ml'}(\varphi,\theta,-\varphi) \tag{2.11}$$

Then, the probability of the transition can be obtained by squaring 2.11 and summing over all possible l' values.

$$W(\cos\theta,\varphi) \propto \sum_{l'=\pm1} |B_{l'}|^2 \tag{2.12}$$

Substituting the matrix elements $\mathcal{D}^{1*}_{ml'}$, one gets:

$$\begin{aligned} W(\cos\theta,\varphi) \propto \frac{\mathcal{N}}{(3+\lambda_\theta)}(1 &+ \lambda_\theta\cos^2\theta \\ &+ \lambda_\varphi\sin^2\theta\cos 2\varphi + \lambda_{\theta\varphi}\sin 2\theta\cos\varphi \\ &+ \lambda^\perp_\varphi\sin^2\theta\sin 2\varphi + \lambda^\perp_{\theta\varphi}\sin 2\theta\sin\varphi) \end{aligned} \tag{2.13}$$

where:

$$\mathcal{N} = |a_0|^2 + |a_{+1}|^2 + |a_{-1}|^2 \tag{2.14}$$

The λ values (called *polarization parameters*) are directly related to the amplitudes a_m of the decay process, themselves proportional to the amplitudes of the J/ψ angular mo-

mentum eigenstates:

$$
\begin{aligned}
\lambda_\theta &= \frac{\mathcal{N} - 3|a_0|^2}{\mathcal{N} + |a_0|^2} \\
\lambda_\varphi &= \frac{2\mathrm{Re}[a_{+1}^* a_{-1}]}{\mathcal{N} + |a_0|^2} \\
\lambda_{\theta\varphi} &= \frac{\sqrt{2}\mathrm{Re}[a_0^*(a_{+1} - a_{-1})]}{\mathcal{N} + |a_0|^2} \\
\lambda_\varphi^\perp &= \frac{2\mathrm{Im}[a_{+1}^* a_{-1}]}{\mathcal{N} + |a_0|^2} \\
\lambda_{\theta\varphi}^\perp &= \frac{-\sqrt{2}\mathrm{Im}[a_0^*(a_{+1} - a_{-1})]}{\mathcal{N} + |a_0|^2}
\end{aligned}
\tag{2.15}
$$

The last two terms in 2.13 ($\lambda_\varphi^\perp \sin^2\theta \cos 2\varphi$ and $\lambda_{\theta\varphi}^\perp \sin 2\theta \cos\varphi$) introduce an asymmetry of the distribution with respect to the (x, z) plane, which is defined as the plane containing the momentum of the particles that produce the quarkonium and the quarkonium momentum, i.e. the production plane (see Figure 2.4). In the study of quarkonia produced in hadron collision experiments, the (x, z) plane is defined by the momenta of the colliding hadrons and of the quarkonium, a definition that does not coincide event-by-event with the natural (x, z) plane which would contain instead the directions of the colliding partons, thus, when averaging over multiple collision events, an azimuthal asymmetry is not observable, and consequently the last two terms of 2.13 vanish and the experimental accessible decay distribution is:

$$
\begin{aligned}
W(\cos\theta, \varphi) \propto \frac{1}{(3 + \lambda_\theta)}(1 &+ \lambda_\theta \cos^2\theta \\
&+ \lambda_\varphi \sin^2\theta \cos 2\varphi + \lambda_{\theta\varphi} \sin 2\theta \cos\varphi)
\end{aligned}
\tag{2.16}
$$

From the relations 2.15, under the condition that λ_θ can take values in the interval $[-1; +1]$, in any reference system; and after applying some algebraic properties of complex numbers, one can deduce the following relations among the λ parameters:

$$
\begin{aligned}
|\lambda_\varphi| &\leq \frac{1}{2}(1 + \lambda_\theta) \\
\lambda_\theta^2 + 2\lambda_{\theta\varphi} &\leq 1 \\
|\lambda_{\theta\varphi}| &\leq \frac{1}{2}(1 - \lambda_\varphi) \\
(1 + 2\lambda_\varphi)^2 + 2\lambda_{\theta\varphi}^2 &\leq 1 \quad \text{for} \quad \lambda_\varphi < -1/3
\end{aligned}
\tag{2.17}
$$

From the inequalities 2.17 it can be seen that independently of the λ_θ value $|\lambda_\varphi| < 1$ and $|\lambda_{\theta\varphi}| < 1/\sqrt{2}$. The allowed phase space of the λ parameters is shown in Figure 2.2.

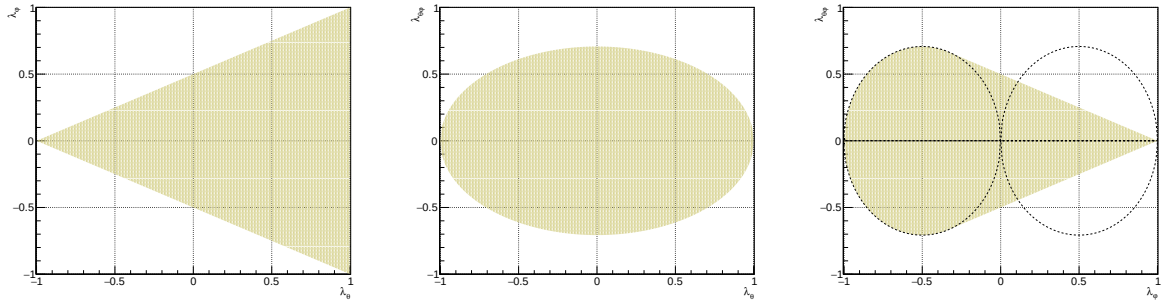

Figure 2.2: Allowed domain of variation of the polarization parameters λ_θ, λ_φ and $\lambda_{\theta\varphi}$, given by the relations 2.17. *Left*: (λ_θ; λ_φ) plane. *Middle*: (λ_θ; $\lambda_{\theta\varphi}$) plane. *Right*: (λ_φ; $\lambda_{\theta\varphi}$) plane.

2.1.1 One-dimensional method

A two dimensional analysis of the data (and multi-parameter fit to the function 2.16) is often limited by the available statistics; a common strategy is based on the integration of $W(\cos\theta, \varphi)$ over θ and φ and simplify the analysis to one dimensional angular distributions, as following:

$$W(\cos\theta) \propto \frac{1}{3+\lambda_\theta}(1+\lambda_\theta \cos^2\theta) \tag{2.18}$$

$$W(\varphi) \propto 1 + \frac{2\lambda_\varphi}{3+\lambda_\theta}\cos 2\varphi \tag{2.19}$$

$$W(\tilde{\varphi}) \propto 1 + \frac{\sqrt{2}\lambda_{\theta\varphi}}{3+\lambda_\theta}\cos\tilde{\varphi} \tag{2.20}$$

where $\tilde{\varphi}$ is defined as follows:

$$\tilde{\varphi} = \begin{cases} \varphi - \frac{3}{4}\pi & \text{for} \quad \cos\theta < 0 \\ \varphi - \frac{1}{4}\pi & \text{for} \quad \cos\theta > 0 \end{cases} \tag{2.21}$$

This methodology (also referred to as 1-D fit method) is the one used in the present work. Figure 2.3 shows the shapes of the $W(\cos\theta)$, $W(\varphi)$ and $W(\tilde{\varphi})$ distributions that would be experimentally observed for different values of λ_θ, λ_φ and $\lambda_{\theta\varphi}$.

2.1.2 Asymmetry of angular distribution method

As an alternative and simpler method from the experimental point of view, one could also extract the polarization parameters by studying the asymmetry between the populations (P) of two angular topologies [60]. If we call:

$$P(|\cos\theta| < 1/2) = \int_0^{1/2}\int_0^{2\pi} W(\cos\theta, \varphi) d\cos\theta \, d\varphi \tag{2.22}$$

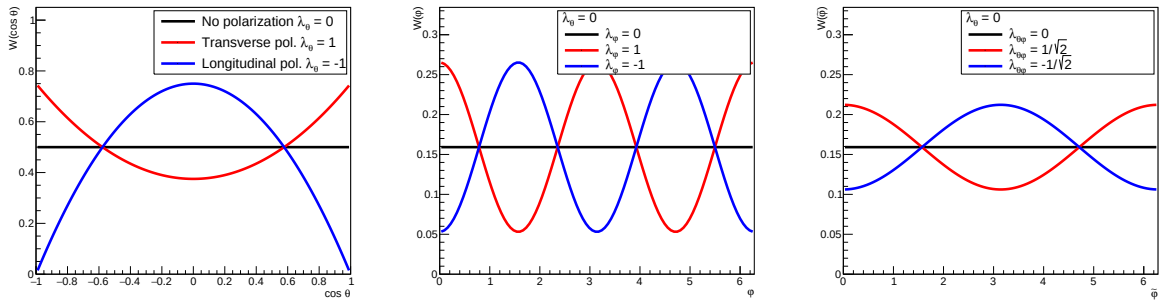

Figure 2.3: Angular distributions $W(\cos\theta)$ (*left*), $W(\varphi)$ (*middle*) and $W(\tilde{\varphi})$ (*right*) for two extreme and an intermediate values of the λ parameters.

$$P(|\cos\theta| > 1/2) = \int_{1/2}^{1}\int_{0}^{2\pi} W(\cos\theta, \varphi) d\cos\theta \, d\varphi \tag{2.23}$$

one can obtain the λ_θ parameters as:

$$\frac{P(|\cos\theta| > 1/2) - P(|\cos\theta| < 1/2)}{P(|\cos\theta| > 1/2) + P(|\cos\theta| < 1/2)} = \frac{3}{4}\frac{\lambda_\theta}{3+\lambda_\theta} \tag{2.24}$$

and similarly for λ_φ and $\lambda_{\theta\varphi}$, on gets:

$$\begin{aligned} \frac{P(\cos 2\varphi > 0) - P(\cos 2\varphi < 0)}{P(\cos 2\varphi > 0) + P(\cos 2\varphi < 0)} &= \frac{2}{\pi}\frac{2\lambda_\varphi}{3+\lambda_\theta} \\ \frac{P(\sin 2\theta\cos\varphi > 0) - P(\sin 2\theta\cos\varphi < 0)}{P(\sin 2\theta\cos\varphi > 0) + P(\sin 2\theta\cos\varphi < 0)} &= \frac{2}{\pi}\frac{2\lambda_{\theta\varphi}}{3+\lambda_\theta} \end{aligned} \tag{2.25}$$

2.2 Reference systems

2.2.1 Classical reference axis

There are different conventions to define the polarization reference frames, i.e. the frame in which the angular distribution is built. The reference system is always chosen as the quarkonium rest frame and the y axis perpendicular to the *production plane* i.e. the plane containing the momenta of the colliding beams and of the quarkonium in the laboratory frame (see Figure 2.4 left).
The quantization axis z can be defined (see Figure 2.4 right) by the direction of one of the colliding beams (Gottfried-Jackson system), by the bisector of the angle between the momentum of one beam and the opposite of the other beam (Collins-Soper frame) or as the direction of the J/ψ momentum in the center of mass of the colliding beams (Helicity frame).
The *natural* polarization axis is defined as the one for which the polar angular anisotropy is maximal. Figure 2.5 shows a graphical representation of the decay angular distribution for the cases of *natural longitudinal* polarization in the Collins-Soper frame (Figure 2.5 a),

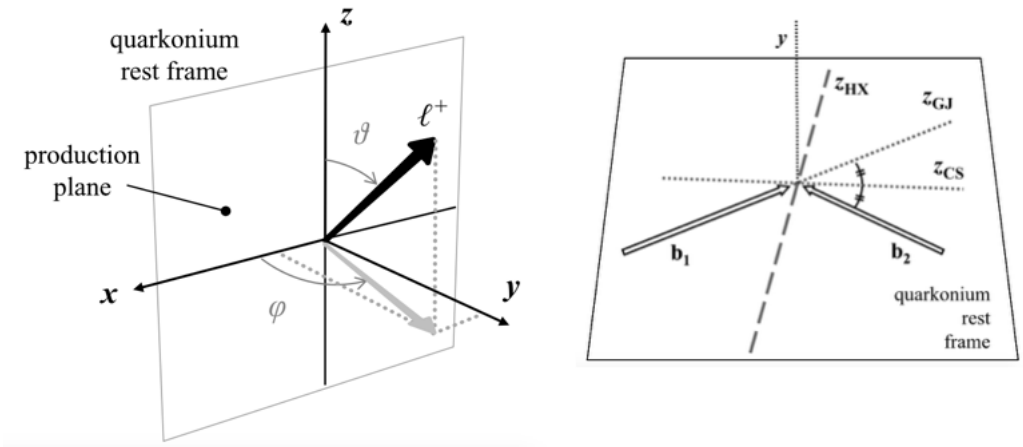

Figure 2.4: *Left*: Coordinate system for the measurement of the dilepton decay angular distribution. The y axis is defined perpendicular to the production plane, for colliding systems it is the plane that contains the colliding beams and the momentum of the quarkonium. *Right*: Different conventions for the definition of the z axis within the (x,z) plane. Figure from [60].

b) and c)) and *natural transverse* polarization in the Helicity frame (Figure 2.5 d), e) and f)). The experimental determination of the main polarization parameter λ_θ will result $\lambda_\theta = \quad 1$ in the Collins-Soper frame in the first case (Figure 2.5 a)) and $\lambda_\theta = 1$ in the Helicity frame in the second case (Figure 2.5 d)). The angle defined by the Collins-Soper's and Helicity's z axes depends on the quarkonium kinematics. Figures 2.5 b), c), e) and f) illustrate the differences we could observe experimentally when studying the angular distributions in an axis different from the "natural" one, b) and e) show the case in which the z axis is rotated by 45° with respect to the "natural" axis, while c) and f) when both axes are perpendicular. These pictures illustrate how a non-ideal definition of the z axis can hide some of the characteristics of the angular distributions. For instance, in the case of natural longitudinal polarization (Figure 2.5 a)), if the λ_θ parameter is measured in a reference system rotated by 45° (Figure 2.5 b)) the result would be $\lambda_\theta = \quad 1/3$, indicating only a partial longitudinal polarization. If the natural and experimental z axes are perpendicular (Figure 2.5 c)), a naturally full longitudinal polarization will result in the measurement of full transverse polarization $\lambda_\theta = +1$. And similarly in the case of transverse polarization (Figure 2.5 d)), for $\delta_{(zz')} = 45°$ (Figure 2.5 e)) $\lambda_\theta = 1/5$, and for 90° (Figure 2.5 f)) $\lambda_\theta = \quad 1/3$.
Particularly, the case c) would induce a misleading interpretation of the results, with $\lambda_\theta = 1$, similar to d), while both cases are completely different. A better understanding of this situation can be achieved by looking at the azimuthal distributions (for simplicity let us assume $\lambda_{\theta\varphi} = 0$). In d) for instance λ_φ would be equal to zero, indicating an isotropic azimuthal distributions while in c), λ_φ will be maximal ($\lambda_\varphi = \quad 1$).

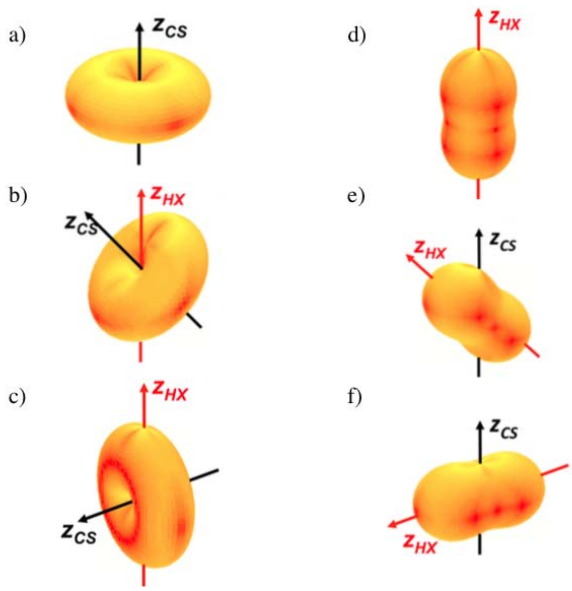

Figure 2.5: Shapes of the decay particles angular distributions in the cases of fully longitudinal (left) and fully transverse (right) J/ψ polarization (Figure adapted from [60]). The z axis is chosen as the J/ψ natural quantization axis for illustration. *Left*: Natural full longitudinal polarization in the Collins-Soper frame. *Right*: Natural full transverse polarization in the Helicity frame.

2.2.2 Frame invariant formalism

Since all the definitions of the z axis lie in the *production plane*, a simple rotation around the y axis is sufficient to bring one polarization frame to coincide with an other. If the angle between the z and z' is δ, a rotation of the form:

$$R = \begin{pmatrix} \cos\delta & 0 & \sin\delta \\ 0 & 1 & 0 \\ \sin\delta & 0 & \cos\delta \end{pmatrix} \tag{2.26}$$

transforms the vector $r = x, y, z$ in (x', y, z'). One could apply this transformation to the decay angular distribution 2.16 so that in the "z'" system one obtains:

$$\begin{aligned} W(\cos\theta', \varphi') \propto \frac{1}{(3+\lambda'_\theta)}(1 + \lambda'_\theta \cos^2\theta' \\ + \lambda'_\varphi \sin^2\theta' \cos 2\varphi' + \lambda'_{\theta\varphi} \sin 2\theta' \cos\varphi') \end{aligned} \tag{2.27}$$

The angular distribution is invariant under such rotation, but the λ parameters change in a correlated way. The relation between the polarization parameters λ' in the rotated

frame and λ in the initial reference frame are given by:

$$\lambda'_\theta = \frac{\lambda_\theta - 3\Lambda}{1+\Lambda} \qquad \lambda'_\varphi = \frac{\lambda_\varphi + \Lambda}{1+\Lambda}$$
$$\lambda'_{\theta\varphi} = \frac{\lambda_{\theta\varphi}\cos 2\delta - \frac{1}{2}(\lambda_\theta - \lambda_\varphi)\sin 2\delta}{1+\Lambda} \tag{2.28}$$
$$\Lambda = \frac{1}{2}(\lambda_\theta - \lambda_\varphi)\sin^2\delta - \frac{1}{2}\lambda_{\theta\varphi}\sin 2\delta$$

These transformation relations imply that the quantity $\mathcal{F}$ defined as:

$$\mathcal{F}_{\{c1,c2,c3\}} = \frac{(3+\lambda_\theta) + c_1(1-\lambda_\varphi)}{c_2(3+\lambda_\theta) + c_3(1-\lambda_\varphi)} \tag{2.29}$$

is invariant under frame transformations.
The following combination:

$$\tilde{\lambda} = \mathcal{F}_{\{-3,0,1\}} = \frac{\lambda_\theta + 3\lambda_\varphi}{1-\lambda_\varphi} \tag{2.30}$$

proposed by [61, 62] involving the λ_θ and λ_φ parameters is the quantity considered by most experimental measurements and will be the one used in this analysis.

2.3 Experimental review

2.3.1 Quarkonium polarization measurements at collider experiments

Results from Tevatron

Using the data collected during Tevatron Run I in $p\bar{p}$ collisions at $\sqrt{s}$= 1.8 TeV, the CDF collaboration measured the polarization of prompt J/ψ and ψ(2S) in the p_T ranges $4 < p_T < 20$ GeV/c and $5.5 < p_T < 20$ GeV/c respectively and at central rapidity, $|y| < 0.6$ [26]. At the moment, those measurements constituted an important test of the NRQCD calculations which, using the data from production measurements to compute the LDMEs had provided predictions for the polarization observable. The expected output of the measurements was a transverse J/ψ polarization increasing with p_T in the Helicity frame.
The CDF measurements are shown in Figure 2.6. The predictions from NRQCD calculations [25, 63, 64] are in clear disagreement with the data in the high-p_T region. The feed-down contribution from P-wave was included in the theoretical predictions, and it decreases the expected J/ψ polarization at high-p_T (Figure 2.6 b)) but not enough to be able to describe the data.

Also with the Run I data CDF measured the Υ(1S) polarization in $0 < p_T < 20$ GeV/c in $|y| < 0.6$ [27] and the results are compatible with unpolarized Υ(1S) production (see

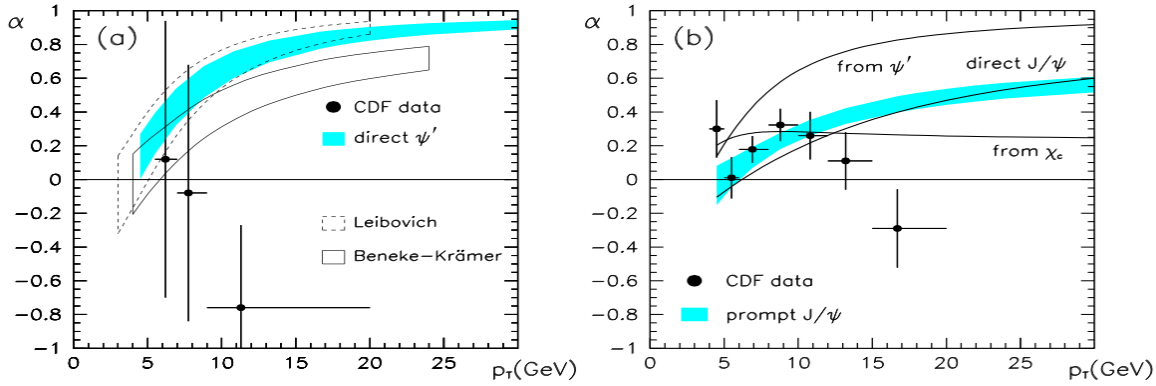

Figure 2.6: ψ(2S) (*left*) and J/ψ(*right*) polarizations ($\alpha \equiv \lambda_\theta$) measured by the CDF experiment in p$\bar{\text{p}}$ at $\sqrt{s}$= 1.8 TeV collisions [26]). The plotted α parameter corresponds to the λ_θ parameter (introduced in Section 2.1), the measurements are referred to the Helicity frame. Data are compared to theoretical calculations within the NRQCD approach from [25, 63, 64] for ψ(2S) and [63] for the J/ψ. Figure taken from [63].

also Figure 2.9).
Few years later, the D0 collaboration also measured the polarization of the Υ(1S) and Υ(2S) with the Tevatron Run II data at $\sqrt{s}$= 1.96 TeV [28]. The measurements were performed in the central rapidity region $|y| < 1.8$ and p_{T} from 0 to 20 GeV/c. The observation of a significant longitudinal polarization for Υ(1S) at low-p_{T} was in contradiction with the previous CDF results [27] and with predictions from NRQCD [65] and the k_T factorization model [66]. Figure 2.7 shows the p_{T} dependence of the λ_θ parameter (called α in the plots) for both states. In the case of Υ(2S) a better agreement with the predictions was reached, within the large uncertainties of both experimental and theoretical predictions.
With the higher statistics Tevatron Run II data, the CDF collaboration studied again the J/ψ and ψ(2S) polarizations in p$\bar{\text{p}}$ collisions at $\sqrt{s}$= 1.96 TeV [29]. In contradiction with results from Run I (Figure 2.6 right), the J/ψ polarization parameter λ_θ is always negative and its absolute value increases with p_{T}, towards a stronger longitudinal polarization. The ψ(2S) polarization shows a similar trend to the J/ψ. The results are shown in Figure 2.8 together with the comparison with NRQCD predictions from [25, 63, 67] and k_T factorization model [68]. Once again data disfavored the strong transverse polarization predicted by NRQCD, and it is not compatible with the k_T factorization model, which can reproduce the trend but not the magnitude of the λ_θ parameter.

Given this unclear experimental situation, CDF carried out the measurement of the Υ states polarization in p$\bar{\text{p}}$ collisions at $\sqrt{s}$= 1.96 TeV, by measuring not only λ_θ but the three polarization parameters and in the Collins-Soper and Helicity frames [69] which allowed also to cross-check the measurements through the frame invariant quantity $\tilde{\lambda}$. The results are consistent for all resonances and in both frames with an unpolarized production scenario. Figure 2.9 (left) shows the experimental results for the three Υ states in

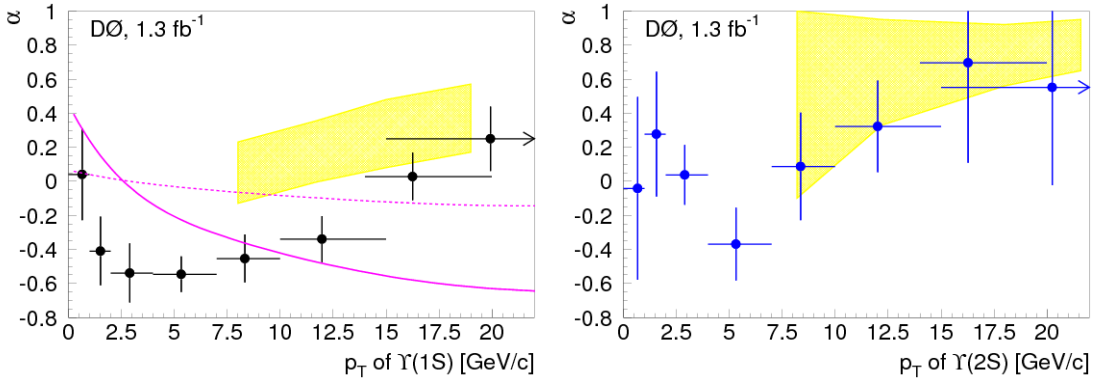

Figure 2.7: $\Upsilon(1S)$ (*left*) and $\Upsilon(2S)$ (*right*) main polarization parameter ($\alpha \equiv \lambda_\theta$) in the Helicity frame, as a function of p_T and for central rapidity ($|y| < 1.8$) measured for by the D0 collaboration. Data are compared with theoretical predictions from NRQCD [65] and the k_T factorization model [66]. Figure from [28]

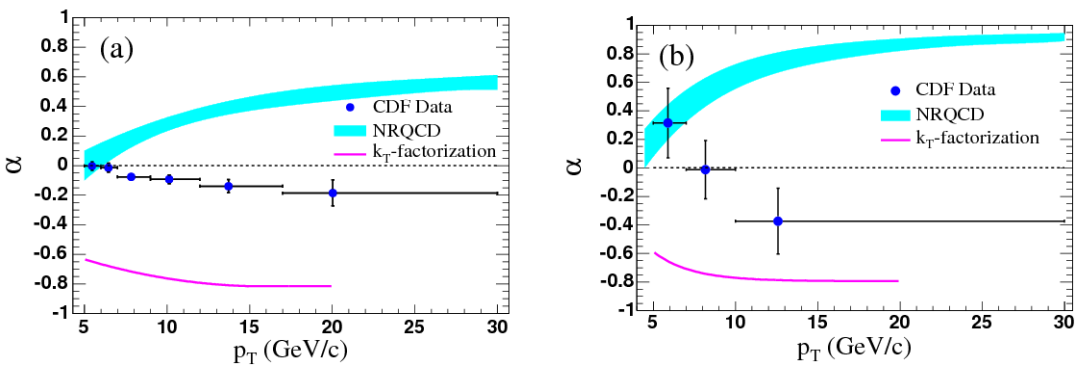

Figure 2.8: J/ψ (*left*) and $\psi(2S)$ (*right*) polarizations ($\alpha \equiv \lambda_\theta$) in the Helicity frame as a function of p_T and for $|y| < 0.6$ measured by the CDF collaboration. Data are compared with theoretical predictions from NRQCD [25, 63, 67] and the k_T factorization model [68]. Figure from [29].

terms of the $\tilde{\lambda}$ parameter in Collins-Soper and Helicity frames, compatible with zero in the full p_T range. In Figure 2.9 (right) the inconsistency among CDF Run I and CDF and D0 Run II measurements is shown as an illustration of the unclear experimental situation at the time.

Results from RHIC

The PHENIX collaboration measured the inclusive J/ψ polarization in the central rapidity region $|y| < 0.35$ and for $p_T < 5$ GeV/c in the Collins-Soper, Helicity and Gottfried-Jackson frames in pp collisions at $\sqrt{s} = 200$ GeV [70]. The results and comparison with theoretical predictions are shown in Figure 2.10 for the Helicity frame. The measurements

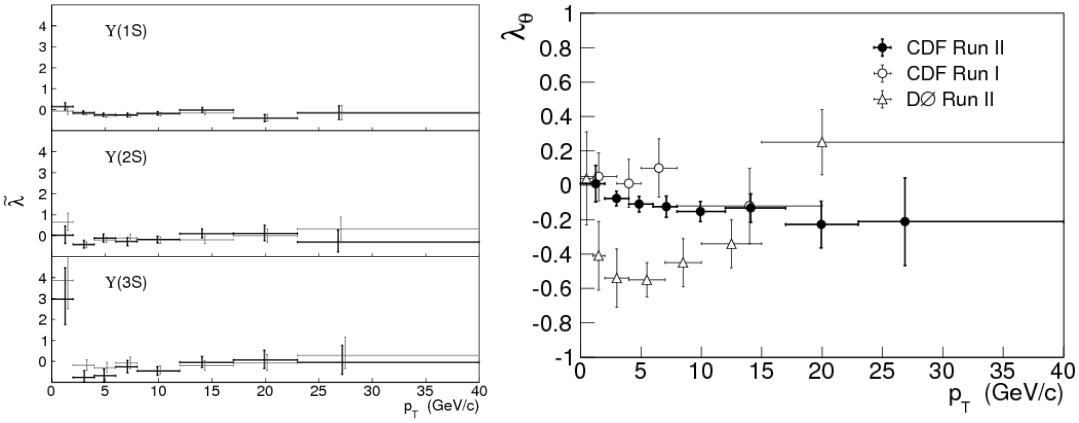

Figure 2.9: *Left*: $\tilde{\lambda}$ parameter in Collins-Soper (dark points) and Helicity (gray points) frames for Υ(1S), Υ(2S) and Υ(3S) as a function of p_{T} and for $|y| < 0.6$ measured for by CDF [69]. *Right*: Comparison of different measurements of the Υ(1S) λ_θ as a function of p_{T} in the Helicity frame. Figure from [69].

are compatible with a small J/ψ longitudinal polarization slightly increasing with p_{T}.

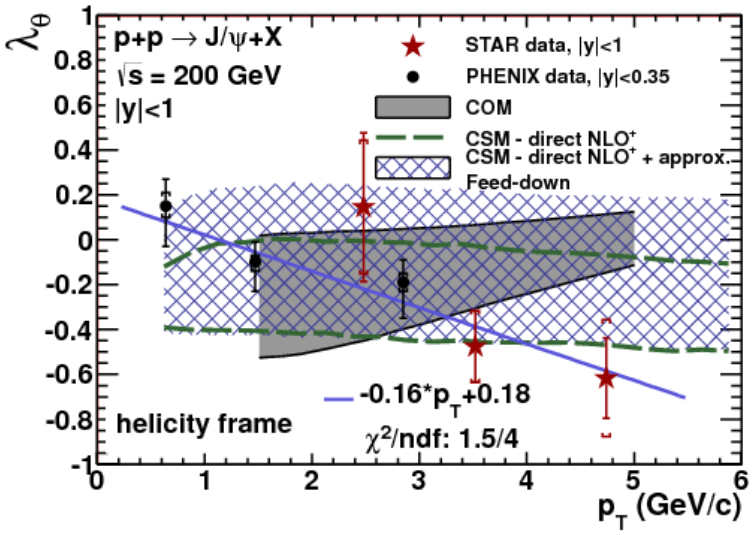

Figure 2.10: J/ψ polarization parameter λ_θ as a function of p_{T} in the Helicity frame measured at central rapidity in pp collisions at $\sqrt{s} = 200$ GeV by the PHENIX [70] and STAR collaborations [71]. Data are compared to theoretical predictions from [72] and [73] (Figure from [71]).

Figure 2.10 also shows the comparison between PHENIX and STAR results. The STAR collaboration measured the inclusive J/ψ polarization in pp collision at $\sqrt{s} = 200$ GeV [71] for central rapidity ($|y| < 1$) and p_{T} from 2 to 6 GeV/c. The study was performed in the Helicity frame where the λ_θ p_{T} dependence was measured. The results show a trend towards longitudinal polarization for $p_{\mathrm{T}} > 3$ GeV/c. The theoretical calculations from

Leading Order Color-Octet Model (LO COM) [72] do not reproduce the data: the model predicts an increase of λ_θ towards transverse polarization. Calculations within the NLO* CSM [73] predict a small p_{T} dependence of λ_θ but values consistent with longitudinal polarization and there is an agreement with the data within theoretical and experimental uncertainties.
Recent results by the STAR collaboration in pp collision at $\sqrt{s}$ = 500 GeV in the same rapidity range and for J/ψ p_{T} from 5 to 16 GeV/c [74], confirm the trend towards J/ψ longitudinal polarization in the Helicity frame as p_{T} increases. The measurement is also performed in the Collins-Soper frame and for the λ_φ parameter (Figure 2.11).

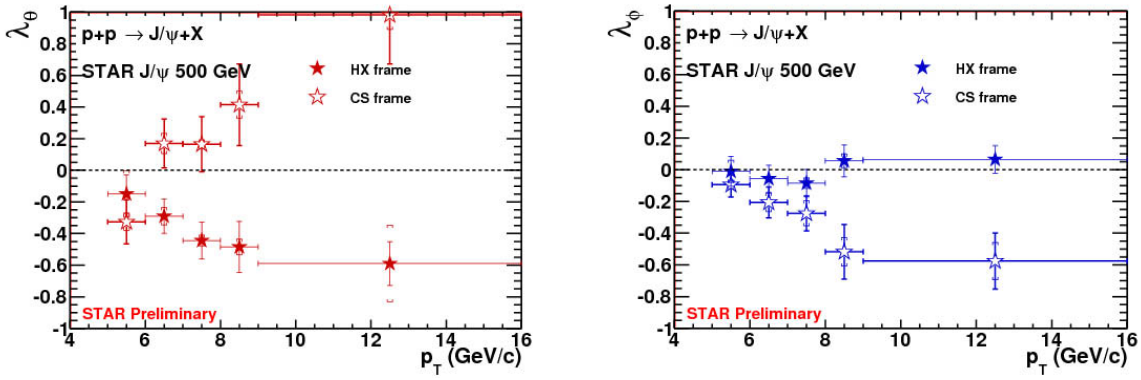

Figure 2.11: J/ψ polarization measured by the STAR collaboration in pp collisions at $\sqrt{s}$ = 500 GeV and central rapidity ($|y| < 1$). The plots show the p_{T} dependencies of λ_θ (*left*) and λ_φ (*left*) in the Helicity (HX) and Collins-Soper (CS) frames. Figure from [74].

Results from LHC

The CMS collaboration has measured the prompt J/ψ and ψ(2S) [75], and Υ(nS) [76] polarizations at mid-rapidity through the dimuon decay channel in pp collisions at $\sqrt{s}$ = 7 TeV. The measurements were performed in three different polarization frames (Collins-Soper, Helicity, and perpendicular to Helicity frame) and in the rapidity and p_{T} ranges: $|y| < 1.2$ and $14 < p_{\mathrm{T}} < 70\,\mathrm{GeV}/c$ for J/ψ, $|y| < 1.5$ and $14 < p_{\mathrm{T}} < 50\,\mathrm{GeV}/c$ for ψ(2S) and $|y| < 1.2$ and $10 < p_{\mathrm{T}} < 50\,\mathrm{GeV}/c$ for Υ(1S), Υ(2S) and Υ(3S). No evidence of large transverse or longitudinal polarization was observed for any state in the three frames studied.
The experimental values are compared to NLO NRQCD predictions from [16] for J/ψ and ψ(2S) λ_θ in the Helicity frame as shown in Figure 2.12, the measurements and predictions are in clear disagreement.
The LHCb collaboration measured the polarization of prompt J/ψ [77] and ψ(2S) [78], through the dimuon decay channel in pp collisions at $\sqrt{s}$ = 7 TeV. The measurements were performed in the Collins-Soper and Helicity frames in several rapidity bins within the rapidity range covered by the detector ($2.0 < y < 4.5$) and p_{T} from 2 to 15 GeV/c for J/ψ and from 3.5 to 15 GeV/c for ψ(2S). The data show a small sign of longitudinal

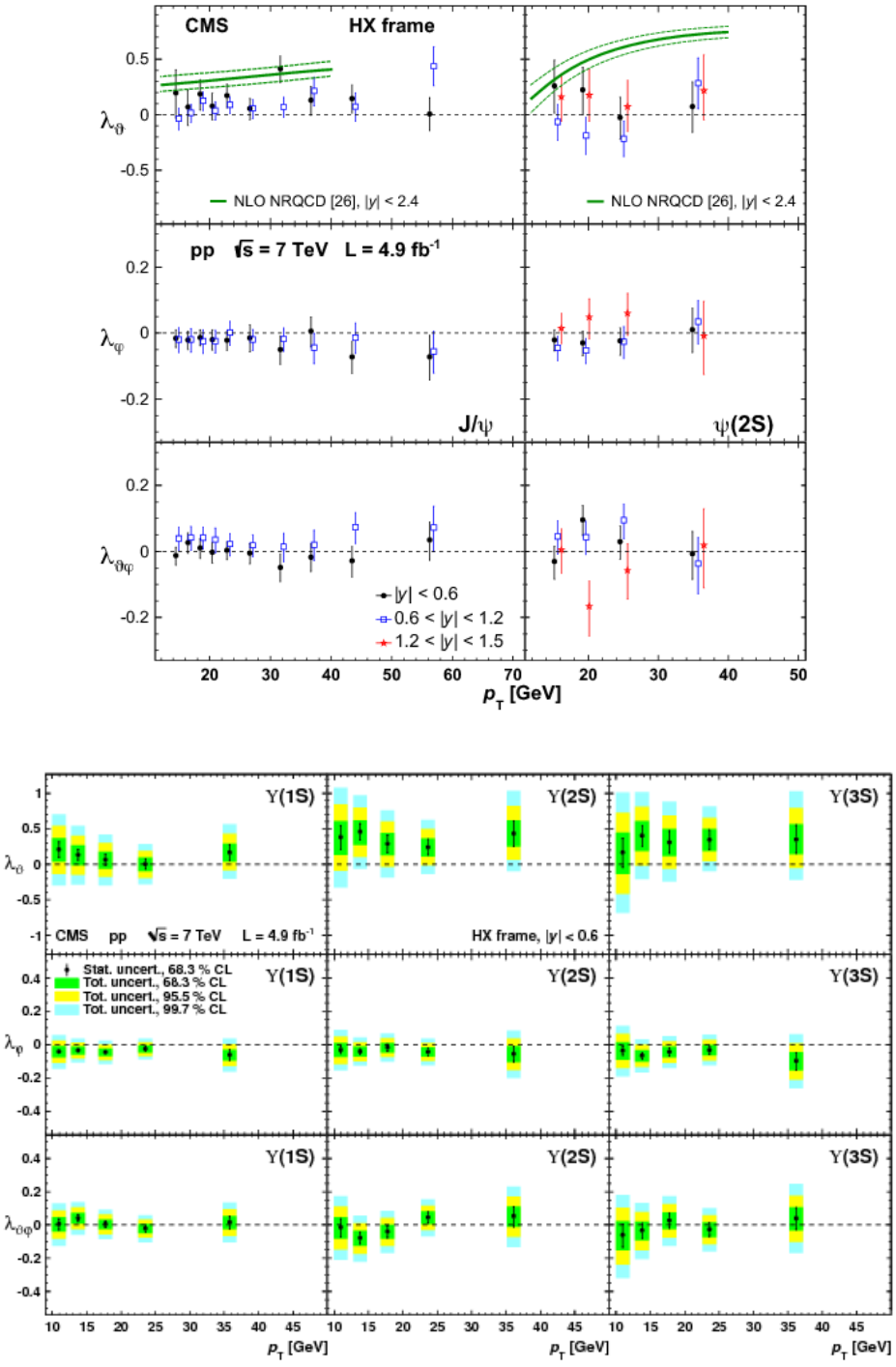

Figure 2.12: J/ψ and $\psi(2S)$ (*top*) and $\Upsilon(1S)$, $\Upsilon(2S)$ and $\Upsilon(3S)$ (*bottom*) polarization parameters as a function of p_T at central rapidity measured by CMS. The λ_θ p_T dependences for J/ψ and $\psi(2S)$ are compared to NLO NRQCD predictions from [16]. Figures taken from [75] and [76].

polarization for J/ψ in the Helicity frame with an average $\lambda_\theta = \quad 0.145 \pm 0.027$, while for $\psi(2S)$ results are compatible with zero. The λ_φ and $\lambda_{\theta\varphi}$ parameters are compatible with zero for both resonances in the whole kinematic domain studied.

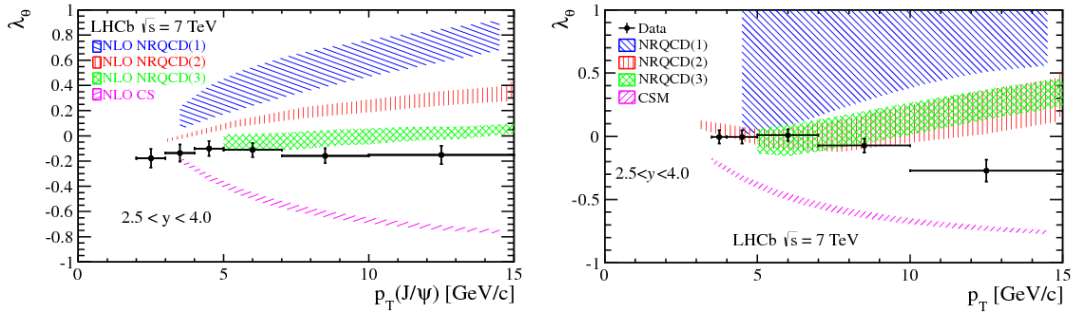

Figure 2.13: Polarization of J/ψ (*left*) and $\psi(2S)$(*right*) measured by the LHCb experiment in pp collisions at $\sqrt{s}$= 7 TeV in the rapidity interval $2.5 < y < 4.0$. Data are compared to NLO CSM from [15] and NLO NRQCD calculations from (1) [15], (2) [16] and (3) [17, 79]. Figures from [77] and [78].

Figure 2.13 shows the y-integrated ($2.5 < y < 4$) p_{T} dependence of the λ_θ values in the Helicity frame, compared to NLO CSM [15] and different NRQCD calculations [15–17, 79] (the NRQCD calculation differ in the experimental data samples used to evaluate the LDMEs). Calculations within the CSM are in strong disagreement with the data both in size and in the p_{T} dependence. It should be noted that calculations from [15] do not include feed-down contributions from χ_c and $\psi(2S)$, however the comparison with $\psi(2S)$ data, not sensitive to feed-down, also reflects a disagreement. For J/ψ resonance, the best agreement data-theory is achieved by the NRQCD calculation from [17, 79]. $\psi(2S)$ data also favors the calculations from [17, 79] and from [16] at low-p_{T} however the increasing transverse polarization at high p_{T} predicted by all NRQCD calculations is not confirmed by the data.
ALICE measured the J/ψ polarization in pp collisions at $\sqrt{s}$= 7 TeV [80]. The λ_θ and λ_φ parameters where measured in the p_{T} range from 2 to 8 GeV/c and integrated rapidity range $2.5 < y < 4.0$. Measurements were performed in the Collins-Soper and Helicity frames as shown in Figure 2.14. The J/ψ data sample collected by ALICE also contains the non-prompt contribution coming from the b-hadrons decay which is not possible to extract. It was estimated that its contribution was less important than the size of systematic uncertainties of the measurements, and therefore included within the error bars.

Figure 2.14 also shows the comparison with theoretical predictions from LO and NLO NRQCD calculations [15] including only color-singlet and color-singlet plus color-octet contributions. Measurements slightly favor the CS+CO prediction from [15].

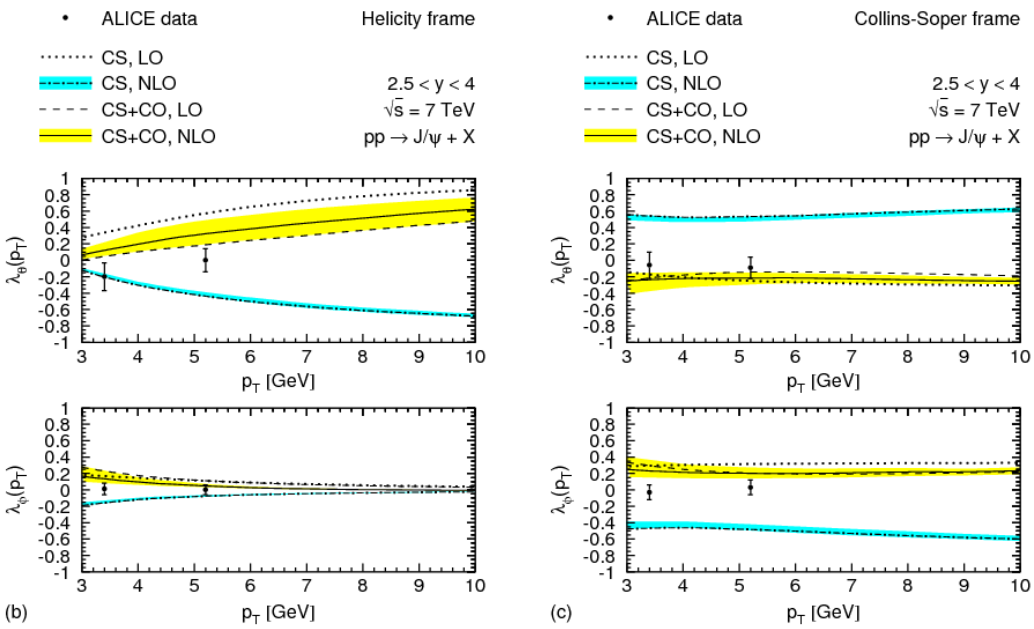

Figure 2.14: J/ψ polarization parameters λ_θ and λ_φ as a function of p_{T} in the Helicity (*left*) and Collins-Soper (*right*) frames measured at forward rapidity in pp collisions at $\sqrt{s}$ = 7 TeV by the ALICE experiment. Data are compared to predictions of different LO and NLO CS and CS+CO calculations [15]. Figure from [15].

2.3.2 Results from fixed-target experiments

The NA60 collaboration measured the J/ψ polarization in p-A collisions in the rapidity range $0.28 < y < 0.78$ and for incident proton energy of 158 and 400 GeV and target composed of several sub-targets (Be, Al, Cu, In, W, Pb and U) [81]. The measurements were performed in the Helicity reference frame (Figure 2.15 left). The λ_θ values are negative at very low-p_{T} in agreement with HERA-B results [82] and compatible with zero at higher p_{T}. λ_φ and $\lambda_{\theta\varphi}$ are compatible with zero in the kinematic range.
Results from In-In collisions show no p_{T} dependence of the λ_θ in the Helicity frame and consistent with zero polarization. The azimuthal parameter λ_φ also shows no p_{T} dependence and small values. No dependence on the centrality of the collision was observed.
The HERA-B experiment measured the J/ψ polarization in p-C and p-W collisions at $\sqrt{s}$= 41.6 GeV and in the transverse momentum interval p_{T} up to 5.4 GeV/c [82]. The measurement was performed for all polarization parameters and in three reference frames (CS, HX and GJ). The results show an asymmetry of the decay particles angular distributions which is maximal in the CS frame, and compatible with J/ψ longitudinal polarization at very low-p_{T}, and increases at higher transverse momentum.

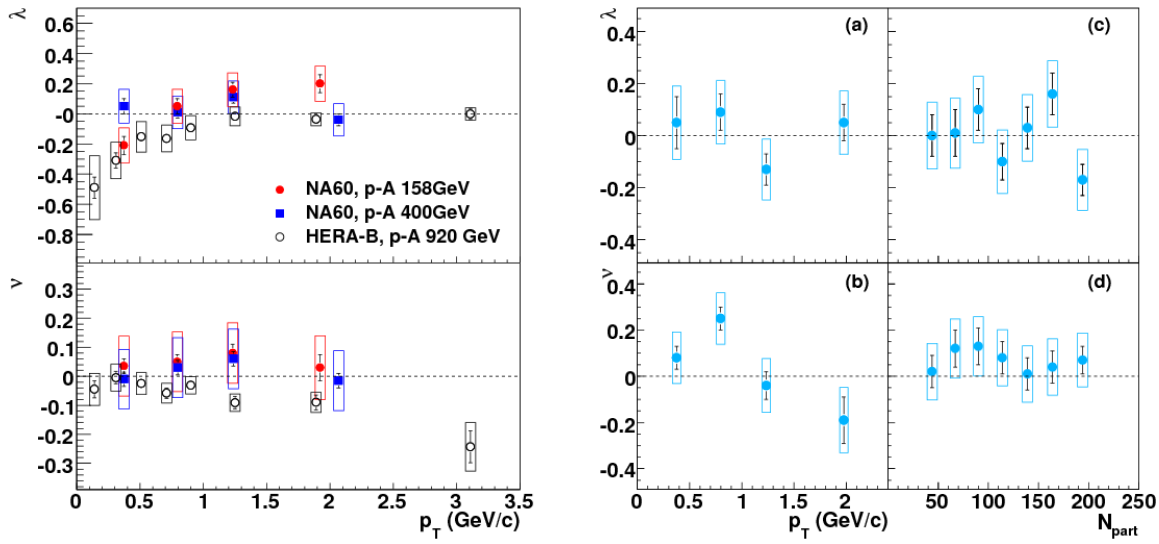

Figure 2.15: *Left*: J/ψ polarization parameters in the Helicity frame ($\lambda \equiv \lambda_\theta$, $\nu \equiv \lambda_\varphi$) measured by the NA60 collaboration in p–A collisions [81] and compared to HERA-B results [82]. *Right*: J/ψ polarization parameters in the Helicity frame measured by the NA60 collaboration in In–In collisions as a function of p_{T} (plots on the left) and centrality (plots on the right) [81].

2.3.3 Conclusions

All results obtained in the last twenty years on quarkonium polarization show the difficulty to perform experimentally this kind of measurement at hadron colliders ($p\bar{p}$, pp or p–A).

Nevertheless, the confused situation of beginning at the 2000's seems to be clarified with the LHC era and the improvement in data analysis, as illustrated by the compilation of measurements of Figure 2.16. No strong disagreement is observed between the different measurements at the LHC for data recorded in pp collisions at $\sqrt{s} = 7$ TeV.

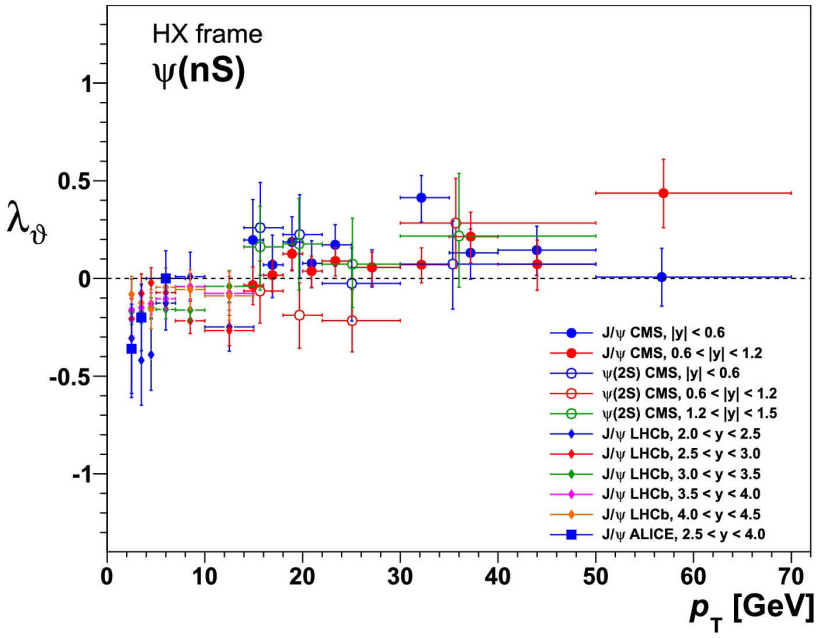

Figure 2.16: Compilation of LHC experimental results on charmonium polarization in pp collisions at $\sqrt{s} = 7$ TeV. From [83].

Chapter 3

Experimental facility

This chapter introduces the experimental context of the measurements presented in this work. It starts with a brief introduction of the Large Hadron Collider in Section 3.1. Section 3.2 gives a general description of the ALICE detector. The ALICE sub-detectors, their design requirements and performance are presented in Sections 3.3, 3.4 and 3.5. The last section briefly introduces the ALICE Upgrade strategy for the LHC Runs 3 and 4.

3.1 The Large Hadron Collider

The LHC is a synchrotron-type accelerator and collider installed between $45 - 170$ m under surface in the border between France and Switzerland (Figure 3.1), in the tunnel that originally hosted the CERN Large Electron Positron (LEP) collider. After several years of design and construction, it started operation at the end of 2009 with proton-proton collisions at center of mass energy of 900 GeV.
The LHC machine accelerates opposite direction beams in two rings of 27 km of circumference. The total rings length is composed of eight straight and eight arc sections originally conceived for radio-frequency (RF) cavities and bending magnets of the LEP machine. Four crossing points (from the original eight, numbered from 1 to 8, see Figure 3.1) have been equipped to record the data from collisions. Data is recorded by four multipurpose detectors: ATLAS [84] at Point 1, ALICE [85] at Point 2, CMS [86] at Point 5 and LHCb [87] at Point 8.
At the LHC all the RF system is concentrated at Point 4 and operates at a frequency of 400 MHz. The beam path bending is achieved thanks to very powerful (8.3 T) superconducting dipole magnets of 14.3 m length. There is a total of 1232 dipole magnets situated in the arcs and at the dispersion suppressors located at each end of the straight sections. Additionally, a total number of 392 quadrupole magnets are placed all along the arcs and straight sections for beam collimation purposes. Points 3, 6 and 7 are used for beam collimation and dumping [88].
The proton beam acceleration chain [89], see Figure 3.2 left, starts at the linear accelerator LINAC2 where protons get up to an energy of 50 MeV. The beams are then injected to the Proton Synchrotron Booster (PSB) where they get up to 1.4 GeV. They subsequently go to the Proton Synchrotron (PS) where beams reach up to 25 GeV. The last pre-LHC acceleration step is performed by the Super Proton Synchrotron (SPS). Finally, beams

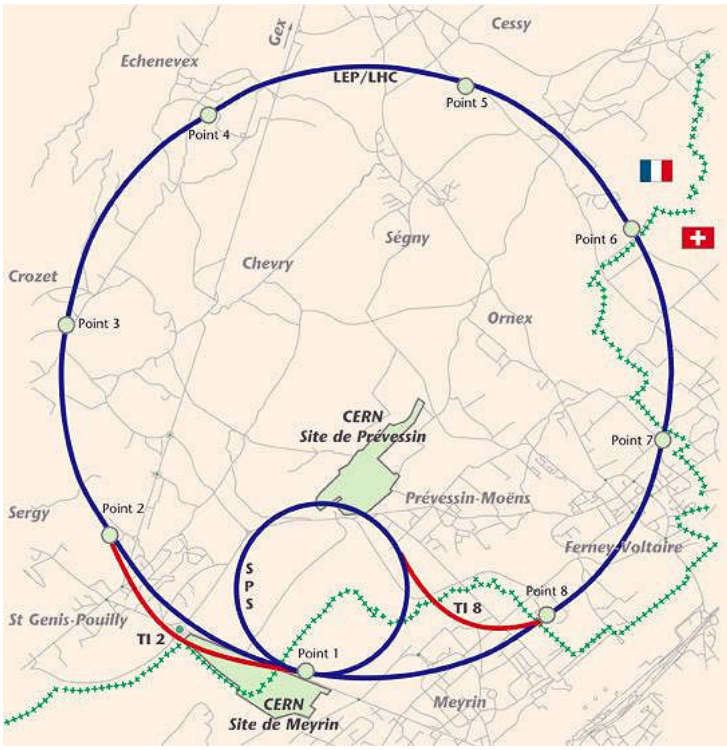

Figure 3.1: The LHC and SPS facilities, situated underground at the French-Switzerland border.

are injected to the LHC rings at energies of 450 GeV at Points 2 and 8.
The heavy ions beams follow a different path before being injected to the LHC, see Figure 3.2 right. The injection chain [90] starts at LINAC3 where the lead ions are accelerated up to 4.2 MeV per nucleon. They subsequently pass to the Low Energy Ion Ring (LEIR) where they reach up to 72.2 MeV per nucleon. After LEIR, beams are injected to the PS ring, and from this point the ions and protons beams follow the same path, i.e. they circulate in the PS where they get 5.9 GeV per nucleon, then pass to the SPS for further acceleration (up to 177 GeV per nucleon) to finally being injected at Points 2 and 8 to the LHC.
The LHC machine has been designed to achieve center of mass energies of $\sqrt{s} = 14$ TeV and $\sqrt{s_{\mathrm{NN}}} = 5.5$ TeV in pp and Pb–Pb collisions, respectively.

The standard LHC filling schemes take into account the compromise among the detectors requirements, the optimal machine performance and the injector chain capabilities. The minimum bunch spacing considered for an optimal machine performance is 25 ns for pp collisions in the four interaction points [91].
The LHC has been designed for maximum luminosities of $10^{34}\mathrm{cm}^{-2}\mathrm{s}^{-1}$ and $10^{27}\mathrm{cm}^{-2}\mathrm{s}^{-1}$ in pp and Pb–Pb collisions, respectively. Beam degradation factors such as the collisions,

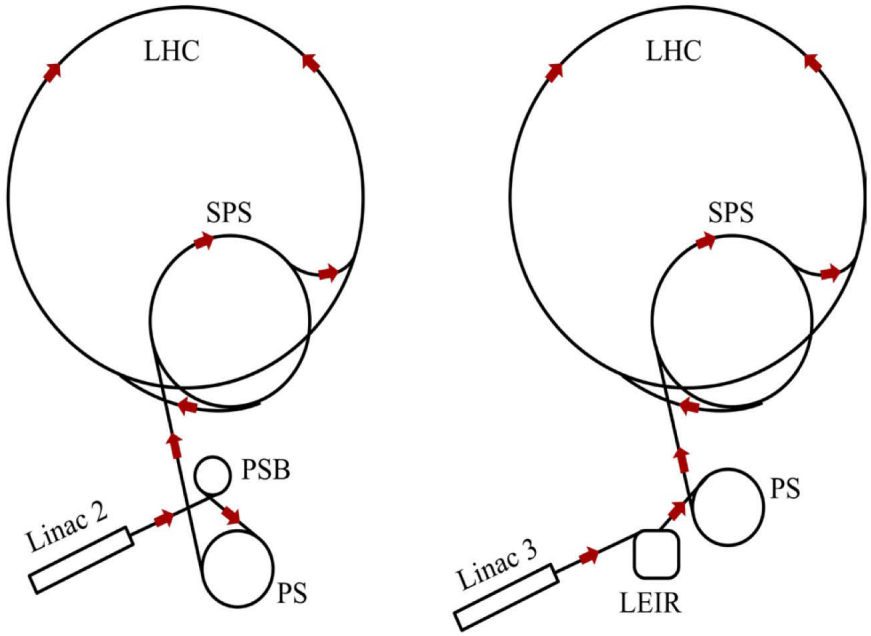

Figure 3.2: The LHC injection chain for proton (*left*) and heavy-ion (*right*) beams.

beam-gas interactions[1], and machine imperfections imply that beam intensities and luminosities decay with the time, and consequently the LHC runs last from hours or tens of hours before refilling the machine.

3.2 The ALICE detector

The ALICE detector [85] has been optimized for the study of the hot medium created in Pb–Pb collisions. At the maximum LHC luminosities in Pb–Pb collisions, the expected interaction rate is relatively low (∼10 kHz). This allows the use of slow detectors. On the other hand, the particle multiplicities are expected to be of the order of few thousands charged particles per rapidity unity at mid-rapidity, which requires the use of detectors of high granularity.
In pp collisions, where the interaction rate is much higher, in order to avoid pile-up and ageing effects, ALICE operates at limited luminosities compared to the maximum LHC luminosities. Typical luminosities for pp data taking are of the order of $10^{29}\mathrm{cm}^{-2}\mathrm{s}^{-1}$ for minimum-bias data taking and $10^{31}\mathrm{cm}^{-2}\mathrm{s}^{-1}$ with rare trigger configurations.
The ALICE apparatus is composed of 17 sub-detectors (Figure 3.3) grouped in three categories: 1. the central barrel detectors (Section 3.3), 2. forward or global detectors

[1]Beam-gas interactions refers to the interactions of particles from the beam with the residual gas in the beam pipes due to limitations of the vacuum system. The beam-gas interactions besides being one of the factors contributing to the degradation of luminosity, constitute a source of background to the experiments.

(Section 3.4) and 3. the muon spectrometer (Section 3.5).

3.2.1 The ALICE coordinate system

The ALICE coordinate system (see Figure 3.4) is a right-handed orthogonal Cartesian system. It has been defined in accordance with the LHC rules. The origin of the system $(x,y,z) = (0,0,0)$ coincides with the beam interaction point (IP). The x axis is perpendicular to the main beam direction and points to the accelerator center, the y axis is also perpendicular to the main beam direction and points upward and the z is parallel to the main beam direction at the IP2, i.e LHC anticlockwise (that means that the ALICE muon arm is at negative z).

There exists also a convention to label the different sides of the ALICE detector. The side from the IP towards positive z is labeled A, while the opposite side i.e. at negative z is labeled C, the elements around $z = 0$ are labeled B. The elements at positive and negative x are labeled Inside (I) and Outside (O), respectively. And positive and negative y are called Up (U) and Down (D), respectively.

3.2.2 The ALICE trigger system

The triggers in ALICE are handled by a hardware (the Central Trigger Processor) and a software trigger (High-Level Trigger) [92].
The Central Trigger Processor combines the trigger signals provided by several detectors to generate a trigger decision. The trigger signals delivered by the CTP are organized in three levels, depending on the different arrival times of the trigger inputs. The Level 0 (L0) decision is provided at $\sim$0.9 μs after the collision, using the inputs from V0 (Section 3.4.2), T0 (Section 3.4.3), EMCal (Section 3.3.7), PHOS 3.3.6 and the MTR (Section 3.5.3). The events accepted by L0 are then evaluated by the Level 1 (L1) trigger algorithm. The L1 decision is made $\sim$6.5 μs after L0. The L0 and L1 signals are delivered to the detectors using Local Trigger Units with a latency of 300 ns. The Level 2 (L2) decision, is constrained by the TPC drift time, so is only available after $\sim$100 μs. Once the L2 decision, the event data is sent to the Data Acquisition System (DAQ) and to the High-Level Trigger.
The CTP also takes care of downscaling certain event rates to suit the physics requirements or restrictions imposed by the bandwidth of the DAQ and HLT systems. Another important feature of the CTP is that it provides past-future protection against pile-up. The basic principle of the past-future protection is to reject events if any other event occurs within a specific time window but further events selection can be performed depending on the collision system. For instance in Pb–Pb collisions, two central collisions in the same event are non-reconstructible, so additional past-future protection specifications on the event centrality is applied in this case.
The High-Level Trigger performs the online processing of the information from all major detectors at a software level. Its main task is to select the data in order to reduce its volume while keeping the most relevant physics information.

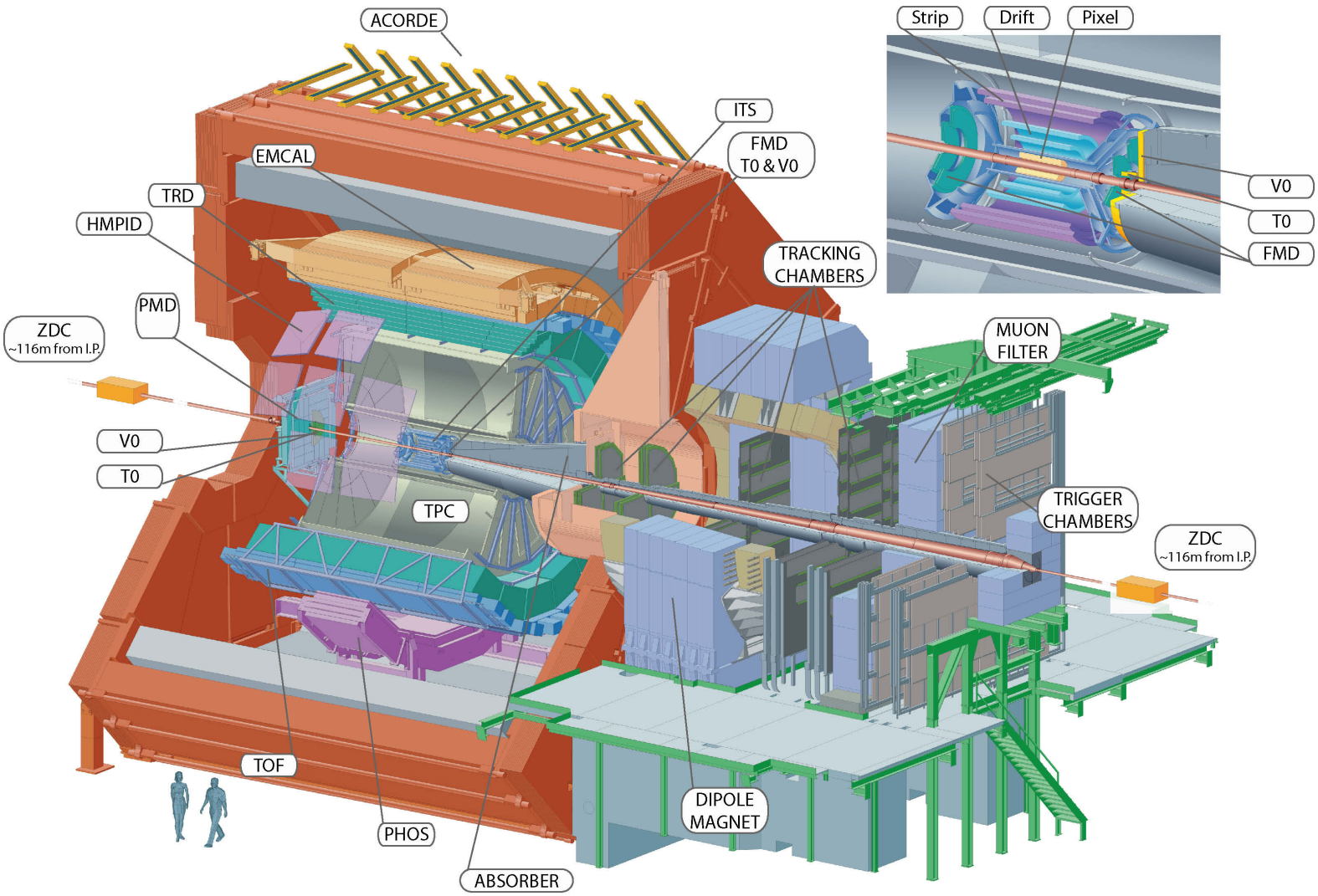

Figure 3.3: 3-D view of the ALICE detector with its different sub-detectors. The insert shows the different sub-detectors surrounding the interaction point. The length of the ALICE detector is about 24 m. The two ZDC are located at more than 100 m from the interaction point. Figure from [85].

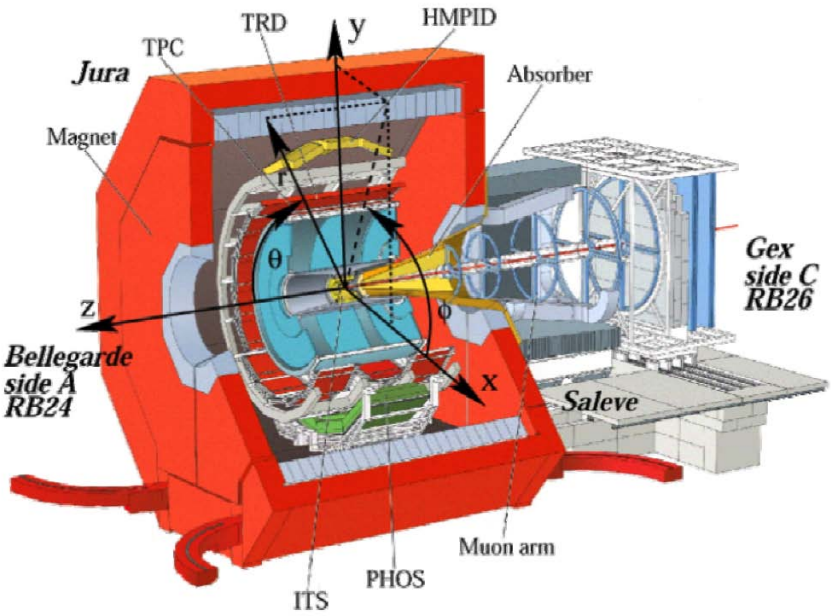

Figure 3.4: Definition of the ALICE coordinate system axis, angles and detector sides.

3.3 Central Barrel

The ALICE central barrel is composed of several detectors, starting from the interaction point towards increasing radius, the detectors are: Inner Tracking System (ITS), Time Projection Chamber (TPC), Transition Radiation Detector (TRD), Time Of Flight detector (TOF), High Momentum Particle Identification (HMPID), PHOton Spectrometer (PHOS) and the Electromagnetic Calorimeter (EMCal). All the central barrel detectors are placed inside a large solenoid magnet, called L3[2], that generates a magnetic field almost parallel to the z axis of $B \leq 0.5$ T. The central barrel detectors perform the tracking and particle identification of charged particles and photons within the pseudo-rapidity range $|\eta| \leq 0.9$. In the following the main characteristics of each detector will be described.

3.3.1 Inner Tracking System

The Inner Tracking System of the ALICE detector is a cylindrical silicon tracker surrounding the beam pipe at the IP. It has been optimized to provide precise track and primary vertex reconstruction with a resolution better than 100 μm. The ITS improves the position, angle and momentum resolution of tracks reconstructed in the TPC, identifies secondary vertices from decays of hyperons and heavy flavored hadrons, and performs the standalone reconstruction of particles that can not be detected by the TPC due to acceptance limitations.
The ITS is made of six layers of three different silicon detector technologies, the two innermost layers are made of Silicon Pixel Detectors (SPD), the next two layers are Silicon

[2]This solenoid magnet was first used by the L3 experiment during the LEP era.

Drift Detectors (SDD), and the outermost layers are Silicon Strip Detectors (SSD) (Figure 3.5).

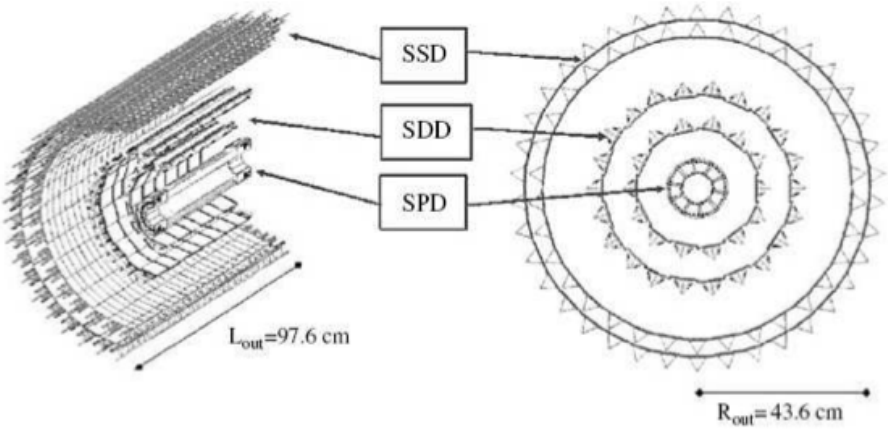

Figure 3.5: The ITS layout showing the six layers of silicon detectors, from the interaction point to its outer surface: 2 SPD, 2 SDD and 2 SSD layers.

The SPD layers are formed by bi-dimensional sensor matrix modules. Both SPD layers have 240 matrix modules in total (for a total number of 9.8×10^6 pixels), arranged in 10 azimuthal sectors, each sector containing 8 and 16 modules in the inner and outer layer respectively. The spatial resolution reached by the SPD is of the order of 12 and 100 μm in $r\phi$ and z respectively. The SPD layers cover an extended pseudo-rapidity range ($|\eta| < 2.0$ and $|\eta| < 1.4$ respectively) in order to, together with the FMD (Section 3.4.4), provide continuous coverage for the measurement of charged particles multiplicities.
The SDD layers are composed of a total of 14×6 (14 ladders of 6 modules) and 22×8 modules in the first and second SDD layers respectively. Each SSD module is divided in 2 drift regions (with drift field of $\sim$ 500 V/cm) by a central cathode, and the anode rows are parallel to the z direction; the position along $r\phi$ coordinate is determined by the drift time of ionization electrons (using as a reference the trigger time) and the z position is obtained as the centroid of the collected charge along the anodes. The SDD layers configuration allows a position precision of 35 μm in $r\phi$ and 25 μm in z.
The SPD and SDD technologies and their segmentation design were driven by the requirement on the impact parameter resolution in the high particle density environment of heavy-ions collisions.
The SSD layers are composed of a total of 1698 modules (of double-sided strip detectors) arranged in 34 and 38 ladders for the inner and outer layer respectively. Modules are disposed inside ladders in order to get the optimal spatial resolution of $\sim$ 20 μm) in the $r\phi$ direction (while in the z direction it is $\sim$ 830 μm) and to provide continuous pseudo-rapidity coverage.
The SDD and SSD layers are used for particle identification via specific energy loss for low-momentum and highly ionizing particles.
The specific energy loss per unit path length $\mathrm{d}E/\mathrm{d}x$ is determined for each track using the truncated mean of the $\mathrm{d}E/\mathrm{d}x$ measurements of each layer. For each layer the $\mathrm{d}E/\mathrm{d}x$ is calculated track by track, and it is given by the measured cluster charge normalized by the

path length (obtained from the reconstructed track parameters). The $\mathrm{d}E/\mathrm{d}x$ measurements combined with stand-alone tracking capabilities of the ITS provide low momentum particle identification up to a minimum of ∼100 MeV/c for pions, 200 MeV/c for kaons, and 400 MeV/c for protons. Figure 3.6 shows the stand-alone PID performance of the ITS in Pb–Pb collisions at $\sqrt{s_{\mathrm{NN}}} = 2.76$ TeV during the LHC Run 1.

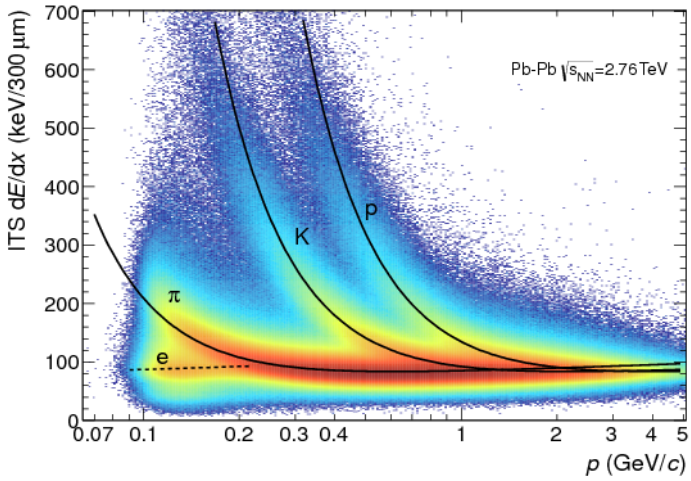

Figure 3.6: Specific energy loss $\mathrm{d}E/\mathrm{d}x$ in the ITS as a function of the particles momenta in Pb–Pb collisions at $\sqrt{s_{\mathrm{NN}}} = 2.76$ TeV. Figure from [93].

3.3.2 Time Projection Chamber

The TPC is the main tracking detector of ALICE. It has a cylindrical shape, with an inner radius of 85 cm, an outer radius of 250 cm and an overall length of 500 cm along the beam direction. Its volume is filled with 90 m^3 of a gas mixture composed by Ne, CO_2 and N_2 and is divided into two halves by a central electrode (Figure 3.7).
The central electrode, together with a voltage divider network at the surfaces of the inner and outer cylinders, create a highly uniform electrostatic field (of 400 V/cm) in each of the two halves, converting them in symmetric drift regions, with readout elements placed at both end-plates. The end-plates are divided in 18 trapezoidal sectors, each sector composed by two readout chambers based on Multi-Wire Proportional Chamber (MWPC) technology with cathode pad readout. The pad sizes vary in accordance to the radial dependence of track density, with a total of 159 pad rows along the radial direction.
The ionization electrons created by charged particles inside the TPC volume, drift to the end plates[3] where their positions in the XY plane are precisely determined. The distance from their creation point to the end plates is also estimated by measuring their arrival

[3]The maximum electrons drift time is about 90 μs. This constitute the main limiting factor to the interaction rates at which ALICE can be operated. It is the reason why the luminosity delivered by the LHC in pp collisions has to be reduced, in order to avoid pile-up effects.

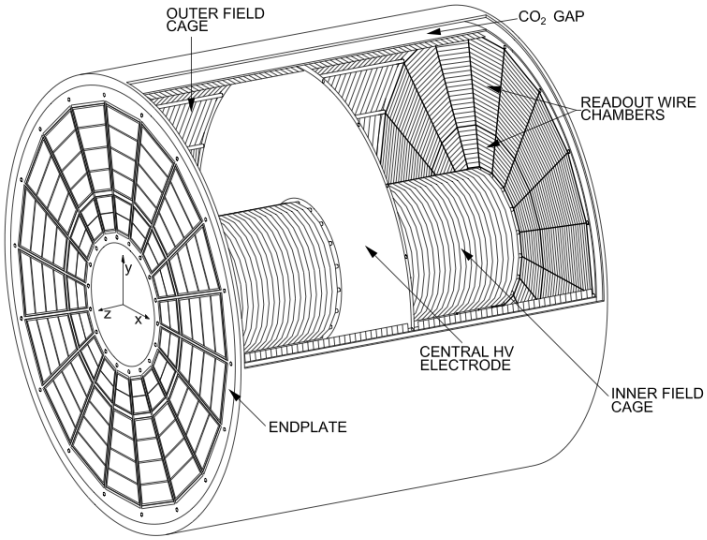

Figure 3.7: 3-D view of the TPC field cage.

time relative to an external reference, thus providing precise three-dimensional information of charged particles trajectories.
Figure 3.8 left shows the TPC tracking efficiency as a function of p_{T} for Pb–Pb and pp collisions, it does not depend significantly on the occupancy of the detector; at low p_{T} values it suddenly drops due to energy losses and multiple scattering interactions preventing particles to reach the detector volume.
Additionally, the $\mathrm{d}E/\mathrm{d}x$ is estimated track by track, allowing to perform particle identification over a wide range of momentum, from few hundreds of MeV/c up to about 20 GeV/c. The $\mathrm{d}E/\mathrm{d}x$ values are estimated for each track using the clusters associated to them. For each cluster the amplitude at the local maximum is divided by the corresponding track length, and $\mathrm{d}E/\mathrm{d}x$ is afterwards calculated by a truncated mean method. The TPC performance for particle identification is illustrated in Figure 3.8 right.
The TPC gas composition, the segmentation of cathode pads and the readout electronics have been optimized to provide a track finding efficiency larger than 80% (Figure 3.8), a good two-track separation in the region $p_{\mathrm{T}} < 10$ GeV/c and $|\eta| < 0.9$ and good charged particle momentum resolution in the range from 100 MeV/c to 100 GeV/c and particle identification with $\mathrm{d}E/\mathrm{d}x$ resolution better than 10%, all in a high multiplicity environment such as the conditions reached with Pb–Pb collisions at nominal LHC luminosity.

3.3.3 Transition Radiation Detector

The main purpose of the TRD is the identification of electrons for momenta above 1 GeV/c and in conjunction with the data from the ITS and TPC, contribute to the study of light and heavy vector-mesons production, the dilepton continuum, and open-heavy flavors through their semi-leptonic decays, in pp and Pb–Pb collisions.
The TRD consists of 6 individual layers divided in 18 azimuthal sectors with 5-fold seg-

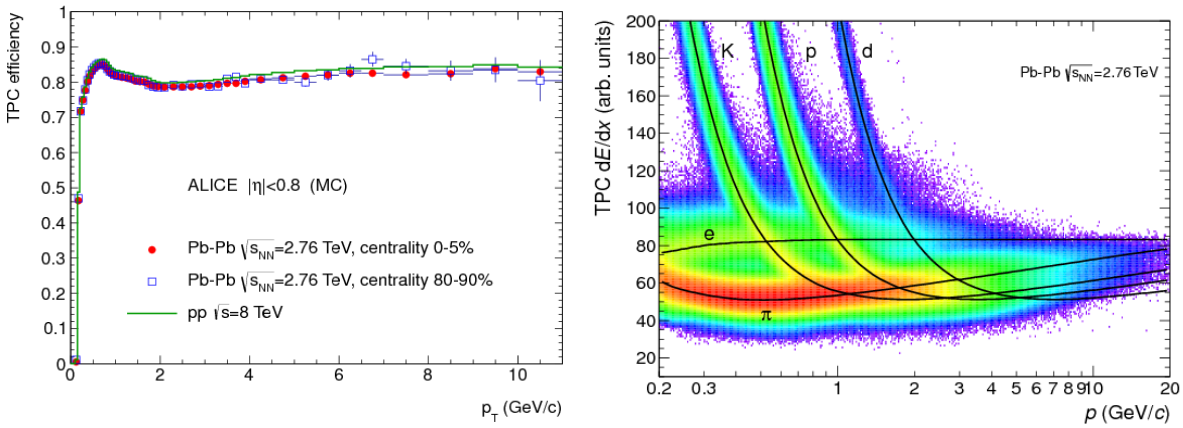

Figure 3.8: *Left:* TPC tracking efficiency as a function of p_T for pp at $\sqrt{s} = 8$ TeV and Pb–Pb at $\sqrt{s_{\mathrm{NN}}} = 2.76$ TeV collisions for two centrality ranges. *Right:* Specific energy loss $\mathrm{d}E/\mathrm{d}x$ in the TPC as a function of the particles momenta in Pb–Pb collisions at $\sqrt{s_{\mathrm{NN}}} = 2.76$ TeV. Figure from [93].

mentation along the beam direction for a total of 540 modules (Figure 3.9).

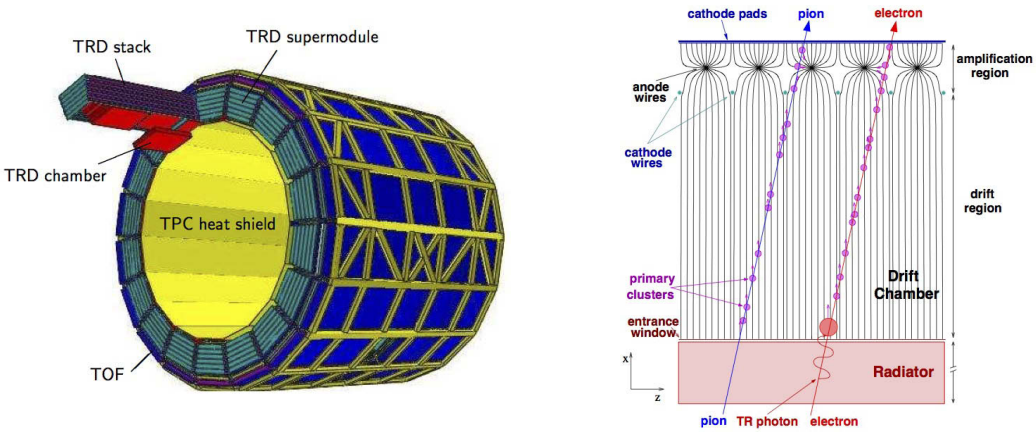

Figure 3.9: 3-D view of the TRD surrounded by TOF (*left*) and scheme of a TRD module (*right*).

Each module is formed by a radiator of 4.8 cm thickness, a readout chamber and the front-end electronics associated to this chamber (Figure 3.9 right). The radiator is composed of a 3.2 cm of polypropylene fiber sandwiched between two Rohacell foam sheets 0.8 cm thick each, and its outer surface is reinforced with 0.1 mm carbon fiber sheet. The readout chamber is filled with a mixture of Xe and CO_2 gases and operates at a drift field of 700 V/cm; it is divided in a drift and conversion region, 30 cm thick, and a Multi-Wire Proportional Chamber with cathode pad readout 7 cm thick.
Charged particles and transition radiation photons (produced in the radiator by the electrons) produce ionization and X-ray conversions electrons respectively, that drift towards

the anode wires inducing signals on the cathode pads. The cathode pads signals are sampled in time bins and in this way the specific energy losses per unit path length, and the transition radiation energy can be measured. The TRD perform pion rejection up to a factor 100 for electrons with momenta above 1 GeV/c, based on the dE/dx and the transition radiation measurements. The ratio of collected charge by the adjacent pads allows to reconstruct the track segment position for each chamber, and from its inclination (it is assumed that tracks come from the primary vertex) to estimate their momentum. The TRD detector also provides information on dE/dx of particles thus improving the identification of hadrons. The distributions of deposited energy in each layer are obtained for the different kind of particles so the PID weights are estimated, and then used to assign and overall probability P_i (probability of being a particle of type i) for the six layers. The TRD identification capabilities are enhanced trough the transition radiation energy measurements, providing good electron/pion separation, as can be seen in Figure 3.10.

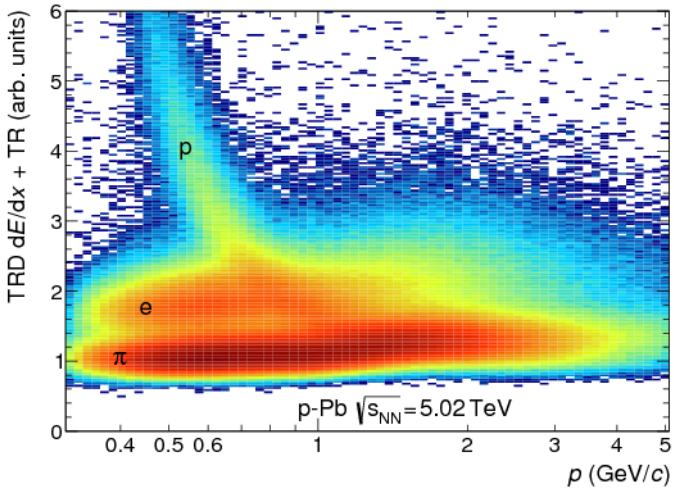

Figure 3.10: dE/dx and transition radiation combined measurements in the TRD as a function of momenta in p–Pb collisions at $\sqrt{s_{\mathrm{NN}}} = 5.02$ TeV. Figure from [93].

3.3.4 Time Of Flight

The TOF detector covers a cylindrical surface of about 160 m^2, between radius 370 and 399 cm, it is the outermost detector having full azimuthal coverage (see Figure 3.9 left). The TOF detector elements are Multi-Gap Resistive Pad Chamber, arranged in the 18×5 modules. The strip geometry as well as the size of readout pads have been chosen in order to cope with the maximum foreseen charged particle multiplicity density, keeping the occupancy level at a maximum of 16 % at the highest charged particle density, while the number of gaps and gap spacing are optimized for a time resolution better than 100 ps. The TOF detector has been designed to perform particle identification in the intermediate momentum range by the time of flight technique, using as a reference the time provided by the T0 detector (Section 3.4.3). It identifies pions and kaons up to 2.5 GeV/c, protons

up to 4 GeV/c with a π/K and K/p separation better than 3σ. The overall time resolution for particle identification in TOF is 86 ps in Pb–Pb and 120 ps for pp collisions, which allows a good particle separation up to momenta 2.5 GeV/c for pions and kaons, and 4 GeV/c for protons and kaons. Figure 3.11 illustrates the good performance of TOF for particle identification in Pb–Pb collisions at the intermediate momentum range (as measured by the TPC).

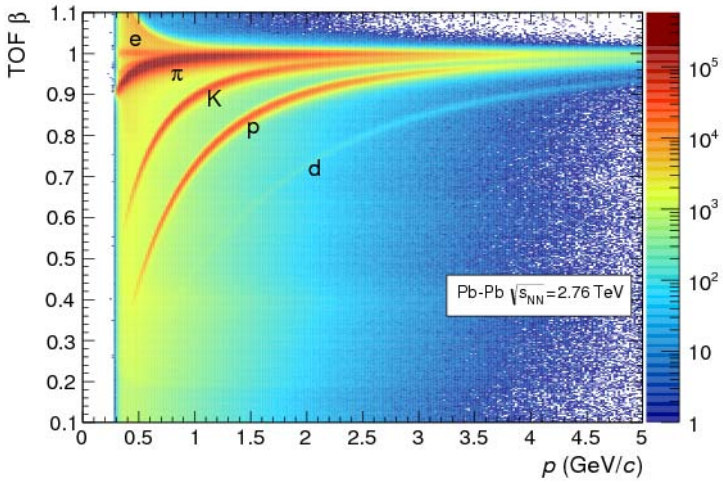

Figure 3.11: Distribution of the TOF measured velocity β versus tracks momentum in Pb–Pb collisions at $\sqrt{s_{\mathrm{NN}}} = 5.02$ TeV. Figure from [93].

3.3.5 High Momentum Particle Identification

The HMPID detector is aimed to enhance the particle identification capabilities of ALICE, it identifies high momentum hadrons, for which the $\mathrm{d}E/\mathrm{d}x$ (in the ITS and TPC) and time of flight (in TOF) measurements do not provide enough separation power on a track-by-track basis. The PID capabilities are extended up to 3 GeV/c for the separation between pions and kaons and up to 5 GeV/c for kaons and protons (Figure 3.12).
Since for Pb–Pb collisions at LHC energies, the yield of high momentum particles is relatively low, it was designed to cover only 5 % of the central barrel phase space, the pseudo-rapidity and azimuthal coverage are $|\eta| < 0.6$ and 58°, respectively (Figure 3.13 left).
The HMPID detector is composed of 7 identical modules, based on proximity focusing Ring Imaging Cherenkov (RICH) counters of 12 m^2 (Figure 3.13 right). The RICH's radiator is a 12 mm thick layer of C_6F_{14} liquid, its refractive index n (equals to 1.29 at 170 nm) establishes a momentum threshold of $p_{\mathrm{T}}^{th} \sim 1.26 \times m$ GeV/c where m is the mass of the particle. Cherenkov photons are collected by a CsI films deposited onto the cathode pad of a Multi-Wire Proportional Chamber. The proximity gap between the radiator and the MWPC have been optimized in order to improve the resolution of the measured Cherenkov angle.

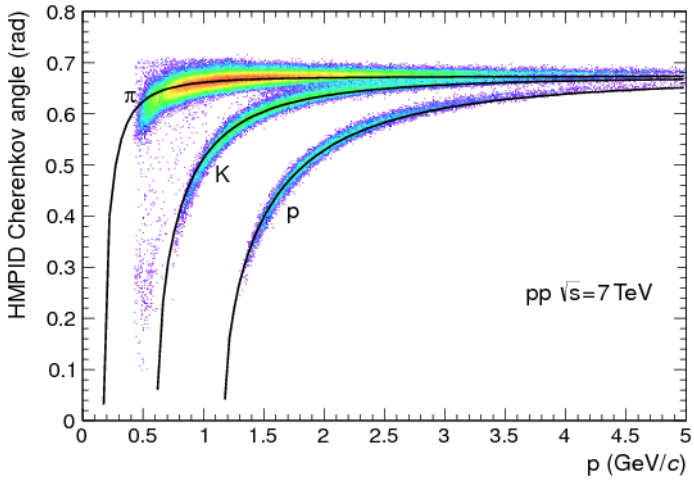

Figure 3.12: Cherenkov angle measured by the RICH modules of HMPID in pp collisions at $\sqrt{s} = 7$ TeV, as a function of track momentum. Figure from [93].

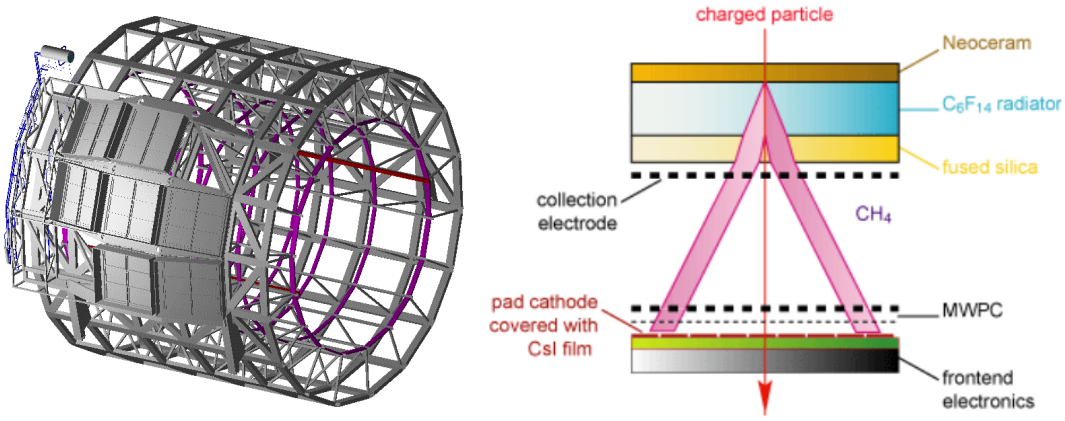

Figure 3.13: 3-D view of the HMPID detector in the TOF support (*left*) and schema of a Ring Imaging Cherenkov counter of the HMPID detector (*right*).

3.3.6 Photon Spectrometer

The Photon Spectrometer (PHOS) is one of the two ALICE electromagnetic calorimeters, it has been designed for the measurement of photons and light mesons π^0 and η through their two-photon decay channel, in a range of p_{T} that goes from hundreds of MeV/c to tens of GeV/c. Its main physics objectives are the test of thermal and dynamical properties of the initial phase of the collisions, by means of low p_{T} direct photons and the study of jet quenching through the measurement of high-p_{T} π^0 and γ-jet correlations.
PHOS is placed at a radius of 460 cm and has 100° azimuthal coverage. The detector is divided in 5 modules each containing an electromagnetic calorimeter EMC and a Charged Particle Veto (CPV) detector. The EMCs are based on $PbWO_4$ scintillator crystals (64×56 cells each module) readout by Avalanche Photo-Diodes (APD). The CPVs consist of MWPCs with cathode pad readout, filled with a mixture of Ar and CO_2.

To discriminate photons against charged and neutral hadrons, the contributions to the deposited energy in the crystals by the hadrons can be refused by selection cuts on the energy after clusterization or by analyzing shower shape parameters. The CPV detectors located in front of the EMCs, perform additional charged hadron rejection.

3.3.7 Electromagnetic Calorimeter

The ALICE EMCal covers the region between the HMPID and PHOS with an azimuthal covering of $\sim 110°$ and pseudo-rapidity range $-0.7 \leq \eta \leq 0.7$. It is divided in 12 supermodules containing a total of 12 288 cells based on layered lead-scintillator sampling calorimeter with wavelength shifting fibers for light collection coupled to APD.
EMCal measures high momentum photons, π^0 and electrons, it provides electron-hadron separation for momenta larger than 10 GeV/$c$and γ/π^0 discrimination up to 30 GeV/c. It significantly improves jet measurements in ALICE by accounting for their neutral energy. Additionally it functions as a trigger on high energy jets, photons and electrons.

3.4 Global Detectors

The ALICE global detectors comprise the Zero Degree Calorimeter (ZDC), the Photon Multiplicity Detector (PMD) and the so called forward detectors: the Forward Multiplicity Detector, TZERO (T0) and VZERO (V0). They are all placed around the beam pipe at different positions from the interaction point (IP) and are mainly used to determine global characteristics of the collision such as the centrality or event plane, and for triggering.

3.4.1 Zero Degree Calorimeters

The ALICE Zero Degree Calorimeters provide an estimation of the collision centrality in Pb–Pb collisions by measuring the number and energy of spectator nucleons from the collisions. For most central collisions, c (the centrality class) is lower than 50 %, it is assumed that the zero degree (with respect to the beam pipe) energy E_{ZDC} decreases, as the collision centrality increases, following the relation:

$$c \approx \frac{1}{N_{\mathrm{ev}}} \int_0^{E_{\mathrm{ZDC}}} \frac{dn}{dE_{\mathrm{ZDC}}} dE_{\mathrm{ZDC}} \tag{3.1}$$

The ZDC system is composed of 4 hadronic calorimeters: two ZN and two ZP (for neutrons and protons, respectively) placed on both sides and at 116 m from the IP, and an electromagnetic calorimeter (ZEM) placed 7 m from the IP at forward rapidities (opposed to the Muon Spectrometer).
The ZEM is aimed at improving the centrality trigger by measuring the energy of particles produced in the interaction and emitted at forward rapidities. It also helps to resolve the ambiguity between most central and peripheral collisions: in both situations the hadrons calorimeters signals are minimal because of the small number of spectator nucleons, in the first case, and due to the number of undetected nucleons (out of the hadrons calorimeters acceptance, or due to loses in the beam pipe) in the second case, correlating the hadrons

calorimeters signal with the signal from ZEM the ambiguity is resolved.
The technology used by all ZDCs is quartz fibers calorimetry: an absorber or passive material where particles showers are created, contains an array of quartz fibers separated by a distance no larger than the radiation length of the absorber. Shower particles produce Cherenkov radiation in the fibers, which propagates along the fiber up to its end where it is detected by photomultiplier tubes (PMT), providing a very fast response. The ZN calorimeters are located between the two beam pipes (which at 116 m from the IP are separated by a distance of 8 cm), while ZP are placed externally since protons are deflected by the magnetic elements of the beam line, and have bigger dimensions. Due to geometry constrains, the ZN absorbers are made of a dense material (tungsten alloy) while ZP absorbers are built of copper and zinc. For the electromagnetic calorimeters lead was used.

3.4.2 V0

The V0 detector is mainly used for triggering (MB and centrality triggers). It also provides determination of the collision centrality through particle multiplicity measurements. For central collisions, it is assumed that charged particle multiplicity dN_{ch}, increases as the collision centrality increases. It can be expressed as:

$$c \approx \frac{1}{N_{\mathrm{ev}}} \int_{N_{\mathrm{ch}}}^{\infty} \frac{dn}{dN_{\mathrm{ch}}} dN_{\mathrm{ch}} \tag{3.2}$$

so, by measuring the multiplicity of charged particles it is possible to estimate the centrality of the collision, as illustrated in Figure 3.14.

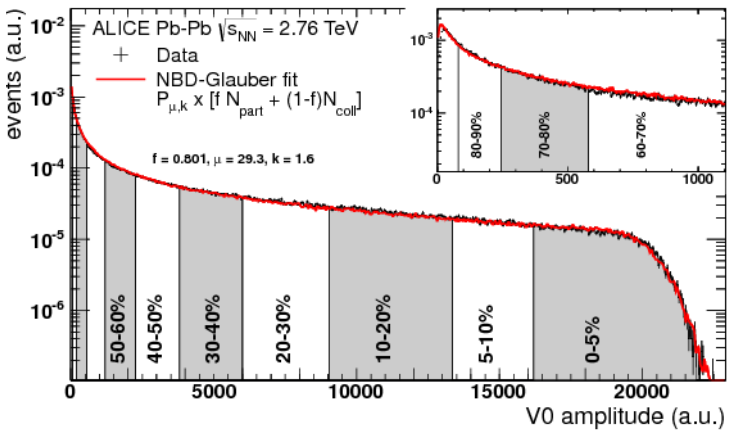

Figure 3.14: Distribution of V0 amplitudes for Pb–Pb collisions at $\sqrt{s_{\mathrm{NN}}} = 2.76$ TeV, the centrality bins have been delimited by integrating equation 3.2 from left to right.

The V0 is formed by two array of scintillator counters V0A and V0C placed on both sides of the IP (at 340 cm and -90 cm respectively). Each array is segmented radially into 4 rings, divided in 8 sectors each. Each elementary counter is made of a plastic scintillator with embedded wavelength shift fibers which are read by PMTs, the time resolution of each individual counter being better than 1 ns. A time coincidence signal between the

two arrays provides online monitoring of the luminosity delivered to ALICE.
V0 time signals are also used to discriminate between collisions and background evens at trigger level as well as in offline processing: when background events created from the interaction of circulating beams with the residual gas in the machine are produced, the V0 on the side from which the beam arrives produces and earlier signal compared with the signal time of particles coming from the IP after the collision, thus the V0 arrival times allow to discriminate between collision and background events (Figure 3.15), this information complemented with measurements of SPD allows to reject more than 90% of background events.

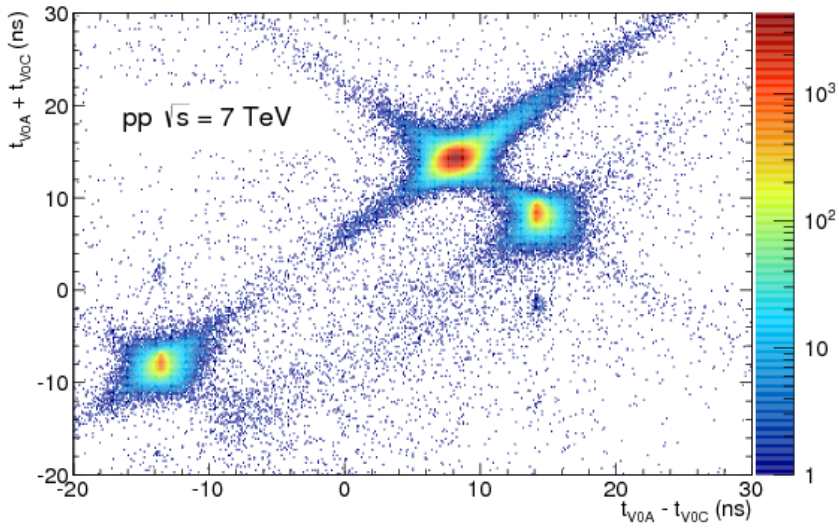

Figure 3.15: Performance of V0 detector for machine induced background rejection in pp collisions at $\sqrt{s} = 7$ TeV. The plot shows three differentiable regions corresponding to beam-beam interactions (the highest intensity region), beam from A side or beam from C side interacting with residual gas in the beam pipe, on the left and and the right regions, respectively. Figure from [93].

3.4.3 T0

The T0 detector is formed by two arrays of Cherenkov counters placed at 350 and -70 cm from the interaction point. Each array is composed of 12 counters based on a quartz radiator read by PMTs. The time resolution of each individual array is about 37 ps. Time signals from T0 are used as pre-trigger signals for TRD (prior to L0) and give the start signal to the TOF detector. It also measures particle multiplicities what makes it able to generate three possible trigger signals (MB[4] and 2 centrality triggers). The time difference between both T0 arrays allows to determine the position of the primary vertex with a precision of ±1.3 cm and then generate a L0 trigger if the estimated position of

[4]In practice, its smaller rapidity range coverage, compared to V0, makes it difficult to use T0 as minimum bias trigger.

the primary vertex is within the preset values.

3.4.4 Forward Multiplicity Detector

The FMD provide charged particle multiplicity measurements at forward rapidities ($-3.4 < \eta < -1.7$ and $1.7 < \eta < 5.0$), extending the ITS pseudo-rapidity coverage (Figure 3.16).

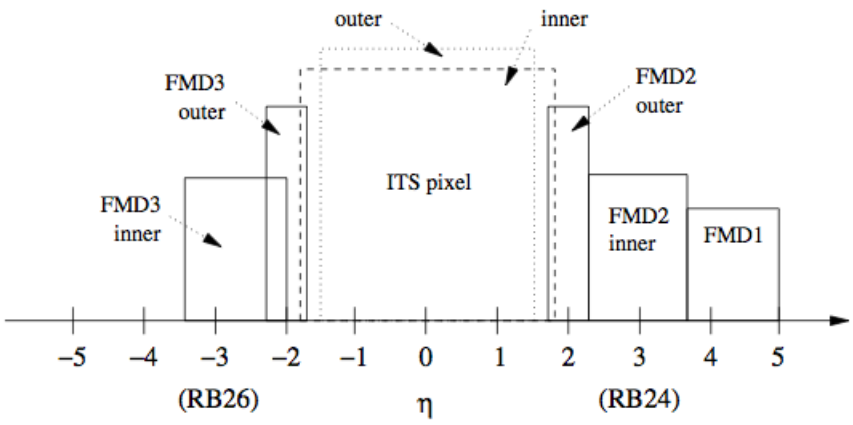

Figure 3.16: Pseudorapidity coverage of the different FMD rings and the two innermost ITS layers.

It is a Si detector formed by 5 rings placed at different distances on both sides of the IP. Rings are formed by hexagonal sensors, each sensor azimuthally segmented into 2 sectors which are radially segmented into strips, such that less than 3 particles hit the detector elements in most central (0-5%) Pb–Pb collisions and in this way, providing an accurate estimation of particle multiplicities. Multiplicity is determined in the FMD either by measuring the total energy deposited in a strip or a group of strips and dividing by the expected average energy deposition by particles, or by counting the number of strips that have been hit and comparing to the number of empty strips. The FMD also allows to determine the event plane inclination for elliptic flow studies.

3.4.5 Photon Multiplicity Detector

The PMD measures the multiplicity and spatial distribution of photons at forward rapidities and provides the estimation of transverse electromagnetic energy and the reaction plane, on an event-by-event basis.
The PMD is placed at 360 cm from the IP and covers the rapidity range $2.3 \leq \eta \leq 3.5$. It is formed by two identical detector planes separated by a lead layer $3X_0$ thick. The detector planes are formed by a large number of cells of gas proportional counters with wire readout filled with a mixture of Ar (70%) and CO_2 (30%). The front detector plane is called Charged Particle Veto (CPV) and the plane behind the lead conversion layer is called the Preshower plane. The CPV is aimed at improving the photon-hadron discrimination. Charged particles arriving at the CPV will produce hits, then pass through the

lead layer and produce signals mostly in just one of the Preshowers cells, while photons will not produce signals in the CPV but will suffer conversion in the lead layer giving rise to an electromagnetic shower, so hitting more than one cell in the preshower plane.

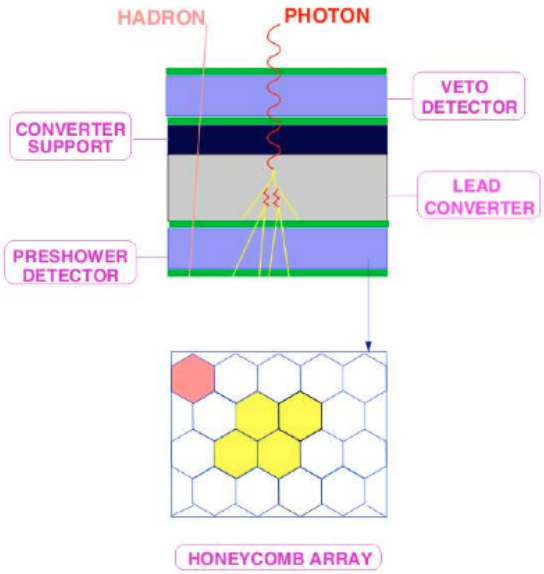

Figure 3.17: Layout of the PMD. The figure shows a representation of an hadron and a photon passage trough the detector and the activation of the preshower detector cells.

3.5 Forward muon spectrometer

The muon spectrometer performs the identification and reconstruction of muons in the pseudo-rapidity range $-4.0 < \eta < -2.5$. It has been designed for the study of heavy quarkonia (J/ψ, ψ', Υ, Υ', Υ'') and low mass mesons (ρ, ω, ϕ), as well of the open heavy flavours and weak bosons production via their muonic decay channel. The ALICE Muon Spectrometer is composed of a front absorber, a beam shield, a muon filter, a dipole magnet, and a set of trigger and tracking chambers (Figure 3.18). Its geometrical acceptance is restricted by the beam shield and the volume of the TPC. Muons are identified in the angular range from 171° to 178° (corresponding to $-4.0 < \eta < -2.5$). The front absorber material, the intrinsic spatial resolution of the tracking system and the strength of the bending magnet were conceived in order to achieve an invariant mass resolution of 70 MeV/c^2 around the J/ψ mass region and of 100 MeV/c^2 around the Υ mass, required to separate all resonance sub-states.
Figure 3.19 shows the dimuon invariant mass spectra for the the full 2011 data taking with pp collisions. The ω, ϕ, J/ψ, ψ' and Υ resonances are distinguishable by sight.

3.5.1 Absorbers and shielding

The different absorbers of the muon spectrometer have as a purpose to limit the hadronic background level for the tracking and trigger chambers. Three types of absorbers were conceived and are described in the following sections.

Front absorber

The front absorber of the Muon Spectrometer is located inside the L3 magnet, 90 cm away from the interaction point (Figure 3.18). It was designed to attenuate as much as possible the hadronic flux coming from the reaction and to suppress the low-p_{T} muon background arising from the decay of primary pions and kaons in the tracking chambers; and at the same time limiting the energy losses and small-angle scattering of traversing muons inside its material. In order to fulfill these requirements low-Z materials (carbon and concrete) were chosen for the layers closer to the IP while high-Z materials (lead, tungsten) were used for its rear end (Figure 3.20). Additionally, to avoid the contamination to other ALICE detectors from secondary particles produced inside the absorber, a lead shielding layer covers all its external area.

Beam shield

A dense absorber tube surrounds the beam pipe all through the spectrometer length to protect the tracking and trigger chambers from very small angle particles from the interaction and from the secondaries produced in the beam pipe. The beam shield is made of tungsten and lead, a stainless steal tube covers its exterior surface.

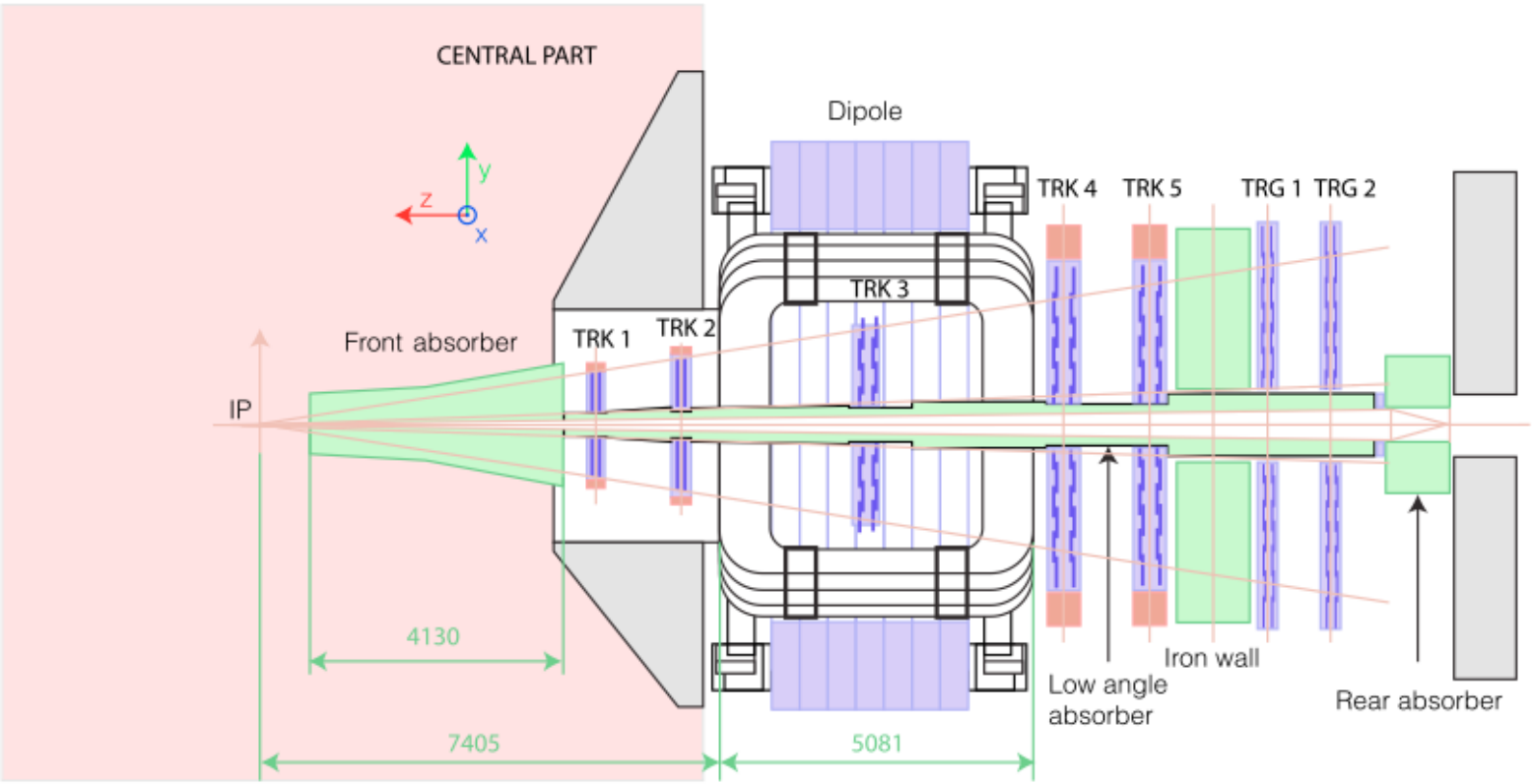

Figure 3.18: General layout of the Muon Spectrometer. From left to right: the front absorber, the five tracking stations and dipole magnet, the muon iron wall and the two trigger planes.

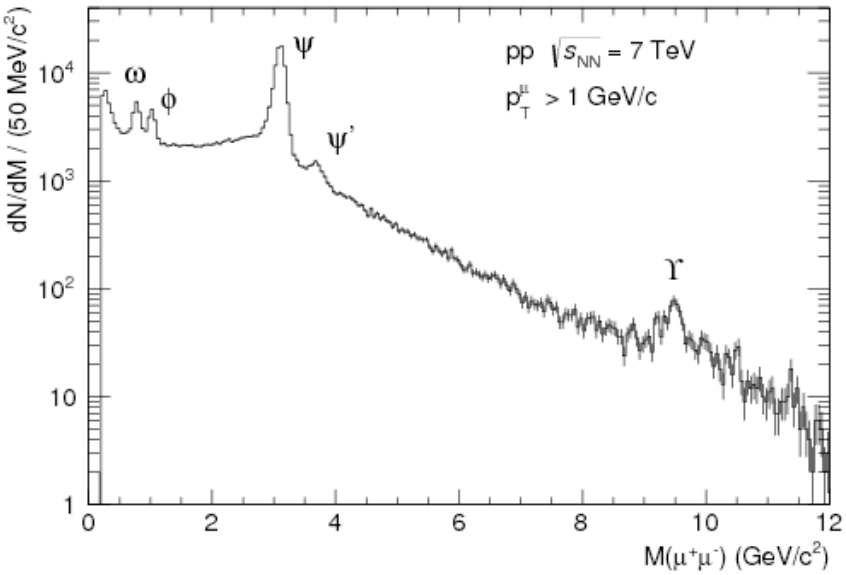

Figure 3.19: Invariant mass distribution of unlike-sign muon tracks reconstructed by the muon spectrometer in pp collisions at $\sqrt{s} = 7$ TeV.

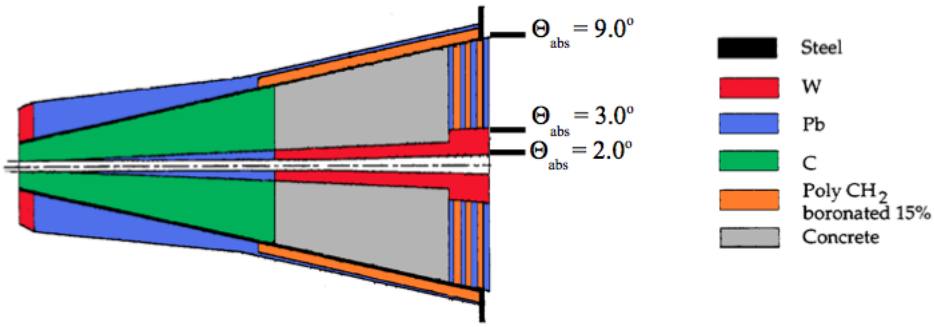

Figure 3.20: Longitudinal view of the front absorber showing its material composition.

Muon filter

This is an iron wall 1.2 m thick placed between the tracking and trigger systems (15 m away from the IP) in order to provide further hadronic background attenuation to the trigger chambers. Its presence together with the effect of the front absorber sets a minimum value of 4 GeV/c for the momenta of muons reaching the trigger chambers.

3.5.2 Tracking system

The tracking system of the muon spectrometer was conceived in order to achieve a spatial resolution of the order of 100 μm, required to resolve the bottomonium states in the large background environment of central Pb–Pb collisions. It is composed of five tracking stations, the first two of them located just behind the front absorber and before the dipole

magnet, one inside the magnet, and the other two after the magnet and before the muon filter (Figure 3.18).
Each station contains two planes of Multiwire Proportional Chambers, and each chamber is equipped with two segmented cathode planes which are both read out in order to obtain bidimensional information. Figure 3.21 shows the working principle of the MWPC. A chamber is composed of a central anode plane made of equally parallel strips, sandwiched between two segmented cathode planes. A typical high voltage of 1650 V is applied between the wires and the cathode planes. A mixture of 80% Ar, 20% CO_2 is used as ionizing gas.

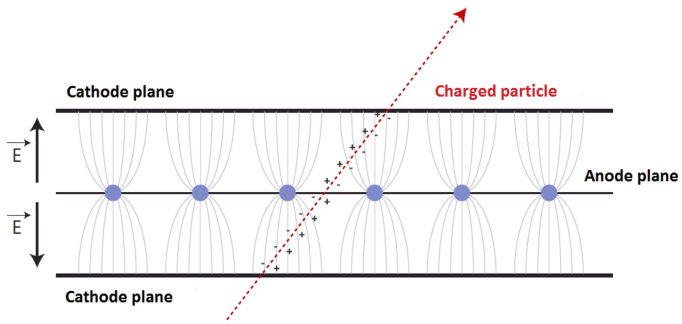

Figure 3.21: Working principle of a Multiwire Proportional Chamber.

The segmentation of the cathode pads was designed in order to keep the occupancy at a 5% level. For the first two stations where a higher particle density flux is expected (and also due to their smaller area) a higher granularity was required, cathode pads are as small as 4.2×6 mm^2 close to the beam pipe[5], and a quadrant geometry was chosen. The readout electronics is distributed over the surface of the cathode planes as can be seen in Figure 3.22 left. Due to their bigger dimensions stations 3, 4 and 5 have a slat geometry and readout electronic placed on the side of the cathode pads (Figure 3.22 right). An overlap among the slats and quadrants was foreseen in order to avoid detector dead zones. The volume between the cathode planes is filled with a composite gas mixture of 80 % Ar and 20 % CO_2 in order to minimize multiple muon scattering inside the chambers. The resulting chamber thickness corresponds to about 0.03 X_0.
The alignment of the tracking chambers is regularly adjusted in control runs performed with and without the magnetic field. Any residual misalignment due to the switching-on of the magnets or to the thermal expansion of chambers and their support in normal data taking conditions is monitored and recorded by the Geometry Monitor System (GMS).
The trajectory of particles across the five tracking stations is reconstructed by a Kalman filter based algorithm [94]. The track finding procedure starts by creating track seeds from the track segments found in the last two tracking stations and then the track seeds are followed to the first station. In order to validate a track, at least one cluster in each

[5]The pad sizes depend on the required spatial resolution which should be better than 100 μm in the bending plane (y axis), however for the non-bending plane (x axis) a resolution of about 2 mm is enough to ensure a good track reconstruction, hence the bigger size in the direction parallel to the non-bending plane.

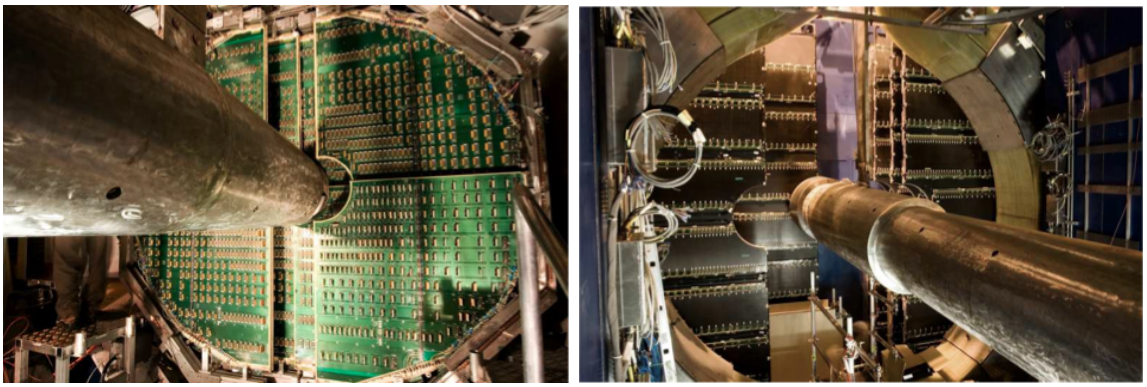

Figure 3.22: *Left*: Quadrant geometry of tracking stations 1 and 2. *Right*: Slat geometry of stations 3, 4 and 5.

of the first three stations and 3 clusters in three different chambers of stations 4 and 5 are required. Also, the matching with Muon Trigger tracks is required. The reconstructed tracks are then extrapolated to the measured primary vertex position and their parameters corrected by the multiple scattering and energy losses in the front absorber.
The track reconstruction efficiency in Pb–Pb collisions during Run 1 is shown in Figure 3.23. The drop in the tracking efficiency for the most central collisions is associated to fake tracks. After the $p \times$ DCA and normalized χ^2 cuts on track quality, the relative loss is efficiency for the most central collisions is significantly improved.

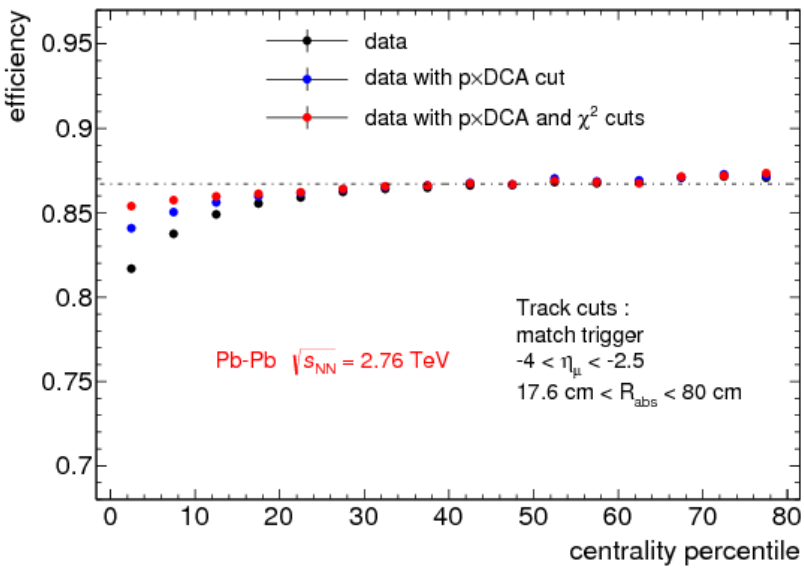

Figure 3.23: Muon track reconstruction efficiency in Pb–Pb collisions at $\sqrt{s_{\mathrm{NN}}} = 2.76$ TeV as a function of the centrality of the collision. Figure from [93].

Dipole magnet

The dipole magnet is placed 7 m away from the interaction point, it is equipped with resistive coils on a horseshoe shape. The dipole magnet provides a nominal field of 0.7 T in the x direction and 3 Tm field integral from the IP to the Muon filter which deflects charged particles passing through it, thus allowing the determination of particle charge and momenta.

3.5.3 Trigger system

The purpose of the muon trigger system is to select events containing muon tracks, either unlike-sign muon pairs from the decay of resonances or single muons from the open heavy flavors and W boson muonic decay channel. A hardware cut on the transverse momentum of each individual muon can be applied to reduce as much as possible the background from low-p_{T} muon tracks from pion and kaon decays. Two different cuts are defined (low and high p_{T}) in the range from ~ 0.5 to ~ 4.2 GeV/c. Taking into account the compromise between efficiency and background rejection, the low-p_{T} cut optimized for J/ψ is ~ 1 GeV/c while the high-p_{T} cut, for the Υ signal is ~ 2 GeV/c. The p_{T} cut implementation is based on the deviation induced by the dipole magnet to the muon tracks and then can be measured with the use of position sensitive detectors.
The trigger system is formed by two trigger stations (called MT1 and MT2) located at 16 and 17 m from the interaction point, respectively. Each station consists of two planes of 18 single-gap Resistive Plate Chambers (Figure 3.24) providing bi-dimensional information with a spatial resolution of the order of few millimeters. The trigger planes are named MT11 and MT12 in the station one, and MT21 and MT22 in the station two. The total detector area is about 150 m^2.

The Resistive Plate Chamber (RPC) detectors are large area gaseous detectors equipped with two parallel resistive electrode plates which are connected to different potentials creating an electric field inside the gaseous volume (see Figure 3.24). The electrons produced by the incident ionizing particles drift towards the anode plates inducing a signal in the pick-up electrodes. The pick-up electrodes are segmented in parallel strips and are placed on both sides of the RPC, with 90 degrees rotation between them. The strips parallel to x-axis give the y position in the bending plane, and the strips parallel to y the x position in the non-bending plane.
The RPCs are operated in maxi-avalanche mode with a gas mixture of 89.7% $C_2H_2F_4$, 10% C_4H_{10}, and 0.3% SF_6 with 37 % relative humidity. The typical high voltage applied to the RPCs is about 10 kV. More details about the RPCs operating mode and performance during Run 1 will be given in Section 4.1.

The p_{T} cut working principle

The transverse momentum of muons crossing the trigger chambers can be estimated by measuring the deviation produced by the dipole magnet to the muon tracks (see Figure 3.25).

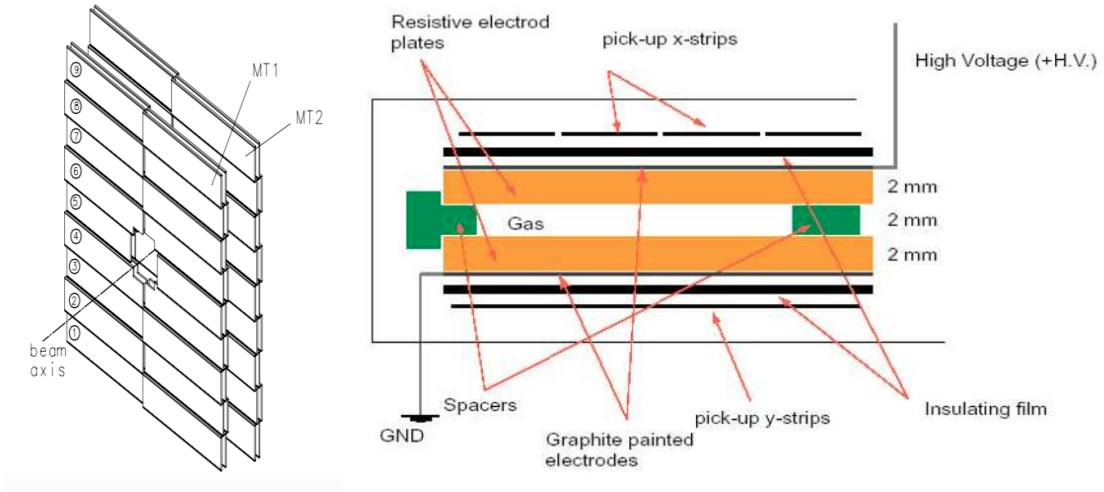

Figure 3.24: *Left*: Illustration of the two trigger stations (MT1 and MT2) each one containing two detection planes composed of 18 Resistive Plate Chambers (RPC) detectors. *Right*: Cross-sectional view of an RPC showing its different components: 2 mm thick Bakelite foils, 2 mm thick gas gap, and array of cylindrical spacers are inserted in the gap. The inner surface of the Bakelite foils are painted with linseed oil, and the outer surface with graphite, One graphite layer is connected to the HV and the second one to the ground.

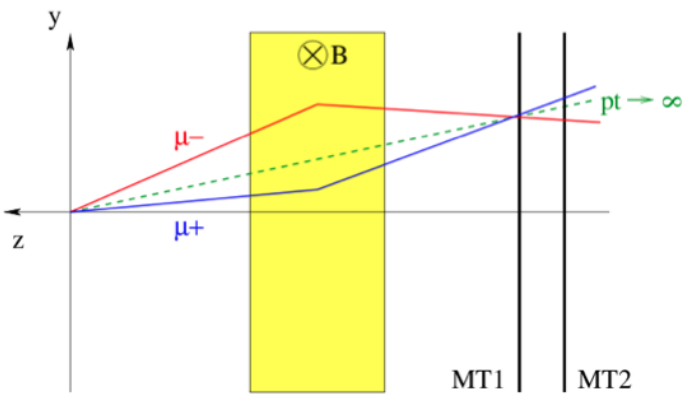

Figure 3.25: Illustration of the working principle of the muon trigger.

The muon track momentum in the bending plane yz, can be expressed as:

$$p_{\mathrm{yz}} = \left| \frac{qLB}{\theta_d} \right| \tag{3.3}$$

for small deviation angles θ_d, being L the length of the dipole magnet, q the particle's charge and B the magnetic field.

Then, the deviation angle can be calculated by the reconstructed track positions in the two trigger stations (MT1 and MT2) and is given by:

$$\theta_d = \frac{1}{z_f} \frac{z_1 y_2 - z_2 y_1}{z_2 - z_1} \tag{3.4}$$

where z_f correspond to the position of the dipole magnet along the z axis, and (y_1, z_1) and (y_2, z_2) to the muon tracks crossing positions to the first and second trigger stations. The transverse momentum component is then:

$$p_{\mathrm{T}} = p_{\mathrm{yz}} \frac{\sqrt{x_f^2 + y_f^2}}{x_f} \tag{3.5}$$

where (x_f, y_f) correspond to the position where the muon track crosses the center plane of the dipole magnet, and can be estimated by extrapolating the track positions (x_1, y_1, z_1) and (x_2, y_2, z_2) corresponding to the trigger stations 1 and 2, respectively:

$$x_f = x_1 \cdot \frac{z_f}{z_1} \quad \text{and} \quad y_f = y_2 - \frac{y_2 - y_1}{z_2 - z_1} \cdot (z_2 - z_f) \tag{3.6}$$

In practice, the trigger condition is evaluated by measuring the deviation $\delta y = y_2 - y_2^{\infty}$, where y_2^{∞} corresponds to the y position in MT2 of a muon track of infinite transverse momentum i.e. the straight line extrapolation towards the IP from the position measured at MT1. If the deviation is smaller than a given δy_{cut} corresponding to the given $p_{\mathrm{T\,cut}}$, the trigger condition is satisfied.
There are six possible trigger signal to deliver to the ALICE CTP, the corresponding trigger classes are:

- MSL: single muon track above the low-p_{T} threshold
- MSH: single muon track above the high-p_{T} threshold
- MUL: pair of unlike-sign muon tracks above the low-p_{T} threshold
- MUH: pair of unlike-sign muon tracks above the high-p_{T} threshold
- MLL: pair of like-sign muon tracks above the low-p_{T} threshold
- MLH: pair of like-sign muon tracks above the high-p_{T} threshold

The muon trigger decision is used at L0 and therefore must be provided to the CTP very fast ($\leq 1\,\mu$s).

The muon trigger chamber segmentation and electronics

The signals from the RPCs are collected in each plane by a total of 20992 strips located on both sides of the RPCs, each one connected to one Front-End Electronics (FEE) channel. The x-strips are the strips parallel to the x axis and measure the bending deviation due to the dipole magnet (y direction), which is used to estimate the tracks p_{T}. The y-strips measure the x position in the non-bending direction, this information is used to check that tracks point back to the interaction point. The RPCs read-out planes collect opposite sign electrical signals: positive signal for x-strips and negative signals for y-strips.
The strip segmentation is different for one plane and the other (bending and non-bending directions) conditioned by the spatial resolution needed for the p_{T} cut. Their sizes vary as a function of the distance from the beam pipe (see Figure 3.26) in order to keep the occupancy constant over all the detector area.

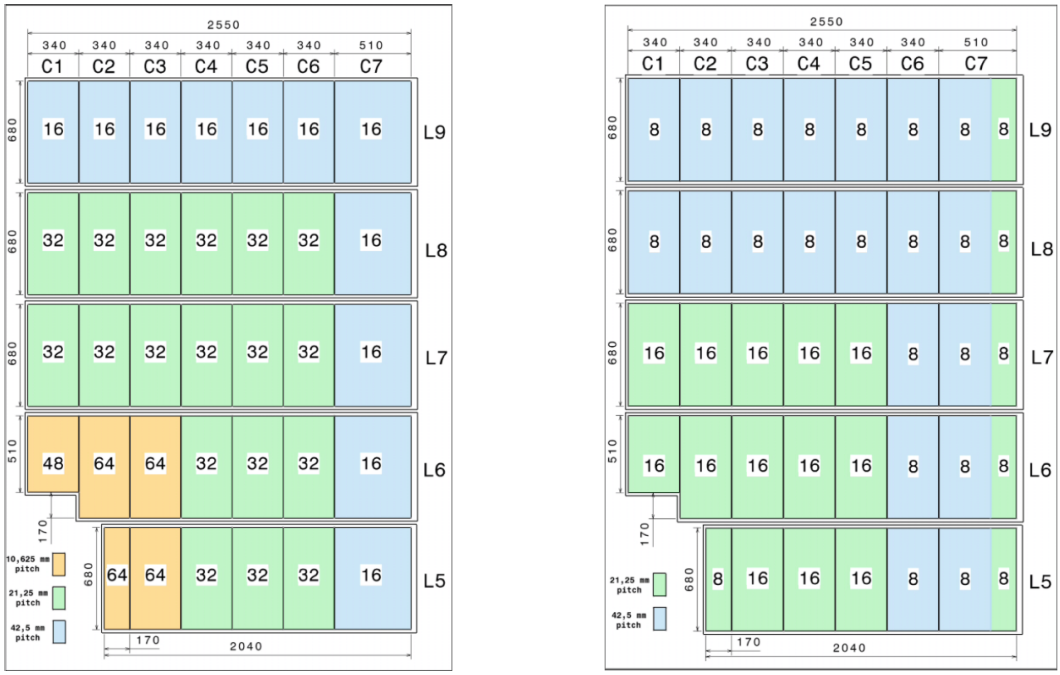

Figure 3.26: Strip segmentation in the bending (*left*) and non-bending (*right*) planes. The maps represent the top-right quadrant ($x > 0$, $y > 0$ in the ALICE coordinate system) of the first trigger plane (MT11). The different colors correspond to the regions of different strip widths: 10.625 mm (yellow), 21.25 mm (green) and 42.5 cm (blue), also the number of strips in each region is shown. The strips length vary from 170 to 510 mm in the bending plane and from 510 to 680 mm in the non-bending plane. The strip dimensions in each plane follow a projective geometry relative to the interaction point.

The FEE produces a digital signal when a valid (above threshold) analogical signal is read-out in the corresponding channel. The sequence of FEE signals is called "bit-pattern" and is labeled as X1, Y1, X2, Y2, X3, Y3, X4, Y4 for the four planes. The four X and Y patterns are then sent to the local trigger electronics.

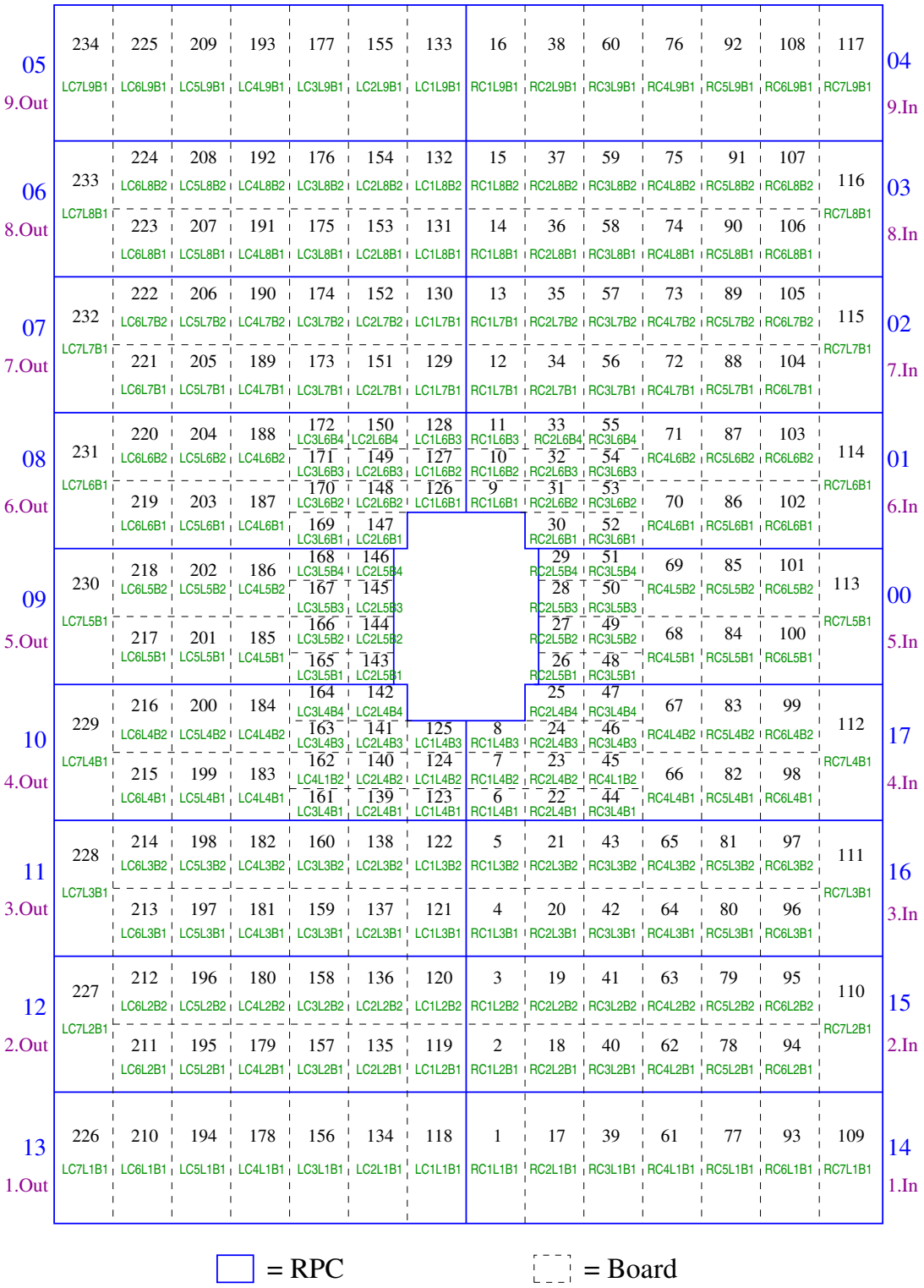

Figure 3.27: RPC and Local board segmentation of the Muon Trigger planes. The RPCs are numbered following two conventions: 1. From 1 to 9 (bottom to top) in the IN and OUT sides and 2. From 0 to 17 in counterclockwise direction, starting at $\phi = 0$, according to the ALICE coordinate system.

The trigger system (from the trigger electronics point-of-view) is divided in projective areas from the four planes, organized in three levels: local, regional and global. The smallest areas are covered by the local boards with a segmentation that varies as function of the distance from the beam line (as for the strip segmentation), as shown in Figure 3.27. The local boards are interfaced with the readout system and at the same time perform a first trigger selection, based on the transverse momentum of the single muon tracks. The information from the local boards is then passed to the regional cards, 16 in total, which deliver a signal for single muons and muon pairs. The regional pre-trigger information is then mixed at global level to deliver the dimuon trigger signal to the ALICE CTP.

3.6 ALICE Upgrade project

A major upgrade of the ALICE detector is foreseen during the next LHC long shutdown (2019-2020) [95]. The motivation of the upgrade project is to achieve higher readout rates in Pb–Pb collisions, which will allow precise measurements of the QGP (measurement of heavy-flavor transport parameters, quarkonia down to zero p_{T}, low mass di-leptons, jet quenching and fragmentation, study of exotic heavy nuclear states). The goal is to collect about 10 nb^{-1} of Pb–Pb data integrated on LHC Run 3 and 4 at luminosities up to $6 \cdot 10^{27}\mathrm{cm}^{-2}\mathrm{s}^{-1}$, corresponding to collisions rates of 50 kHz. The present ALICE readout capabilities are limited to 500 Hz in Pb–Pb collisions. The ALICE upgrade project [95,96], includes:

- Replacement of the present ITS by a new, high-resolution, low-material thickness ITS, to improve the Distance of Closest Approach (DCA) measurements and the standalone ITS tracking performance [97].
- Upgrade of the TPC by the replacement of the current readout chambers (based on MWPC) by Gas Electron Multiplier (GEM) detector and a new readout electronics [98]. This upgrade will make the TPC readout dead-time free.
- Upgrade of the readout of all other detectors, including the Muon Spectrometer, and trigger (CTP) and acquisition (DAQ) systems to cope with higher rates [99].
- Inclusion of the Muon Forward Tracker [100].

Muon Identifier

After the LS2 upgrades, the Muon Trigger system of the present Forward Muon Spectrometer will no longer keep its trigger functionality, all the muon detector (tracking and trigger chambers) will be read out for each minimum bias trigger to maximize the muon physics potential. However, the present trigger chambers will keep their role as muon identifier, consequently, after the LS2, instead of Muon Trigger the new system will be named Muon Identifier (MID). A replacement of the RPC front-end electronics is foreseen, more details will be given in next chapter.

Muon Forward Tracker

The Muon Forward Tracker (MFT) [100] will be placed around the beam pipe inside the ITS outer barrel and between the ITS inner barrel and the front absorber of the Muon Spectrometer (Figure 3.28 left). The MFT is aimed to improve the performance of the Muon Spectrometer with the possibility to perform new measurements not accessible up to now. In particular the MFT will allow to discriminate muons from charm and beauty decays down to low-p_{T}, measure $\psi(2\mathrm{S})$ in central Pb–Pb collisions, and disentangle the prompt and non-prompt J/ψ components.
The MFT is a high spatial resolution detector, it will consist of two half-cones placed along the beam axis between -460 and -768 mm from the IP and containing five half disks of silicon pixel sensors (Figure 3.28 right). The MFT will cover a smaller pseudo-rapidity range ($-3.6 < \eta < -2.45$) than the Muon Spectrometer due to integration constraints.

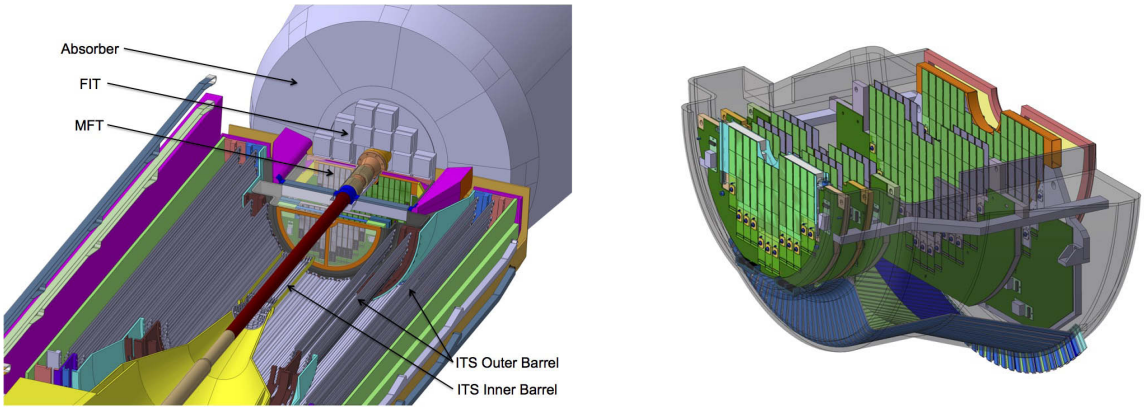

Figure 3.28: Muon Forward Tracker layout. *Left*: Position around the beam inside the ITS layers and in upstream the front absorber of the Muon Spectrometer. *Right*: Half cone of the Muon Forward Tracker present design.

Chapter 4

Performance of a new Front-End Electronics (FEERIC) for the Muon Trigger RPCs

Among the ALICE upgrade strategies for the LHC Run 3, the replacement of the front-end electronics (FEE) of the Resistive Plate Chambers (RPC) of the Muon Trigger system has been proposed. In this chapter the first performance tests of the new FEE (FEERIC, Front-End Electronics Rapid Integrated Circuit) in the ALICE cavern are described.

4.1 RPCs original working conditions

The design considerations of the ALICE muon trigger chambers was mainly driven by the data taking conditions expected in Pb–Pb collisions [101]. The muon trigger RPCs were originally conceived to operate in streamer mode which has the advantage of good time resolution, noise robustness and low cluster size compared to the avalanche mode, but as a drawback it presents a limit on the rate capabilities of the RPCs. The peak counting rates reported were about 100 Hz/cm^2 [102–104]. Under the streamer mode of operation, the electric field inside the gas is intense enough to initiate spark breakdown near the crossing path of the ionizing particles. The large charge released inside the gas causes a local decrease of the voltage between the electrodes, and since the electrodes are usually constructed of high resistivity materials, tens or hundreds of milliseconds are necessary to reestablish the working high voltage. During this time the detector is blind.
In order to optimize the rate capabilities, a gas composition of 49% Ar, 7% i-C_4H_{10}, 40% $C_2H_2F_4$ and 4% SF_6 was chosen so that the charge released in the streamer is reduced and the HV recovery time was improved with the choice of "low-resitivity" Bakelite electrodes ($\rho \simeq 3 \cdot 10^9\,\Omega$cm). This allowed to improve the short-term rate capabilities up to about 1 kHz/cm^2 in test beam [105].
The signal induced to the pick-up strips is high enough such that no amplification stage is required in the FEE. The original FEE design (Figure 4.1), called ADULT (acronym for A DUaL Threshold discrimination technique [106]), includes a discriminator stage followed

by a shaper [107]. It provides output signals of about 20 ns width which ensures the correct signal capture by the trigger electronics (at 40 MHz clock frequency).

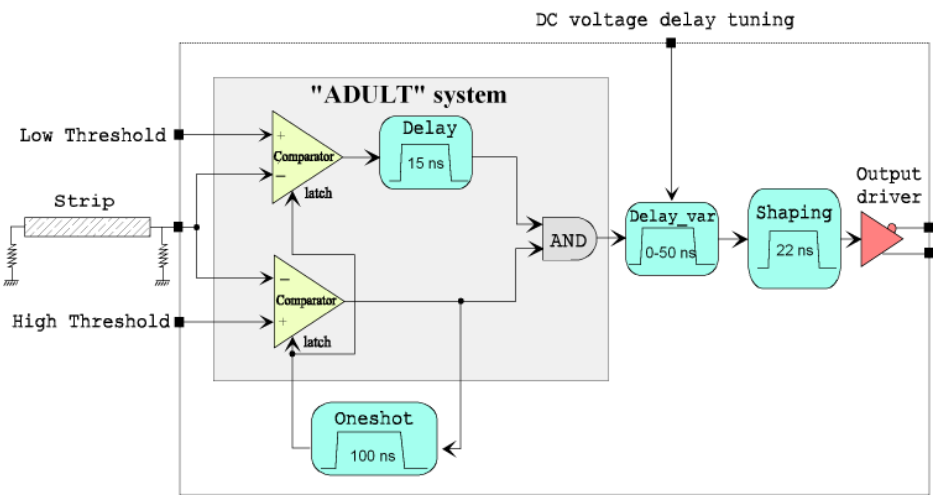

Figure 4.1: Block diagram of a single channel of the ADULT ASIC.

Given the higher interaction rates expected in pp and the longer data taking periods compared to Pb–Pb collisions, the RPCs operation in avalanche mode (adopted by the CMS and ATLAS detectors) can be more appropriated to reduce the ageing effects induced by the large accumulated doses. In order to keep the same FEE the possibility to work in a highly-saturated avalanche mode was studied [108]. This working condition can be achieved by replacing the gas mixture by a highly quenched gas composition (89.7% $C_2H_2F_4$, 10% C_4H_{10}, and 0.3% SF_6), to avoid the streamer formation but keeping the gain high enough to allow signal discrimination without need of amplification.
Both working conditions (with the different gas mixtures) were foreseen for the Run 1 data taking. In practice, during Run 1 and 2 all data have been taken in highly-saturated avalanche mode, also called "maxi-avalanche".

4.2 Perspectives for the LHC Run 3

The instantaneous counting rate in the current RPCs working conditions is limited to 50 Hz/cm^2 [99] for long-term safe operation. This value is two times lower than the expected peak rates after the LS2 [95, 99]. Assuming that the same working conditions hold (with 100 pC/hit as reported in [109]) at rates of 50 Hz/cm^2, the safe operation of the RPCs could not be guaranteed after 10 months of operation due to a cumulated dose larger than 50 mC/cm^2 (limit reached during R&D). Taking into account these limitations (counting rate and detector ageing), the operation of RPCs in "saturated avalanche" mode (as in ATLAS and CMS RPCs) was proposed for the LHC Run 3 [95].
In saturated avalanche mode the electric field in the gas gap is reduced and so does the current produced in a single discharge, what allows to improve the rate capability. A robust signal amplification is required at the FEE level for the saturated avalanche mode

and the current ADULT chips need to be replaced.
The proposed new FEE chip (Figure 4.2) is called FEERIC (for Front-End Electronics Rapid Integrated Circuit). It consists of a two stage trans-impedance amplifier which amplify the analogical signals from the RPCs, a zero-Crossing discriminator that provides the digital signal, followed by a shaper (one-shot system) that provides a 23 ns width output signal in LVDS standard (Low-Voltage Differential Signal) [110].

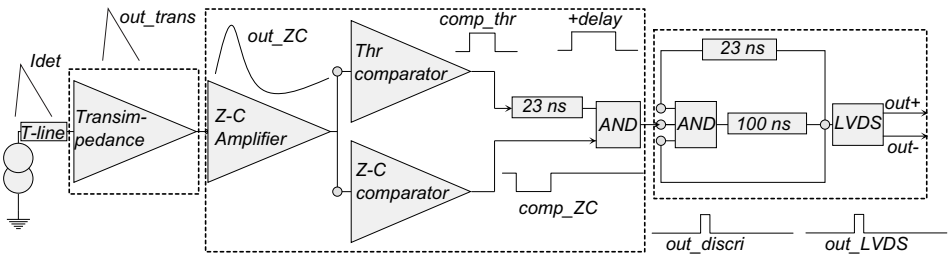

Figure 4.2: Block diagram of one channel of the FEERIC ASIC.

The development of the new FEE cards started in the year 2012 at LPC Clermont-Ferrand. The first prototype (FEERIC-1) tests were performed by the end of 2013 using the RPC production test bench in Turin. The comparison of the RPC efficiency obtained with ADULT and FEERIC cards showed that the efficiency knee with FEERIC can be reached at about 700 V (depending on the discrimination threshold) below the working point with ADULT [99]. After this encouraging result the R&D on the electronic cards continued up to the development of the FEERIC-3 cards.
Figure 4.3 shows the efficiency curves obtained in test bench in Turin for the FEERIC-3 cards, for different thresholds[1]. The plot also shows the results obtained with the ADULT cards for comparison, a reduction of about 600-700 V in the operating HV is possible for the RPCs working in saturated avalanche versus maxi-avalanche mode.

During the LS1, one of the RPCs in the ALICE cavern has been fully equipped with a pre-production of FEERIC-3 cards, which allows to quantify in a long time scale the RPC performance in realistic conditions. The RPC equipped with the FEERIC front-end electronics is located at position 16 (see Figure 3.27) of the last trigger plane (MT22). It is equipped with strips of 2 and 4 centimeters in both the bending and non-bending planes. The total number of installed cards is: 35 (24 and 11, in bending and non-bending planes respectively) for strips of 2 cm, and 4 (2 cards in each plane) for strips of 4 cm. Each card processes the signal from 8 strips.

[1]The threshold value expressed in "mV" is referred to the amplitude of the signal corresponding to a given charge collected by the strip (70 mV and 130 fC for instance, in this case). The relation between both is proportional and the proportional factor is the so called "gain" which depends mostly on the FEE amplification and strip width (different impedances).

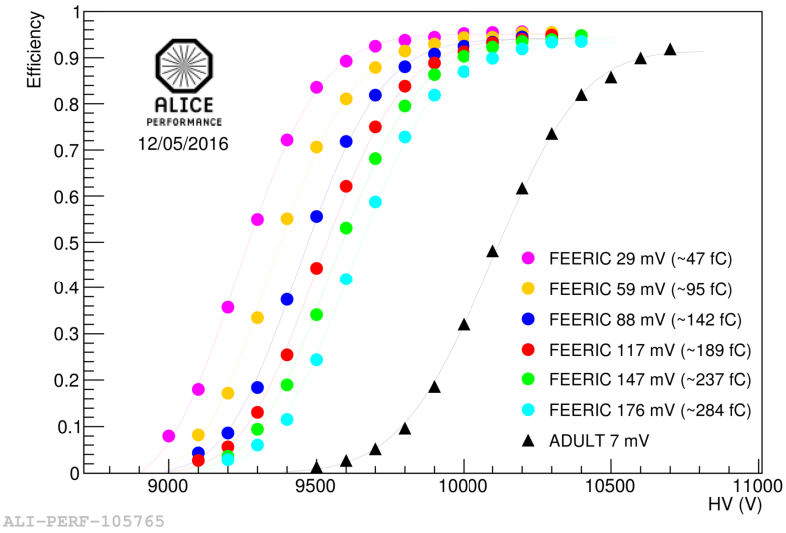

Figure 4.3: Efficiency as a function of the HV for the RPC equipped with FEERIC-3 and ADULT front-end electronic cards. The different colors represent the different discrimination thresholds that have been tested for FEERIC.

4.3 RPC performance monitoring

4.3.1 Efficiency

The RPC efficiency during the data taking periods is permanently monitored using a method introduced in [111], which is currently integrated into the AliRoot framework. This method relies on the redundancy on the number of trigger planes to define a straight track. The trigger algorithm produces a trigger signal if a particle fires the strips (of both bending and non-bending, independently) of at least three out of the four trigger planes. The trigger efficiency depends on the chamber detection efficiency. The number of particles $N_{3/3}^{ch}$ that would produce a trigger signal even if the plane *ch* does not provide a signal is given by[2]:

$$N_{3/3}^{ch} = N_{tot} \prod_{\substack{11 \leq i \leq 14 \\ i \neq ch}} \varepsilon_i \tag{4.1}$$

where N_{tot} is the total number of particles traversing the trigger chambers. Out of the number of triggered events, a fraction of particles would have fired the four chambers. This number, labeled as $N_{4/4}$, can be expressed as:

$$N_{4/4} = N_{tot} \prod_{11 \leq i \leq 14} \varepsilon_i \tag{4.2}$$

[2]In the AliRoot notation the four trigger planes are numbered from 11 to 14 instead of 11, 12 and 21, 22 for the first and second trigger stations.

So, the efficiency of chamber ch can by evaluated as the ratio of $N_{4/4}$ over $N_{3/3}^{ch}$:

$$\varepsilon_{ch} = \frac{N_{4/4}}{N_{3/3}^{ch}} \tag{4.3}$$

The numbers $N_{3/3}^{ch}$ and $N_{4/4}$ are determined by searching the fired strips associated to the same track in all chambers. The algorithm starts by identifying the strip position corresponding to the intersection point of the reconstructed track (extrapolated from the Muon Tracking) in the first trigger plane and then searches for strips fired in a narrow road in the following planes.

4.3.2 Cluster size

The cluster size is defined as the number of consecutive strips fired by the passage of a charged particle through the detector volume. It depends mainly on the operating HV and the strip widths, and factors like the gas composition and the FEE threshold, linked to the RPC operating mode. For the muon trigger RPCs, a spatial resolution at the sub-centimeter level is required in order to perform the p_{T} cut [101]. Also it was desirable to keep the occupancy as low as possible and as constant as possible over the chamber area. Taking this into account, the strip width and segmentation have been properly chosen [101]. For cluster sizes equal to 3 a significant degradation of the spatial resolution is observed [112].
The cluster size can be determined from the bit patterns sent by the FEE electronics to the local boards. The patterns contain the information of the strips that collected a lower (0) or higher (1) charge than a given threshold. For a given muon track the AliRoot reconstruction algorithm provides the bit patterns for both planes of each trigger chamber.

4.3.3 Current

The current drawn by each RPC is monitored by the Detector Control System (DCS) and stored in the Offline Condition Database (OCDB). During a data taking period at any variation of the current of the RPCs, the current i_k is registered together with its corresponding time stamp (t_k). The information is saved for regular data taking runs and for the control runs with no beam, the later are used to monitor the dark current, which should be kept at minimal level. The average current value for each RPC is computed run by run as:

$$i_{\mathrm{run}} = \frac{\sum_{k=0}^{n-1} i_k \cdot (t_{k+1} - t_k)}{\sum_{k=0}^{n-1} t_{k+1} - t_k} \tag{4.4}$$

where n is the number of entries recorded in the OCDB for a given run.

4.3.4 Charge per hit

The charge per hit (q_h) integrated in the RPC areas, is computed run by run as the ratio between the current and the hit rate (f_h).

$$q_h = \frac{i_{\text{run}}}{f_h} \tag{4.5}$$

The RPC counting rate can be retrieved from the trigger scalers which are periodically recorded in the OCDB. The trigger scalers give the number of counts, i.e. strips fired, each 10 minutes typically. It can be accessed at the local board level. Once corrected by the cluster size, the hit rate corresponding to a single RPC is computed taking into account the information from all local boards associated to it.

4.3.5 Summary of RPC performance during Run 1

During the LHC Run 1, the trigger system of the ALICE muon spectrometer provided L0 trigger signals for all collision systems (pp, p–Pb, and Pb–Pb) in the data taking periods from 2010 to 2013. The RPCs were operated in the highly-saturated avalanche mode. The FEE discrimination thresholds were set at 7 mV for low and high thresholds. The RPCs working high voltage was optimized for each RPC and ranged between 10 to 10.4 kV [113].
The muon trigger chamber performance during Run 1 [114] showed very satisfying results and in line with the design specifications.
The trigger chamber efficiencies were monitored (independently, for the bending and non-bending planes) and had a quite stable behavior over time (2010-2013), the efficiency values kept always higher than 95%. The individual RPC efficiencies showed a good stability over time and, with very few exceptions, values are higher than 95% (Figure 4.4).

The cluster size for the different strip widths was also monitored and was found to be stable over time, as it can be seen in Figure 4.5.
The cluster size measured in Pb–Pb collisions from the 2011 data taking are reported in Table 4.1 (from [115]) as an example of typical cluster size values.

Table 4.1: Average cluster size values measured in Pb–Pb collisions at $\sqrt{s_{\text{NN}}}$= 2.76 TeV for the three strip widths [115].

Strip width	Av. CS
1 cm	2.08 ± 0.06
2 cm	1.46 ± 0.02
4 cm	1.15 ± 0.01

The counting rates on the whole active surface reached up to 7.5 Hz/cm^2 in pp collisions, 10 Hz/cm^2 in p–Pb collisions and 2 Hz/cm^2 in Pb–Pb collisions. The average charge per hit was about 100 pC for an integrated charge (in the whole Run 1 data taking) of 4

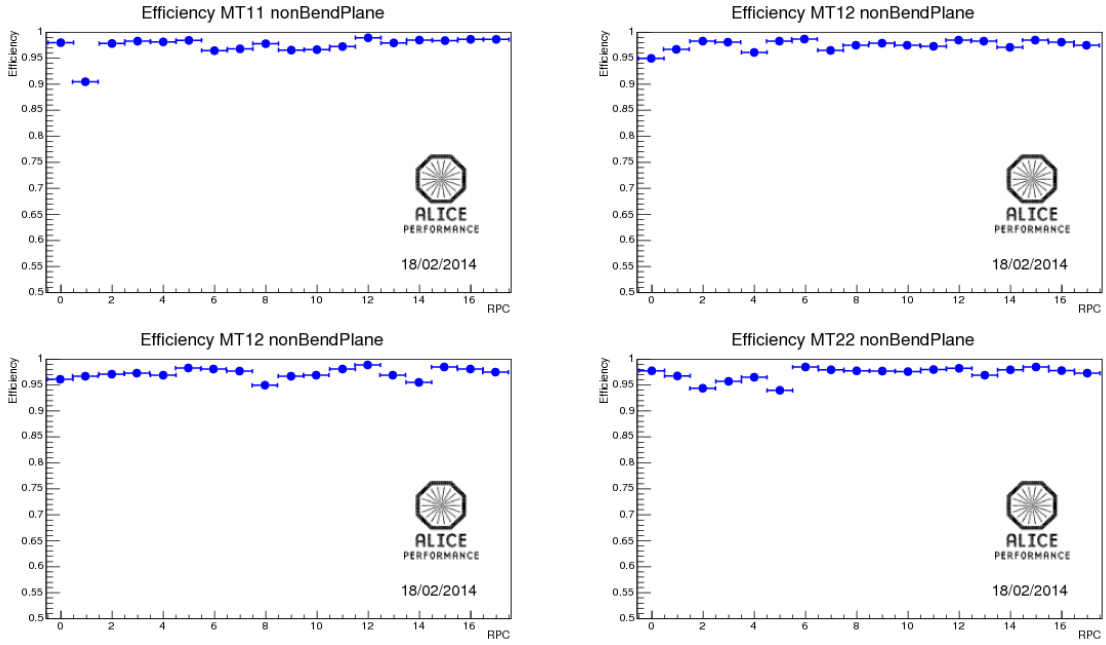

Figure 4.4: Efficiency in the non-bending plane for all RPCs (in the four planes: MT11, MT12, MT21, MT22). The data corresponds to the 2013 data taking. Figure from [114].

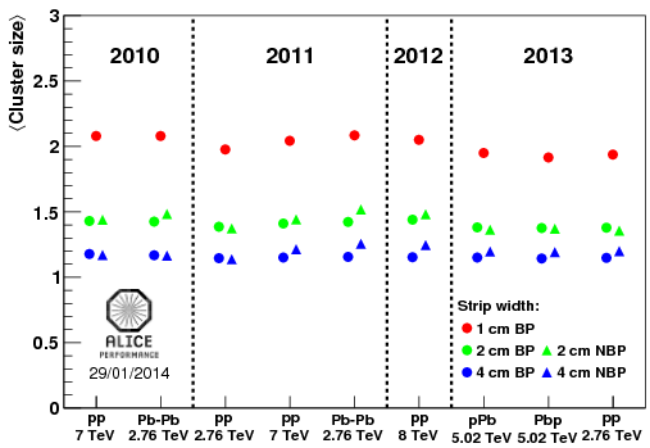

Figure 4.5: Cluster size as a function of the data taking period. The different colors correspond to the different strip widths, and values are evaluated independently for the bending and non-bending planes. Figure from [114].

mC/cm^2 [114].
The dark rate and dark current were regularly monitored in the periods of no colliding beams (just after the beam dump or cosmics runs). The dark rate values kept very low (< 0.1 Hz/cm^2) and stable over time. A slight increase of the averaged dark current from the beginning to the end of the yearly data taking periods was observed, and an overall increase over the full three year period. The averaged effect was due to individual RPC dark current increases, however there is no evidence that the effect could be due to

radiation damage or degradation of the electrode surface.

4.4 FEERIC performance study in cavern

The performance study presented here corresponds to the first data collected by the RPC equipped with FEERIC after its installation in cavern (February 2015) up to August 2015, i.e. the cosmic runs collected by ALICE before the first circulating beams of the LHC Run 2 and the first data taking with beam-beam collisions.
From the test bench study performed in Turin, a nominal HV value (of 9624 V) was initially set to the RPC installed in cavern. Since the working HV and discrimination threshold have to be set with data from collisions (the efficiency algorithm is not optimized for cosmics), the first tests performed were based only on the dark current and dark rates for different points around the nominal HV and different discrimination thresholds. Figures 4.6 and 4.7 show the comparison of dark current and dark rate between the RPCs equipped with ADULT and the RPC equipped with FEERIC[3]. Such comparison is only illustrative since the working point of the FEERIC RPC was not optimized. From the results it can be noticed that the dark current is reduced in a half or more depending on the HV and threshold values. The average value for the RPCs with ADULT is about 2 μA which is in agreement with similar results from Run 1. The dark rate of the RPC equipped with FEERIC is higher than for RPCs with ADULT and strongly dependent on the HV and discrimination threshold being maximal for the maximum HV (9824 V) and the lowest threshold (130 fC) combination, but values close to those obtained by the ADULT RPCs can be reached by reducing the HV and increasing the threshold value as can be seen in the plot (Figure 4.7) for the last runs. For the RPCs equipped with ADULT the dark rate keeps constant over time and the average value is about 0.02 Hz/cm^2 which is in agreement with the Run 1 results.

4.4.1 Setting the RPC working conditions

The operating HV value was tunned with the first data from pp collisions. Different FEE discrimination thresholds (70, 105 and 140 mV) for the signal were also tested in order to optimize the detector efficiency.
Figure 4.8 shows the efficiency curves obtained with pp at 13 TeV data, for the bending and non-bending planes, at three different values of the discrimination threshold. A good agreement on the efficiency values for the two planes is observed. The HV working point (defined 400 V above the HV value at which the efficiency is 90 %) is reached at about 9324, 9524 and 9624 V for the three increasing threshold values. Since the main purpose is to reduce as much as possible the working HV, it seemed reasonable to choose a working point at 9324 V (at the end, the voltage was set at a value slightly higher, at 9375 V)

[3]The dark current and dark rate have been evaluated over the same list of runs (from the cosmics data taking). However, the scaler information (necessary to compute the counting rates) was not available in the OCDB for the first 63 runs, this is the reason why the dark rate plot is shown for a shorter time (number of runs) range.

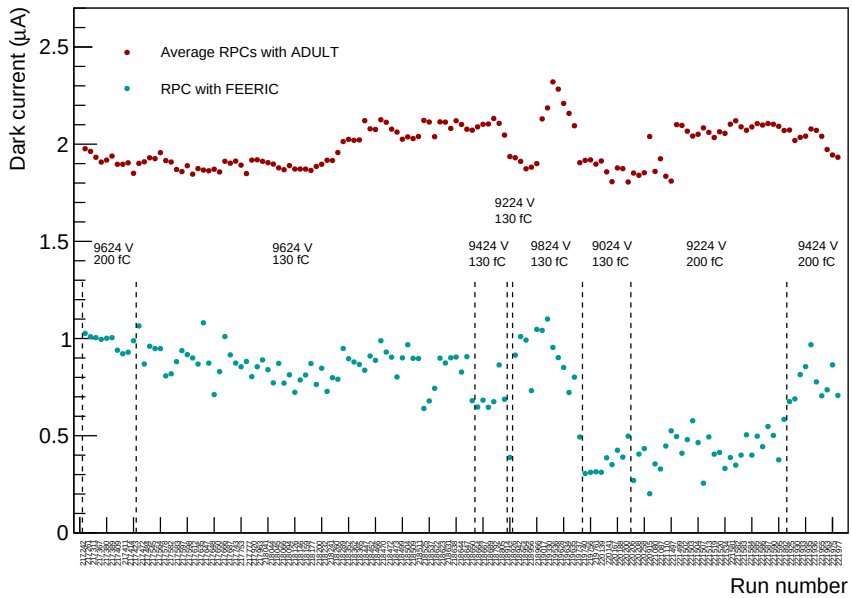

Figure 4.6: Dark current versus time (run number) for the RPC equipped with FEERIC compared to the average values of the RPCs equipped with ADULT. The working point of the RPC equipped with FEERIC is indicated in therms of the RPC HV and electronic threshold (in fC), while for the ADULT RPCs the same working conditions was kept in all runs.

with a discrimination threshold of 70 mV (or 130 fC, in terms of the charge collected by the strip). The choice is also constrained by the noise level (70 mV corresponds to two times above noise threshold).
In order to validate that choice, it is also necessary to study its influence on other performance estimators, like the cluster size. For RPCs operated in avalanche mode, the lower the high voltage, the smaller should be the cluster size, since a smaller discharge will be produced inside the gas. However, the choice of a low threshold can increase the cluster size, with the consequent degradation of the spatial resolution.
Figure 4.9 shows the dependency of the cluster size on the applied high voltage for strips of 2 and 4 cm in the bending and non-bending planes and for the three threshold values.

By comparing the cluster sizes corresponding to the optimal HV and threshold value combinations (colored dashed lines in the plots), it can be noticed that only a slight improvement of the cluster size for the higher threshold is achieved. The cluster values are reported in Table 4.2.
Since the main interest is to reduce the HV, and given that the cluster size is not too much degraded by the choice of the smallest threshold, the working point at 9375 V with 130 fC threshold can be safely set. It is also important to remark that in the upgrade project (MID), the current trigger functionalities (based on the p_{T} cuts on muon tracks) at hardware level will not be kept, so the spatial resolution requirement is less stringent.

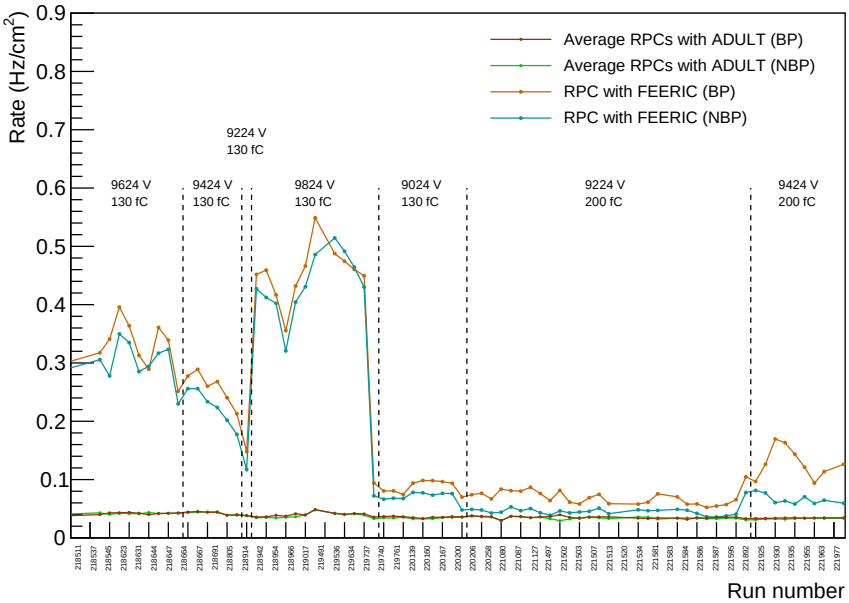

Figure 4.7: Dark rate versus time (run number) for the RPC equipped with FEERIC compared to the average values of the RPCs equipped with ADULT. The working point of the RPC equipped with FEERIC is indicated in therms of the RPC HV and electronic threshold (in fC) by the vertical lines. The working conditions of the RPCs equipped with the ADULT card were the same in all runs.

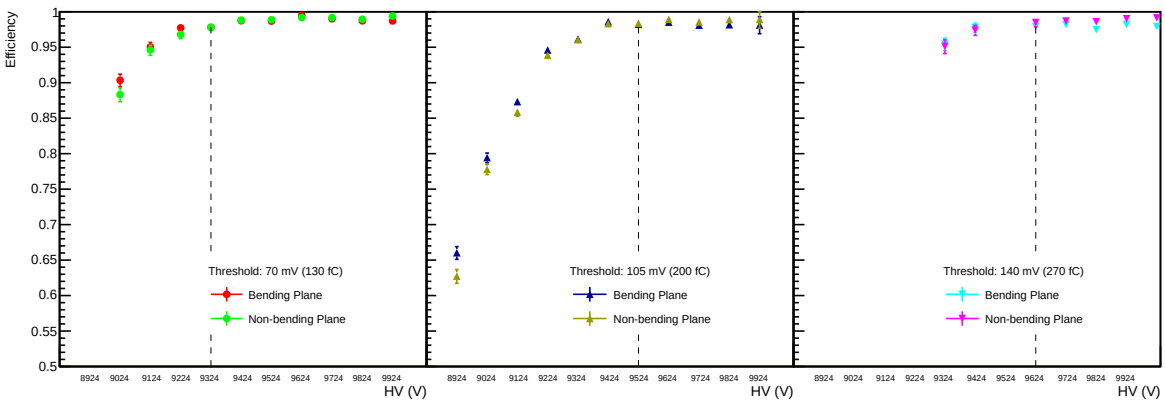

Figure 4.8: RPC detection efficiency (with FEERIC) as a function of the working high voltage. The curves are shown for three different discrimination thresholds, *left*: 70 mV (130 fC), *middle*: 105 mV (200 fC) and *right*: 140 mV (270 fC). The data corresponds to pp collisions at $\sqrt{s} = 13$ TeV recorded in June 2015 at the beginning of the LHC Run 2.

The RPC chambers will contribute to the "offline" muon identification.

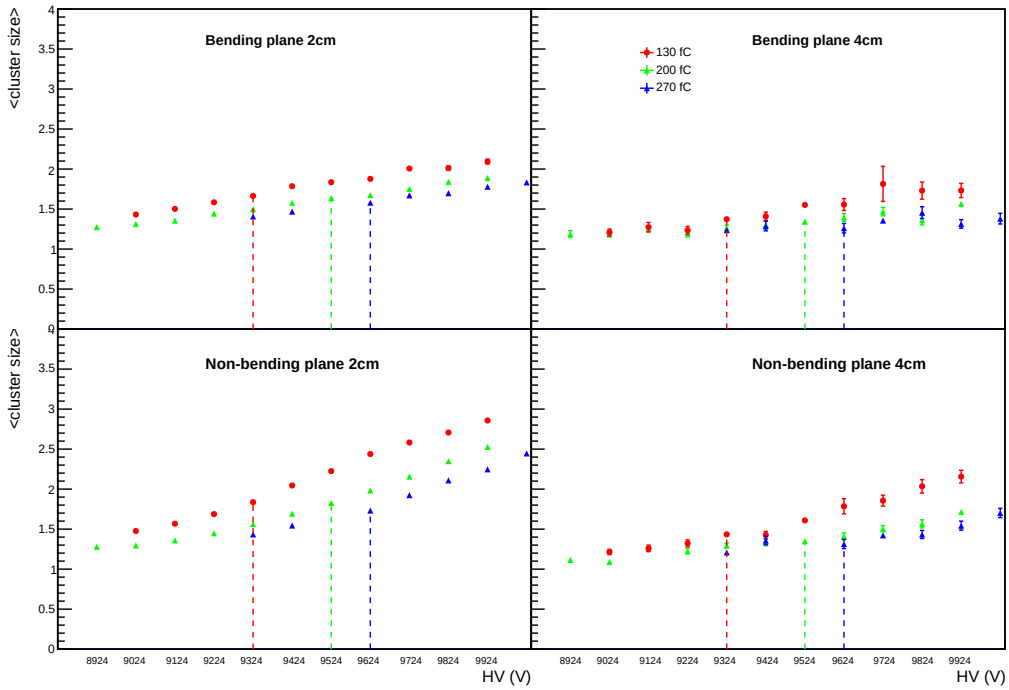

Figure 4.9: Cluster size for the RPC equipped with FEERIC in the bending (*top*) and non-bending (*bottom*) planes for strips of 2 (*left*) and 4 cm (*right*). The dashed lines indicate the threshold HV values from Figure 4.8.

Table 4.2: Average cluster size values for the optimized HV-threshold combinations.

	Bending plane			Non-bending plane		
Strip width	9324 V (130 fC)	9524 V (200 fC)	9624 V (270 fC)	9324 V (130 fC)	9524 V (200 fC)	9624 V (270 fC)
2 cm	1.66 ± 0.01	1.64 ± 0.00	1.58 ± 0.01	1.84 ± 0.01	1.83 ± 0.00	1.73 ± 0.02
4 cm	1.37 ± 0.02	1.34 ± 0.02	1.26 ± 0.06	1.43 ± 0.02	1.35 ± 0.01	1.31 ± 0.06

4.4.2 Charge per hit

Figure 4.10 shows the charge per hit for all RPCs in the four trigger chambers, for the bending and non-bending planes. The plots show the evolution as a function of the run number, for pp collisions at $\sqrt{s} = 13$ TeV. The charge per hit keeps rather constant as a function of the run number and varies from one RPC to the other depending on its different working conditions.

It is not straightforward to compare RPCs working on different conditions (HV, thresholds and operating mode), however, as a general rule, it can be noticed that the produced charge per hit in the RPC equipped with FEERIC is systematically lower than for the rest of RPCs. To quantify the reduction in terms of the charge produced per hit in the RPC volume, the ideal would be to compare the same RPC equipped with one and another front-end electronics in the same working conditions, which is not possible in practice.

However, some ADULT RPCs have been identified that can be compared to the FEERIC RPC (in terms of rate and current with ADULT in Run 1), it can be seen that there is a difference of about a factor 4 (Figure 4.11) in the charge per hit produced in the RPCs equipped with ADULT and the RPC equipped with FEERIC.

In Figure 4.12 the average charge per hit for all RPCs in the bending and non-bending planes is compared to the charge per hit in FEERIC. The average charge per hit for both planes over all runs is about 130 and 160 pC for the RPCs equipped with ADULT in bending and non-bending planes, respectively, and 30 pC for the RPC equipped with FEERIC in both planes.

As a result, the RPC ageing will be reduced after the installation of the new FEERIC cards for the LHC Run 3 data taking.

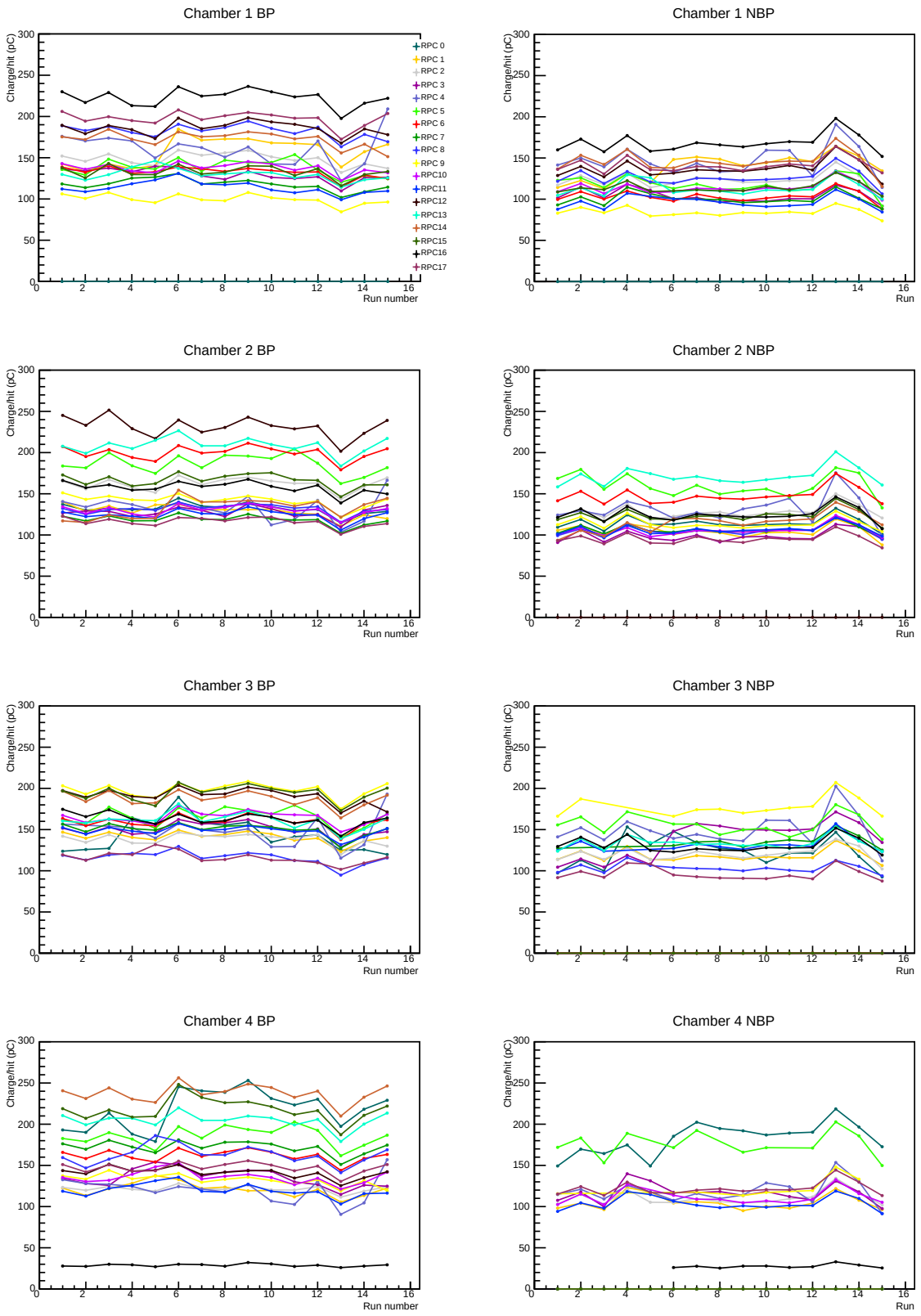

Figure 4.10: Charge per hit RPC by RPC in bending (*left*) and non-bending (*right*) planes for the 4 trigger planes.

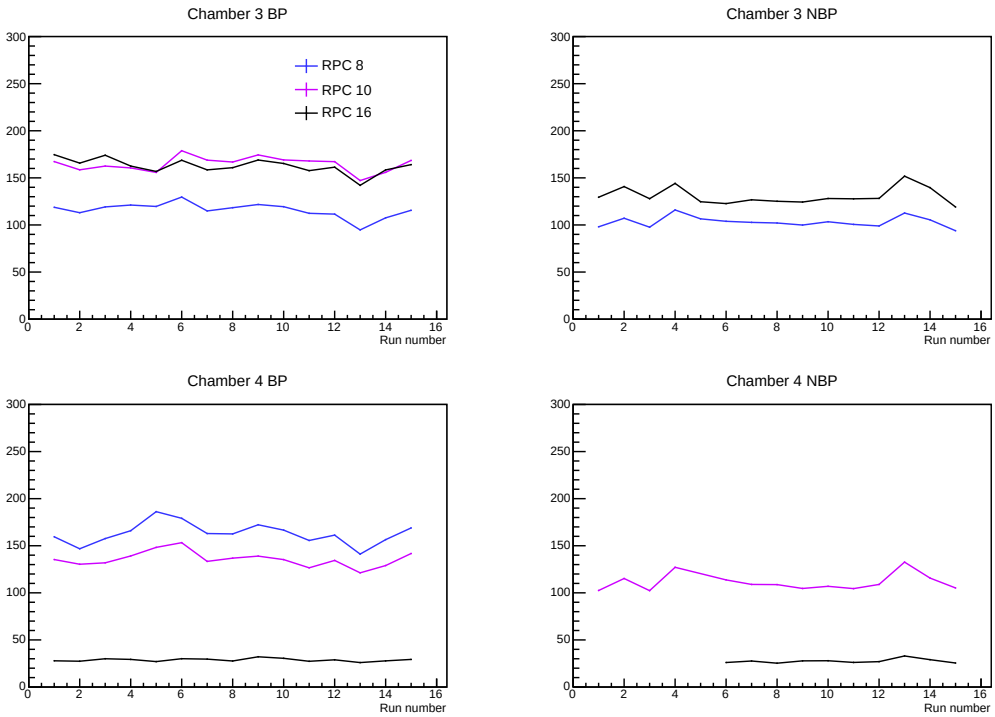

Figure 4.11: Charge per hit for the FEERIC RPC and RPCs 8 and 10 (in the "counter-clockwise notation", see Figure 3.27) equipped with ADULT.

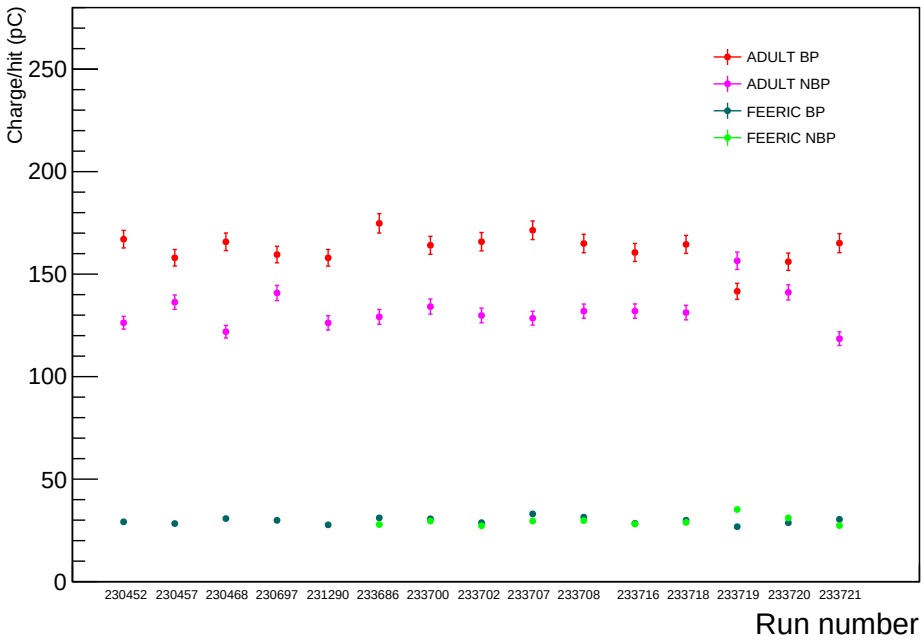

Figure 4.12: Average charge per hit of all RPCs equipped with ADULT and charge per hit for the RPC equipped with FEERIC as a function of the run number.

4.4.3 Recent performance results

The performance of the RPC equipped with FEERIC continues to be monitored during the different Run 2 data taking periods. The results up to February 2016 [116] are presented to illustrate the FEERIC good performance up to now.
Figure 4.13 shows the efficiency as a function of time. As it can be noticed the RPC efficiency has kept stable over time and over 95% regardless the collision system and energy.

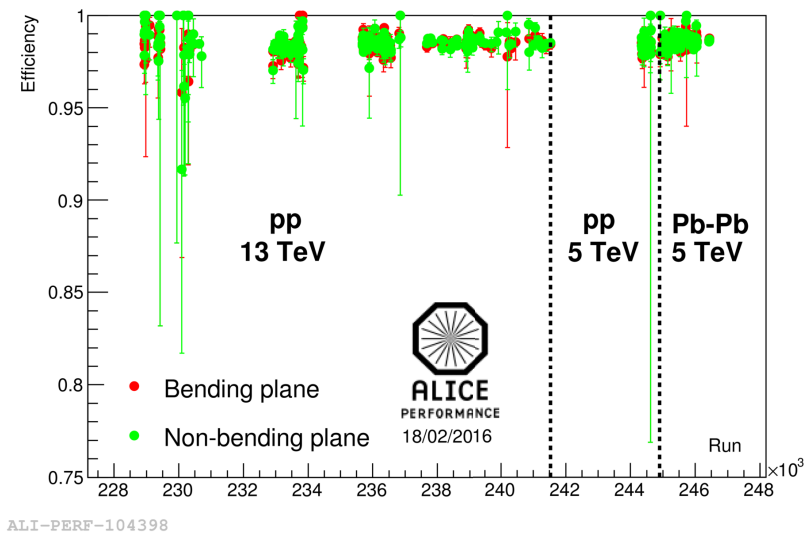

Figure 4.13: Efficiency versus time for the x and y-strips (bending and non-bending planes, respectively) of the RPC equipped with FEERIC. The different data taking are delimited by vertical lines. Figure from [116].

The dark current and rate have been also monitored and have been found stable over time. The dark current values are much lower than for the RPCs equipped with ADULT. Typical dark current values for RPCs with ADULT vary from 2 to 4 μA while the average value for FEERIC is $\sim$ 0.6 μA. This value is compatible with the results from the first test of FEERIC in cavern, although there are no points at the exact working point (which was defined later). It can be seen (Figure 4.6) that points from working conditions 9424 V and 9224 V with 130 fC as threshold are around 0.6 μA. For the dark rate the RPC with FEERIC shows higher values than the RPCs with ADULT (for which the average is $\sim$ 0.05 Hz/cm^2), however the dark rate of the RPC with FEERIC keeps for most of the cases below 0.1 Hz/cm^2. Similar to the dark current, the dark rate values obtained with the cosmic runs (Figure 4.7) are compatible with these results.

Chapter 5

Polarization Analysis

The theoretical considerations for the measurement of J/ψ polarization have been introduced in Chapter 2. In this chapter a review of the methodology from the analysis point of view, with the ALICE Muon Spectrometer, will be presented. The intermediate steps on the procedure will be illustrated in terms of the $W(\cos\theta)$ distributions in the Collins-Soper frame in most of the cases, for the measurement of the λ_θ parameter, and extended to the two other angular distributions and the Helicity frame if needed. More details on the three distributions in both polarization frames can be found in appendices and referred through the text when it corresponds.
In the first section the data selection and cuts to optimize the "data purity" will be discussed. In section 5.2 the feasibilities and limitations of the analysis are introduced based on the total available sample and general considerations on the detector's acceptance and efficiency. Section 5.3 describes in detail all the procedure from the J/ψ signal extraction up to the measurement of the λ parameters. The last section (5.4) will be devoted to the discussion of the possible sources of systematic uncertainties and their estimation.

Analysis methodology

As a general introduction to the methodology and main points to be discussed in this chapter, the following steps summarize the procedure for the measurement of the J/ψ polarization parameters.

1. The data are split in bins of p_{T}, and then for each p_{T} bin in bins of $\cos\theta$, φ and $\tilde{\varphi}$ in the Collins-Soper and Helicity reference frames and the unlike-sign dimuon invariant mass distributions corresponding to each bin are build, after data selection and analysis cuts.

2. The J/ψ signal corresponding to each bin in p_{T}, $\cos\theta$, φ and $\tilde{\varphi}$ is extracted.

3. The raw angular distributions $W(\cos\theta)$, $W(\varphi)$ and $W(\tilde{\varphi})$ are then built for each p_{T} bin and polarization frame.

4. The raw angular distributions are corrected by the acceptance and efficiency $(A\times\varepsilon)$ of the detector.

5. The corrected $W(\cos\theta)$, $W(\varphi)$ and $W(\tilde{\varphi})$ distributions are fitted with the theoretical expected functions 2.18, 2.19 and 2.20, to determine the three polarization parameters λ_θ, λ_φ and $\lambda_{\theta\varphi}$ for each p_{T} bin.

5.1 Data selection and analysis cuts

5.1.1 Event selection

The data used in this analysis correspond to the data collected by the ALICE experiment in pp collisions at $\sqrt{s} = 8$ TeV between October and December of 2012 during the LHC Run I. The LHC was operated at high beam intensities ($\sim 2 \times 10^{14}$ protons/beam) and 50 ns of bunch separation. In order to reduce the luminosity, ALICE took data in beam-satellite mode.
The satellite bunches are, by convention, defined as the bunches in the range of $\pm$ 12.5 ns around the nominally filled RF bucket. In an ideal situation, all particles should be captured in the nominally filled buckets, however, in practice, the nominally empty buckets can also contain small populations of particles. Bunches separated more than $\pm$ 12.5 ns from the main bunch are called "ghosts".
Figure 5.1 shows an example of a real longitudinal particle density distribution in a Pb beam, and the different conventions for the bunch naming.

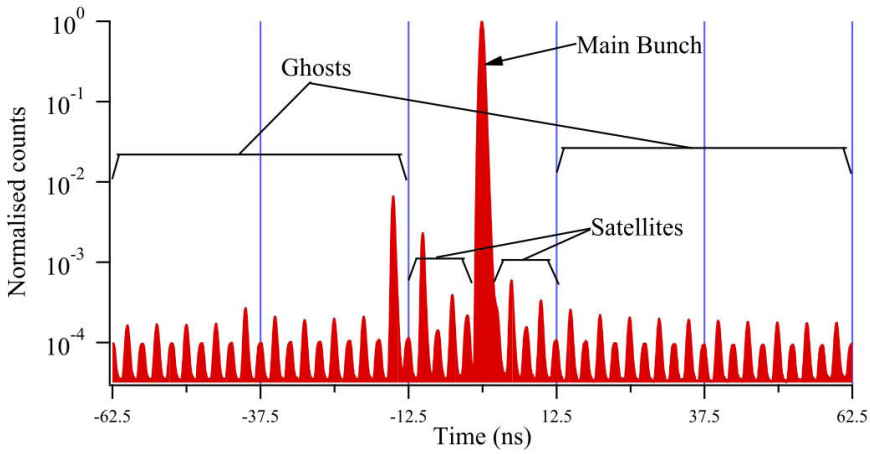

Figure 5.1: Typical longitudinal profile of a Pb beam. The conventions for bunch naming is shown. Figure from [117].

Although the ALICE operation mode for the pp at $\sqrt{s} = 8$ TeV data taking is called "beam-satellite" mode, the recorded data corresponds to beam-ghost collisions, for ghost bunches separated 25 ns from the main bunch. These bunches have an intensity of around 0.15 % of the nominal bunches [118], therefore the luminosity is decreased in the same proportion. The main bunch was coming from the C-side, i.e. the side of the muon arm. Two different Minimum Bias configurations were adopted depending on the interaction

rate, at the beginning of the fill and high interaction rates the T0 detector was used in the T0and configuration (T0A&T0C, i.e. both T0 counters hit) and when the rates dropped to around 200 kHz, the V0and (V0A&V0C) condition was established. A total of 270 runs that passed the Quality Assurance checks[1], in the high and low luminosity periods, have been analyzed.
Events were required to match the Level 0 MUL trigger class, meaning two unlike-sign muon tracks passing a low-p_{T} cut: $p_{\mathrm{T}\,min} \simeq 1\,\mathrm{GeV}/c$ (see Section 3.5.3).

5.1.2 Single muon track cuts

Specific selection criteria are commonly applied to purify the muon tracks data sample for quarkonia analysis.

- Muon tracks reconstructed in the tracking chambers are required to match a track reconstructed in the trigger system: this cut removes mainly the background component associated to hadrons misidentified as muons (most hadrons are stopped at the iron wall placed between the tracking and trigger systems) and tracks produced in the beam shield which are not reconstructed by both tracking and trigger systems.

- For J/ψ reconstruction the low-p_{T} cut (Lpt) of the trigger system is applied to suppress the amount of low p_{T} tracks that contribute to combinatorial background of the dimuon invariant mass spectra.

- The radius at the end of the front absorber R_{abs}, i.e. the perpendicular distance between the track and the beam line, is required to lie within the limits $17.6 < R_{\mathrm{abs}} < 89.5$ cm. The motivation for this cut is to avoid the multiscattering effect of reconstructed tracks due to the interaction with different absorber materials (non-homogeneous on the radial direction).

- The $p \times$ DCA cut[2] has been also applied in order to reduce the high-p_{T} background component of the beam shield induced particles. Beam induced particles show a different $p \times$ DCA distribution compared to muons from other sources. In fact, while for muon tracks from heavy flavors and light hadron decays, the Root Mean Square of the $p \times$ DCA distribution clusters around a central value, independently of the tracks transverse momentum, the beam induced particles shows a $p \times$ DCA distribution that depends on p_{T} [119].

[1]The Quality Assurance checks are several tests performed at different levels of data processing. It includes checks such as the run type, duration, beam energy and stability, detector's status during the run and currents in the L3 and dipole magnets. After the check of all conditions runs are then flagged as "good" or "bad" for the analysis.

[2]The $p \times$ DCA cut was first introduced in [119]. The term p stands for the mean momentum of the incident particles inside the front absorber, the reconstructed track momentum (p_{rec}) corresponds to the momentum reconstructed in the tracking chambers (p_{trk}) after the extrapolation to the interaction primary vertex and correction by energy losses in the absorber material, so the p value entering in the $p \times$ DCA definition is considered in the middle between p_{trk} and p_{rec}. DCA stands for distance of closest approach, referred to the beam line.

· In order to reject muons at the edge of the muon spectrometer acceptance, only muon tracks in the pseudo-rapidity range $-4 < \eta < -2.5$ are analyzed.

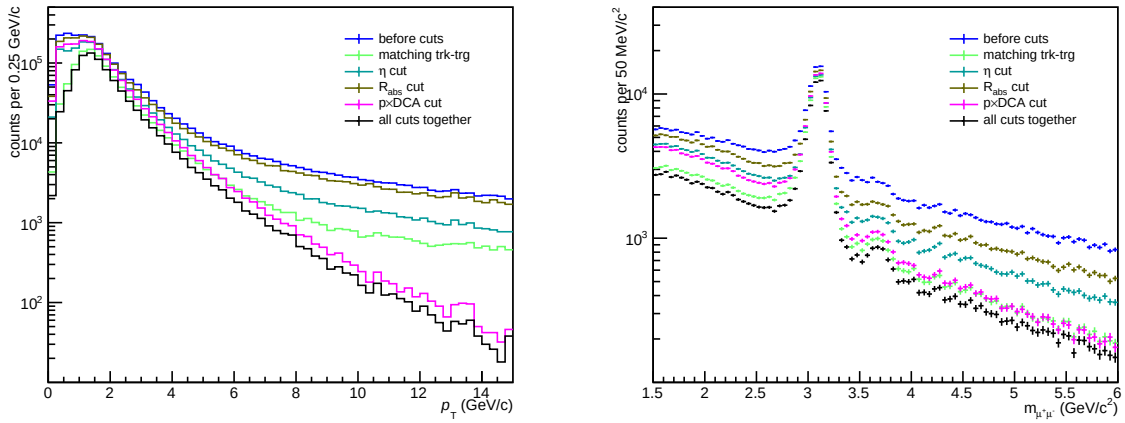

Figure 5.2: Effect of individual cuts applied to muon tracks on the p_{T} spectrum of single muons (*left*) and on the p_{T} and y integrated unlike-sign dimuon invariant mass distribution of real data (*right*). The effect of all cuts applied together is also shown.

In addition to the single track cuts, a cut on the rapidity of unlike-sign dimuon pairs is applied to restrict the analysis to the quarkonium rapidity range $2.5 < y < 4$.
The effect of individual cuts on muon candidates and on the unlike-sign dimuon invariant mass is shown in Figure 5.2. The most important cuts at both, single muon tracks level and unlike-sign muon pairs, are the trigger-tracking matching in addition to "Lpt" and the $p \times$ DCA cuts, to remove the low and high p_{T} background components, respectively. From the unlike-sign dimuon invariant mass distribution (Figure 5.2 *right*) it can be noticed that the cuts remove essentially the combinatorial background with a weak impact on the J/ψ peak.

5.2 Data sample and simulation

5.2.1 Raw data

The unlike-sign dimuon invariant mass spectra were studied in order to define the binning in p_{T} and angular distributions variables, and feasibility of signal extraction in each case. The choice of p_{T} bins has to be done taking into account that a sufficiently high statistics is required in order to further divide the data in angular bins. A lower p_{T} cut at 2 GeV/c was applied since the analysis in this region is limited by the $A \times \varepsilon$ of the detector as it will be discussed later in this section, in addition to that, theoretical predictions on the J/ψ polarization does not go up to smaller p_{T} values. For $p_{\mathrm{T}} > 15$ GeV/c the available statistics is very limited: in the p_{T} range from 15 to 20 GeV/c the number of J/ψ events is around two hundreds, what makes the analysis not possible in terms of angular

dependencies. Figure 5.3 shows a fit to the total data sample used in this analysis, i.e integrated in the kinematic domain $2.5 < y < 4.0$ and $2 < p_{\mathrm{T}} < 15$ GeV/c (details on the signal extraction procedure and fitting functions will be given in Section 5.3.1). The total number of J/ψ events is 50360 ± 289.

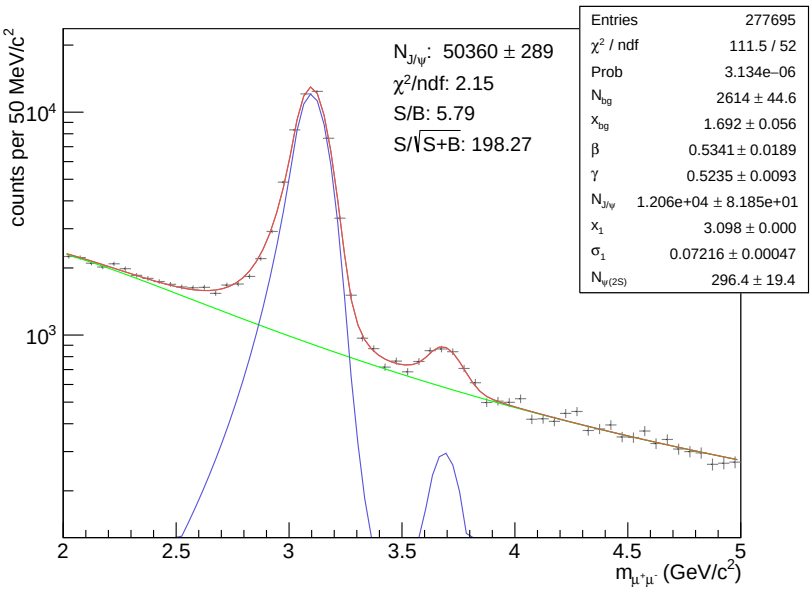

Figure 5.3: Fit to the p_{T} an y-integrated invariant mass distribution ($2.5 < y < 4$ and $2 < p_{\mathrm{T}} < 15$ GeV/c). The invariant mass spectrum is fitted with a Variable Width Gaussian function for the background and two Extended Crystal Ball functions for the J/ψ and ψ(2S) signals, respectively.

Table 5.1 summarizes the choice of bins in p_{T} and the available statistics and signal significance[3] in each case.

Figure 5.4 shows the two dimensional maps of unlike-sign dimuon invariant mass versus $\cos\theta$ in the Collins-Soper frame for two p_{T} bins (in GeV/c): $[2; 3)$ and $[10; 15)$ on the left and right plots, respectively. From these plots it can be noticed that at low-p_{T} the signal extraction feasibility depends on the $\cos\theta$ region, in particular, at $\cos\theta$ close to 1 or -1 the J/ψ peak is no longer identifiable due to a drop in $A \times \varepsilon$ of the detector (further details will be given in Section 5.2.3). While at high p_{T} the drop in $A \times \varepsilon$ is less pronounced, the signal extraction is affected by a poor signal significance no matter the $\cos\theta$ region.
Taking into account the symmetries of the angular distributions and the $A \times \varepsilon$ maps obtained from realistic Monte Carlo (MC) simulations it was possible to define an adequate binning such that the fits to the invariant mass spectra converged and the signal significance was high enough in all cases. The binning choice is discussed in next section

[3]The signal significance is defined as $\frac{S}{\sqrt{S+B}}$ where S represents the integral of the signal function in a region $\pm 3\sigma$ around the peak mean value and $S + B$ represents the sum of the integrals in the same range of the signal and background functions.

Table 5.1: Number of J/ψ obtained from the $\mu^+\mu^-$ invariant mass fits for each p_{T} bin and in the rapidity interval $2.5 < y < 4$.

p_{T} (GeV/c)	$N_{J/\psi}$	$\left(\frac{S}{\sqrt{S+B}}\right)_{J/\psi}$
$[2;3)$	16202 ± 171	109
$[3;4)$	11987 ± 145	96
$[4;5)$	8288 ± 118	81
$[5;7)$	8683 ± 117	84
$[7;10)$	4182 ± 81	59
$[10;15)$	1149 ± 43	30
Total	50361 ± 292	

together with the discussion on $A \times \varepsilon$ of the detector.

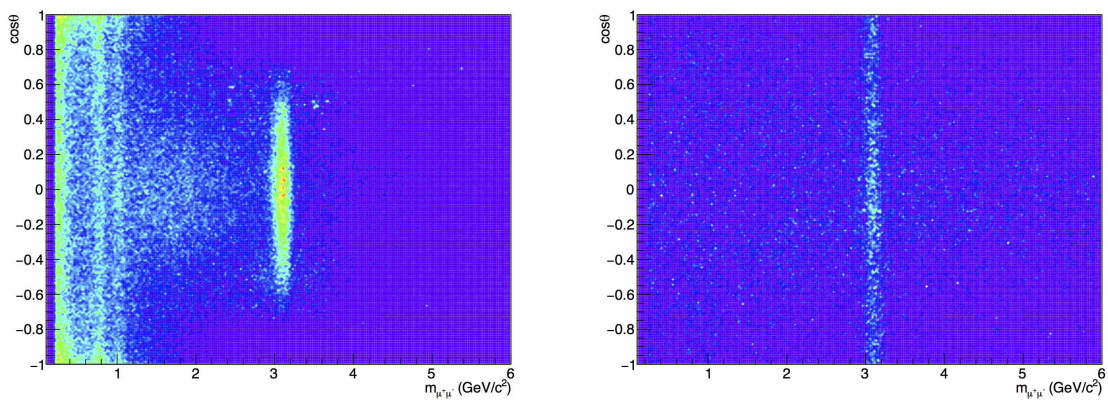

Figure 5.4: $\cos\theta$ vs. $m_{\mu^+\mu^-}$ for the p_{T} bins $2 < p_{\mathrm{T}} < 3\,\mathrm{GeV}/c$ (*left*) and $10 < p_{\mathrm{T}} < 15\,\mathrm{GeV}/c$ (*right*) in the Collins-Soper frame.

J/ψ sample composition

Before continuing the discussion on the analysis procedure, it is useful to have an estimate of the total data sample composition. The J/ψ measurements performed through the dimuon decay channel in the ALICE Muon Spectrometer are inclusive, i.e. they include J/ψ from different origins (Section 1.2.3): the sample contains the directly produced J/ψ's and the contribution from radiative feed-down from $\psi(2\mathrm{S})$ and $\chi_{cn}(1\mathrm{P})$ resonances and from b-hadrons ("non-prompt" J/ψ).
The LHCb experiment has measured the prompt J/ψ [120] and $\psi(2\mathrm{S})$ [121] production cross sections in pp collisions at $\sqrt{s} = 7$ TeV in the kinematic ranges $2 < y \leq 4.5$ and

$p_{\mathrm{T}}(J/\psi) \leq 14$ GeV/c and $p_{\mathrm{T}}(\psi(2\mathrm{S})) \leq 16$ GeV/c, the integrated cross section values are:

$$\sigma_{J/\psi} = 10.52 \pm 0.04\,(\mathrm{stat}) \pm 1.40\,(\mathrm{sys}) \pm^{1.64}_{2.20}\ \mu\mathrm{b}$$
$$\sigma_{\psi(2S)} = 1.44 \pm 0.01\,(\mathrm{stat}) \pm 0.12\,(\mathrm{sys}) \pm^{0.20}_{0.40}\ \mu\mathrm{b}$$

where the last uncertainties represent uncertainties on J/ψ and $\psi(2\mathrm{S})$ polarizations. Also in [120], the non-prompt J/ψ cross section is reported:

$$\sigma_{b\to J/\psi} = 1.14 \pm 0.01\,(\mathrm{stat}) \pm 0.16\ \mu\mathrm{b}.$$

The LHCb collaboration has also measured the ratio $\sigma_{\chi_{cn}(1\mathrm{P})\to J/\psi}/\sigma_{J/\psi}$ as a function of the J/ψ transverse momentum from 2 to 15 GeV/c in pp collisions at $\sqrt{s}$= 7 TeV [122]. Taking into account these measurements and the $\psi(2\mathrm{S}) \to J/\psi$ branching ratio from [2], $B(\psi(2S) \to J/\psi\,\mathrm{anything}) = (60.9 \pm 0.6)\%$, the fraction of $\psi(2\mathrm{S})$ and $\chi_{cn}(1\mathrm{P})$ feed-down contribution to the prompt and inclusive J/ψ and the contribution from b-decays can be evaluated:

$$f^{\mathrm{prompt}}_{\psi(2S)\to J/\psi} = 0.083 \pm 0.013$$
$$f^{\mathrm{prompt}}_{\chi_c\to J/\psi} = 0.158 \pm 0.010$$
$$f^{\mathrm{inclusive}}_{X\to J/\psi} = 0.211 \pm 0.014$$
$$f^{\mathrm{inclusive}}_{b\to J/\psi} = 0.098 \pm 0.012$$

where X refers to $\psi(2\mathrm{S})$ and $\chi_{cn}(1\mathrm{P})$ contributions together.

5.2.2 Simulation

Realistic MC simulations were performed in order to evaluate the acceptance and efficiency of the detector for the $J/\psi\to\ \mu^+\mu^-$ decay. A total number of 11.5 million pure J/ψ events were generated in a run by run basis, proportional to the number of dimuon pairs reconstructed from data in each run. The J/ψ p_{T} and y spectra were produced according to parameterizations obtained from fits to J/ψ cross sections measurements at different pp and p$\bar{\mathrm{p}}$ collisions energies [124]. The simulated spectra were compared to the differential J/ψ production cross sections measured by ALICE in pp collisions at $\sqrt{s}$ = 8 TeV [125] (Figure 5.5), the comparison shows a good agreement between data and simulation.
Only unpolarized J/ψ events were produced, this assumption is not expected to have an important effect in our results, based on the fact that not significant J/ψ polarization has been observed in previous measurements (as discussed in Section 2.3). The effect of this assumption will enter in the systematic error estimation and discussed in Section 5.4.1.
The simulated J/ψ were forced to decay into muon pairs, the possible emission of a photon (radiative decay) was taken into account with a proportion $\mathrm{BR}(J/\psi \to \mu^+\mu^-\gamma, E_\gamma > 100\ MeV)/\mathrm{BR}(J/\psi \to \mu^+\mu^-) = 0.054$ corresponding to theoretical predictions [126].
The passage of muon tracks through the detector elements was performed by the GEANT 3.21 transport code [127] under the detector's real conditions, at the time the data sample was recorded. The detector condition is stored in the Offline Condition Database (OCDB).

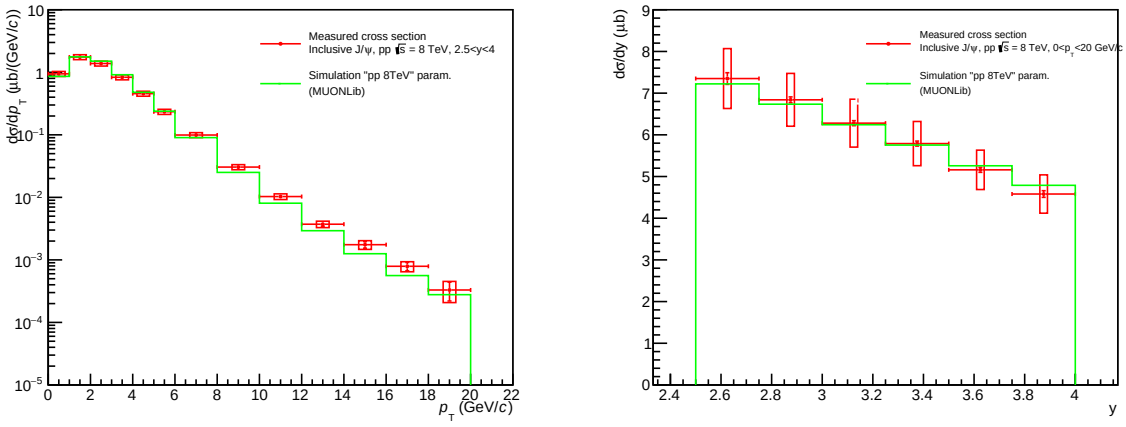

Figure 5.5: Comparison between the measured and simulated J/ψ distributions. In red the p_{T} (*left*) and y (*right*) J/ψ differential production cross sections measured by ALICE in pp collisions $\sqrt{s} = 8$ TeV [125]. The green histograms correspond to the simulated p_{T} and y J/ψ spectra.

The OCDB contains information on the detectors performance in a run-by-run basis. These files are used in MC simulation to reproduce the real detector conditions during the data taking. The information include for instance the efficiencies of tracking and trigger chambers, the residual misalignment of tracking chambers, the map of dead channels and the online track reconstruction parameters.

5.2.3 Acceptance × efficiency maps

The plots in Figure 5.6 show the $A \times \varepsilon$ two-dimensional maps in the Collins-Soper and Helicity frames for the different angle variables as a function of p_{T}. The $A \times \varepsilon$ is evaluated as the total number of reconstructed dimuon pairs (N_{rec}) over the number of generated J/ψ (N_{gen}):

$$A \times \varepsilon = \frac{N_{rec}}{N_{gen}} \tag{5.1}$$

One can see from those plots that $A \times \varepsilon$ significantly decreases at low-p_{T} and $\cos\theta$ close to 1 or -1, especially in the Helicity frame, that would correspond to the case in which one of the muons, the one going in the direction opposite to the J/ψ, is not detected due to its low transverse momentum. For φ close to 0 and π also the $A \times \varepsilon$ show very small values, these cases correspond to the situation where both muons are parallel to the quarkonium production plane; in this configuration the probability to get the two muons in the acceptance of the detector decreases for J/ψ close to the edges of the Muon Spectrometer acceptance. This effect is diluted by construction in the $\tilde{\varphi}$ distribution.
The regions of low $A \times \varepsilon$ constitute a limitation to the signal extraction procedure, for some bins of very low statistics it is not always possible to achieve a converging fit to the dimuon invariant mass spectrum. In order to improve the signal extraction procedure

and taking into account the symmetries of the angular distributions, the analysis regions were limited to $|\cos\theta|$ between 0 and 1, φ between 0 and $\pi/2$ and $\tilde{\varphi}$ between 0 and π. In this way, by single (for $\cos\theta$ and $\tilde{\varphi}$) or double (φ) reflexion it is possible to increase the statistics by factors 2 and 4, respectively. Figure 5.7 illustrates the reflexion procedure for the $\cos\theta$ and φ variables.
For each p_{T} bin the data were further split in 10 $\cos\theta$, φ or $\tilde{\varphi}$ bins as shown in Figure 5.7 for $\cos\theta$ in the Collins-Soper frame. However, due to the low $A\times\varepsilon$ at the lower p_{T} bins, it was necessary in some cases to merge 2, 3, or 4 angular bins to get a good enough signal significance and fit quality. For instance, in the Collins-Soper system (see also Figure 5.7 left panel) the bin limits on $|\cos\theta|$ distribution for the p_{T} bin from 2 to 3 GeV/c were chosen as [0, 0.1), [0.1, 0.2), [0.2, 0.3), [0.3, 0.4), [0.4, 0.5), [0.5, 0.6), [0.6, 1.0) i.e. 7 bins instead of 10 as it is for the higher p_{T} bins ($p_{\mathrm{T}} > 5$ GeV/c), meaning that the four last bins have been merged into one. Table 5.2 summarizes the optimized number of bins for the different angular distributions as a function of p_{T}. For the φ ($\tilde{\varphi}$) distributions, the bin merging is performed for φ ($\tilde{\varphi}$) values close to zero.

Table 5.2: Number of bins used for the signal extraction for each angular distributions as a function of p_{T}.

p_{T} (GeV/c)	[2; 3)	[3; 4)	[4;5)	[5; 7)	[7; 10)	[10; 15)
$\cos\theta_{CS}$	7	8	9	10	10	10
φ_{CS}	10	6	6	10	10	10
$\tilde{\varphi}_{CS}$	10	10	10	10	10	10
$\cos\theta_{HX}$	8	8	8	9	9	8
φ_{HX}	10	6	8	10	10	10
$\tilde{\varphi}_{HX}$	10	10	10	10	10	10

5.3 Study of polarization

5.3.1 Signal extraction and raw angular distributions

Figure 5.8 shows the invariant mass distributions in two different $\cos\theta$ bins in the same p_{T} bin ($3 < p_{\mathrm{T}} < 4$ GeV/c) for raw data (top) and MC (bottom). It can be noticed that the tails and width of the J/ψ peak, the slope of the background component and the signal to background ratio can be very different from bin to bin. Given this fact, and in order to obtain a converging fitting procedure for all bins, the signal extraction algorithm has been conceived in five steps:

1. The regions outside the J/ψ and ψ(2S) peaks were fitted with a given background function $f_{\mathrm{bkg}}(x)$, the initial parameters given to $f_{\mathrm{bkg}}(x)$ being the ones from the fit to the integrated data sample (Figure 5.3).

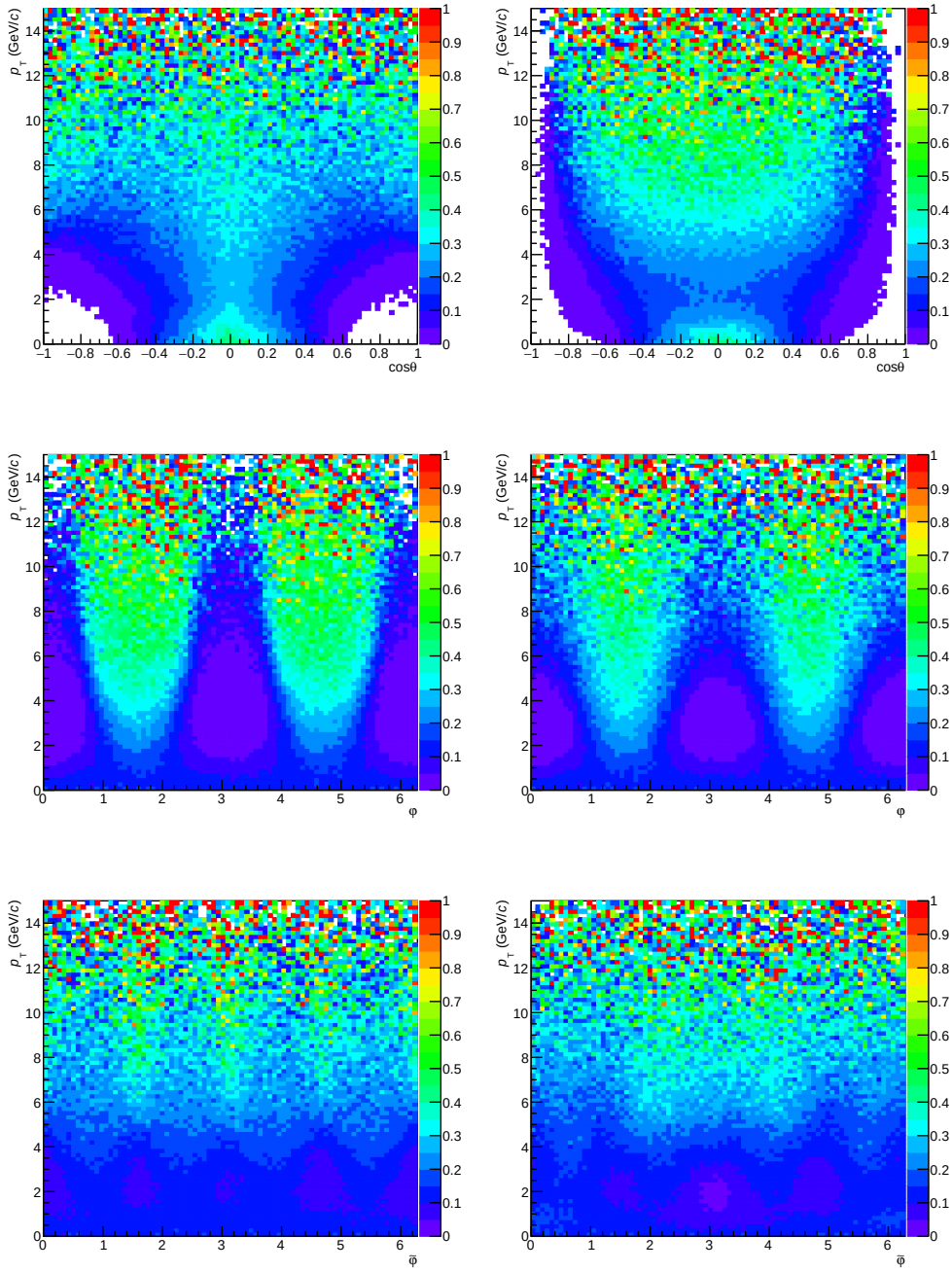

Figure 5.6: $A \times \varepsilon$ maps in the Collins-Soper (*left*) and Helicity frames (*right*). From top to bottom the plots show $\cos\theta$, φ and $\tilde{\varphi}$ vs. p_{T}.

2. The MC dimuon invariant mass distribution is fitted with the signal function $f_{\mathrm{signal}}(x)$, for which the initial parameters have been defined as those of the integrated MC mass distribution.

3. Both signal regions, defined as the intervals $\pm 5\sigma$ around the J/ψ and $\psi(2\mathrm{S})$ PDG

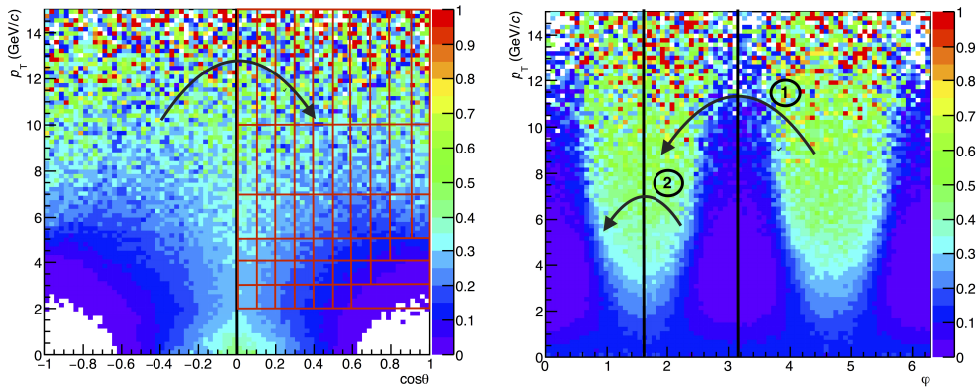

Figure 5.7: $A \times \varepsilon$ maps: $\cos\theta$ (*left*) and φ (*right*) vs. p_{T}; in the Collins-Soper frame. The single or double reflexion is illustrated by black arrows. On the left panel, the red lines illustrate the binning selection.

mass values, are then fitted individually with the signal function $f_{\mathrm{signal}}(x)$ and using as initial parameters those from the fit of the MC spectra in the corresponding bin (from step 2).

4. The parameters obtained from 1 and 3 are introduced as initial parameters of the total function $f_{\mathrm{tot}}(x) = f_{\mathrm{bkg}}(x) + f_{J/\psi\ \mathrm{signal}}(x) + f_{\psi(2\mathrm{S})\ \mathrm{signal}}(x)$, and the global fit is performed.

5. The J/ψ signal function $f_{J/\psi\ \mathrm{signal}}(x)$ is integrated in the full invariant mass range to extract the raw number of J/ψ events. To compute the uncertainty on this number, the covariance matrix error of the signal function parameters is used[4].

[4]Given a function $f_{\mathrm{signal}}(x; p_i)$ used to fit the signal shape (where p_i denotes the function parameters, and the index i goes up to the number of parameters N), the number of J/ψ events is obtained as:

$$N_{J/\psi} = \int_a^b f_{\mathrm{signal}}(x; p_i) dx$$

so, it can be expressed as:

$$N_{J/\psi} = f'(p_i).$$

The uncertainty on $N_{J/\psi}$ is obtained by quadratic propagation of errors:

$$\sigma^2_{N_{J/\psi}} = \sum_i \sum_j \frac{\partial f'}{\partial p_i} \frac{\partial f'}{\partial p_j} M_{ij}$$

where M_{ij} denotes the elements of the covariance matrix of the parameters of f'. The sum goes up to N.
In ROOT $\sigma^2_{N_{J/\psi}}$ is given by the method TF1::IntegralError(), and it is computed as:

$$\sigma^2_{N_{J/\psi}} = \sum_i \sum_j \frac{\partial}{\partial p_i} \int f_{\mathrm{signal}}(x; p_i) dx \, \frac{\partial}{\partial p_j} \int f_{\mathrm{signal}}(x; p_i) dx \, M_{ij}$$

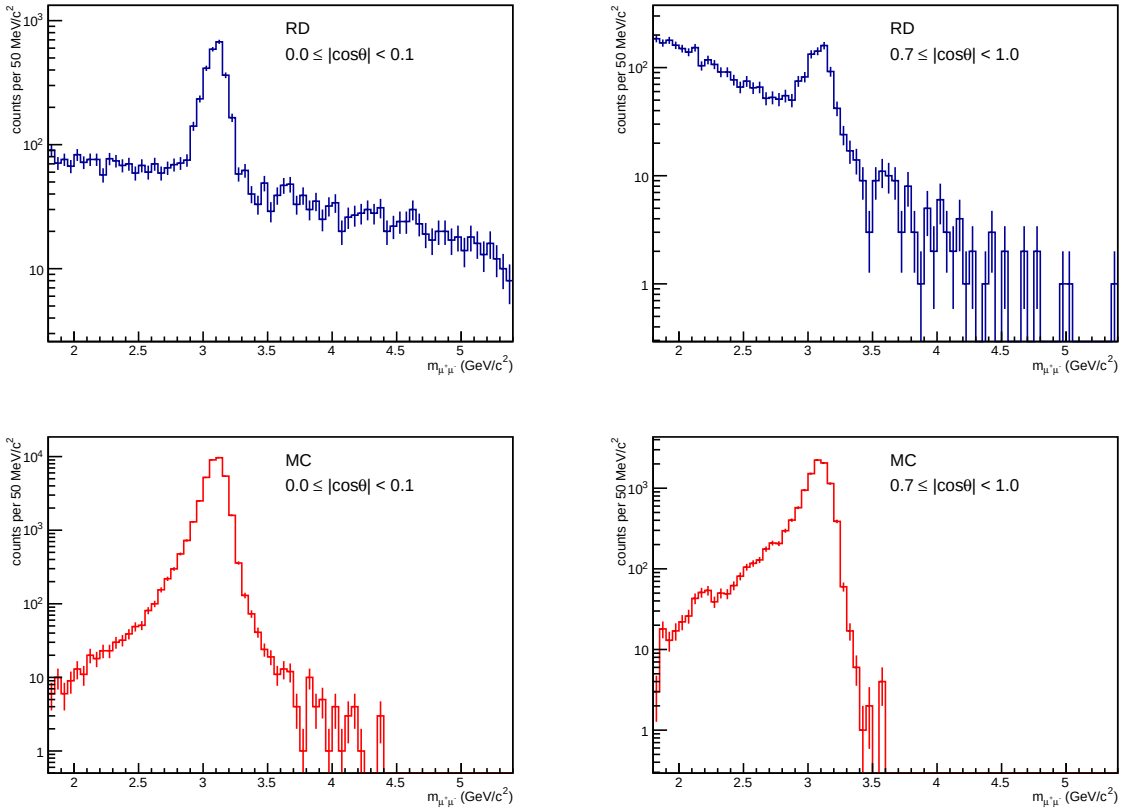

Figure 5.8: Unlike-sign dimuon invariant mass distributions for raw data (*top*) and MC (*bottom*) in the p_{T} bin from 3 to 4 GeV/c and $0 \leq |\cos\theta| < 0.1$ (*left*) and $0.7 \leq |\cos\theta| < 1.0$ (*right*).

At the end, the raw data angular distributions are constructed for each p_{T} bin.
. The J/ψ signal is extracted under several fitting conditions to consider the systematic effect associated to the different choices.
The background was described by a Variable Width Gaussian (VWG) function:

$$f_{\mathrm{bkg}}(x) = N \cdot \exp\left[-\frac{(x-\mu)^2}{2\sigma^2}\right] \quad \text{with} \quad \sigma(x) = \beta + \gamma \cdot \left[\frac{(x-\mu)}{\mu}\right] \tag{5.2}$$

And as an alternative function, the multiplication of a Gaussian with an exponential

---

Once the function parameters have been estimated in the fit (in this analysis, the χ^2 method was used), the matrix elements are computed as:

$$(M^{-1})_{ij} = \frac{1}{2}\frac{\partial^2\chi^2}{\partial p_i \partial p_j}|_{p_k}$$

where p_k denotes the set of parameters given by the fit.

(GExp) was considered:

$$f_{\text{bkg}}(x) = N \cdot \exp\left[-\frac{(x-\mu)^2}{2\sigma^2}\right] \cdot \exp\left(-\alpha x\right) \tag{5.3}$$

For the peaks, two Extended Crystal Ball or two NA60 functions (one for the J/ψ signal and a second one for $\psi(2S)$) were chosen.
The Extended Crystal Ball function was first introduced by the Crystal Ball collaboration [128] and consists of a Gaussian core with power law tails, its analytical form is:

$$f_{\text{signal}}(x;\mu,\sigma,\alpha,n) = N \cdot \begin{cases} \exp\left[\frac{(x-\mu)^2}{2\sigma^2}\right] & \text{for} \quad \alpha_L > \frac{(x-\mu)}{\sigma} > -\alpha_R \\ A \cdot \left[B - \frac{(x-\mu)}{\sigma}\right]^{-n_L} & \text{for} \quad \frac{(x-\mu)}{\sigma} \leq \alpha_L \\ C \cdot \left[D - \frac{(x-\mu)}{\sigma}\right]^{-n_R} & \text{for} \quad \frac{(x-\mu)}{\sigma} \geq \alpha_R \end{cases} \tag{5.4}$$

where

$$A = \left(\frac{n_L}{|\alpha_L|}\right)^{n_L} \exp\left(-\frac{|\alpha_L|^2}{2}\right) \quad C = \left(\frac{n_R}{|\alpha_R|}\right)^{n_R} \exp\left(-\frac{|\alpha_R|^2}{2}\right)$$

$$B = \frac{n_L}{|\alpha_L|} - |\alpha_L| \qquad D = \frac{n_R}{|\alpha_R|} - |\alpha_R|$$

and α_L, n_L and α_R, n_R are the left and right parameters of the tails.
The NA60 function, introduced by the NA60 collaborations in the study of charmonia [129], is a Gaussian of variable sigma, it can be written as:

$$f_{\text{signal}}(x;\mu,\sigma,\alpha,n) = N \cdot \exp\left[-\frac{1}{2}\left(\frac{t}{t_0}\right)^2\right] \tag{5.5}$$

where

$$t = \frac{(x-\mu)}{\sigma}$$

and

$$t_0 = \begin{cases} 1 + p_{1L}(\alpha_L - t)^{(p_{2L} - p_{3L}\sqrt{\alpha_L - t})} & \text{for} \quad t < \alpha_L \\ 1 & \text{for} \quad \alpha_L \leq t < \alpha_R \\ 1 + p_{1R}(t - \alpha_R)^{(p_{2R} - p_{3R}\sqrt{t - \alpha_R})} & \text{for} \quad t \geq \alpha_R \end{cases}$$

As for the Extended Crystal Ball function the L and R subscripts indicate left and right tail parameters respectively. In both cases the tail parameters are fixed to the ones obtained in the fits of simulated J/ψ to reduce the number of free parameters of the total fit.
Before generalizing this procedure to all bins, it was checked in high statistics bins (low p_{T}) that the MC tails can reproduce the raw data shapes. Figure 5.9 shows an example of fits to the first and last $\cos\theta_{CS}$ bins in the range $3 < p_{\text{T}} < 4$ GeV/c. The middle plots

show the fit results by fixing the tails parameters to those obtained from the simulations (upper plots) and in the bottom plots tails have been left free (and the background fixed to the same parameters as for the middle plots). From the fit results, it can be seen that the MC tails and the ones obtained from the raw data fit are in agreement within uncertainties. Also, the n_L and n_R parameters have large uncertainties when they are left free in the raw data fit, which results in a bigger uncertainty on the number of J/ψ extracted. As a consequence, it was decided to fix the tail parameters to the ones from the MC, since they describe correctly the signal shape in data.
The number of signal events are compatible within statistical errors for both fitting conditions. The fact of leaving the tail parameters free makes the total fit function to fail in finding a minimum χ^2 in most cases.
To further reduce the number of free parameters of the fit, the mass and sigma of $\psi(2S)$ are constrained to those of the J/ψ as:

$$\mu_{\psi(2S)} = \mu_{J/\psi} + m^{\mathrm{PDG}}_{\psi(2S)} - m^{\mathrm{PDG}}_{J/\psi} \quad \text{and} \quad \sigma_{\psi(2S)} = \sigma_{J/\psi} \frac{\sigma^{\mathrm{MC}}_{\psi(2S)}}{\sigma^{\mathrm{MC}}_{J/\psi}}$$

with

$$m^{\mathrm{PDG}}_{J/\psi} = 3096.916 \pm 0.011\,\mathrm{MeV}/c^2 \quad \text{and} \quad m^{\mathrm{PDG}}_{\psi(2S)} = 3686.108 \pm 0.011\,\mathrm{MeV}/c^2$$

Since in our MC simulation we generated only pure J/ψ events, the value $\sigma^{\mathrm{MC}}_{\psi(2S)}$ was taken from [125].
The mass interval considered in the fit was varied from the standard range usually adopted by different analyses ($2 < m_{\mu^+\mu^-} < 5$ GeV/c^2) to a smaller ($2.2 < m_{\mu^+\mu^-} < 4.5$ GeV/c^2) and larger ($1.5 < m_{\mu^+\mu^-} < 6$ GeV/c^2) mass intervals.
In summary, the different fitting conditions used were:

- 2 ECB + VWG in the range $[2.0; 5.0]$ GeV/c^2
- 2 ECB + VWG in $[2.2; 4.5]$ GeV/c^2
- 2 ECB + VWG in $[1.5; 6.0]$ GeV/c^2
- 2 NA60 + VWG in $[2.0; 5.0]$ GeV/c^2
- 2 ECB + GExp in $[2.0; 5.0]$ GeV/c^2

The fit quality is not affected by the use of one or another signal function neither by the combination to a background function, and the χ^2 values clustered around the same value in both cases: $\langle\chi^2\rangle = 1.21$, $\sigma_{\mathrm{RMS}} = 0.31$.
Figure 5.10 shows a comparison between the ECB and NA60 functions in terms of the number of signal events for each $\cos\theta_{CS}$ bin and for p_{T} between 2 and 3 GeV/c (on the left), and the bin by bin evolution of the signal function parameters: mass (center) and mass resolution (right).
The J/ψ mass obtained from the fit with the NA60 function is systematically higher than the one obtained with the ECB, which is also closer to the PDG reported value, for this

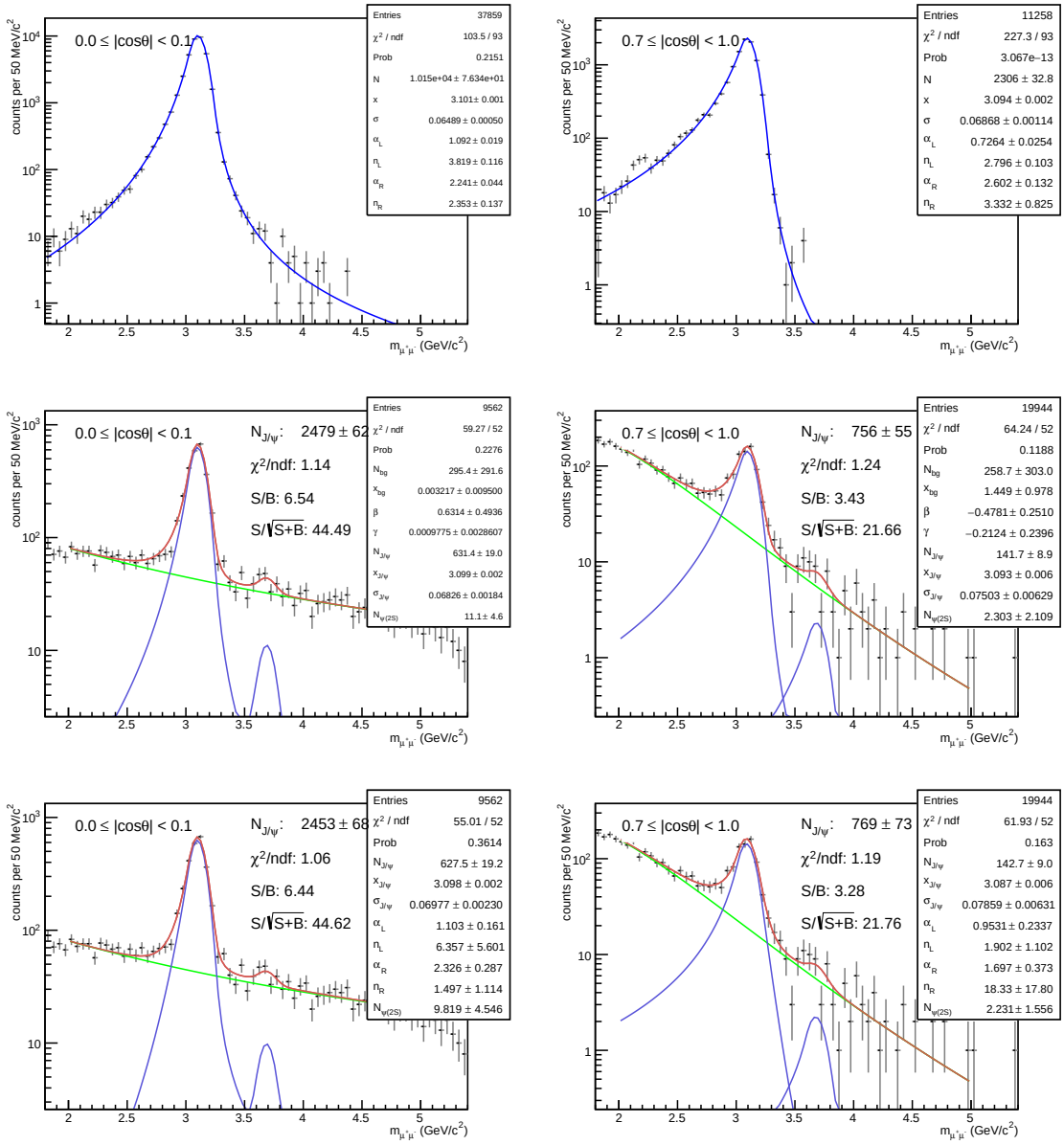

Figure 5.9: Fits to the unlike-sign dimuon invariant mass distributions in the p_{T} bin from 3 to 4 GeV/c and $0 \leq |\cos\theta| < 0.1$ (*left*) and $0.7 \leq |\cos\theta| < 1.0$ (*right*). *Top*: Invariant mass distributions at the reconstruction level of simulations fitted with the Extended Cristal Ball function. *Middle*: Invariant mass distributions from raw data fitted with the sum of two ECB functions and a Variable Width Gaussian, the tails of the ECB are fixed to the ones obtained from the fit to MC data (plots on the *top*). *Bottom*: Same as the *middle* plots but the tails of the ECB are left free.

reason the ECB is chosen as "default" function to describe the peaks and test the different fit ranges, while the NA60 is an alternative peak shape function mostly taken into account to evaluate the systematic error associated to one or another choice and entering

in only one of the fit settings. In all cases the numbers of signal events obtained by the use of NA60 are compatible to those obtained from the fit with the Extended Crystal Ball function.

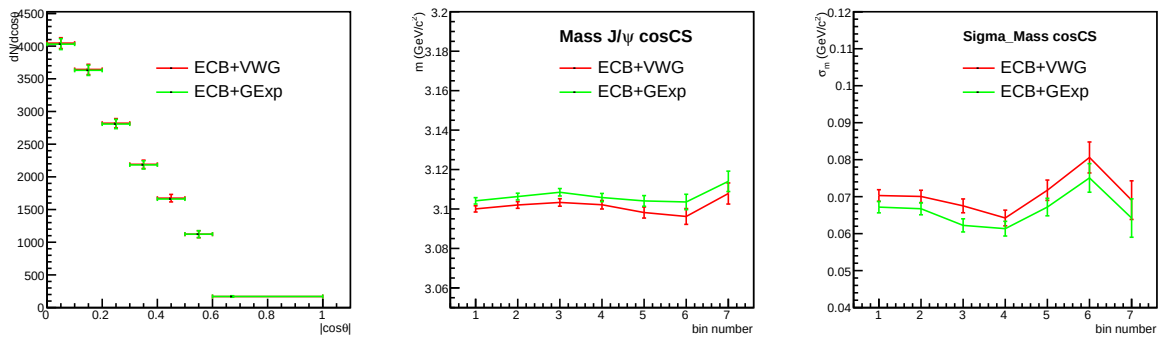

Figure 5.10: Results from the use of Extended Crystal Ball and NA60 functions to describe the signal shape. *Left*: Raw $W(\cos\theta)$, *Center*: J/ψ mass and *Right*: mass resolution evolution as a function of $\cos\theta$ bin (label 1 corresponds to the bin $0 \leq \cos\theta < 0.1$ and so on). All plots refer to the p_{T} bin from 2 to 3 GeV/c and in Collins-Soper frame.

The fit range can affect its quality and stability: the different background proportion around the peaks can constrain in less or higher degree the global fit function, however this fact does not have a significant impact on the signal extraction quality and χ^2 values are only slightly smaller and closer to 1 in the case of the biggest fit interval compared to the other two cases (Figure 5.11).
The number of signal events obtained in the three cases were found to vary within statistical uncertainties and no pattern indicating a global effect was observed (Figure 5.12), the mass and mass resolution of the J/ψ peak follows the same trend as a function of p_{T} and angular bin.

5.3.2 Corrected angular distributions

The raw number of J/ψ, $N^{raw}_{\mathrm{J}/\psi}$ is corrected by the acceptance and efficiency factor $A \times \varepsilon$:

$$N^{corr}_{\mathrm{J}/\psi} = \frac{N^{raw}_{\mathrm{J}/\psi}}{A \times \varepsilon} \tag{5.6}$$

For the raw $W(|\cos\theta|)$, the uncertainties on the number of signal events are given by the error of the TF1::IntegralError() method of ROOT applied to the defined signal function (ECB or NA60) which properly perform error propagation taking into the correlation among all function parameters. The $A \times \varepsilon$ distributions are built by the ratio N_{rec}/N_{gen}. The uncertainties are computed under the assumption that N_{rec} follows a binomial dis-

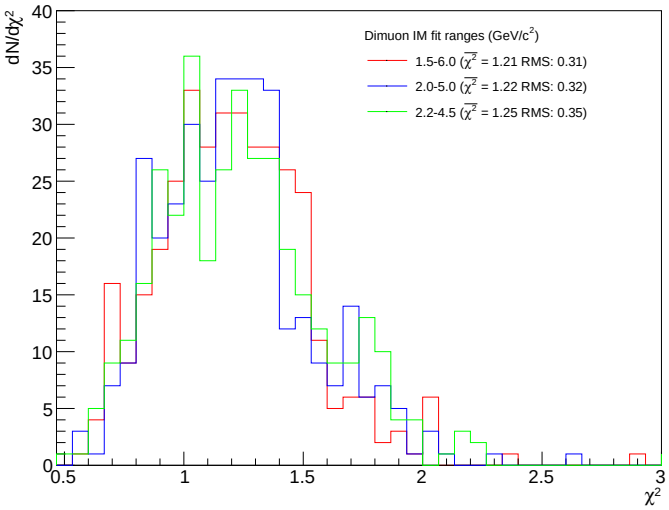

Figure 5.11: χ^2 (per degree of freedom) distributions for the different fitting ranges considered in the systematics on the signal extraction. Each distribution contains the χ^2 values corresponding to all bins in p_{T}, $\cos\theta$, φ and $\tilde{\varphi}$ in both polarization frames (i.e. around 360 entries in each distribution).

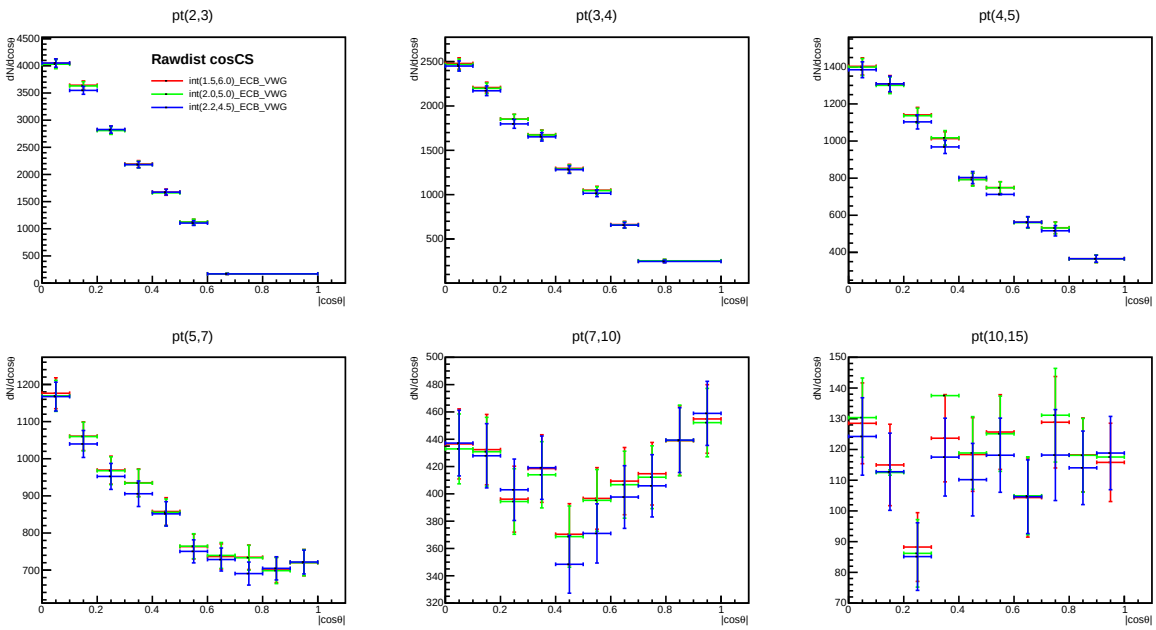

Figure 5.12: Raw number of signal events obtained by the fits in three different fit intervals of the dimuon invariant mass distribution with the combination of two Extended Crystal Ball and a Variable Width Gaussian function. The graphs show the $W(\cos\theta)$ distributions in the Collins-Soper frame for all p_{T} bins.

tribution[5]. The uncertainty on the corrected distributions is estimated by the quadratic error propagation:

$$\left(\frac{\sigma^{corr}_{\mathrm{J}/\psi}}{N^{corr}_{\mathrm{J}/\psi}}\right)^2 = \left(\frac{\sigma^{raw}_{\mathrm{J}/\psi}}{N^{raw}_{\mathrm{J}/\psi}}\right)^2 + \left(\frac{\sigma_{A\times\varepsilon}}{A\times\varepsilon}\right)^2 \tag{5.7}$$

Figure 5.13 illustrates, for one p_{T} bin and set of measurements corresponding to one of the aforementioned fit conditions, the raw distribution and the correction by $A \times \varepsilon$. The final step in the extraction of polarization parameters is the fit of the corrected angular distribution as shown also in the figure. The results for all p_{T} bins, and the same fit conditions (ECB+VWG in the mass range 2-5 GeV/c^2), are shown in Appendix A.
In Appendix B the raw (Table B.1) and corrected (Table B.2) number of J/ψ for each p_{T} bin (by adding the J/ψ signal over all angular bins[6]), and in both frames for all angular distributions, are reported. Table B.1 shows the coherence on the number of signal events, independently of the frame or angular distribution studied. Table B.2 shows that after the $A \times \varepsilon$ correction the numbers are still in agreement indicating that the correction is not affected by bias in the $A \times \varepsilon$ computation.

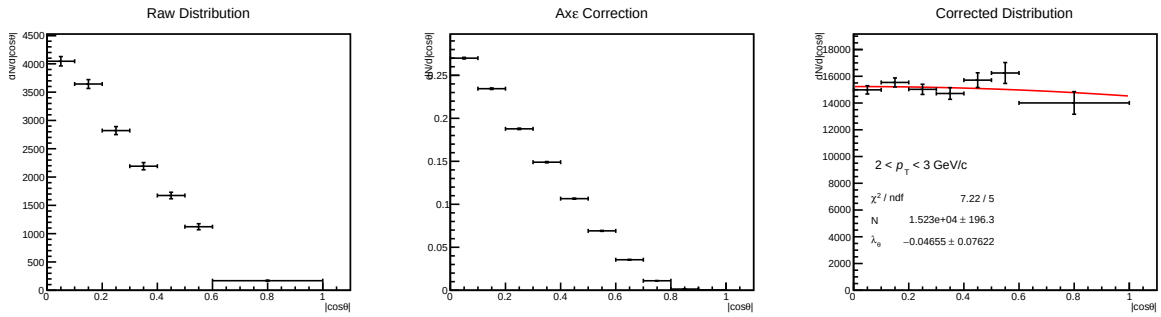

Figure 5.13: *Left*: Raw $W(|\cos\theta|)$ obtained from the fit with ECB+VWG in the mass range 2-5 GeV/c^2, *Center*: $A \times \varepsilon$ as a function of $|\cos\theta|$ and *Right*: Corrected $W(|\cos\theta|)$ distributions and fit in the first p_{T} bin ([2;3) GeV/c) for the Collins-Soper frame.

5.3.3 Polarization parameters as a function of p_{T}

All polarization parameter measurements performed in this way for the same p_{T} bin, i.e. with the different fitting conditions, were combined and the mean value is reported as the

[5]The $A \times \varepsilon$ can be interpreted as the probability of a number of success N_{rec} out of N_{gen} number of trials. In this way the mean value of the distribution is $A \times \varepsilon = N_{rec}/N_{gen}$ and its standard deviation is given by:

$$\sigma_{A\times\varepsilon} = \sqrt{\frac{A\times\varepsilon\cdot(1-A\times\varepsilon)}{N_{gen}}}$$

[6]All the invariant mass fits of raw for each p_{T} and angular bins, and for both frames, are presented in an ALICE Analysis Note to be submitted to the Collaboration.

final result:

$$\langle\lambda\rangle = \frac{\sum_i \lambda_i}{N} \quad \text{and} \quad \sigma_{\langle\lambda\rangle} = \frac{\sum_i \sigma_{\lambda_i}}{N} \tag{5.8}$$

The subscript i refers to the different fit conditions described in 5.3.1. For the propagation of uncertainties, a full correlation of the individual measurements was assumed[7].
The λ_θ dependence on p_T in the Collins-Soper frame obtained under the different fit conditions for the signal extraction is shown in Figure 5.14.

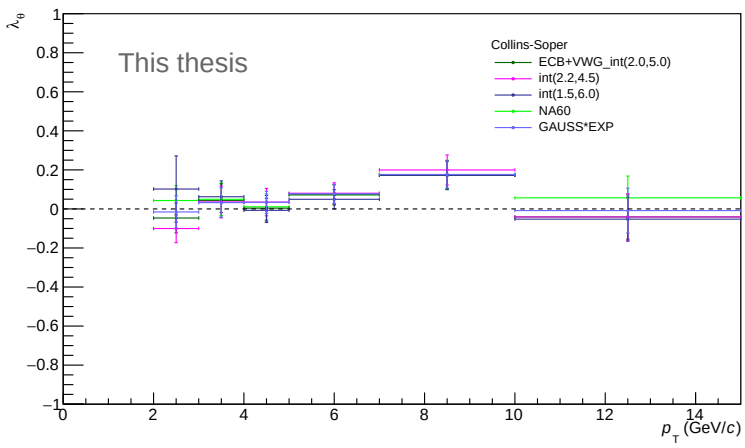

Figure 5.14: λ_θ in the Collins-Soper frame as a function of p_T obtained by applying different fit conditions for the signal extraction.

[7]From the general expression of quadratic propagation of errors:

$$\sigma^2_{\langle\lambda\rangle} = \frac{1}{N^2}\sum_i\sum_j \sigma_i\sigma_j\rho_{ij}$$

where ρ_{ij} denotes the correlation coefficient of measurements i and j.
Assuming $\rho_{ij} = 1$, the equation 5.8 is obtained:

$$\sigma_{\langle\lambda\rangle} = \frac{1}{N}\sqrt{\sum_i \sigma_i^2 + \sum_i \sum_{j(j\neq i)} \sigma_i\sigma_j} = \frac{1}{N}\sqrt{\left(\sum_i \sigma_i\right)^2}$$

5.4 Systematic Uncertainties

For the estimation of systematics uncertainties, the procedure adopted was to proceed up to the end of the analysis method, i.e. building the corrected angular distributions and getting the λ_i parameter resulting from each different condition. The associated uncertainty to each kind of systematic (labeled X in the following) is computed as:

$$\sigma_{sys\,X} = |\lambda_X - \langle\lambda\rangle| \tag{5.9}$$

The different systematic sources considered are listed below:

- Signal extraction
- Input p_{T} and y distributions in simulation
- Input polarization parameters
- Radiative decay fraction
- Trigger response function
- J/ψ from b-hadrons

The calculation of systematics due to the signal extraction is straightforward (all values for the full set of polarization parameters are reported in Appendix C.1). The uncertainties due to the chosen input p_{T} and y and angular distributions as well as the contribution from radiative decay fraction are described in subsection 5.4.1. In subsection 5.4.2 the procedure to estimate the error due to the trigger response function is detailed. The J/ψ fraction from b-hadron and its contribution to the systematics is calculated in Section 5.4.3.

5.4.1 Systematics associated to the input MC

p_{T} and y parameterizations

As it was already mentioned (in section 5.2.2), the J/ψ p_{T} and y distributions were generated according to parameterizations obtained from the extrapolation from lower collision energies. The input distributions are:

$$f(p_{\mathrm{T}};\sqrt{s}) = \frac{p_{\mathrm{T}}}{\left[1 + 0.363\left(\frac{p_{\mathrm{T}}}{1.04\cdot(\sqrt{s})^{0.101}}\right)\right]^{3.9}} \quad \text{and} \quad f(y;\sqrt{s}) = \exp\left[-\frac{\left(\frac{y}{\lg\sqrt{s}/3.097}\right)^2}{2\cdot 0.4^2}\right]$$

To evaluate the associated systematic uncertainty, these distributions have been slightly modified to the corresponding shapes at a lower collision energy ($\sqrt{s} = 5$ TeV). The new distributions were produced by a re-weighting of the MC sample. A weight w_i, was

applied to each generated J/ψ event at a given p_{T} and y. The corresponding weights are computed as:

$$w_i = \frac{f(p_{\mathrm{T}}; \sqrt{s} = 5\mathrm{TeV})}{f(p_{\mathrm{T}}; \sqrt{s} = 8\mathrm{TeV})} \quad \text{or} \quad w_i = \frac{f(y; \sqrt{s} = 5\mathrm{TeV})}{f(y; \sqrt{s} = 8\mathrm{TeV})}$$

the same weight w_i was then assigned to the event at the reconstruction level and finally the $A \times \varepsilon$ maps recomputed.
Figure 5.15 shows the original and modified p_{T} and y distributions at generation level as well as a the comparison in terms of $A \times \varepsilon$ distributions. The $A \times \varepsilon$ from one or another

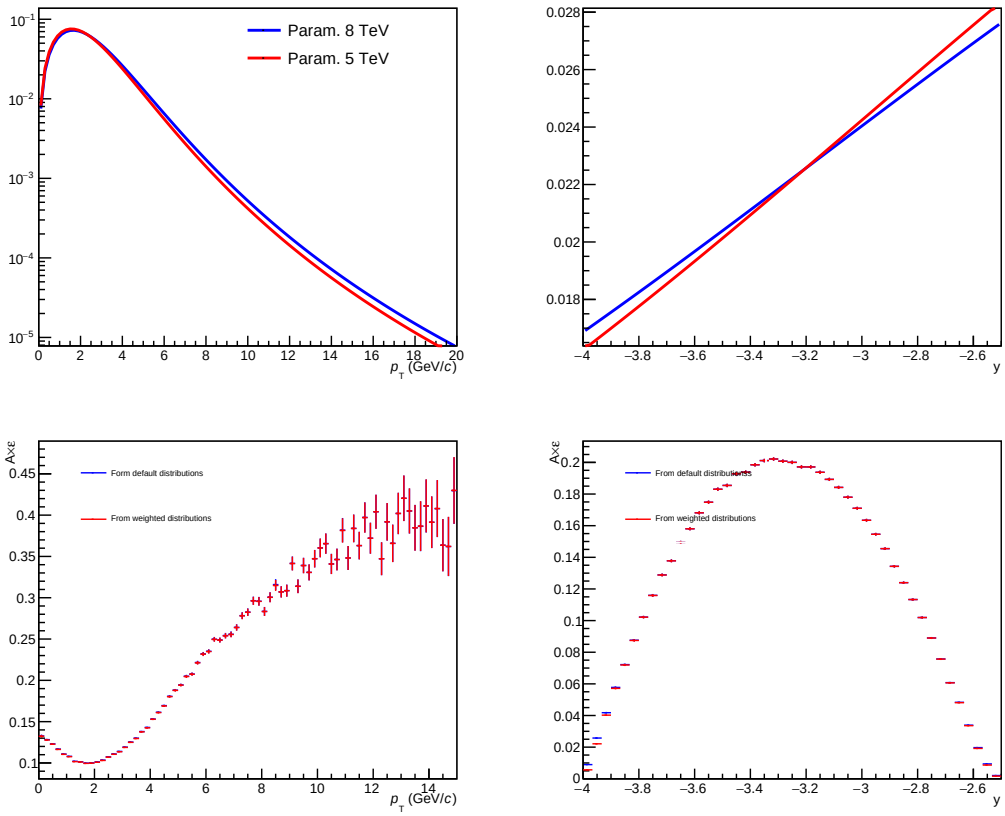

Figure 5.15: *Top*: J/ψ p_{T} (*left*) and y (*right*) distributions from parameterizations for pp collisions at $\sqrt{s} = 8$ TeV(blue) and $\sqrt{s} = 5$ TeV(red). *Bottom*: $A \times \varepsilon$ distributions as a funtion on p_{T} and y from the two collision energy paramaterizations.

parameterizations are quite similar, so the uncertainties associated to these sources should in principle be not significant. However, small variations in the $A \times \varepsilon$ angular distributions can represent a bigger variation on the corrected angular distributions and the final fit with the W functions give λ values more or less deviated from the reference value.
The magnitude of uncertainties depend on the polarization system and λ parameter. Figure 5.16 shows the λ_θ parameter in the Collins-Soper frame as a function of p_{T} estimated

with the "default" parameterizations and the p_{T} and y changed functions. The biggest uncertainties are associated to the λ_θ parameter in most p_{T} bins due to the fact that the $|\cos\theta|$ distributions are more sensitive to $A \times \varepsilon$ effects, especially in the lower p_{T} bins compared to the φ and $\tilde{\varphi}$ distributions (Figure 5.6). All errors for the complete set of parameters in both frames are lower than 0.05.

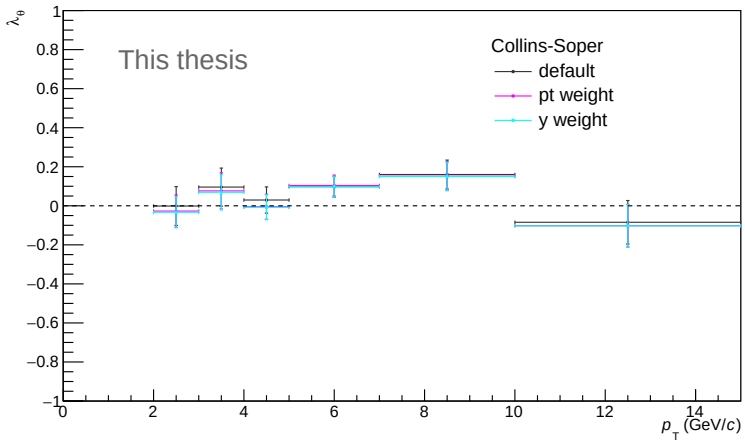

Figure 5.16: λ_θ in the Collins-Soper frame as a function of p_{T} for the "default" p_{T} and y parameterizations and resulting from the p_{T} and y re-weighted simulation.

Radiative decay fraction

The uncertainty on the branching ratio for the radiative decay $J/\psi \to \mu^+\mu^-\gamma$ can be also considered as a source of systematic uncertainty. Since the importance of the radiative tail on the dimuon invariant mass shape can affect the signal extraction, in the estimation of this uncertainty the full procedure for the measurement of polarization parameters have to be performed, i.e. from the dimuon invariant mass fits in angular and p_{T} bins to the fits of the corrected angular distributions.
There is no PDG reported value for this branching ratio but only theoretical predictions [126]. The same calculations are in good agreement with experimental results for the $e^+e^-\gamma$ decay channel [131]. The measured ratio of $BR(J/\psi \to e^+e^-\gamma; E_\gamma > 100\,\mathrm{MeV})$ and $BR(J/\psi \to e^+e^-)$ gives 0.147 ± 0.022 and the corresponding number for the $\mu^+\mu^-\gamma$ and $\mu^+\mu^-$ decays is expected to be smaller by a factor 2.6. The MC simulations reproduce this ratio as shown in Figure 5.17. Assuming an uncertainty on the branching ratio for $\mu^+\mu^-\gamma$ similar to the one reported for $B(J/\psi \to e^+e^-\gamma)$ i.e.$\sim$ 16%, the systematic effect introduced by the unknown $\mu^+\mu^-\gamma$ branching ratio can be roughly estimated.
Figure 5.17 shows the impact of variations to the radiative decay branching ratio on the unlike-sign dimuon invariant mass distributions at generation and reconstruction levels of simulation. A $\pm 2\sigma$ variation is found to be not significant and to be of the same order of statistical fluctuations of the reconstructed distributions. For this reason a stronger

variation has been introduced: the assumption of no radiative contribution at the simulation level, as represented by the red curve in Figure 5.17. This choice although not physical has three motivations: 1. it will give the higher limit to the systematic error associated to the radiative decay branching ratio; 2. since in the invariant mass fits for the signal extraction the tails are fixed to those obtained from the fit of the reconstructed distributions from simulation, the choice also allows to test the fits with a different set of tails from MC and 3. the presence of a photon (three body decay) bias the calculation of angular distributions, so, removing the contribution of radiative decay is also a way to estimate the associated bias to the three body decay.

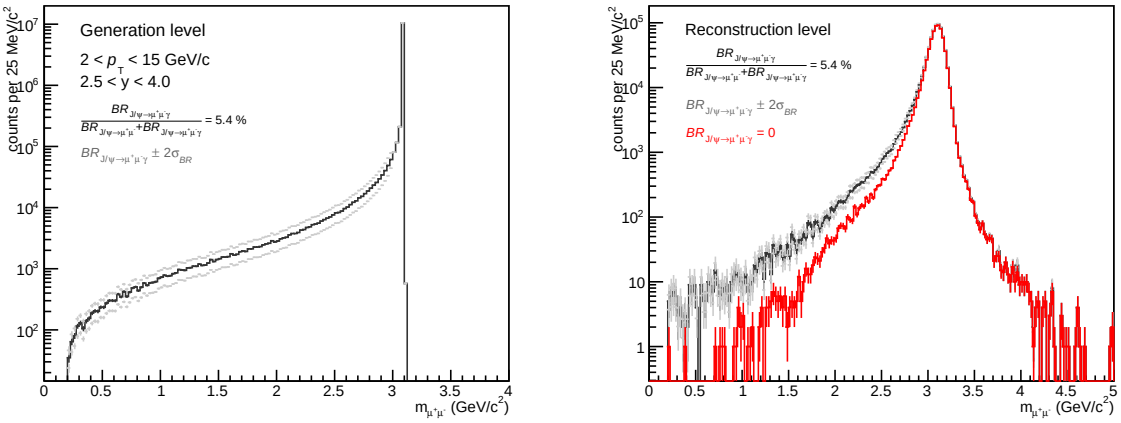

Figure 5.17: *Left*: Dimuon invariant mass distribution at generation level (gray points histograms show the effect of the branching ratio variation in $\pm 2\sigma$). *Right*: Dimuon invariant mass distribution at reconstruction level (gray and red distributions correspond to the cases of $\pm 2\sigma$ variation and the full removal of the fraction corresponding to radiative decay, respectively).

Figure 5.18 shows the measured λ_θ as a function of p_{T} for the Collins-Soper and Helicity frame, under both branching ratio assumptions. Even applying this strong assumption, the difference is very small and the errors of the order 0.01, independent of p_{T}.

Input polarization

As it was previously mentioned, the generated J/ψ in the MC simulation were assumed to be unpolarized. This can in fact have an impact on the estimated $A \times \varepsilon$ of the detector and thus on the corrected W distributions, with a possible bias on the measured polarization parameters. Assuming no polarization at the J/ψ generation level is however not such a strong conjecture based on most experimental observations, where only slight polarizations have been reported (Section 2.3).
To evaluate the possible impact of this assumption on the measurements, as a first step, two extreme (since do not correspond to our measurements) and opposite scenarios have been conceived: 1. full longitudinal polarization ($\lambda_\theta = -1$), and 2. full transverse polarization ($\lambda_\theta = 1$). In a way similar to the one described for the p_{T} and y parameterizations,

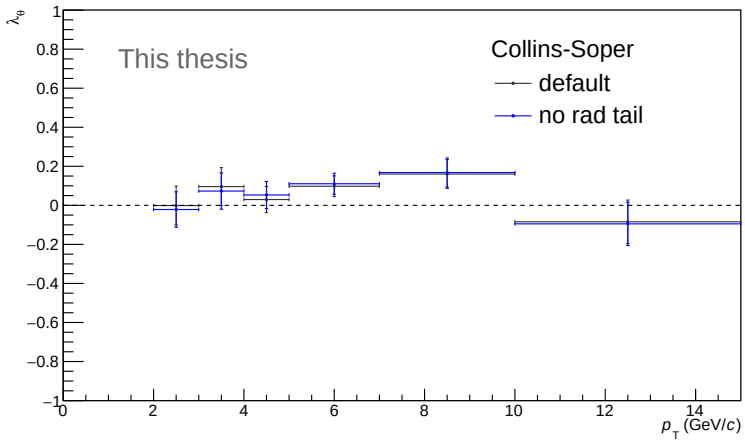

Figure 5.18: λ_θ as a function of p_{T} for the cases of $\mathrm{BR}(J/\psi \to \mu^+\mu^-\gamma)/\mathrm{BR}(J/\psi \to \mu^+\mu^-) = 0.54$ and $\mathrm{BR}(J/\psi \to \mu^+\mu^-\gamma) = 0$ in Collins-Soper frame.

the MC samples have been re-weighted to reproduce the desired shapes. Figure 5.19 shows the original ($\lambda_\theta = 0$) and weighted $W(\cos\theta)$ distributions in the Collins-Soper frame at generation and reconstruction levels of simulation.

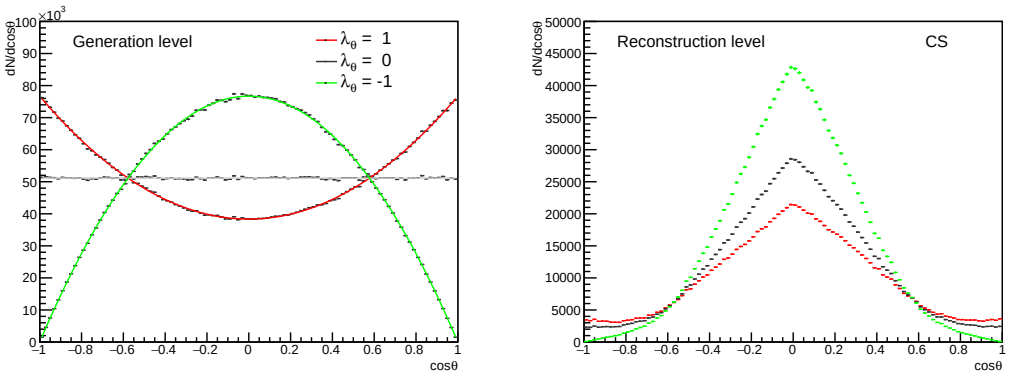

Figure 5.19: $W(\cos\theta)$ distributions in the Collins-Soper frame at generation (*left*) and reconstruction (*right*) levels of simulation for three λ_θ values.

Within these assumptions the variations on λ_θ mean values range from 0.006 to 0.036 as a function of the p_{T} bin for both polarization frames and all values lie within the range $[-0.2; 0.2]$, one fifth of the maximum possible value of λ_θ. So, a more realistic estimation on the upper limit to this systematic error would be then given by the input assumptions: $\lambda_\theta = 0 \pm 0.2$.
Figure 5.20 shows λ_θ as a function of p_{T} in Collins-Soper and the systematic uncertainty associated to the input polarization assumption. The variation from the "unpolarized assumption" is small everywhere and of the same order of the associated uncertainties to the p_{T} and y parameterizations. The uncertainties associated to all sources of systematic

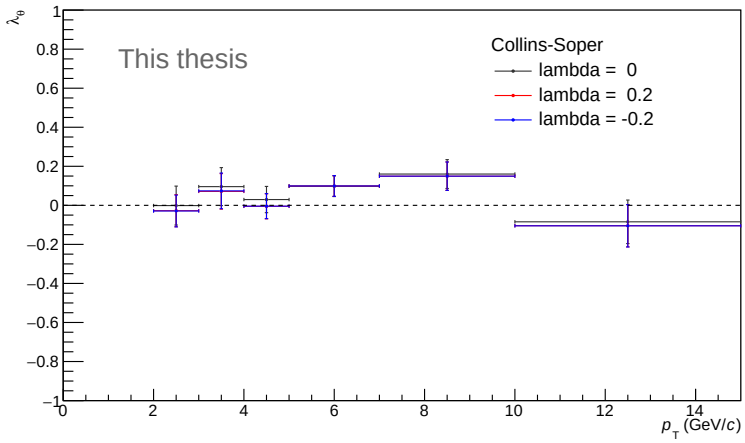

Figure 5.20: λ_θ as a function of p_{T} in the Collins-Soper frame for the different input polarization assumptions ($\lambda_\theta = 0$; ± 0.2).

effects described in this section, for all polarization parameters in both frames, are given in Appendix C.2.

5.4.2 Trigger response function

The trigger response function corresponds to the ratio of muon tracks passing the low-p_{T} cut trigger condition (referred as "Lpt" sample from now on) over the total number of muon tracks (or "Apt" sample, with "A" from all-p_{T} condition). To build the "Lpt/Apt" distributions the same run list as for the polarization analysis has been used, to have a data sample reflecting the same detector configuration. Since the intention is to evaluate the muon trigger response function, the event's trigger class does not contain any MUON trigger input, only the Minimum Bias condition is required. As it was mentioned before (subsection 5.1.1), during the 2012 pp at $\sqrt{s}$= 8 TeV data taking two MB trigger configurations were used: the "T0and" condition was set at the beginning of the fill and then the "V0and" trigger for the rest of the fill at lower luminosity. These configurations correspond to the trigger classes CINT8 and CINT7, respectively, so, all events tagged by either one or the other trigger classes have been analyzed. Then, apart from the muon trigger related conditions (the first two cuts on the list in section 5.1.2), all the rest of standard cuts are applied to the muon tracks.
Figure 5.21 shows the "Lpt/Apt" distributions obtained from simulated and real data for the V0 and T0 samples, i.e. the V0 and T0 triggered events. Besides the statistical fluctuations, there is a hint of a systematic effect for p_{T} lower than 1.2 GeV/c. In the low p_{T} region the trigger response function from simulation is systematically slightly higher than the real one. In order to take into account this effect, the simulation is corrected by introducing a new response function $rf(p_{\mathrm{T}})$ at the time of applying the trigger low-p_{T} cut to the simulated muon tracks. The function $rf(p_{\mathrm{T}})$ is considered as the probability for a muon track of a given $p_{\mathrm{T}\mu}$ to pass the low-p_{T} condition.

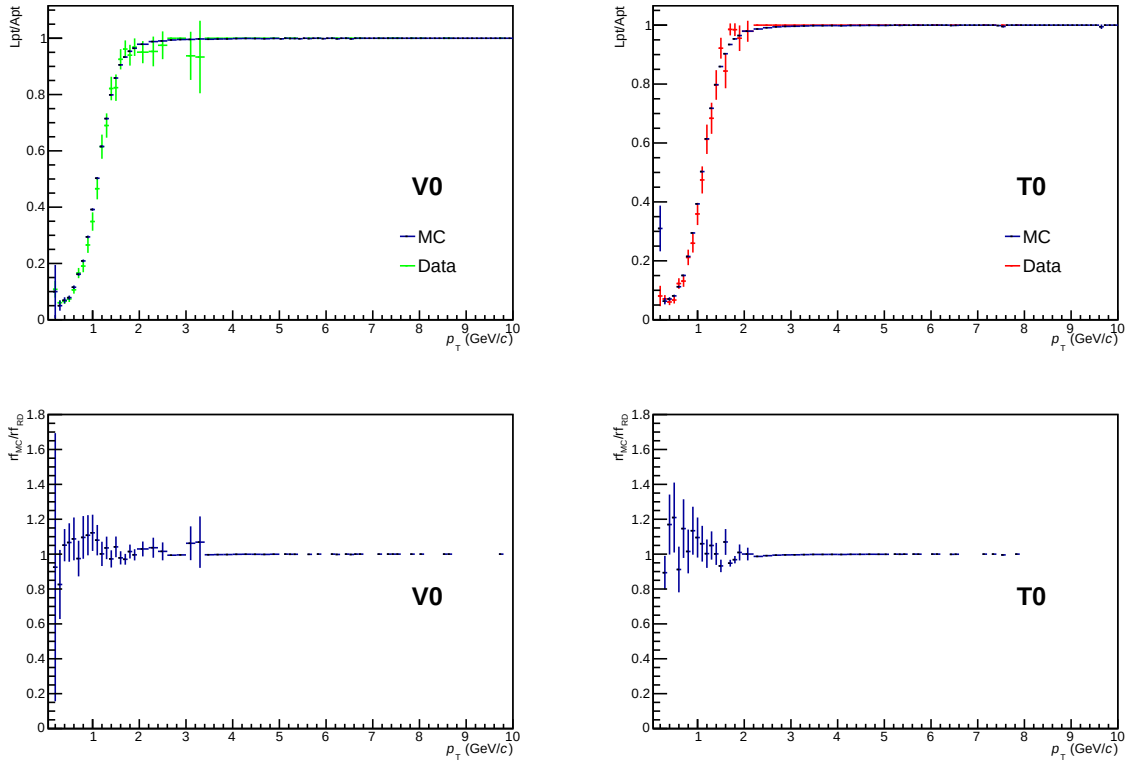

Figure 5.21: *Top*: "Lpt/Apt" distribution (also called response function *rf*) evaluated from data and simulation as a function of p_{T} for the V0 (*left*) and T0 (*right*) data samples. *Bottom*: Ratio of "Lpt/Apt" distributions from simulations and data: $rf_{\mathrm{MC}}/rf_{\mathrm{RD}}$.

The response function can be described by a smooth threshold function:

$$rf(x) = \frac{1}{1 + \mathrm{e}^{-b(x-x_0)}} \tag{5.10}$$

where x_0 represents the p_{T} value at which the efficiency is 50% i.e. the threshold cut; while the b parameter corresponds to the slope of the rising part of the function. To estimate the b and x_0 parameters a fit to the "Lpt/Apt" distributions is performed. Then the systematic error is evaluated based on the differences of $rf(p_{\mathrm{T}})$ from MC and RD, the procedure will be better detailed later in this section.
The comparison between the "Lpt/Apt" distributions from both data samples: V0 and T0 (Figure 5.22); shows a good agreement, and their ratio compatible with unity within statistical fluctuations in the full p_{T} range. Taking this into account, in order to increase the statistics, all data (V0 and T0) were merged and analyzed together.
The "Lpt" cut is applied at hardware level via look-up-table encoded in each local board. As explained in Section 3.5.3 this cut is based on the deviation of the measured track in the trigger chambers compared to a straight line track coming from the interaction point. The precision on the deviation measurement is limited by the strip segmentation of the

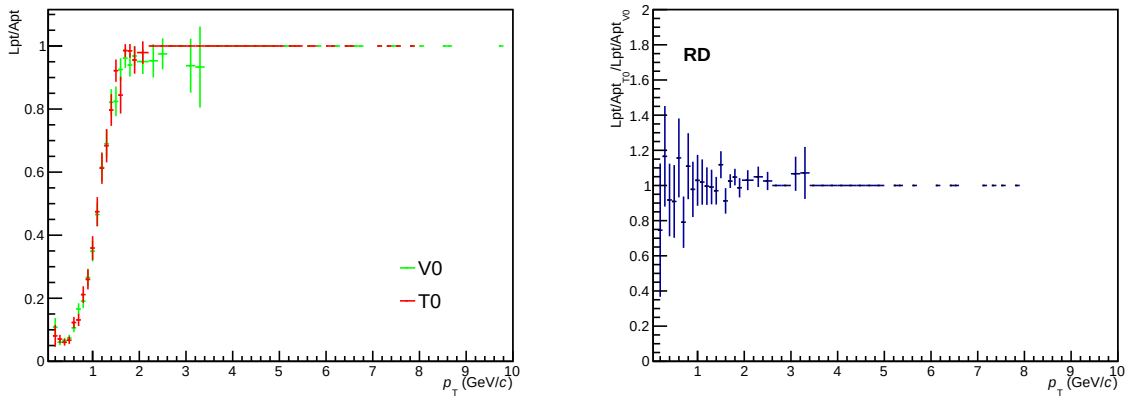

Figure 5.22: *Left*: Comparison between"Lpt/Apt" distributions obtained from raw data V0 and T0 data samples. *Right*: Ratio of "Lpt/Apt" distributions from T0 and V0 samples.

muon trigger chambers, which change from a projective region (defined by a local board) to another. So, the look-up-table is defined local board by local board. That means that a realistic error estimation would imply to analyze individually each local board of the muon trigger chambers by associating each muon track to the corresponding board and build the "Lpt/Apt" plots in each case. This means that the total statistics will be divided by 234 (number of local boards) which is in practice not feasible; indeed, the total number of unbiased single muon tracks in the whole data sample (V0 and T0) is about 16000. Instead the data have been split according to the η and ϕ[8] of muon tracks. For each of the variables the distributions have been split in 6 equally spaced bins within the respective full variation ranges $\eta \epsilon [-4; -2.5]$ and $\phi \epsilon [0; 2\pi]$.
As an illustration, Figure 5.23 shows the integrated in η and ϕ "Lpt/Apt" for MC and RD data, fitted with the *rf* function.
Figure 5.24 shows how the b and x_0 parameters evolve from bin to bin (in η and ϕ) for the RD and MC distributions and the comparison to the function parameters obtained from the integrated distributions, all numbers are summarized in Table 5.3. The differential analysis gives a more realistic estimation of the systematic effect of the trigger response function.
From the functions $rf_{\mathrm{MC}}(p_{\mathrm{T}}, \eta)$, $rf_{\mathrm{RD}}(p_{\mathrm{T}}, \eta)$, $rf_{\mathrm{MC}}(p_{\mathrm{T}}, \phi)$ and $rf_{\mathrm{RD}}(p_{\mathrm{T}}, \phi)$, the $A \times \varepsilon$ distributions as a function of $\cos\theta$, φ and $\tilde{\varphi}$ are re-evaluated and the raw W dependencies re-calculated giving as a result a different set of λ parameters as a function of p_{T}.
The error associated to each λ value is given by the difference between the λ parameters obtained when the $A \times \varepsilon$ is evaluated from $rf_{\mathrm{MC}}(p_{\mathrm{T}})$ and $rf_{\mathrm{RD}}(p_{\mathrm{T}})$, i.e. $\sigma_\lambda = |\lambda_{\mathrm{MC}} - \lambda_{\mathrm{RD}}|$. This method to evaluate the uncertainty is motivated by the fact that the function *rf* used to fit the data points is an approximation of the real response function. Thus, both parameters λ_{MC} and λ_{RD} are biased by the same approximation, in the difference $|\lambda_{\mathrm{MC}} - \lambda_{\mathrm{RD}}|$ the bias cancels out. The total systematic uncertainty for the reported λ

[8] Azimuthal angle in the transverse plane (x,y) of the ALICE coordinate system (Figure 3.4).

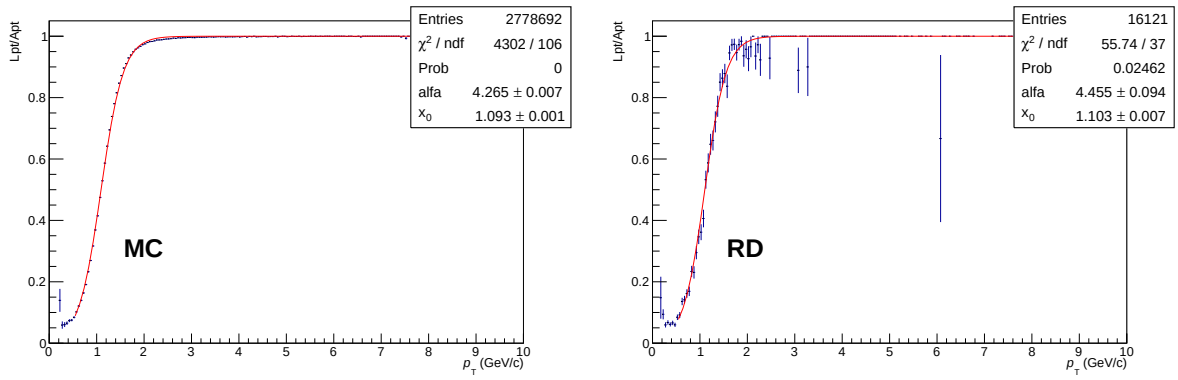

Figure 5.23: Fits to the "Lpt/Apt" distributions for MC (*left*) and RD (*right*) samples.

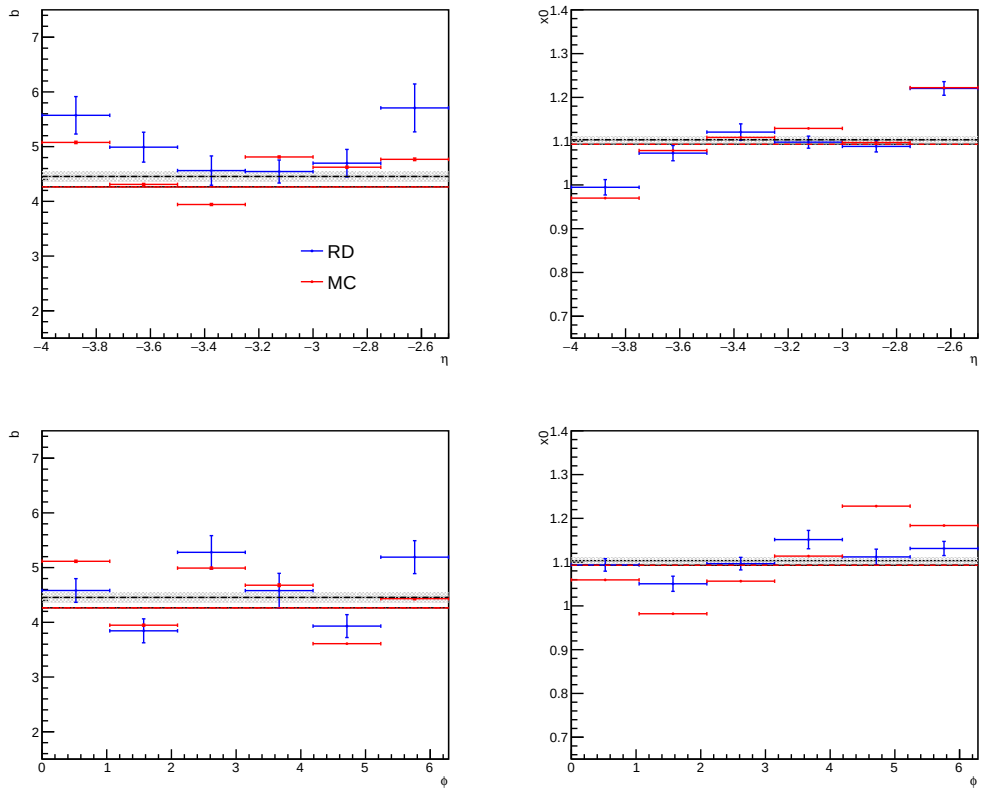

Figure 5.24: Muon trigger response function b (*left*) and x_0 (*right*) parameters evolution as a function of η (*top*) and ϕ bins (*bottom*) from raw data (in blue) and simulations (in red). The parameters obtained from fit to the integrated distributions and their associated errors are also shown in black lines for raw data and in red for simulation.

value is given by the quadratic sum of the errors obtained from the differential in η and

Table 5.3: Trigger response function parameters from RD and MC data fits for all η and ϕ bins.

η bin	$x_{0\,\mathrm{RD}}$	$x_{0\,\mathrm{MC}}$	b_{RD}	b_{MC}
$[-4.00, -3.75)$	0.994±0.017	0.970±0.001	5.572±0.342	5.077±0.022
$[-3.75, -3.50)$	1.073±0.017	1.079±0.001	4.990±0.273	4.310±0.018
$[-3.50, -3.25)$	1.121±0.019	1.109±0.001	4.562±0.268	3.942±0.019
$[-3.25, -3.00)$	1.098±0.014	1.129±0.001	4.545±0.210	4.811±0.018
$[-3.00, -2.75)$	1.088±0.013	1.097±0.001	4.698±0.251	4.624±0.018
$[-2.75, -2.50)$	1.220±0.016	1.222±0.001	5.708±0.438	4.768±0.023

ϕ bin	$x_{0\,\mathrm{RD}}$	$x_{0\,\mathrm{MC}}$	b_{RD}	b_{MC}
$[0, \pi/3)$	1.094±0.014	1.060±0.001	4.582±0.218	5.115±0.020
$[\pi/3, 2\pi/3)$	1.050±0.017	0.982±0.002	3.844±0.219	3.947±0.018
$[2\pi/3, \pi)$	1.097±0.014	1.057±0.001	5.279±0.305	4.991±0.018
$[\pi, 4\pi/3)$	1.151±0.021	1.114±0.001	4.579±0.316	4.678±0.024
$[4\pi/3, 5\pi/3)$	1.112±0.018	1.228±0.001	3.931±0.210	3.610±0.015
$[5\pi/3, 2\pi)$	1.131±0.016	1.184±0.001	5.191±0.301	4.432±0.019

ϕ response functions:

$$\sigma_{\mathrm{rf}} = \sqrt{\sigma_{\lambda,\mathrm{rf}(\eta)}{}^2 + \sigma_{\lambda,\mathrm{rf}(\phi)}{}^2} \tag{5.11}$$

Figure 5.25 shows an example of the contributions to the systematics uncertainties associated to the trigger response function. As a general remark for all polarization parameters in both frames, the contribution from this systematic error source is more important for the lower p_{T} bins, decreasing in one order of magnitude for most of the cases from the first to the last p_{T} bin. The uncertainties from the η-differential and ϕ-differential estimation contribute in the same order to the total which stays less than 0.05 for λ_θ in the Collins-Soper frame.
The values of systematic uncertainties for all polarization parameters in both frames, are given in Appendix C.2.

5.4.3 J/ψ from b-hadron decays

The J/ψ polarization measurement at forward rapidities in ALICE includes prompt and non-prompt J/ψ components, however theoretical predictions are usually given for prompt or direct J/ψ production.
The CDF collaboration has reported the polarization of J/ψ from b-hadrons in the Helicity frame and was found to be $\lambda_\theta = -0.106 \pm 0.033_{\mathrm{stat}} \pm 0.007_{\mathrm{syst}}$ [29]. To estimate how much

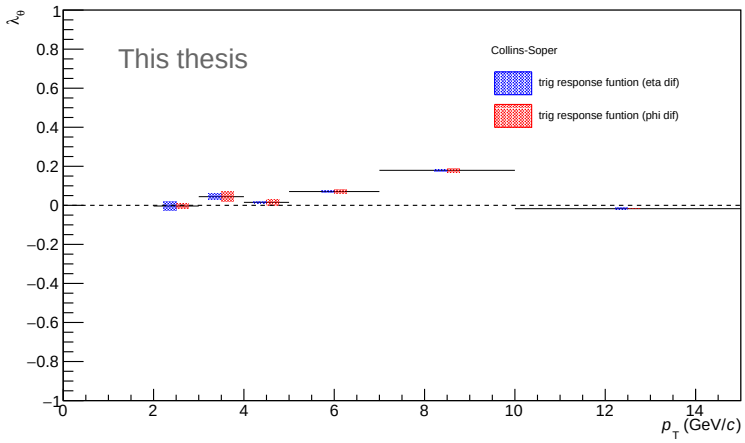

Figure 5.25: λ_θ in the Collins-Soper frame as a function of p_{T}. The contribution from the differential in η and ϕ error estimations are shown individually.

the inclusive polarization measurements could be affected by a polarized non-prompt component, the fraction of non-prompt to inclusive have been computed and taken into account in the fits of angular distributions.
The J/ψ prompt and non-prompt production has been measured by the LHCb experiment in pp collisions at $\sqrt{s} = 7$ TeV [120] and $\sqrt{s} = 8$ TeV [132]. The p_{T} and y integrated fraction $f^{\mathrm{inclusive}}_{b\to J/\psi} = \sigma_{b\to J/\psi}/\sigma_{J/\psi}$ for both collision energies are compatible. From the results in pp at collisions $\sqrt{s} = 8$ TeV, the corresponding fraction in the ALICE rapidity range $2.5 < y < 4.0$ and for $p_{\mathrm{T}} \leq 14$ GeV/c is:

$$f^{\mathrm{inclusive}}_{b\to J/\psi} = 0.105 \pm 0.007$$

The values for each p_{T} bin from the LHCb measurements [132], as reported in Table 5.4., where the last p_{T} bin value is computed with the measurements in the range $10 \leq p_{\mathrm{T}} \leq 14$ GeV/c.

Table 5.4: Fraction of J/ψ from b-hadron decays to the inclusive J/ψ sample in pp collision at $\sqrt{s}$= 8 TeV (from measurements reported in [132]).

p_{T} (GeV/c)	[2;3)	[3;4)	[4;5)	[5;7)	[7;10)	[10;15)
$f^{\mathrm{inclusive}}_{b\to J/\psi}$ (in %)	10.0 ± 0.1	11.5 ± 0.1	12.9 ± 0.1	15.0 ± 0.2	19.6 ± 0.2	25.3 ± 0.5

Then, the corrected $|\cos\theta|$, φ and $\tilde{\varphi}$ distributions are fitted with modified $W(\cos\theta)$, $W(\varphi)$ and $W(\tilde{\varphi})$ functions. A fraction $f^{\mathrm{inclusive}}_{b\to J/\psi}$ (from Table 5.4) was assumed to come from b-hadrons decays and have a polarization given by $\lambda^B_\theta = 0.0 \pm 0.2$. Assuming the double of the CDF reported value on the polarization of J/ψ coming from b-hadrons can give an upper limit on the systematic effect due to the unmeasured non-prompt J/ψ polarization.

The $W(\cos\theta)$ fit function can be written as (and similarly for the two other distributions):

$$W(\cos\theta;\lambda_\theta) = N \cdot \left[(1 - f^{\text{inclusive}}_{b\to J/\psi})W_{\text{prompt}}(\cos\theta;\lambda_\theta) + f^{\text{inclusive}}_{b\to J/\psi} \cdot W_B(\cos\theta;\lambda^B_\theta)\right]$$

were the λ^B_θ parameters are fixed to 0 and ± 0.2.
The two functions, $W_{\text{prompt}}(\cos\theta;\lambda_\theta)$ and $W_B(\cos\theta;\lambda^B_\theta)$, are of the form of 2.18
Figure 5.26 shows the results obtained from the mentioned fit, assuming $\lambda^B_\theta = 0$, compared to the inclusive results.

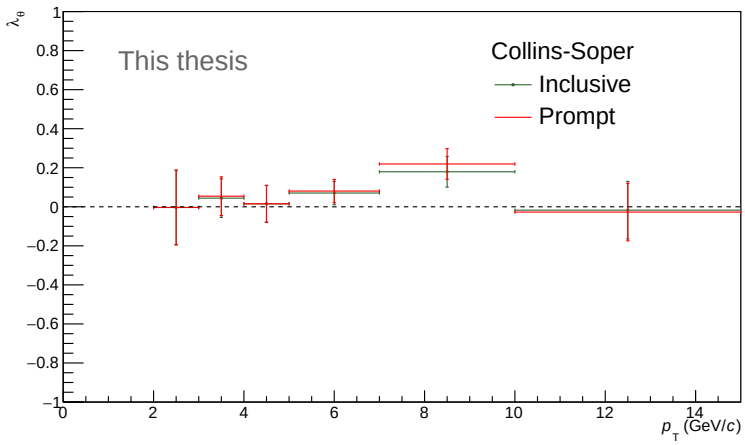

Figure 5.26: λ_θ in the Collins-Soper frame as a function of p_{T} for inclusive and prompt i.e. corrected by the non-prompt component J/ψ fraction (under the assumption $\lambda^B_\theta = 0$).

The estimated influence of the non-prompt component varies from bin to bin in p_{T} and is more important for the λ_θ parameters in both polarization frames. The highest deviations from the inclusive measurement are observed in the cases of higher λ values, specially for λ_θ in the HX frame and last p_{T} bin where the non-prompt component represents 25 % of the inclusive J/ψ sample. The higher is the "unpolarized" non-prompt fraction the more polarized should be the prompt J/ψ's w.r.t the inclusive measurements such that the inclusive λ values are in between both degrees of polarization.

5.4.4 Combination of systematics

From figures 5.14, 5.16, 5.18 and 5.20 it is visible that the systematic effect on the signal extraction, p_{T} and y parameterizations, radiative decay fraction and polarization assumption are not correlated bin to bin in p_{T}, and this is also the case of the trigger response function systematic uncertainty. So, the total systematic uncertainty is computed as the quadratic sum of errors from each of these inputs:

$$\sigma_{sys} = \sqrt{\sum_i (\lambda_i - \langle\lambda\rangle)^2} \tag{5.12}$$

For the systematic due to the non-prompt to inclusive J/ψ fraction, a bin to bin correlation has been observed so this uncertainty is reported independently.

Chapter 6

Results and discussion

6.1 J/ψ polarization in pp collisions at $\sqrt{s} = 8$ TeV

6.1.1 Inclusive J/ψ results

The full analysis procedure presented in Chapter 5 was performed for the three polarization parameters λ_θ, λ_φ and $\lambda_{\theta\varphi}$ in the Collins-Soper and Helicity frames. The final results for the three polarization parameters as a function of p_{T} are shown in Figure 6.1 and Table 6.1.
In the Collins-Soper frame λ_θ is compatible with zero within uncertainties for most p_{T} bins, the highest λ_θ value is obtained for p_{T} between 7 and 10 GeV/c but still compatible with the general trend within $2.3\,\sigma$ (when summing in quadrature statistical and systematic uncertainties). No hint of a p_{T} dependence is observed. The λ_φ and $\lambda_{\theta\varphi}$ parameters show a rather constant behavior as a function of p_{T} and values are compatible with zero.
In the Helicity frame the λ_θ parameter shows a slight p_{T} dependence towards an increasing longitudinal polarization at high p_{T}, even if it is only $1.8\,\sigma$ deviated from zero. The λ_φ and $\lambda_{\theta\varphi}$ parameters show no significant deviation from zero, except for $\lambda_{\theta\varphi}$ in the last p_{T} bin (at $2\,\sigma$ from zero), a slight p_{T} dependence can be also noticed.
Systematic effects dominate the total uncertainties in the low-p_{T} bins for λ_θ and λ_φ parameters in both reference frames while the statistical errors become more important at high p_{T}. The systematics associated to the signal extraction are particularly important (~ 3 times higher than other sources of systematics) at low-p_{T} where, due to an $A \times \varepsilon$ effect, several bins with very poor statistics in the $|\cos\theta|$ and φ angular distributions have been integrated to be able to perform the dimuon invariant mass fit (see Table 5.2); as a consequence the shape of the angular distributions and the fit with $W(\cos\theta)$ and $W(\varphi)$ functions are very sensitive to the width and statistical uncertainty corresponding to those integrated bins. All systematic uncertainties are reported in Appendix C.

Cross-check of the measurements

As a cross check to the method used to extract the polarization parameters, the whole set of λ values was also measured using the method introduced in Section 2.1.2, i.e. the

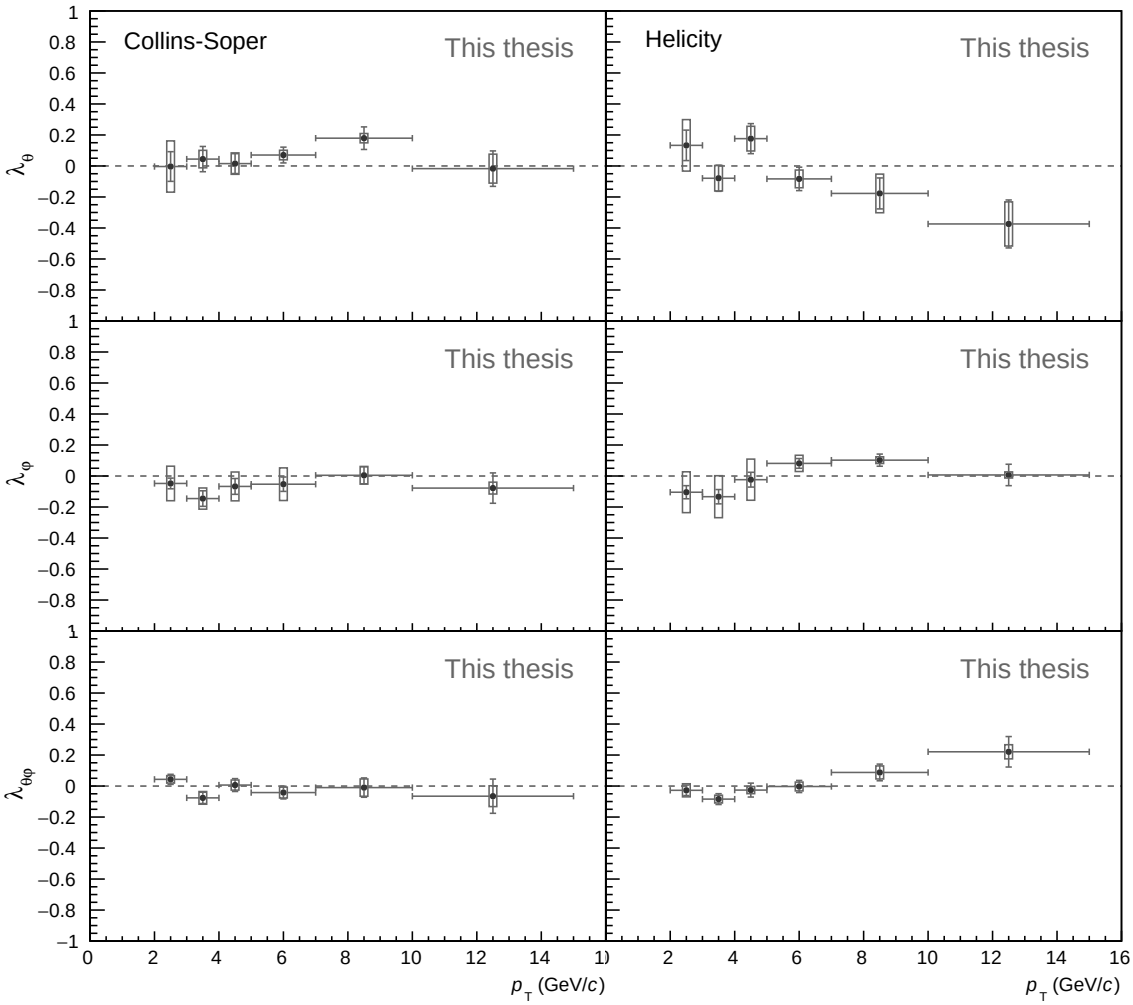

Figure 6.1: From top to bottom the polarization parameters λ_θ, λ_φ and $\lambda_{\theta\varphi}$ measured in the Collins-Soper (*left*) and Helicity (*right*) frames, as a function of p_{T} and for inclusive J/ψ in the rapidity range $2.5 < y < 4.0$. Bars correspond to statistical uncertainties while boxes represents systematics (signal extraction, p_{T} and y parameterization, radiative decay fraction, polarization assumption and trigger response function).

asymmetry of populations of two angular topologies. The counting population method has the advantage that the whole data sample is split in only two bins for the extraction of each λ parameter, so the fit to the dimuon invariant mass distributions can be easily performed and less affected by the low statistics regions due to the $A \times \varepsilon$ of the detector. On the other side, this method is less under control for the determination of the polarization parameters. Indeed, as acceptance-efficiency effects are important, there is no way with the counting population method to check that corrected numbers of J/ψ extracted from the two angular topologies are non strongly biased. The situation is different with the fit of the angular distribution, because in that case, the quality of the fit (χ^2/ndf)

Table 6.1: Measured inclusive J/ψ polarization parameters in the Collins-Soper (CS) and Helicity (HX) frames in the different p_{T} bins. The first uncertainty is statistical and the second systematics.

p_{T} (GeV/c)	$\lambda_{\theta\,\mathrm{CS}}$	$\lambda_{\varphi\,\mathrm{CS}}$	$\lambda_{\theta\varphi\,\mathrm{CS}}$
$2-3$	$0.000 \pm 0.099 \pm 0.165$	$-0.044 \pm 0.034 \pm 0.110$	$0.042 \pm 0.033 \pm 0.024$
$3-4$	$0.047 \pm 0.083 \pm 0.055$	$-0.139 \pm 0.050 \pm 0.061$	$-0.082 \pm 0.037 \pm 0.031$
$4-5$	$0.011 \pm 0.066 \pm 0.066$	$-0.051 \pm 0.051 \pm 0.057$	$0.003 \pm 0.042 \pm 0.029$
$5-7$	$0.069 \pm 0.052 \pm 0.030$	$-0.035 \pm 0.046 \pm 0.066$	$-0.045 \pm 0.041 \pm 0.033$
$7-10$	$0.180 \pm 0.074 \pm 0.030$	$0.011 \pm 0.055 \pm 0.049$	$-0.017 \pm 0.063 \pm 0.047$
$10-15$	$-0.019 \pm 0.114 \pm 0.093$	$-0.072 \pm 0.098 \pm 0.029$	$-0.073 \pm 0.111 \pm 0.057$

p_{T} (GeV/c)	$\lambda_{\theta\,\mathrm{HX}}$	$\lambda_{\varphi\,\mathrm{HX}}$	$\lambda_{\theta\varphi\,\mathrm{HX}}$
$2-3$	$0.133 \pm 0.098 \pm 0.166$	$-0.105 \pm 0.042 \pm 0.132$	$-0.028 \pm 0.034 \pm 0.042$
$3-4$	$-0.079 \pm 0.084 \pm 0.082$	$-0.133 \pm 0.046 \pm 0.135$	$-0.084 \pm 0.035 \pm 0.025$
$4-5$	$0.176 \pm 0.097 \pm 0.080$	$-0.024 \pm 0.048 \pm 0.133$	$-0.026 \pm 0.045 \pm 0.023$
$5-7$	$-0.083 \pm 0.076 \pm 0.057$	$0.081 \pm 0.031 \pm 0.052$	$-0.003 \pm 0.039 \pm 0.029$
$7-10$	$-0.177 \pm 0.100 \pm 0.125$	$0.102 \pm 0.039 \pm 0.022$	$0.088 \pm 0.054 \pm 0.042$
$10-15$	$-0.374 \pm 0.155 \pm 0.142$	$0.007 \pm 0.069 \pm 0.020$	$0.221 \pm 0.098 \pm 0.046$

allows to "detect" a possible bias in the corrected numbers. A bad χ^2/ndf can indicates that the acceptance-efficiency correction factors are biased, and points out possible wrong hypothesis in the simulated events. For this reason, the counting population method is only used as a cross check of the main analysis.
Both results are compatible within uncertainties, as shown in Figure 6.2. We can note that the statistical uncertainty of counting population method is negligible compare to the one obtained by fitting the angular distributions. Two reasons can explain this result. First the fitting method is sensitive to the normalization of the distribution which is a free parameter in the fit; and second the points of the angular distributions with bringing the biggest weight in the fit are more affected by the acceptance-efficiency, so their statistical significance is less decreased (i.e. the relative statistical uncertainty is more important). In contrary, in the counting population method, there is no normalization factor, the polarization parameter is directly obtained from the counting numbers of J/ψ after acceptance-efficiency correction. And in this case, the statistical significance of the two angular topologies are more important than individual bins of the corresponding angular distribution.

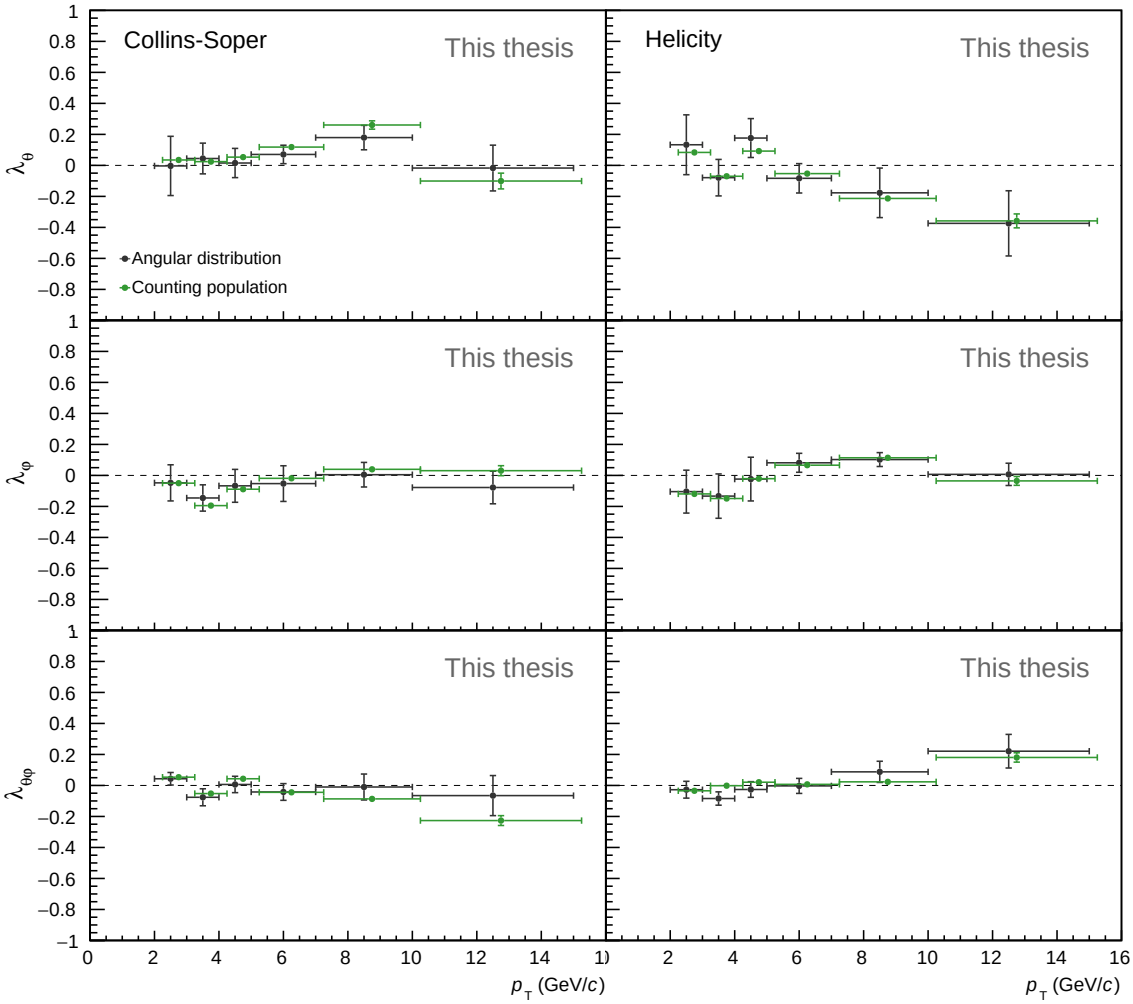

Figure 6.2: From top to bottom the polarization parameters λ_θ, λ_φ and $\lambda_{\theta\varphi}$ of inclusive J/ψ as a function of p_{T} in the Collins-Soper (*left*) and Helicity (*right*) frames measured by two different methods: 1. fitting the angular distributions (black points, bars correspond to statistical and systematics uncertainties are added in quadrature) and 2. measuring the asymmetry of two angular topology populations (green points, only statistical uncertainties are shown). For clarity the green points are shifted in p_{T} by 0.25 GeV/c.

6.1.2 Prompt J/ψ results

As it was discussed in Section 5.4.3, a correction from the non-prompt polarization can be computed from the non-prompt-to-inclusive fraction ($f^{\text{inclusive}}_{b\to J/\psi}$, Table 5.4). The assumed polarization of the non-prompt component was $\lambda^B_\theta = 0.0 \pm 0.2$.
Figure 6.3 shows the comparison between the inclusive J/ψ polarization parameter values and the ones corrected by the non-prompt J/ψ fraction, labeled as "Prompt" in the plots, and summarized in Table 6.2.

The central values of the "Prompt" points correspond to the correction with $\lambda^B_\theta = 0$,

Table 6.2: Prompt J/ψ polarization parameters in the Collins-Soper (CS) and Helicity (HX) frames in the different p_{T} bins. The first uncertainty is statistical and systematics uncertainties of inclusive measurements added in quadrature. The second uncertainty corresponds to the assumption of the non-prompt component ($\lambda^B_\theta = 0.0 \pm 0.2$).

p_{T} (GeV/c)	$\lambda_{\theta\,\mathrm{CS}}$	$\lambda_{\varphi\,\mathrm{CS}}$	$\lambda_{\theta\varphi\,\mathrm{CS}}$
$2-3$	$-0.004 \pm 0.191 \pm 0.020$	$-0.048 \pm 0.117 \pm 0.000$	$0.043 \pm 0.040 \pm 0.000$
$3-4$	$0.054 \pm 0.099 \pm 0.020$	$-0.166 \pm 0.085 \pm 0.000$	$-0.086 \pm 0.055 \pm 0.000$
$4-5$	$0.015 \pm 0.094 \pm 0.030$	$-0.077 \pm 0.106 \pm 0.000$	$0.006 \pm 0.053 \pm 0.000$
$5-7$	$0.081 \pm 0.060 \pm 0.030$	$-0.063 \pm 0.115 \pm 0.000$	$-0.052 \pm 0.054 \pm 0.000$
$7-10$	$0.219 \pm 0.079 \pm 0.050$	$0.005 \pm 0.079 \pm 0.000$	$-0.010 \pm 0.084 \pm 0.000$
$10-15$	$-0.019 \pm 0.114 \pm 0.093$	$-0.072 \pm 0.098 \pm 0.029$	$-0.073 \pm 0.111 \pm 0.057$

p_{T} (GeV/c)	$\lambda_{\theta\,\mathrm{HX}}$	$\lambda_{\varphi\,\mathrm{HX}}$	$\lambda_{\theta\varphi\,\mathrm{HX}}$
$2-3$	$0.143 \pm 0.193 \pm 0.020$	$-0.115 \pm 0.138 \pm 0.000$	$-0.028 \pm 0.054 \pm 0.000$
$3-4$	$-0.089 \pm 0.118 \pm 0.020$	$-0.143 \pm 0.143 \pm 0.000$	$-0.094 \pm 0.043 \pm 0.000$
$4-5$	$0.206 \pm 0.125 \pm 0.030$	$-0.024 \pm 0.141 \pm 0.000$	$-0.026 \pm 0.050 \pm 0.000$
$5-7$	$-0.093 \pm 0.095 \pm 0.030$	$0.101 \pm 0.061 \pm 0.000$	$-0.003 \pm 0.048 \pm 0.000$
$7-10$	$-0.217 \pm 0.160 \pm 0.040$	$0.122 \pm 0.045 \pm 0.000$	$0.108 \pm 0.068 \pm 0.000$
$10-15$	$-0.494 \pm 0.210 \pm 0.040$	$0.007 \pm 0.072 \pm 0.000$	$0.281 \pm 0.108 \pm 0.000$

and the boxes represent the limits given by the ± 0.2 variation.
The impact of the non-prompt polarization is very small everywhere and smaller than 0.04 variation with respect to the inclusive λ, except for the last p_{T} bin in the Helicity frame where the λ_θ and $\lambda_{\theta\varphi}$ parameters vary in 0.12 and 0.06, respectively. However both set of parameters, "Inclusive" and "Prompt" are always compatible within the statistical and systematic uncertainties.
In the following sections all λ values are reported for prompt J/ψ.

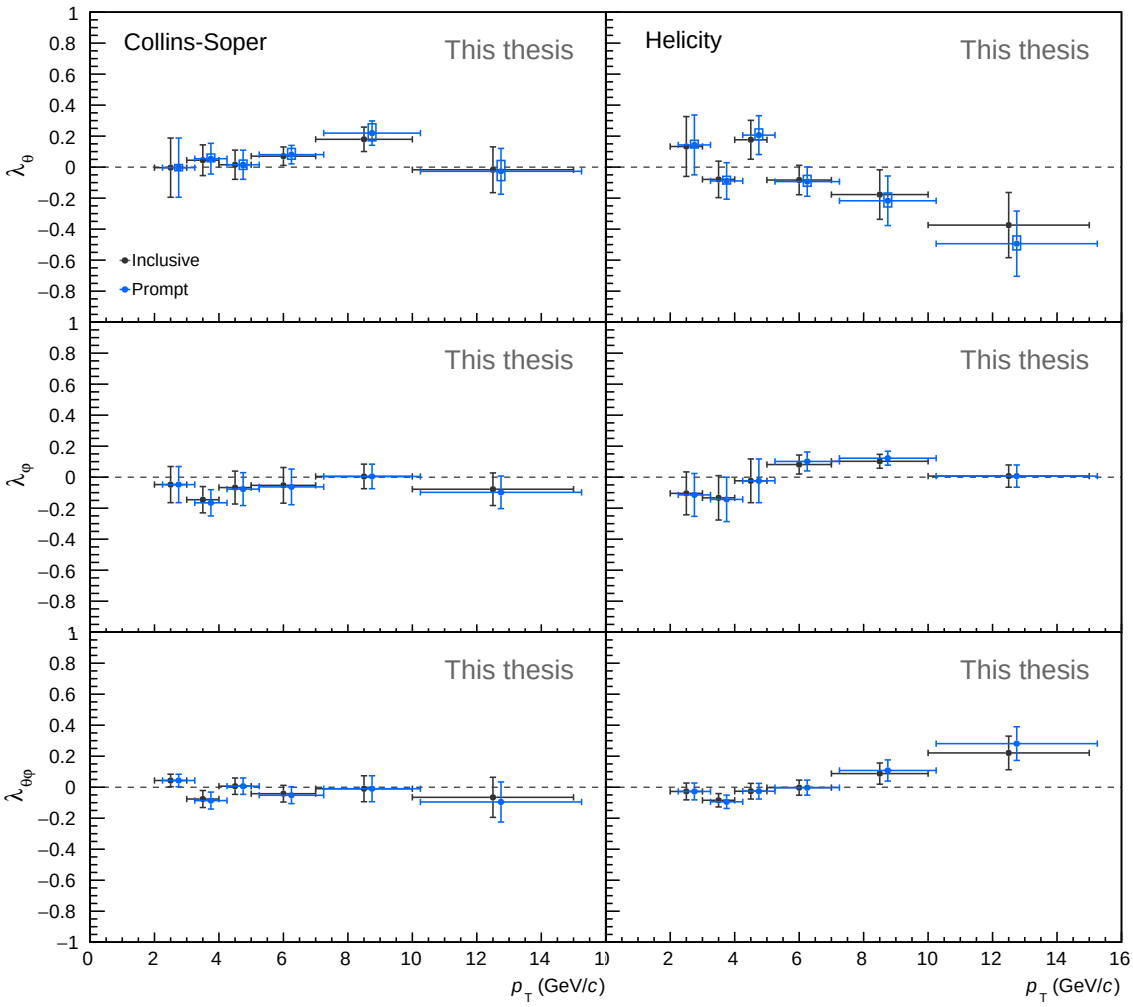

Figure 6.3: From top to bottom polarization parameters λ_θ, λ_φ and $\lambda_{\theta\varphi}$ as a function of p_{T} measured in the Collins-Soper (*left*) and Helicity (*right*) frames, for inclusive J/ψ (black points, bars correspond to statistical and systematics uncertainties are added in quadrature) and prompt J/ψ (blue points, bars correspond to statistical and systematics uncertainties are added in quadrature, and boxes correspond to the uncertainties associated to the polarization assumption of the non-prompt J/ψ component). For clarity the blue points are shifted in p_{T} by 0.25 GeV/c.

Frame-independent polarization parameter

The frame invariant parameter:

$$\tilde{\lambda} = \frac{\lambda_\theta + 3\lambda_\varphi}{1 \quad \lambda_\varphi} \tag{6.1}$$

introduced in Section 2.2.2, was evaluated for the Collins-Soper and Helicity frames and it is shown in Figure 6.4. For the error propagation, the statistical uncertainties were assumed to by fully correlated, since the same data sample is used for the measurement of all polarization parameters. The systematics uncertainties were considered as uncorrelated. Error bars represent the quadratic sum of statistical and systematic uncertainties. A good agreement is observed for both sets of measurements within uncertainties indicating no strong bias in the analysis.

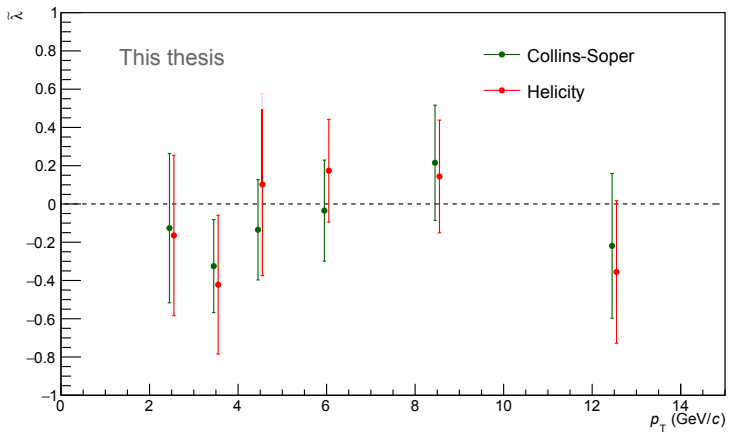

Figure 6.4: Invariant parameter $\tilde{\lambda}$ as a function of p_T in the Collins-Soper and Helicity frames. For clarity the green points are shifted in p_T by 0.25 GeV/c.

Integrated values

The p_T-averaged polarization parameters have been computed with the use of the p_T differential cross section of inclusive J/ψ measured by ALICE in pp collisions at $\sqrt{s}$ = 8 TeV [125] corrected by the fraction $f^{\text{inclusive}}_{b\to J/\psi}$ from Table 5.4 in teh following way: $\sigma^{\text{prompt}} = (1 \quad f^{\text{inclusive}}_{b\to J/\psi})\sigma^{\text{inclusive}}$. The averaged values are given by:

$$\langle\lambda\rangle = \frac{1}{\sigma_{\text{tot}}} \sum_j \sigma_j \lambda^j$$

with j running over the 6 p_T bins of this analysis, σ_j is the integrated J/ψ cross section in the p_T bin j and λ^j is the measured polarization parameter in the corresponding bin.

The resulting p_{T}-averaged values are:

$$\begin{aligned}
\langle\lambda_\theta^{\mathrm{CS}}\rangle &= 0.031 \pm 0.092 & \langle\lambda_\theta^{\mathrm{HX}}\rangle &= 0.048 \pm 0.096 \\
\langle\lambda_\varphi^{\mathrm{CS}}\rangle &= 0.083 \pm 0.060 & \langle\lambda_\varphi^{\mathrm{HX}}\rangle &= 0.078 \pm 0.075 \\
\langle\lambda_{\theta\varphi}^{\mathrm{CS}}\rangle &= 0.009 \pm 0.025 & \langle\lambda_{\theta\varphi}^{\mathrm{HX}}\rangle &= 0.035 \pm 0.028
\end{aligned}$$

To check the consistency of measured polarization parameters with respect to the theoretical constraints on their variation domain (introduced in Section 2.1), the averaged values are plotted, together with their allowed region of variation in two-dimensional plots, as shown in Figure 6.5.

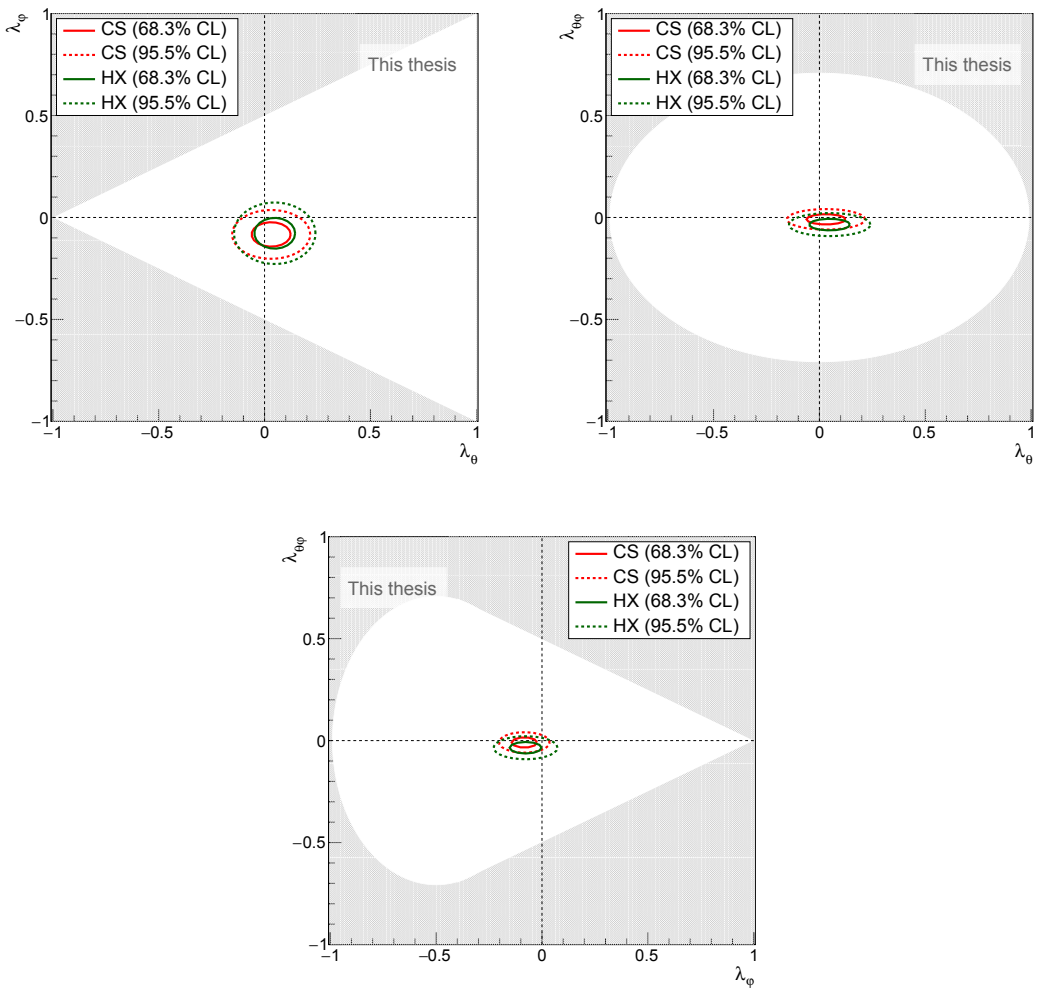

Figure 6.5: Average (p_{T}-integrated over $2 < p_{\mathrm{T}} < 15$ GeV/c in the rapidity range $2.5 < y < 4$) polarization parameters $\langle\lambda_\theta\rangle$, $\langle\lambda_\varphi\rangle$ and $\langle\lambda_{\theta\varphi}\rangle$ from the prompt J/ψ component in the allowed two-dimensional regions (white areas). Full (dashed) ellipses show 1σ (2σ) contour in CS (red) and HX (green) frames.

6.2 Comparison with previous experimental results

The ALICE and LHCb experiments have measured the J/ψ polarization in pp collisions at 7 TeV at forward rapidity for inclusive (ALICE [80]) and prompt (LHCb [77]) samples. As shown in Figure 6.6, there is no significant difference expected between the J/ψ's produced in pp collisions at $\sqrt{s} = 7$ TeV and 8 TeV, and the measured J/ψ polarizations in both cases are thus expected to be directly comparable.
For the NRQCD-2 calculation from [17,133], the uncertainty band at $\sqrt{s} = 8$ TeV was updated compared to their prediction at $\sqrt{s} = 7$ TeV reported in the LHCb publication [77] and used in Figure 6.6. A new evaluation of the uncertainty band at 7 TeV is presented in [133].

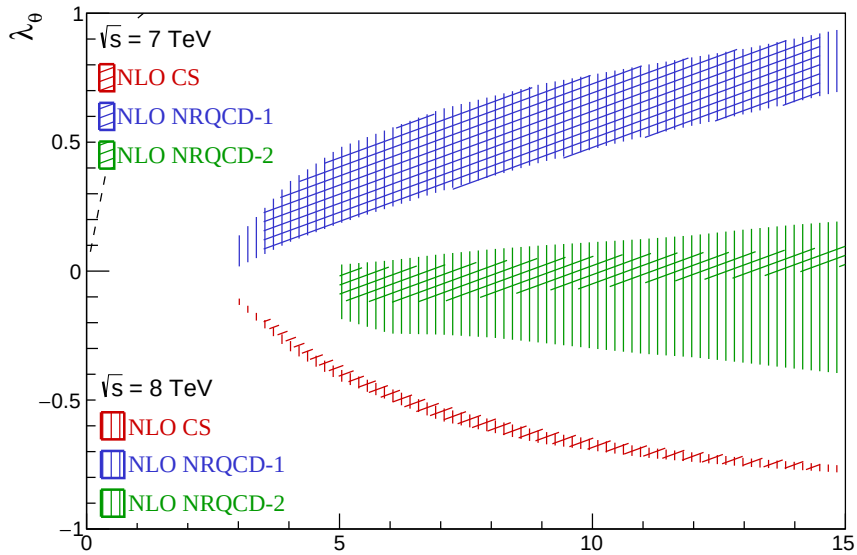

Figure 6.6: p_{T} dependence of the λ_θ parameter in the Helicity frame predicted by NLO CS and NLO NRQCD-1 from [15] and NLO NRQCD-2 from [17,133] for pp collisions at two energies $\sqrt{s} = 7$ TeV and $\sqrt{s} = 8$ TeV.

Furthermore the expected non-prompt J/ψ polarization influence on the inclusive ALICE measurements is considered negligible and well inside the systematics uncertainties, and thus the measurements to be a good estimate of the prompt J/ψ polarization.
Figure 6.7 shows the comparison between the two ALICE and the LHCb results for the same rapidity ranges ($2.5 < y < 4.0$). Except for the λ_θ parameter in the Helicity frame parameter, both ALICE measurements are in good agreement everywhere. Although for λ_θ in Collins-Soper the 8 TeV measurements are systematically higher than the 7 TeV data, both results are in agreement within error bars. The major discrepancy is observed in the Helicity frame for λ_θ in the first and third p_{T} bins, as it was mentioned in Section 5.2.3, the $W(\cos\theta)$ and thus the λ_θ measurements are particularly affected in this frame by the $A \times \varepsilon$ of the detector (and, as a matter of fact, the analysis at 7 TeV

was restricted to the $|\cos\theta| < 0.8$ region), meaning that a small variation in these low statistics regions can affect the result of the angular distribution fits and thus explain the discrepancy.
Concerning the comparison between ALICE and LHCb results, a rather good agreement is observed everywhere within the uncertainties except for few cases of about 2 σ discrepancy. The case of the $\lambda_{\theta\varphi}$ parameter is particular: in the Collins-Soper frame a systematic effect is evident, all ALICE points are bellow the LHCb values, in the Helicity frame, while for the LHCb the $\lambda_{\theta\varphi}$ values are quite constant in p_{T}, a slight p_{T} dependence is observed by the ALICE measurements and the biggest discrepancy between both experimental results is observed in this case for the last p_{T} bin where values are $\lambda_{\theta\varphi} = 0.28 \pm 0.11$ and $\lambda_{\theta\varphi} = 0.00 \pm 0.03$ for ALICE and LHCb, respectively (the quoted error corresponds to the statistical and systematic uncertainties added in quadrature).

6.3 Comparison with theoretical predictions

Figure 6.8 shows the comparison with NLO CSM and NRQCD predictions from [15] (and private communication) for all polarization parameters and with a different NRQCD calculation from [17,133] (and private communication) for λ_θ in the Helicity frame (labeled as NLO NRQCD2). Both calculations include the feed-down contributions. The difference between both NRQCD calculations comes from the data used to compute the LDMEs.

In the Collins-Soper frame a disagreement between data and theory is observed for the λ_θ and λ_φ parameters, while $\lambda_{\theta\varphi}$ can be reproduced by the calculations within uncertainties. Both, NLO CS and NRQCD calculations from [15] predict a rather small variation with p_{T} for all parameters which agrees with the measured p_{T} dependences but fail in reproducing the λ_θ and λ_φ magnitudes, a closest approximation is obtained by the NRQCD calculations including both color-singlet and color-octet contributions.
In the Helicity frame, the large transverse J/ψ polarization (λ_θ) predicted by the NRQCD [15], is in clear contradiction with the experimental observations, while the NLO CSM reproduce the observed increasing with p_{T} longitudinal polarization, but not the magnitudes of λ_θ. The predictions from [17,133] favor either zero or longitudinal polarizations within the theoretical uncertainties and show a good agreement with the measurements in the intermediate p_{T} range ($5 < p_{\mathrm{T}} < 10$ GeV/c), at higher p_{T} data and theory also agree within error bars and for $p_{\mathrm{T}} < 5$ GeV/c the calculation is not reliable.
The λ_φ and $\lambda_{\theta\varphi}$ transverse momentum dependencies are better described by the NLO CSM calculations, in rather well agreement with the measured λ_φ within experimental uncertainties but not with $\lambda_{\theta\varphi}$ where the predicted values are systematically lower than measurements by about $5\,\sigma$ in the full p_{T} range.
Figure 6.9 shows the p_{T} dependency of the invariant quantity $\tilde{\lambda}$ in the Collins-Soper and Helicity frames compared to predictions from NLO CSM and NRQCD prediction from [15]. None of the two theoretical predictions describe the measured invariant frame p_{T} dependency. The NRQCD prediction is in better agreement with the data points for intermediate transverse momentum values, within the experiemental and theoretical uncertainties.

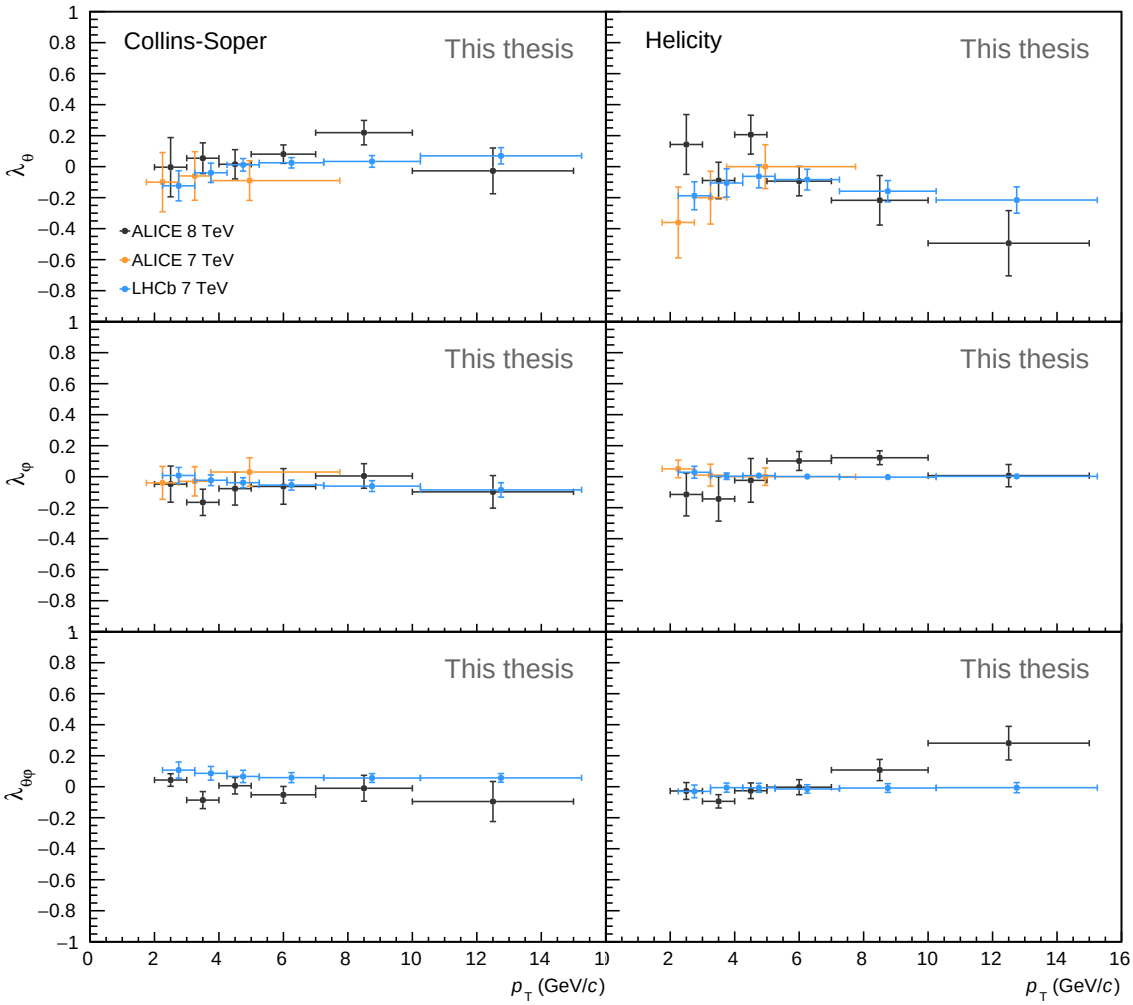

Figure 6.7: J/ψ polarization parameters λ_θ, λ_φ and $\lambda_{\theta\varphi}$ as a function of p_T in the Collins-Soper (*left*) and Helicity (*right*) frames in pp collisions at $\sqrt{s} = 7$ TeV by ALICE (inclusive J/ψ, orange points) and LHCb (prompt J/ψ, blue points) and ALICE at $\sqrt{s} = 8$ TeV (prompt J/ψ, black points, this analysis). For clarity the orange and blue points are shifted in p_T by ± 0.25 GeV/c, respectively.

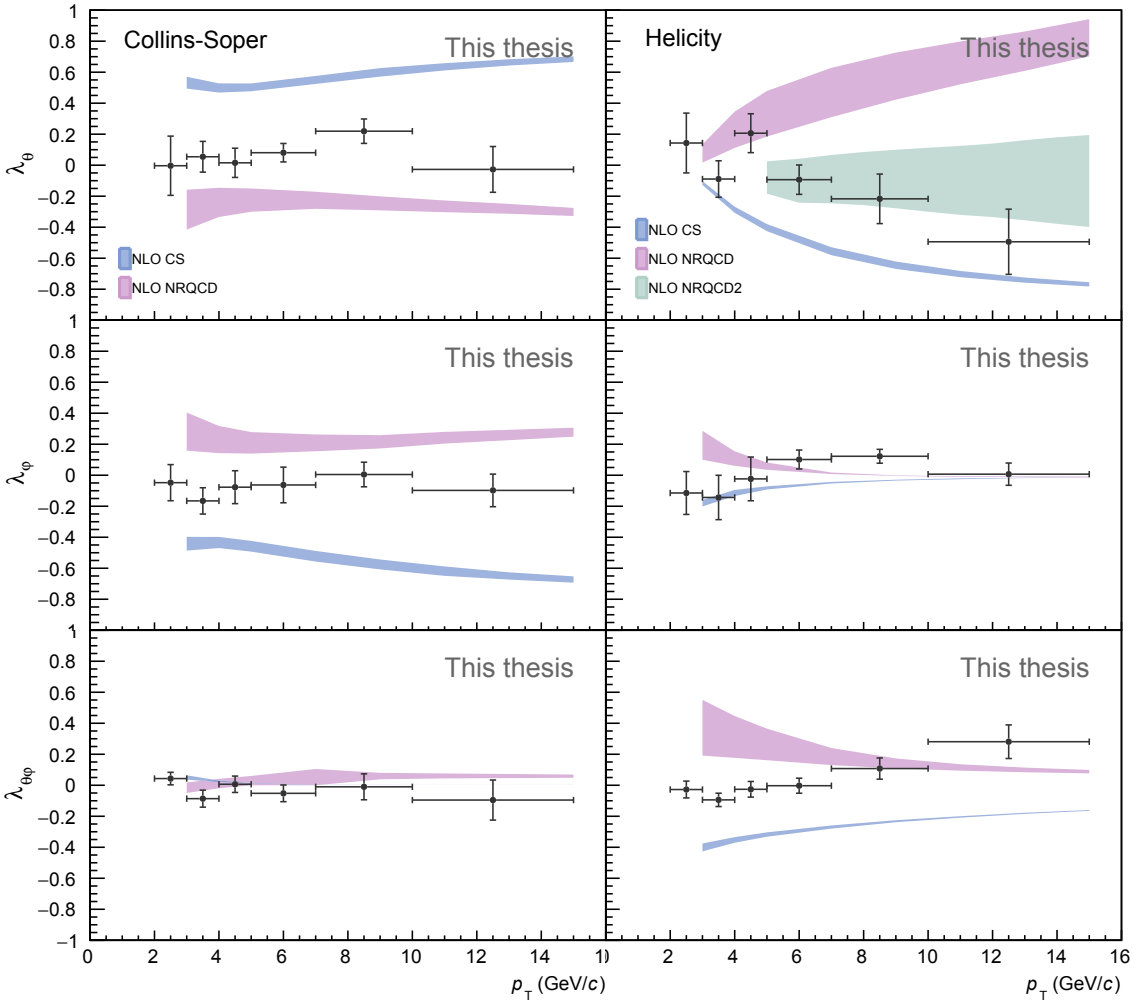

Figure 6.8: "Prompt" J/ψ polarization parameters λ_θ, λ_φ and $\lambda_{\theta\varphi}$ as a function of p_{T} measured in the Collins-Soper (*left*) and Helicity (*right*) frames compared with NLO CS from [15] and two NRQCD [15] and NRQCD2 [17, 133] calculations.

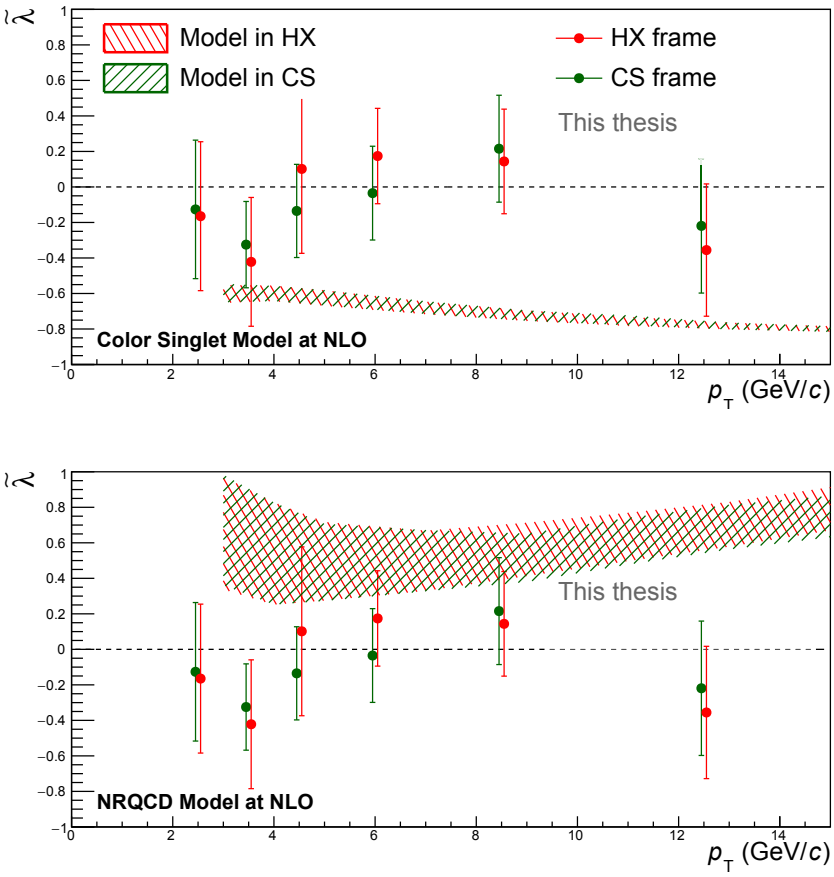

Figure 6.9: Invariant frame quantity $\tilde{\lambda}$ for prompt J/ψ from ALICE 8 TeV measurements in the Helicity (red) and Collins-Soper (green) frames compared with model prediction: NLO CSM (top plot) and NRQCD (bottom plot) from [15].

Conclusions

This thesis has presented the results on inclusive J/ψ polarization in pp collisions at $\sqrt{s} = 8$ TeV for J/ψ transverse momentum $2 \leq p_{\mathrm{T}} \leq 15$ GeV/c and rapidty range $2.5 < y < 4$ as measured with the ALICE Muon Spectrometer in the J/ψ dimuon decay channel. An estimation of the prompt J/ψ polarization was performed taking into account the b-hadrons production cross section and branching ratios to J/ψ as reported by the LHCb experiment in the same momentum and rapidity ranges, and collision system.

The measurements were performed for the full set of polarization parameters, i.e. λ_θ, λ_φ and $\lambda_{\theta\varphi}$, in two polarization frames: Collins-Soper and Helicity. The analysis of the decay muon angular distributions, was validated by the comparison with an alternative and simpler method (population counting). The frame invariant quantity $\tilde{\lambda}$ was also computed to exclude a possible bias in the analysis procedure in both frames.

The observed result is a J/ψ polarization consistent with zero in the Collins-Soper frame. In the Helicity frame, a hint of increasing longitudinal polarization with increasing p_{T} has been found, even though the maximal polarization (in the p_{T} bin from 10 to 15 GeV/c) does not exceed 2σ deviation from zero.

The comparison with previous LHC measurements in the same rapidity range, shows a good agreement among the results and confirms the improved experimental situation for quarkonia measurements in the LHC era.

Different theoretical predictions for the J/ψ polarization within the NRQCD framework (including color-singlet and color-octet pre-resonance state contributions to the J/ψ production) and the Color-Singlet Model (CSM) were confronted to the data. Concerning the CSM, the predictions fail to describe the magnitude of the λ parameters at different levels in both frames. Within the NRQCD framework, the results are very different depending of the data used to fit the long-distance matrix elements introduced in the calculations. A good agreement with the data is observed for one of the two calculations, unfortunately only available for λ_θ in the Helicity frame and in a restricted transverse momentum range $5 \leq p_{\mathrm{T}} \leq 15$ GeV/c. The calculation for the full set of polarization parameters in both frames would be useful to validate this conclusion. The other NRQCD calculation, available for all λ values in both frames and also for the invariant quantity $\tilde{\lambda}$, fails to describe the magnitude of the polarization parameters. And in particular for λ_θ in the Helicity frame, the predicted behavior of increasing transverse polarization with p_{T} goes in opposite direction compared to the experimental observations. From those results it seems that the impact of the LDMEs in the NRQCD calculations is important and not

completely under control.

The data from higher pp collision energies foreseen in the next years of data taking in ALICE will provide new constraints to theoretical models and contribute to the understanding of quarkonium production. And in particular, for the LHC Run 3 the inclusion of the Muon Forward Tracker detector will enhance the ALICE capabilities for the measurements of J/ψ in the dimuon channel, with the separation of "prompt" and "non-prompt" J/ψ components. The higher statistics data taking foreseen for the LHC Run 3 would also allow to increase the p_{T} range of the measurements and open the possibility to study the polarization of different quarkonia systems (ψ(2S) and the Υ family) in ALICE.

Another interesting subject is the study of quarkonium polarization in heavy ions collisions. A change of the magnitude of λ_θ in the Helicity frame, is expected when going from hadron to heavy ions collisions, and the difference to be higher if the Quark Gluon Plasma is formed. From the experimental point of view, this kind of measurements constitutes a challenge due to the high background environment of heavy-ions collisions and consequently the poor signal to background ratio of the dimuon invariant mass spectrum. The higher statistics Pb–Pb data taking foreseen for the LHC Run 3 with the ALICE detector could allow to look into this unexplored feature of quarkonium as a probe of QGP.

In the context of the ALICE upgrade project (in view of the high luminosity data taking from the LHC Run 3), the evaluation of the performance of the RPC detectors of the ALICE Muon Spectrometer, with a new proposed front-end electronics was carried out. The first performance studies in terms of efficiency, cluster size and charge per hit of the RPC (in cavern) equipped with the upgraded electronics were performed at the beginning of the LHC Run 2 data taking. The initial measurements allowed to establish the RPC working conditions and confirmed the design expectations in terms of charge per hit produced inside the RPC volume. The proposed electronic will thus prevent the RPC ageing effects that are induced by high cumulated doses. The new electronics performance and the working of the associated RPC will continue to be monitored during the full Run 2 data taking, which will allow its good characterization on a long term (four years) and a possible adjustment before the complete replacement of the front-electronics cards in the next LHC long shutdown foreseen in 2018.

Appendix A

Angular distributions

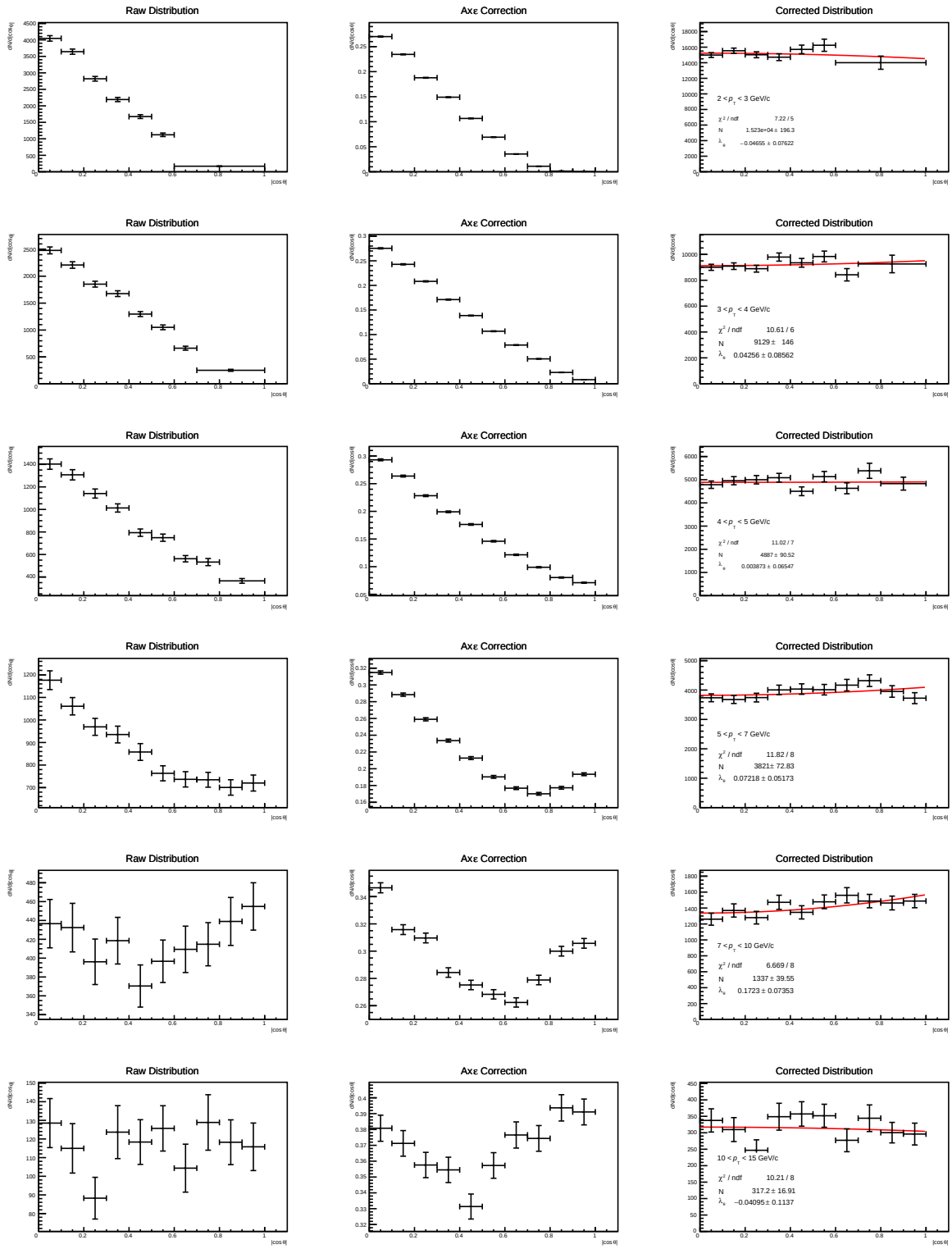

Figure A.1: $|\cos\theta|$ distributions in the Collins-Soper frame of raw number of J/ψ with default VWG+2ECB fit (left column), acceptance-efficiency with default MC (middle column) and corrected number of J/ψ with $W(|\cos\theta|)$ fit result (right column). From top to bottom the p_{T} bins are respectively (in GeV/c): $[2;3)$, $[3;4)$, $[4;5)$, $[5;7)$, $[7;10)$ and $[10;15)$.

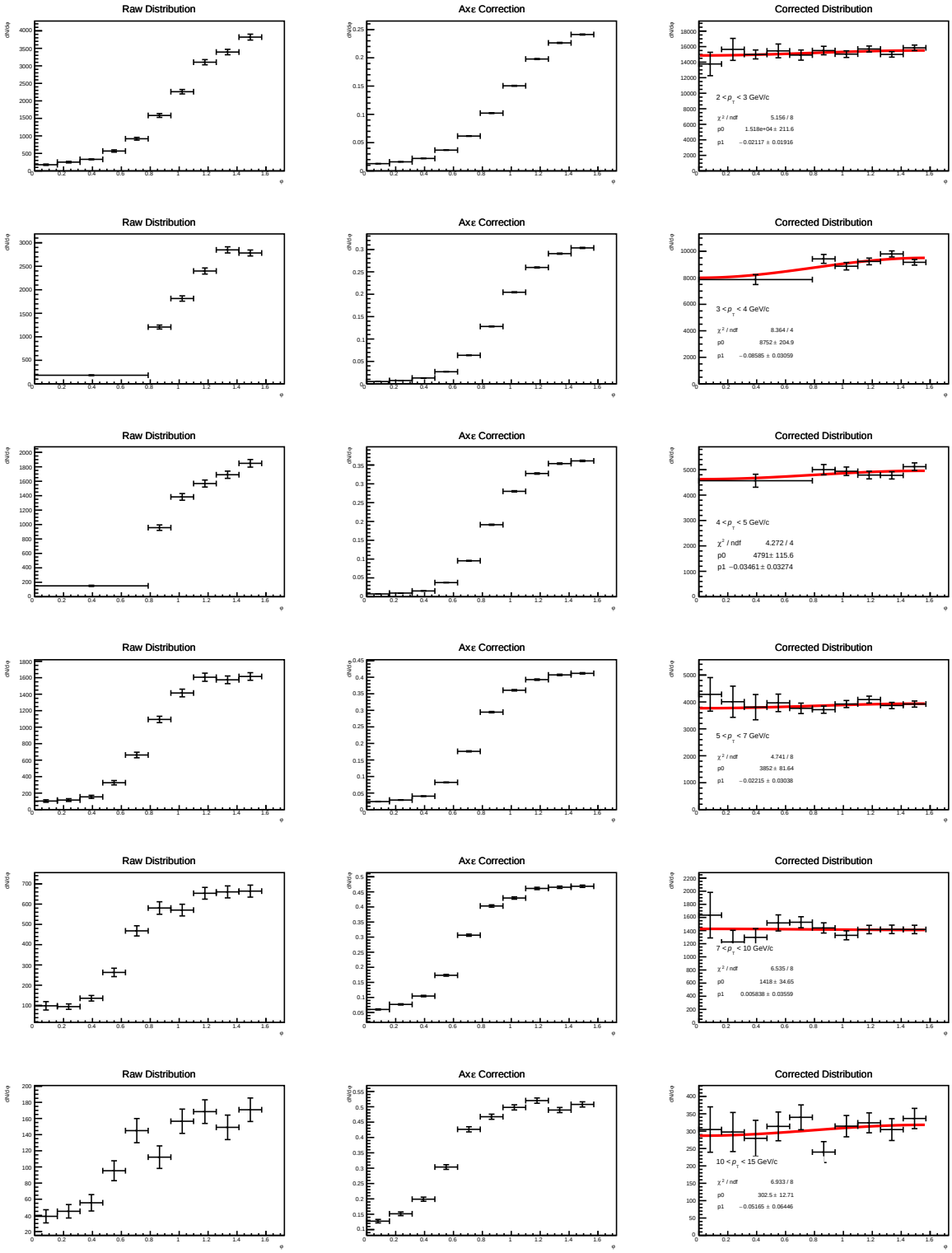

Figure A.2: φ distributions in the Collins-Soper frame of raw number of J/ψ with default VWG+2ECB fit (left column), acceptance-efficiency with default MC (middle column) and corrected number of J/ψ with $W(\varphi)$ fit result (right column). From top to bottom the p_{T} bins are respectively (in GeV/c): $[2;3)$, $[3;4)$, $[4;5)$, $[5;7)$, $[7;10)$ and $[10;15)$.

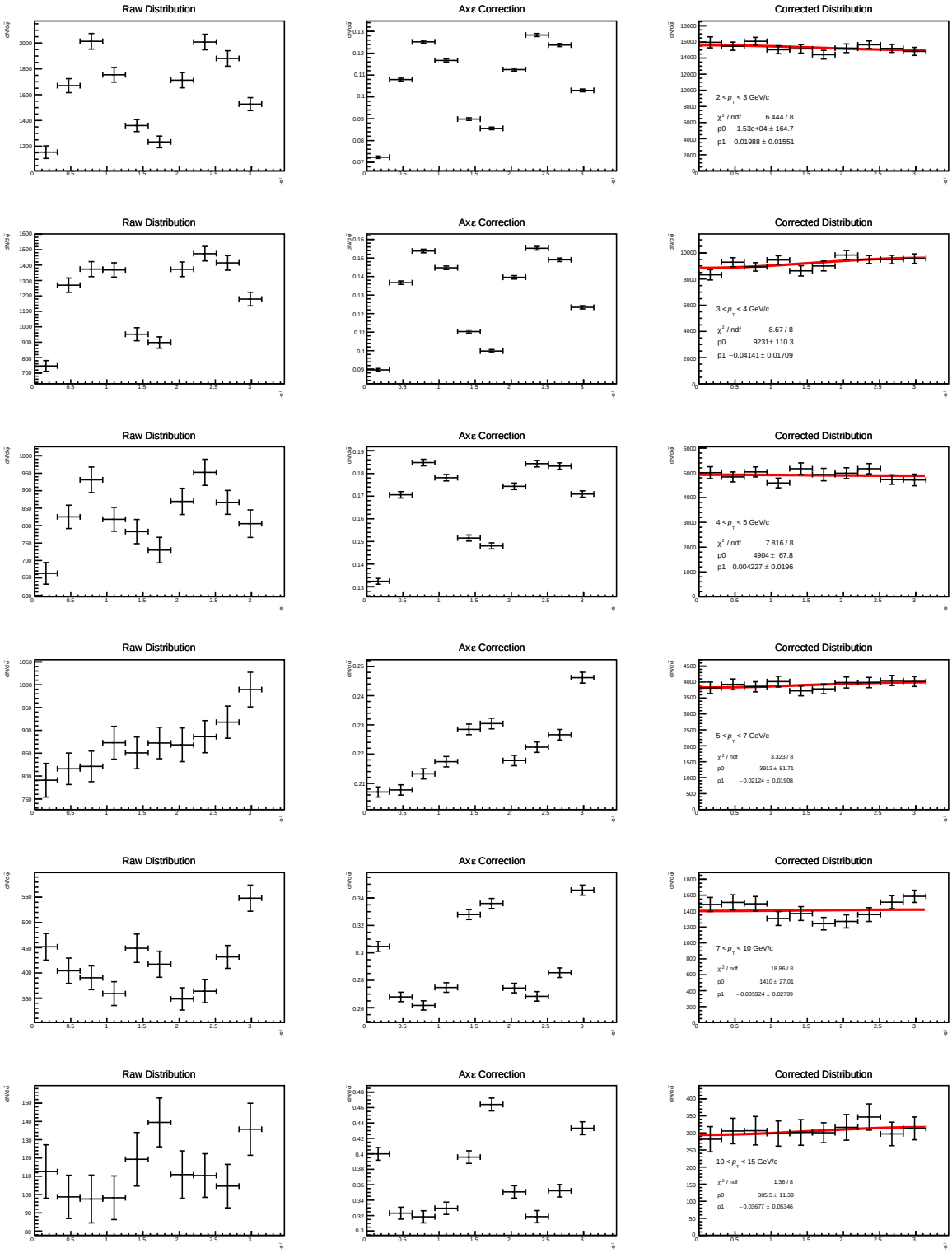

Figure A.3: $\tilde{\varphi}$ distributions in the Collins-Soper frame of raw number of J/ψ with default VWG+2ECB fit (left column), acceptance-efficiency with default MC (middle column) and corrected number of J/ψ with $W(\tilde{\varphi})$ fit result (right column). From top to bottom the p_{T} bins are respectively (in GeV/c): $[2;3)$, $[3;4)$, $[4;5)$, $[5;7)$, $[7;10)$ and $[10;15)$.

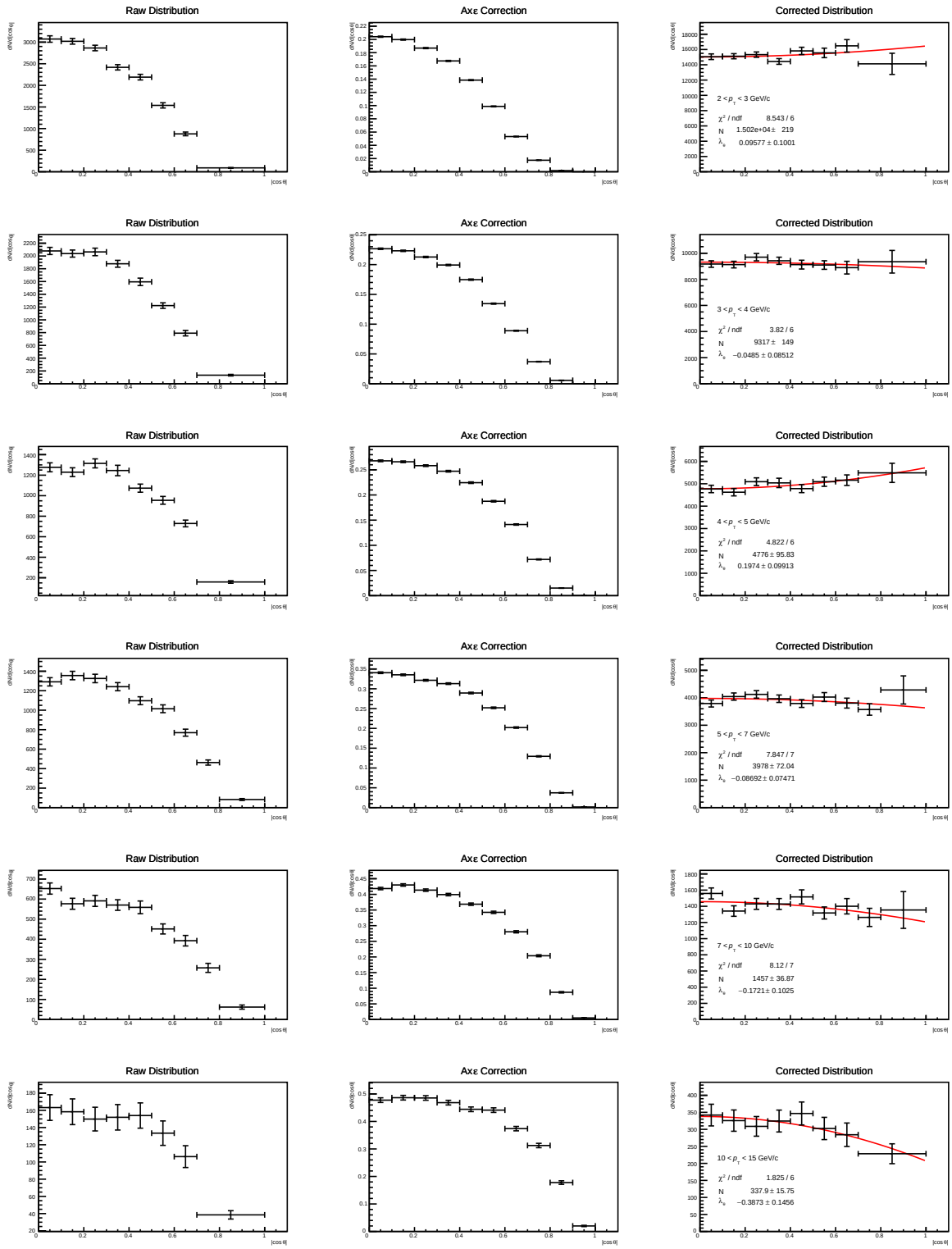

Figure A.4: $|\cos\theta|$ distributions in the Helicity frame of raw number of J/ψ with default VWG+2ECB fit (left column), acceptance-efficiency with default MC (middle column) and corrected number of J/ψ with $W(|\cos\theta|)$ fit result (right column). From top to bottom the p_{T} bins are respectively (in GeV/c): $[2;3)$, $[3;4)$, $[4;5)$, $[5;7)$, $[7;10)$ and $[10;15)$.

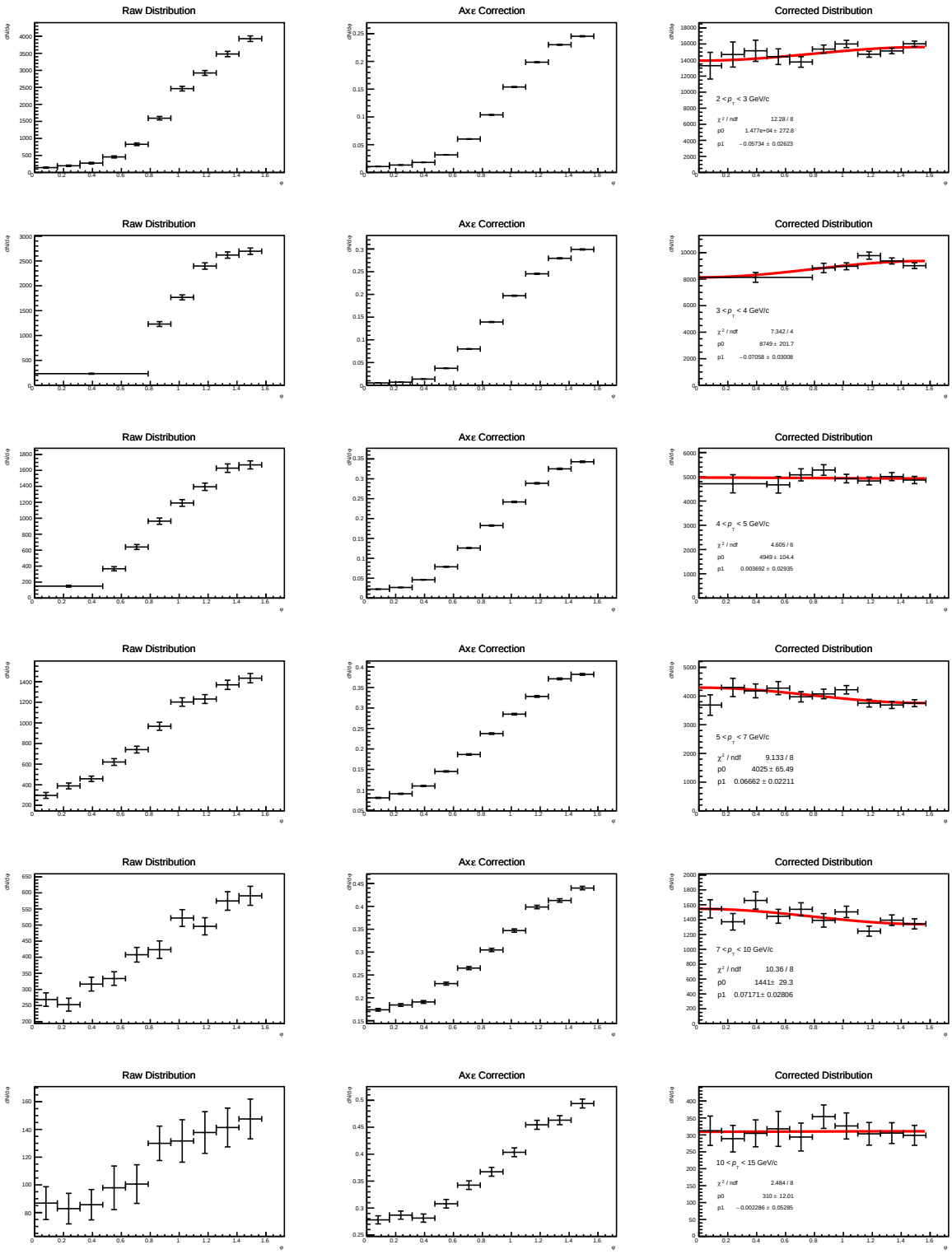

Figure A.5: φ distributions in the Helicity frame of raw number of J/ψ with default VWG+2ECB fit (left column), acceptance-efficiency with default MC (middle column) and corrected number of J/ψ with $W(\varphi)$ fit result (right column). From top to bottom the p_{T} bins are respectively (in GeV/c): $[2;3)$, $[3;4)$, $[4;5)$, $[5;7)$, $[7;10)$ and $[10;15)$.

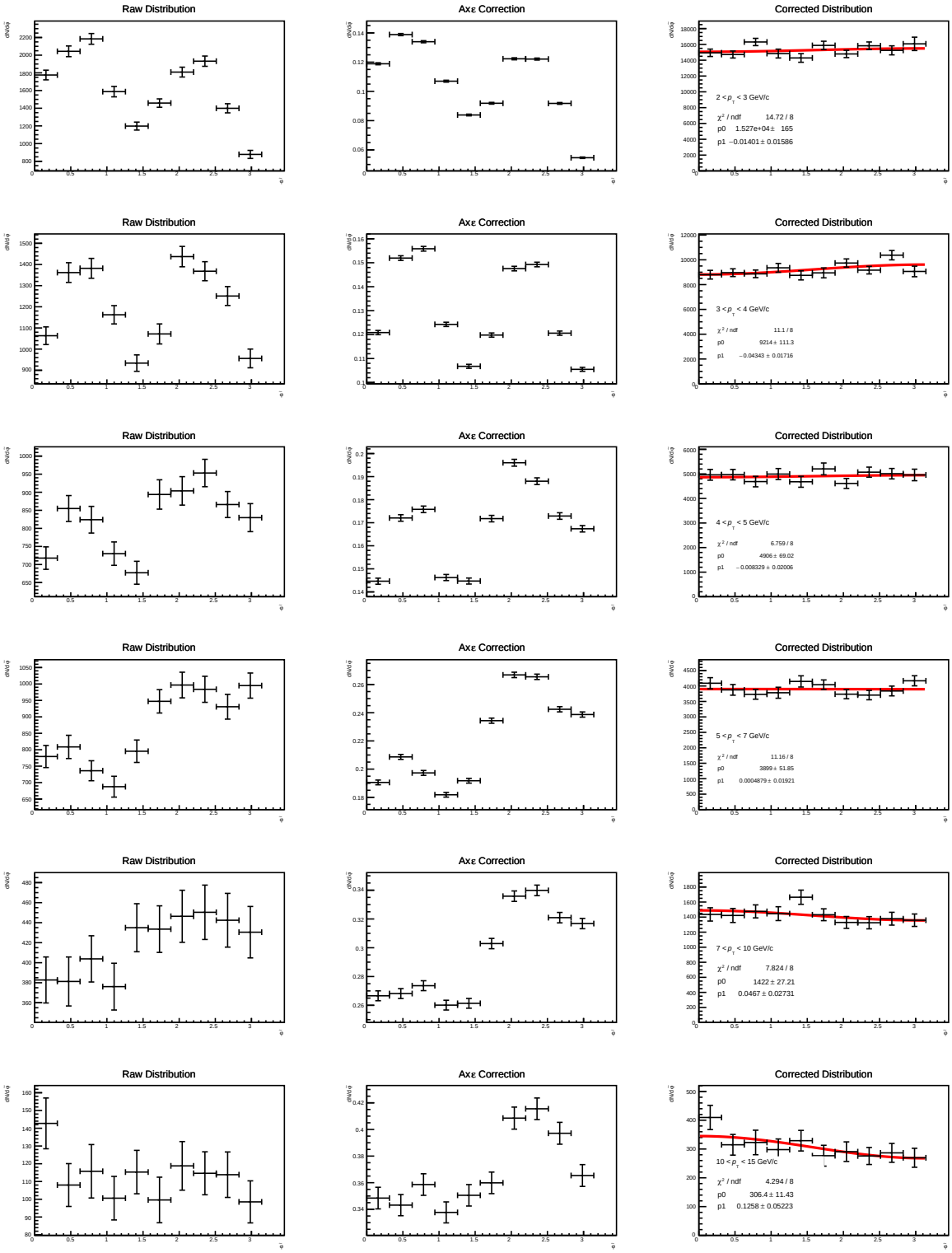

Figure A.6: $\tilde{\varphi}$ distributions in the Helicity frame of raw number of J/ψ with default VWG+2ECB fit (left column), acceptance-efficiency with default MC (middle column) and corrected number of J/ψ with $W(\tilde{\varphi})$ fit result (right column). From top to bottom the p_{T} bins are respectively (in GeV/c): $[2;3)$, $[3;4)$, $[4;5)$, $[5;7)$, $[7;10)$ and $[10;15)$.

Appendix B

Checks on the signal extraction and $A \times \varepsilon$ correction

Table B.1: Number of J/ψ obtained from dimuon mass spectrum fit for each p_{T} bin in the three angular distributions of CS and HX frames.

p_{T} (GeV/c)	$\cos\theta_{\mathrm{CS}}$	φ_{CS}	$\tilde{\varphi}_{\mathrm{CS}}$	$\cos\theta_{\mathrm{HX}}$	φ_{HX}	$\tilde{\varphi}_{\mathrm{HX}}$
$[2;3)$	16173 ± 173	16408 ± 171	16316 ± 172	16250 ± 168	16288 ± 171	16265 ± 171
$[3;4)$	11982 ± 148	11961 ± 139	12048 ± 140	12068 ± 145	11873 ± 141	11987 ± 142
$[4;5)$	8233 ± 113	8199 ± 114	8244 ± 113	8300 ± 117	8299 ± 117	8250 ± 114
$[5;7)$	8656 ± 115	8666 ± 114	8686 ± 112	8724 ± 114	8708 ± 116	8661 ± 113
$[7;10)$	4169 ± 77	4188 ± 79	4164 ± 78	4175 ± 79	4186 ± 78	4182 ± 78
$[10;15)$	1167 ± 41	1137 ± 41	1128 ± 41	1133 ± 41	1142 ± 43	1128 ± 41
Total	50379 ± 292	50559 ± 287	50586 ± 287	50649 ± 289	50496 ± 290	50473 ± 288

Table B.2: Number of J/ψ after $A \times \varepsilon$ correction for each p_{T} bin in the three angular distributions of CS and HX frames.

p_{T} (GeV/c)	$\cos\theta_{\mathrm{CS}}$	φ_{CS}	$\tilde{\varphi}_{\mathrm{CS}}$	$\cos\theta_{\mathrm{HX}}$	φ_{HX}	$\tilde{\varphi}_{\mathrm{HX}}$
$[2;3)$	148247 ± 3590	151811 ± 2587	153012 ± 1669	150157 ± 4364	148556 ± 3025	152882 ± 1733
$[3;4)$	92184 ± 2229	85839 ± 1965	92003 ± 1109	92580 ± 2738	86607 ± 1943	92016 ± 1125
$[4;5)$	49133 ± 826	47459 ± 1329	49166 ± 689	51019 ± 1380	48798 ± 1262	49139 ± 694
$[5;7)$	39368 ± 547	39337 ± 1080	39167 ± 518	39690 ± 1115	39896 ± 684	39116 ± 522
$[7;10)$	14203 ± 268	14222 ± 463	14125 ± 271	13962 ± 509	14429 ± 293	14266 ± 272
$[10;15)$	3170 ± 113	3054 ± 133	3067 ± 115	2919 ± 122	3105 ± 123	3074 ± 114
Total	346304 ± 4350	341722 ± 3704	350539 ± 2201	350327 ± 5474	341391 ± 3884	350493 ± 2260

Appendix C

Systematic uncertainties

C.1 Systematic uncertainties associated to the signal extraction

Bin-by-bin difference between the polarization parameters λ_i with a given fit configuration (including different fit ranges, noted as $[m_{\text{min}}\,;\,m_{\text{max}}]$ in GeV/c^2) and the mean values $\langle\lambda\rangle$. The notation for the different fit functions is the same as in 5.3.1.

Table C.1: λ_θ^{CS}

p_{T} (GeV/c)	ECB+VWG [2,5]	ECB+VWG [2.2,4.5]	ECB+VWG [2.2,4.5]	NA60+VWG [2,5]	ECB+GExp [2,5]
$2-3$	-0.043	-0.097	0.105	0.047	-0.012
$3-4$	-0.002	-0.009	0.018	0.005	-0.012
$4-5$	-0.011	0.020	-0.023	-0.004	0.019
$5-7$	0.002	0.010	-0.021	0.003	0.007
$7-10$	-0.007	0.020	-0.006	-0.004	-0.003
$10-15$	-0.024	-0.024	-0.035	0.074	0.009

Table C.2: λ_ϕ^{CS}

p_{T} (GeV/c)	ECB+VWG [2,5]	ECB+VWG [2.2,4.5]	ECB+VWG [2.2,4.5]	NA60+VWG [2,5]	ECB+GExp [2,5]
$2-3$	0.017	-0.003	-0.002	0.005	-0.017
$3-4$	0.015	-0.008	0.004	0.017	-0.027
$4-5$	0.015	0.049	-0.018	0.020	-0.066
$5-7$	0.019	0.050	-0.031	0.034	-0.073
$7-10$	0.005	-0.001	0.016	0.006	-0.026
$10-15$	0.002	0.015	0.006	0.000	-0.023

Table C.3: $\lambda_{\theta\phi}^{CS}$

p_{T} (GeV/c)	ECB+VWG [2,5]	ECB+VWG [2.2,4.5]	ECB+VWG [2.2,4.5]	NA60+VWG [2,5]	ECB+GExp [2,5]
$2-3$	-0.002	-0.009	0.004	0.004	0.003
$3-4$	-0.013	-0.004	0.016	-0.023	0.024
$4-5$	0.003	-0.022	-0.000	0.006	0.013
$5-7$	-0.004	-0.018	0.021	-0.010	0.010
$7-10$	-0.003	-0.045	0.014	0.008	0.026
$10-15$	-0.011	-0.010	0.033	-0.043	0.031

Table C.4: λ_{θ}^{HX}

p_{T} (GeV/c)	ECB+VWG [2,5]	ECB+VWG [2.2,4.5]	ECB+VWG [2.2,4.5]	NA60+VWG [2,5]	ECB+GExp [2,5]
$2-3$	-0.037	-0.060	0.006	-0.036	0.128
$3-4$	0.031	-0.041	-0.026	0.015	0.020
$4-5$	0.021	-0.010	-0.020	0.027	-0.018
$5-7$	-0.004	0.032	0.005	-0.005	-0.029
$7-10$	0.005	-0.091	0.077	-0.017	0.027
$10-15$	-0.013	0.026	0.045	-0.019	-0.038

Table C.5: λ_{ϕ}^{HX}

p_{T} (GeV/c)	ECB+VWG [2,5]	ECB+VWG [2.2,4.5]	ECB+VWG [2.2,4.5]	NA60+VWG [2,5]	ECB+GExp [2,5]
$2-3$	0.016	-0.004	0.029	0.009	-0.050
$3-4$	0.029	0.058	-0.020	0.035	-0.102
$4-5$	0.030	0.057	-0.030	0.035	-0.091
$5-7$	0.016	0.021	-0.014	0.016	-0.039
$7-10$	-0.001	-0.001	0.015	-0.012	-0.002
$10-15$	-0.010	0.006	-0.004	-0.004	0.012

Table C.6: $\lambda_{\theta\phi}^{HX}$

p_{T} (GeV/c)	ECB+VWG [2,5]	ECB+VWG [2.2,4.5]	ECB+VWG [2.2,4.5]	NA60+VWG [2,5]	ECB+GExp [2,5]
$2-3$	-0.003	0.008	-0.017	0.002	0.011
$3-4$	-0.006	0.013	-0.003	-0.010	0.006
$4-5$	0.007	-0.001	0.004	0.002	-0.012
$5-7$	0.004	0.011	0.001	0.007	-0.023
$7-10$	0.006	0.013	-0.012	0.015	-0.021
$10-15$	0.011	-0.001	0.005	0.009	-0.025

C.2 Systematic uncertainties associated to the MC input

Bin-by-bin systematic uncertainties on each polarization parameters λ_i due to the MC simulation to determine the $A \times \varepsilon$. The "η-diff." and "ϕ-diff." columns correspond to the muon trigger response function uncertainty with its η and ϕ dependencies, respectively.

Table C.7: λ_θ^{CS}

p_{T} (GeV/c)	p_{T} param.	y param.	BR_{rad}	$\lambda_\theta \pm 0.2$	η-diff.	ϕ-diff.
$2-3$	±0.026	±0.032	±0.020	±0.028	±0.021	±0.012
$3-4$	±0.020	±0.027	±0.023	±0.023	±0.017	±0.027
$4-5$	±0.035	±0.037	±0.023	±0.037	±0.006	±0.015
$5-7$	±0.006	±0.000	±0.013	±0.009	±0.003	±0.012
$7-10$	±0.009	±0.010	±0.008	±0.006	±0.004	±0.012
$10-15$	±0.018	±0.018	±0.011	±0.018	±0.006	±0.000

Table C.8: λ_φ^{CS}

p_{T} (GeV/c)	p_{T} param.	y param.	BR_{rad}	$\lambda_\theta \pm 0.2$	η-diff.	ϕ-diff.
$2-3$	±0.009	±0.000	±0.003	±0.067	±0.082	±0.071
$3-4$	±0.010	±0.009	±0.010	±0.101	±0.038	±0.041
$4-5$	±0.007	±0.008	±0.011	±0.119	±0.022	±0.014
$5-7$	±0.013	±0.015	±0.010	±0.032	±0.000	±0.015
$7-10$	±0.032	±0.033	±0.003	±0.033	±0.009	±0.006
$10-15$	±0.017	±0.018	±0.002	±0.028	±0.007	±0.004

Table C.9: $\lambda_{\theta\varphi}^{CS}$

p_{T} (GeV/c)	p_{T} param.	y param.	BR_{rad}	$\lambda_\theta \pm 0.2$	η-diff.	ϕ-diff.
$2-3$	±0.007	±0.004	±0.002	±0.018	±0.019	±0.000
$3-4$	±0.004	±0.000	±0.000	±0.026	±0.013	±0.002
$4-5$	±0.006	±0.002	±0.004	±0.025	±0.017	±0.005
$5-7$	±0.005	±0.011	±0.001	±0.009	±0.005	±0.008
$7-10$	±0.001	±0.006	±0.002	±0.013	±0.008	±0.005
$10-15$	±0.000	±0.008	±0.016	±0.013	±0.003	±0.005

Table C.10: λ_θ^{HX}

p_{T} (GeV/c)	p_{T} param.	y param.	BR_{rad}	$\lambda_\theta \pm 0.2$	η-diff.	ϕ-diff.
$2-3$	±0.008	±0.014	±0.003	±0.051	±0.029	±0.061
$3-4$	±0.022	±0.035	±0.007	±0.010	±0.029	±0.014
$4-5$	±0.033	±0.049	±0.003	±0.010	±0.019	±0.022
$5-7$	±0.003	±0.021	±0.006	±0.032	±0.023	±0.018
$7-10$	±0.000	±0.012	±0.009	±0.029	±0.000	±0.003
$10-15$	±0.065	±0.068	±0.081	±0.052	±0.019	±0.003

Table C.11: λ_φ^{HX}

p_{T} (GeV/c)	p_{T} param.	y param.	BR_{rad}	$\lambda_\theta \pm 0.2$	η-diff.	ϕ-diff.
$2-3$	±0.013	±0.015	±0.022	±0.116	±0.090	±0.068
$3-4$	±0.007	±0.010	±0.017	±0.180	±0.029	±0.029
$4-5$	±0.014	±0.019	±0.046	±0.068	±0.020	±0.008
$5-7$	±0.002	±0.004	±0.009	±0.011	±0.004	±0.004
$7-10$	±0.003	±0.006	±0.007	±0.031	±0.000	±0.000
$10-15$	±0.003	±0.005	±0.006	±0.038	±0.002	±0.005

Table C.12: $\lambda_{\theta\varphi}^{HX}$

p_{T} (GeV/c)	p_{T} param.	y param.	BR_{rad}	$\lambda_\theta \pm 0.2$	η-diff.	ϕ-diff.
$2-3$	±0.005	±0.001	±0.022	±0.041	±0.021	±0.019
$3-4$	±0.003	±0.002	±0.002	±0.008	±0.013	±0.010
$4-5$	±0.004	±0.005	±0.009	±0.024	±0.011	±0.010
$5-7$	±0.003	±0.005	±0.006	±0.055	±0.002	±0.005
$7-10$	±0.015	±0.020	±0.008	±0.080	±0.004	±0.009
$10-15$	±0.026	±0.021	±0.002	±0.045	±0.011	±0.003

C.3 Summary of all systematic uncertainties

Table C.13: Systematic uncertaities in the Collins-Soper frame

p_{T} (GeV/c)	λ	Signal extraction	MC input	Trigger response function
$2-3$	λ_θ	±0.157	±0.046	±0.024
	λ_φ	±0.024	±0.009	±0.108
	$\lambda_{\theta\varphi}$	±0.012	±0.008	±0.019
$3-4$	λ_θ	±0.024	±0.040	±0.032
	λ_φ	±0.037	±0.017	±0.055
	$\lambda_{\theta\varphi}$	±0.039	±0.004	±0.013
$4-5$	λ_θ	±0.037	±0.056	±0.016
	λ_φ	±0.088	±0.015	±0.026
	$\lambda_{\theta\varphi}$	±0.026	±0.007	±0.018
$5-7$	λ_θ	±0.025	±0.014	±0.013
	λ_φ	±0.102	±0.022	±0.015
	$\lambda_{\theta\varphi}$	±0.031	±0.012	±0.009
$7-10$	λ_θ	±0.023	±0.015	±0.012
	λ_φ	±0.031	±0.047	±0.011
	$\lambda_{\theta\varphi}$	±0.055	±0.007	±0.010
$10-15$	λ_θ	±0.089	±0.028	±0.006
	λ_φ	±0.028	±0.025	±0.008
	$\lambda_{\theta\varphi}$	±0.065	±0.017	±0.006

Table C.14: Systematic uncertainties in the Helicity frame

p_{T} (GeV/c)	λ	Signal extraction	MC input	Trigger response function
$2-3$	λ_θ	±0.151	±0.017	±0.068
	λ_φ	±0.030	±0.030	±0.113
	$\lambda_{\theta\varphi}$	±0.022	±0.022	±0.028
$3-4$	λ_θ	±0.063	±0.042	±0.032
	λ_φ	±0.021	±0.021	±0.041
	$\lambda_{\theta\varphi}$	±0.018	±0.005	±0.016
$4-5$	λ_θ	±0.045	±0.059	±0.029
	λ_φ	±0.052	±0.052	±0.022
	$\lambda_{\theta\varphi}$	±0.014	±0.011	±0.015
$5-7$	λ_θ	±0.044	±0.022	±0.030
	λ_φ	±0.010	±0.010	±0.006
	$\lambda_{\theta\varphi}$	±0.027	±0.008	±0.005
$7-10$	λ_θ	±0.124	±0.015	±0.003
	λ_φ	±0.010	±0.010	±0.000
	$\lambda_{\theta\varphi}$	±0.032	±0.026	±0.010
$10-15$	λ_θ	±0.068	±0.124	±0.019
	λ_φ	±0.008	±0.008	±0.006
	$\lambda_{\theta\varphi}$	±0.030	±0.033	±0.011

Acknowledgements

All along these three years I had the opportunity to meet many people that have helped me, in many different ways, to finish this thesis. To all of them, the ones I mention and the ones that for practical reasons I don't, my most sincere gratitude.

I would specially like to thank my supervisors Philippe Rosnet and Valérie Ramillien who kindly welcomed me in France and made my insertion to the LPC smooth. I will be always grateful not only for the countless times of discussions, your patience to answer my questions and your support concerning my work, without which all this would have not been possible, but also for your advices concerning my personal life and future, your invaluable help in administrative procedures and specially, for making me feel less distant from home.

My gratitude goes also to all the members of the ALICE team at the LPC for your warm welcome to the group. I appreciate all the time you have devoted to carefully review my slides, poster and proceedings and your useful advices and suggestions each time. I would like to particularly thank Pascal Dupieux for all his help and explanations about my service task, and the time for discussions, about work and life.

This thesis work would not have been possible without the considerable support from the ALICE Collaboration members, working in such a big collaboration has been one of the most important experiences in my life. In particular I would like to mention the members of the Physics Analysis Group 'Jpsitomumu' who, with their fine remarks, questions and cross-checks, have made my analysis advance in solid steps.

I would like to thank all the members of the jury, specially the two referees, Imad Laktineh and Roberta Arnaldi, who have carefully read this document and provided me the necessary corrections, and also different visions about my work. I can not finish without particularly mentioning Javier Castillo and Katherin Schtejer because, before the beginning of everything, they have trusted in me and encouraged me to go on.

Special thanks to my dear friend Sonia, who kindly introduced me to her circle of friends and family, where I found a crucial support in the difficult times of doubts.

To my friends in Cuba, to my parents and sister, my eternal gratitude for always being present, despite the long distance.

List of Figures

List of Tables

Bibliography

[1] Herwig Schopper and Luigi Di Lella, editors. *60 years of CERN experiments and discoveries*, volume 23.23 of *Advanced series on directions in high energy physics*. World Scientific, Hackensack, NJ, 2015.

[2] C. Patrignani et al. Review of Particle Physics. *Chin. Phys.*, C40(10):100001, 2016.

[3] David J. Gross and Frank Wilczek. Ultraviolet behavior of non-abelian gauge theories. *Phys. Rev. Lett.*, 30:1343–1346, Jun 1973.

[4] H. David Politzer. Reliable perturbative results for strong interactions? *Phys. Rev. Lett.*, 30:1346–1349, Jun 1973.

[5] Dominik J. Schwarz. The first second of the universe. *Annalen Phys.*, 12:220–270, 2003.

[6] Henning Heiselberg and Morten Hjorth-Jensen. Phases of dense matter in neutron stars. *Phys. Rept.*, 328:237–327, 2000.

[7] P. Rosnet. Quark-Gluon Plasma: from accelerator experiments to early Universe. In *11th Rencontres du Vietnam: Cosmology: 50 years after CMB discovery Quy Nhon, Vietnam, August 16-22, 2015*, 2015.

[8] A. Bazavov et al. The chiral and deconfinement aspects of the QCD transition. *Phys. Rev.*, D85:054503, 2012.

[9] J. J. Aubert et al. Experimental Observation of a Heavy Particle J. *Phys. Rev. Lett.*, 33:1404–1406, 1974.

[10] J. E. Augustin et al. Discovery of a Narrow Resonance in e+ e- Annihilation. *Phys. Rev. Lett.*, 33:1406–1408, 1974. [Adv. Exp. Phys.5,141(1976)].

[11] A. Boyarski et al. The Quantum Numbers and Decay Widths of the psi (3095). *Phys. Rev. Lett.*, 34:1357, 1975.

[12] B. Jean-Marie et al. Determination of the G Parity and Isospin of psi (3095) by Study of Multi-Pion Decays. *Phys. Rev. Lett.*, 36:291, 1976.

[13] S. L. Glashow, J. Iliopoulos, and L. Maiani. Weak Interactions with Lepton-Hadron Symmetry. *Phys. Rev.*, D2:1285–1292, 1970.

[14] S. W. Herb et al. Observation of a Dimuon Resonance at 9.5-GeV in 400-GeV Proton-Nucleus Collisions. *Phys. Rev. Lett.*, 39:252–255, 1977.

[15] Mathias Butenschoen and Bernd A. Kniehl. J/ψ polarization at Tevatron and LHC: Nonrelativistic-QCD factorization at the crossroads. *Phys. Rev. Lett.*, 108:172002, 2012.

[16] Bin Gong, Lu-Ping Wan, Jian-Xiong Wang, and Hong-Fei Zhang. Polarization for Prompt J/ψ and ψ(2S) Production at the Tevatron and LHC. *Phys. Rev. Lett.*, 110(4):042002, 2013.

[17] Kuang-Ta Chao, Yan-Qing Ma, Hua-Sheng Shao, Kai Wang, and Yu-Jie Zhang. J/ψ Polarization at Hadron Colliders in Nonrelativistic QCD. *Phys. Rev. Lett.*, 108:242004, 2012.

[18] V. G. Kartvelishvili, A. K. Likhoded, and S. R. Slabospitsky. D Meson and ψ Meson Production in Hadronic Interactions. *Sov. J. Nucl. Phys.*, 28:678, 1978. [Yad. Fiz.28,1315(1978)].

[19] R. Baier and R. Ruckl. Hadronic Collisions: A Quarkonium Factory. *Z. Phys.*, C19:251, 1983.

[20] E. W. Nigel Glover, Alan D. Martin, and W. James Stirling. J/psi Production at Large Transverse Momentum at Hadron Colliders. *Z. Phys.*, C38:473, 1988. [Erratum: Z. Phys.C49,526(1991)].

[21] F. Abe et al. J/ψ and $\psi(2S)$ production in $p\overline{p}$ collisions at $\sqrt{s} = 1.8$TeV. *Phys. Rev. Lett.*, 79:572–577, Jul 1997.

[22] F. Abe et al. Production of J/ψ mesons from χ_c meson decays in $p\bar{p}$ collisions at $\sqrt{s} = 1.8$ TeV. *Phys. Rev. Lett.*, 79:578–583, 1997.

[23] A. Sansoni. Quarkonia production at CDF. *Nucl. Phys.*, A610:373C–385C, 1996.

[24] Geoffrey T. Bodwin, Eric Braaten, and G. Peter Lepage. Rigorous QCD analysis of inclusive annihilation and production of heavy quarkonium. *Phys. Rev.*, D51:1125–1171, 1995. [Erratum: Phys. Rev.D55,5853(1997)].

[25] Martin Beneke and Michael Kramer, 1. Direct J/ψ and ψ' polarization and cross-sections at the Tevatron. *Phys. Rev.*, D55:5269–5272, 1997.

[26] T. Affolder et al. Measurement of J/ψ and $\psi(2S)$ polarization in $p\bar{p}$ collisions at $\sqrt{s} = 1.8$ TeV. *Phys. Rev. Lett.*, 85:2886–2891, 2000.

[27] D. Acosta et al. Υ production and polarization in $p\bar{p}$ collisions at $\sqrt{s} = 1.8$ TeV. *Phys. Rev. Lett.*, 88:161802, 2002.

[28] V. M. Abazov et al. Measurement of the polarization of the $\Upsilon(1S)$ and $\Upsilon(2S)$ states in $p\bar{p}$ collisions at $\sqrt{s} = 1.96$ TeV. *Phys. Rev. Lett.*, 101:182004, 2008.

[29] A. Abulencia et al. Polarization of J/ψ and ψ_{2S} mesons produced in $p\bar{p}$ collisions at $\sqrt{s}$ = 1.96-TeV. *Phys. Rev. Lett.*, 99:132001, 2007.

[30] J. P. Lansberg. On the mechanisms of heavy-quarkonium hadroproduction. *Eur. Phys. J.*, C61:693–703, 2009.

[31] D. Acosta et al. Measurement of the J/ψ meson and $b-$hadron production cross sections in $p\bar{p}$ collisions at $\sqrt{s}$ = 1960 GeV. *Phys. Rev.*, D71:032001, 2005.

[32] T. Aaltonen et al. Production of psi(2S) Mesons in p anti-p Collisions at 1.96-TeV. *Phys. Rev.*, D80:031103, 2009.

[33] T. Matsui and H. Satz. J/ψ Suppression by Quark-Gluon Plasma Formation. *Phys. Lett.*, B178:416–422, 1986.

[34] Helmut Satz. Quarkonium Binding and Dissociation: The Spectral Analysis of the QGP. *Nucl. Phys.*, A783:249–260, 2007.

[35] R. Arnaldi et al. J/psi production in indium-indium collisions at 158-GeV/nucleon. *Phys. Rev. Lett.*, 99:132302, 2007.

[36] A. Adare et al. J/ψ suppression at forward rapidity in Au+Au collisions at $\sqrt{s_{NN}}$ = 200 GeV. *Phys. Rev.*, C84:054912, 2011.

[37] G. Aad et al. Measurement of the centrality dependence of J/ψ yields and observation of Z production in leadlead collisions with the ATLAS detector at the LHC. *Phys. Lett.*, B697:294–312, 2011.

[38] Serguei Chatrchyan et al. Suppression of non-prompt J/ψ, prompt J/ψ, and Υ(1S) in PbPb collisions at $\sqrt{s_{NN}}$ = 2.76 TeV. *JHEP*, 05:063, 2012.

[39] P. Braun-Munzinger and J. Stachel. (Non)thermal aspects of charmonium production and a new look at J/ψ suppression. *Phys. Lett.*, B490:196–202, 2000.

[40] Robert L. Thews, Martin Schroedter, and Johann Rafelski. Enhanced J/ψ production in deconfined quark matter. *Phys. Rev.*, C63:054905, 2001.

[41] Jaroslav Adam et al. Differential studies of inclusive J/ψ and psi(2S) production at forward rapidity in Pb-Pb collisions at $\sqrt{s_{\mathrm{NN}}}$ = 2.76 TeV. *JHEP*, 05:179, 2016.

[42] Michael L. Miller, Klaus Reygers, Stephen J. Sanders, and Peter Steinberg. Glauber modeling in high energy nuclear collisions. *Ann. Rev. Nucl. Part. Sci.*, 57:205–243, 2007.

[43] E. G. Ferreiro, F. Fleuret, J. P. Lansberg, and A. Rakotozafindrabe. Impact of the Nuclear Modification of the Gluon Densities on J/ψ production in pPb collisions at $\sqrt{s_{NN}}$ = 5 TeV. *Phys. Rev.*, C88(4):047901, 2013.

[44] D. E. Kharzeev, E. M. Levin, and K. Tuchin. Nuclear modification of the J/ψ transverse momentum distributions in high energy pA and AA collisions. *Nucl. Phys.*, A924:47–64, 2014.

[45] Francois Arleo and Stephane Peigne. J/ψ suppression in p-A collisions from parton energy loss in cold QCD matter. *Phys. Rev. Lett.*, 109:122301, 2012.

[46] R. Vogt. Are the J/ψ and chi(c) A dependencies the same? *Nucl. Phys.*, A700:539–554, 2002.

[47] Sean Gavin and Ramona Vogt. Charmonium suppression by Comover scattering in Pb + Pb collisions. *Phys. Rev. Lett.*, 78:1006–1009, 1997.

[48] Betty Bezverkhny Abelev et al. J/ψ production and nuclear effects in p-Pb collisions at $\sqrt{S_{NN}} = 5.02$ TeV. *JHEP*, 02:073, 2014.

[49] J. L. Albacete et al. Predictions for p-Pb Collisions at $\sqrt{s_{\rm NN}} = 5$ TeV. *Int. J. Mod. Phys.*, E22:1330007, 2013.

[50] Hirotsugu Fujii and Kazuhiro Watanabe. Heavy quark pair production in high energy pA collisions: Quarkonium. *Nucl. Phys.*, A915:1–23, 2013.

[51] Franois Arleo, Rodion Kolevatov, Stphane Peign, and Maryam Rustamova. Centrality and pT dependence of J/ψ suppression in proton-nucleus collisions from parton energy loss. *JHEP*, 05:155, 2013.

[52] E. G. Ferreiro. Excited charmonium suppression in protonnucleus collisions as a consequence of comovers. *Phys. Lett.*, B749:98–103, 2015.

[53] Betty Bezverkhny Abelev et al. Suppression of ψ(2S) production in p-Pb collisions at $\sqrt{s_{\rm NN}} = 5.02$ TeV. *JHEP*, 12:073, 2014.

[54] Jaroslav Adam et al. Rapidity and transverse-momentum dependence of the inclusive J/ψ nuclear modification factor in p-Pb collisions at $\sqrt{s_{N\ N}} = 5.02$ TeV. *JHEP*, 06:055, 2015.

[55] Xingbo Zhao and Ralf Rapp. Medium Modifications and Production of Charmonia at LHC. *Nucl. Phys.*, A859:114–125, 2011.

[56] Kai Zhou, Nu Xu, Zhe Xu, and Pengfei Zhuang. Medium effects on charmonium production at ultrarelativistic energies available at the cern large hadron collider. *Phys. Rev. C*, 89:054911, May 2014.

[57] Ehab Abbas et al. J/Psi Elliptic Flow in Pb-Pb Collisions at $\sqrt{s_{\rm NN}} = 2.76$ TeV. *Phys. Rev. Lett.*, 111:162301, 2013.

[58] B. L. Ioffe and D. E. Kharzeev. Quarkonium polarization in heavy ion collisions as a possible signature of the quark gluon plasma. *Phys. Rev.*, C68:061902, 2003.

[59] Berndt Muller, Jurgen Schukraft, and Boleslaw Wyslouch. First Results from Pb+Pb collisions at the LHC. *Ann. Rev. Nucl. Part. Sci.*, 62:361–386, 2012.

[60] Pietro Faccioli, Carlos Lourenco, Joao Seixas, and Hermine K. Wohri. Towards the experimental clarification of quarkonium polarization. *Eur. Phys. J.*, C69:657–673, 2010.

[61] Pietro Faccioli, Carlos Lourenco, and Joao Seixas. A New approach to quarkonium polarization studies. *Phys. Rev.*, D81:111502, 2010.

[62] Pietro Faccioli, Carlos Lourenco, and Joao Seixas. Rotation-invariant relations in vector meson decays into fermion pairs. *Phys. Rev. Lett.*, 105:061601, 2010.

[63] Eric Braaten, Bernd A. Kniehl, and Jungil Lee. Polarization of prompt J/ψ at the Tevatron. *Phys. Rev.*, D62:094005, 2000.

[64] Adam K. Leibovich. ψ' polarization due to color octet quarkonia production. *Phys. Rev.*, D56:4412–4415, 1997.

[65] Eric Braaten, Sean Fleming, and Adam K. Leibovich. NRQCD analysis of bottomonium production at the Tevatron. *Phys. Rev.*, D63:094006, 2001.

[66] Jeppe R. Andersen et al. Small x phenomenology: Summary and status. *Eur. Phys. J.*, C35:67–98, 2004.

[67] Peter L. Cho and Mark B. Wise. Spin symmetry predictions for heavy quarkonia alignment. *Phys. Lett.*, B346:129–136, 1995.

[68] S. P. Baranov. Highlights from the kT factorization approach on the quarkonium production puzzles. *Phys. Rev.*, D66:114003, 2002. [,162(2002)].

[69] T. Aaltonen et al. Measurements of Angular Distributions of Muons From Υ Meson Decays in $p\bar{p}$ Collisions at $\sqrt{s} = 1.96$ TeV. *Phys. Rev. Lett.*, 108:151802, 2012.

[70] A. Adare et al. Transverse momentum dependence of J/psi polarization at midrapidity in p+p collisions at s**(1/2) = 200-GeV. *Phys. Rev.*, D82:012001, 2010.

[71] L. Adamczyk et al. J/ψ polarization in p+p collisions at $\sqrt{s} = 200$ GeV in STAR. *Phys. Lett.*, B739:180–188, 2014.

[72] Hee Sok Chung, Chaehyun Yu, Seyong Kim, and Jungil Lee. Polarization of prompt J/ψ in proton-proton collisions at RHIC. *Phys. Rev.*, D81:014020, 2010.

[73] J. P. Lansberg. QCD corrections to J/psi polarisation in pp collisions at RHIC. *Phys. Lett.*, B695:149–156, 2011.

[74] Barbara Trzeciak. J/ψ polarization measurements in p+p collisions at $\sqrt{s} = 200$ and 500 GeV with the STAR experiment. *PoS*, EPS-HEP2015:470, 2015.

[75] Serguei Chatrchyan et al. Measurement of the prompt J/ψ and ψ(2S) polarizations in pp collisions at $\sqrt{s} = 7$ TeV. *Phys. Lett.*, B727:381–402, 2013.

[76] Serguei Chatrchyan et al. Measurement of the Υ(1S), Υ(2S) and Υ(3S) polarizations in pp collisions at $\sqrt{s} = 7$ TeV. *Phys. Rev. Lett.*, 110(8):081802, 2013.

[77] R Aaij et al. Measurement of J/ψ polarization in pp collisions at $\sqrt{s} = 7$ TeV. *Eur. Phys. J.*, C73(11):2631, 2013.

[78] Roel Aaij et al. Measurement of $\psi(2S)$ polarisation in pp collisions at $\sqrt{s} = 7$ TeV. *Eur. Phys. J.*, C74(5):2872, 2014.

[79] Hua-Sheng Shao and Kuang-Ta Chao. Spin correlations in polarizations of P-wave charmonia χ_{cJ} and impact on J/ψ polarization. *Phys. Rev.*, D90(1):014002, 2014.

[80] Betty Abelev et al. J/ψ polarization in pp collisions at $\sqrt{s} = 7$ TeV. *Phys. Rev. Lett.*, 108:082001, 2012.

[81] Roberta Arnaldi. J/psi production in p-A and A-A collisions at fixed target experiments. *Nucl. Phys.*, A830:345C–352C, 2009.

[82] I. Abt et al. Angular distributions of leptons from J/ψ ' s produced in 920 GeV fixed-target proton-nucleus collisions. *Eur. Phys. J.*, C60:517–524, 2009.

[83] Carlos Loureno, Pietro Faccioli, Valentin Knnz, Joo Seixas, and Hermine K. Whri. A change of perspective in quarkonium production: All data are equal, but some are more equal than others. *Nucl. Phys.*, A932:466–471, 2014.

[84] G. Aad et al. The ATLAS Experiment at the CERN Large Hadron Collider. *JINST*, 3:S08003, 2008.

[85] K. Aamodt et al. The ALICE experiment at the CERN LHC. *JINST*, 3:S08002, 2008.

[86] S. Chatrchyan et al. The CMS experiment at the CERN LHC. *JINST*, 3:S08004, 2008.

[87] A. Augusto Alves, Jr. et al. The LHCb Detector at the LHC. *JINST*, 3:S08005, 2008.

[88] Thomas Sven Pettersson and P Lefvre. The Large Hadron Collider: conceptual design. Technical Report CERN-AC-95-05-LHC, Oct 1995.

[89] K. Schindl. The injector chain for the LHC. In *LEP performance. Proceedings, 9th Workshop, Chamonix, France, January 26-29, 1999*, pages 47–52, 1999.

[90] A. Beuret. The LHC lead injector chain. In *Proceedings of EPAC04, Lucerne, Switzerland*, pages 1153–1155, 2004.

[91] R Bailey and Paul Collier. Standard Filling Schemes for Various LHC Operation Modes. Technical Report LHC-PROJECT-NOTE-323, CERN, Geneva, Sep 2003.

[92] Christian Wolfgang Fabjan, L Jirdn, V Lindestruth, Lodovico Riccati, D Rorich, Pierre Van de Vyvre, O Villalobos Baillie, and Hans de Groot. *ALICE trigger data-acquisition high-level trigger and control system: Technical Design Report*. Technical Design Report ALICE. CERN, Geneva, 2004.

[93] Betty Bezverkhny Abelev et al. Performance of the ALICE Experiment at the CERN LHC. *Int. J. Mod. Phys.*, A29:1430044, 2014.

[94] R. Fruhwirth. Application of Kalman filtering to track and vertex fitting. *Nucl. Instrum. Meth.*, A262:444–450, 1987.

[95] B Abelev et al. Upgrade of the ALICE Experiment: Letter Of Intent. *J. Phys.*, G41:087001, 2014.

[96] Addendum of the Letter Of Intent for the Upgrade of the ALICE Experiment : The Muon Forward Tracker. Technical Report CERN-LHCC-2013-014. LHCC-I-022-ADD-1, CERN, Geneva, Aug 2013. Final submission of the presetn LoI addendum is scheduled for September 7th.

[97] B Abelev et al. Technical Design Report for the Upgrade of the ALICE Inner Tracking System. Technical Report CERN-LHCC-2013-024. ALICE-TDR-017, Nov 2013.

[98] Upgrade of the ALICE Time Projection Chamber. Technical Report CERN-LHCC-2013-020. ALICE-TDR-016, Oct 2013.

[99] P Antonioli, A Kluge, and W Riegler. Upgrade of the ALICE Readout & Trigger System. Technical Report CERN-LHCC-2013-019. ALICE-TDR-015, Sep 2013. Presently we require a LHCC-TDR reference number. At a later stage we will fill the required information.

[100] Technical Design Report for the Muon Forward Tracker. Technical Report CERN-LHCC-2015-001. ALICE-TDR-018, Jan 2015.

[101] ALICE technical design report of the dimuon forward spectrometer. 1999.

[102] M. Bertino et al. Performance of Resistive Plate Counters at Beam Flux Up to 140-hz/CM**2. *Nucl. Instrum. Meth.*, A283:654–657, 1989.

[103] G. L. Bencze et al. Study of resistive plate chambers for muon detection at hadron colliders. *Nucl. Instrum. Meth.*, A340:466–473, 1994.

[104] T. Moers et al. Measurement of the efficiency and time resolution of double gap resistive plate chambers. *Nucl. Instrum. Meth.*, A345:474–481, 1994.

[105] R. Arnaldi et al. A low-resistivity RPC for the ALICE dimuon arm. *Nucl. Instrum. Meth.*, A451:462–473, 2000.

[106] R. Arnaldi et al. A dual threshold technique to improve the time resolution of resistive plate chambers in streamer mode. *Nucl. Instrum. Meth.*, A457:117–125, 2001.

[107] R. Arnaldi et al. Front-end electronics for the RPCs of the ALICE dimuon trigger. *IEEE Trans. Nucl. Sci.*, 52:1176–1181, 2005.

[108] R. Arnaldi et al. Beam and ageing tests with a highly-saturated avalanche gas mixture for the ALICE p-p data taking. *Nucl. Phys. Proc. Suppl.*, 158:149–153, 2006. [,149(2006)].

[109] Francesco Bossu, Martino Gagliardi, and Massimiliano Marchisone. Performance of the RPC-based ALICE muon trigger system at the LHC. *JINST*, 7:T12002, 2012. [PoSRPC2012,059(2012)].

[110] S. Manen, P. Dupieux, B. Joly, F. Jouve, and R. Vandaele. FEERIC, a very-front-end ASIC for the ALICE muon trigger resistive plate chambers. In *Proceedings, 2013 IEEE Nuclear Science Symposium and Medical Imaging Conference (NSS/MIC 2013): Seoul, Korea, October 26-November 2, 2013*, 2013.

[111] Diego Stocco. *Development of the ALICE Muon Spectrometer: Preparation for data taking and heavy flavor measurement.* PhD thesis, Turin U., 2008.

[112] R. Arnaldi et al. Spatial resolution of RPC in streamer mode. *Nucl. Instrum. Meth.*, A490:51–57, 2002.

[113] M. Gagliardi. Commissioning and first performance of the resistive plate chambers for the ALICE muon arm. *Nucl. Instrum. Meth.*, A661:S45–S49, 2012.

[114] Mattia Fontana. Performance of the ALICE muon trigger RPCs during LHC Run I. *JINST*, 9:C08019, 2014.

[115] Massimiliano Marchisone. *Probing the Quark-Gluon Plasma from bottomonium production at forward rapidity with ALICE at the LHC.* PhD thesis, Clermont-Ferrand U., 2013.

[116] Massimiliano Marchisone. Performance of a resistive plate chamber equipped with a new prototype of amplified front-end electronics. *JINST*, 11(06):C06011, 2016.

[117] A Alici, G Anders, N Bacchetta, V Balagura, C Barschel, E Bravin, H Burkhardt, M Ferro-Luzzi, M Gagliardi, J J Gras, B Heinemann, P Hopchev, M Huhtinen, A Jeff, W Kozanecki, S Pagan Griso, J Panman, S White, and A Zuranski. Study of the LHC ghost charge and satellite bunches for luminosity calibration. Feb 2012.

[118] Roel Aaij et al. Precision luminosity measurements at LHCb. *JINST*, 9(12):P12005, 2014.

[119] X. Zhang. *Study of Heavy Flavours from Muons Measured with the ALICE Detector in Proton-Proton and Heavy-Ion Collisions at the CERN-LHC.* Theses, Université Blaise Pascal - Clermont-Ferrand II, May 2012. N d'ordre: DU 2240 EDSF : 714.

[120] R. Aaij et al. Measurement of J/ψ production in pp collisions at $\sqrt{s} = 7$ TeV. *Eur. Phys. J.*, C71:1645, 2011.

[121] R Aaij et al. Measurement of $\psi(2S)$ meson production in pp collisions at $\sqrt{s}$=7 TeV. *Eur. Phys. J.*, C72:2100, 2012.

[122] R Aaij et al. Measurement of the ratio of prompt χ_c to J/ψ production in pp collisions at $\sqrt{s} = 7$ TeV. *Phys. Lett.*, B718:431–440, 2012.

[123] K. A. Olive et al. Review of Particle Physics. *Chin. Phys.*, C38:090001, 2014.

[124] F. Bossu, Z. Conesa del Valle, A. de Falco, M. Gagliardi, S. Grigoryan, and G. Martinez Garcia. Phenomenological interpolation of the inclusive J/psi cross section to proton-proton collisions at 2.76 TeV and 5.5 TeV. 2011.

[125] Jaroslav Adam et al. Inclusive quarkonium production at forward rapidity in pp collisions at $\sqrt{s} = 8$ TeV. *Eur. Phys. J.*, C76(4):184, 2016.

[126] Alexander Spiridonov. Bremsstrahlung in leptonic onia decays: Effects on mass spectra. 2004.

[127] René Brun, F. Bruyant, Federico Carminati, Simone Giani, M. Maire, A. McPherson, G. Patrick, and L. Urban. GEANT Detector Description and Simulation Tool. 1994.

[128] J. Gaiser. *Charmonium Spectroscopy From Radiative Decays of the J/ψ and ψ'*. PhD thesis, SLAC, 1982.

[129] R Shahoyan. *J/ψ and ψ' production in 450 GeV pA interactions and its dependence on the rapidity and x_F*. PhD thesis, Lisboa U., Geneva, 2001. Presented on 2001.

[130] J. Fleischer and F. Jegerlehner. Radiative Z and $W^{\pm}$ Decays: Precise Predictions From the Standard Model. *Z. Phys.*, C26:629, 1985.

[131] T. A. Armstrong et al. Observation of the radiative decay J / psi —¿ e+ e- gamma. *Phys. Rev.*, D54:7067–7070, 1996.

[132] R Aaij et al. Production of J/psi and Upsilon mesons in pp collisions at sqrt(s) = 8 TeV. *JHEP*, 06:064, 2013.

[133] Hua-Sheng Shao, Hao Han, Yan-Qing Ma, Ce Meng, Yu-Jie Zhang, and Kuang-Ta Chao. Yields and polarizations of prompt J/ψ and $\psi(2S)$ production in hadronic collisions. *JHEP*, 05:103, 2015.

Étude de la polarisation du J/ψ dans les collisions proton-proton avec le détecteur ALICE au LHC

Arianna Batista Camejo

1 Introduction aux quarkonia

Le modèle standard de la physique des particules est un cadre théorique qui regroupe la description de l'interaction électrofaible (unification des interactions électromagnétique et faible) et de l'interaction forte. Le mécanisme de brisure spontanée de symétrie au cœur de l'interaction électrofaible, qui engendre la masse des particules, a été confirmé par la découverte du boson de Brout-Englert-Higgs en 2012 par les expériences ATLAS et CMS auprès du grand collisionneur de protons LHC (*Large Hadron Collider*) au Laboratoire européen de la physique des particules CERN près de Genève. L'interaction forte est décrite par la chromodynamique quantique (ou QCD pour *Quantum ChromoDynamics*) dont le caractère non abélien se traduit par une variation de sa constante de couplage α_s qui devient grande à basse énergie, ce qui engenre le confinement des (anti)quarks dans des hadrons (mésons et baryons), et qui devient négligeable à grande énergie, ce qui se traduit par la liberté asymptotique.

Les quarkonia sont des états liés entre un quarks lourd Q et son antiquark $\bar{Q}$. On distingue la famille des chamonia, états $c\bar{c}$, et celle des bottomonia, états $b\bar{b}$. Les quarkonia sont particulièrement intéressants pour différentes raisons. Tout d'abord, leur mécanisme de prodution dans les collisons hadroniques, comme les collisions proton-proton (pp), ne sont pas très bien compris. Cela tient au fait que les processus de production d'une paire $Q\bar{Q}$, dominés par la fusion de gluons $g + g \rightarrow Q\bar{Q} + X$ aux énergies du LHC, sont décrits par la QCD perturbative, mais le processus d'hadronisation, i.e. la formation de l'état lié $Q\bar{Q}$, relève de la QCD non perturbative. Cette deuxième étape est décrite par plusieurs approches phénoménologiques dont les principales sont le modèle singulet de couleur (ou CSM pour *Color Singlet Model*) et le modèle non relativiste de QCD (ou NRQCD pour *Non Relativistic QCD*). Dans ces approches, la section efficace de production d'un quarkonium $\mathcal{Q}$ lors d'une collision A-B s'écrit :

$$\sigma_{\mathrm{A+B}\rightarrow\mathcal{Q}+\mathrm{X}} = \sum_{i,j,(n)} \iint_0^1 dx_i dx_j f_i^{\mathrm{A}}(x_i,\mu_F) f_j^{\mathrm{B}}(x_j,\mu_F) \hat{\sigma}_{i+j\rightarrow Q\bar{Q}+X}(\mu_F,\mu_R) \langle \mathcal{O}_{\mathcal{Q}}^n \rangle, \quad (1)$$

où i (j) représente les partons d'impulsion relative x_i (x_j) dans le hadron A (B), tandis que les fonctions f_i^{A} (f_j^{B}) sont les fonctions de distributions partoniques à

l'échelle d'énergie de factorisation μ_F. La section efficace au niveau partonique $\hat{\sigma}$ est estimée à l'échelle d'énergie de factorisation μ_F, mais dépend également de l'échelle d'énergie de renormalisation μ_R à laquelle la constane de couplage α_s a été évaluée. Enfin, l'élément $\langle \mathcal{O}^n_{\mathcal{Q}} \rangle$ encode les effets non perturbatifs. Pour le CSM, il se réduit au module au carré de la fonction d'onde $|\Psi(0)|^2$ de la paire $Q\bar{Q}$ évaluée à distance de séparation nulle (soit $n = 0$). Dans l'approche NRQCD, il correspond aux différents éléments de matrice (LDME pour *Long-Distance Matrix Element*) qui donnent la probabilité qu'une paire $Q\bar{Q}$ produite dans l'état quantique n évolue dans un état lié particulier $\mathcal{Q}$.

L'étude de la production des quarkonia dans les collisions proton-proton constitue ainsi un moyen de tester la QCD, surtout dans ses aspects non perturbatifs. Les modèles ne permettaient pas initialement de prédire le bon ordre de grandeur des sections efficaces de production, en particulier différentielle en impulsion transverse des quarkonia. La prise en compte dans le calcul perturbatif des effets d'ordres supérieurs à l'ordre dominant – NLO (*Next-to-Leading Order*), voire NNLO* (*Next-to-Next-to-Leading Order* tronqués au processu que l'on pense dominants) – permet maintenant reproduire assez bien les sections efficaces différentielles, depuis les données p$\bar{\text{p}}$ du Tevatron jusqu'à celles du LHC en mode pp. En revanche, les prédictions concernant l'état de polarisation des quarkonia ne sont pas en accord avec les données expérimentales, lesquelles ont été en désaccord entre elles par le passé, en particulier entre les expériences CDF et D0 du Tevatron.

Par ailleurs, la liberté asymptotique de QCD se traduit par la prédiction d'un nouvel état de la matière, le plasma de quarks et des gluons (ou QGP pour *Quark-Gluon Plasma*), qui était selon le modèle cosmologique standard l'état de l'Univers environ 10 μs après le Big Bang. Cet état peut être reproduit en laboratoire dans des collisions d'ions lourds ultra-relativistes, comme les collisions entre noyaux de plomb Pb-Pb engendrées par le LHC. Comme les quarkonia sont produits dans les processus durs initiaux, et qu'ils ont des énergies de liaison différentes entre eux, ils peuvent être altérés par la présence d'un QGP en fonction de sa température. De plus, la production en abondance de particules dans les collisions d'ions lourds à hautes énergies permet la formation de quarkonia par hadronisation statistique, surtout de charmonia (le quark b étant plus lourd que le quark c, il est produit en moindre abondance), qui renseignent alors sur des aspects collectifs du QGP. Ainsi, les quarkonia permettent de sonder l'évolution du QGP formé dans les collisions d'ions lourds. En revanche, l'interprétation non ambiguë des données nécessite de les comparer à une situation où le QGP n'est pas formé, comme à priori dans les collisions pp, ce qui rend d'autant plus important la compréhension de leur mécanisme de production.

Le J/ψ – le premier état lié $c\bar{c}$ découvert en 1974 – est le charmonium produit le plus abondamment dans les collisions pp. Son étude est donc mise en avant pour toute la physique des quarkonia, que ce soit en tant que "laboratoire" de QCD ou pour sonder le QGP. Le J/ψ est un état lié dont les caractéristiques quantiques sont $J^{PC} = 1^{--}$, i.e. son moment cinétique total J (qui se réduit à son spin) vaut 1, tandis

que ses nombres quantiques de parité P et conjugaison de charge C valent -1.

2 Le concept de polarisation

Une particule de spin 1 possède trois états de projection de spin $\{|+\rangle, |0\rangle, |-\rangle\}$ selon un axe z ; son état de moment cinétique s'écrit alors :

$$|\Psi\rangle = b_+|+\rangle + b_0|0\rangle + b_-|-\rangle,$$

où les b_i sont les amplitudes des différents états de projection. Par analogie avec les états de polarisation du photon (également une particule de spin 1), on dit qu'un quarkonium de spin 1 possède une polarisation transverse si $b_0 = 0$, et à contrario une polarisation longitudinale si $b_+ = b_- = 0$.

En pratique, on étudie souvent les quarkonia dans leur mode de désintégration en paire lepton-antileptons chargés, comme $J/\psi \to \mu^+\mu^-$, ce qui est le cas de ce travail de thèse. Le repérage de la paire de dilepton dans le centre de masse du quarkonium se fait via les coordonnées sphériques définies par rapport à l'axe de référence z et en considérant que le plan de production [1] est (x, z), comme illustré sur la figure 1 (gauche). Comme cette désintégration est gouvernée par l'interaction électromagnétique, la conservation de l'hélicité en QED (électrodynamique quantique) pour des particules de masse négligeable conduit à écrire la distribution angulaire de désintégration en dilepton de quarkonia produits dans des collisions hadroniques sous la forme [1] :

$$W(\cos\theta, \varphi) \propto \frac{\mathcal{N}}{3 + \lambda_\theta} \left[1 + \lambda_\theta \cos^2\theta + \lambda_\varphi \sin^2\theta \cos(2\varphi) + \lambda_{\theta\varphi} \sin(2\theta) \cos\varphi\right], \qquad (2)$$

avec $\mathcal{N} = |a_+|^2 + |a_0|^2 + |a_-|^2$, et où chaque a_i est relié à l'amplitude correspondante b_i via des éléments de matrices de rotation qui connectent les états de moment cinétique de l'axe de référence z à l'axe de la paire de dilepton dans le centre de masse du quarkonium. Les quantités λ_i sont appelées paramètres de polarisation du quarkonium et sont reliées aux a_i par : $\lambda_\theta = \frac{\mathcal{N} - 3|a_0|^2}{\mathcal{N} + |a_0|^2}$, $\lambda_\varphi = \frac{2\mathrm{Re}[a_+^* a_-]}{\mathcal{N} + |a_0|^2}$, $\lambda_{\theta\varphi} = \frac{\sqrt{2}\mathrm{Re}[a_0^*(a_+ - a_-)]}{\mathcal{N} + |a_0|^2}$. Ces paramètres ne peuvent pas prendre n'importent quelles valeurs, les contraintes théoriques sont : $-1 \leq \lambda_\theta \leq 1$, $-1 \leq \lambda_\varphi \leq 1$, $-\frac{1}{\sqrt{2}} \leq \lambda_{\theta\varphi} \leq \frac{1}{\sqrt{2}}$, sachant que les contraintes sur λ_φ et $\lambda_{\theta\varphi}$ dépendent de la valeur de λ_θ.

D'un point de vue expérimental, lorsque la statistique de telles désintégrations est trop limité, on se contente d'étudier les distributions angulaires unidimensionnelles,

1. Le plan de production est défini par l'axe des faisceaux et l'impulsion du quarkonium dans le référentiel du laboratoire.

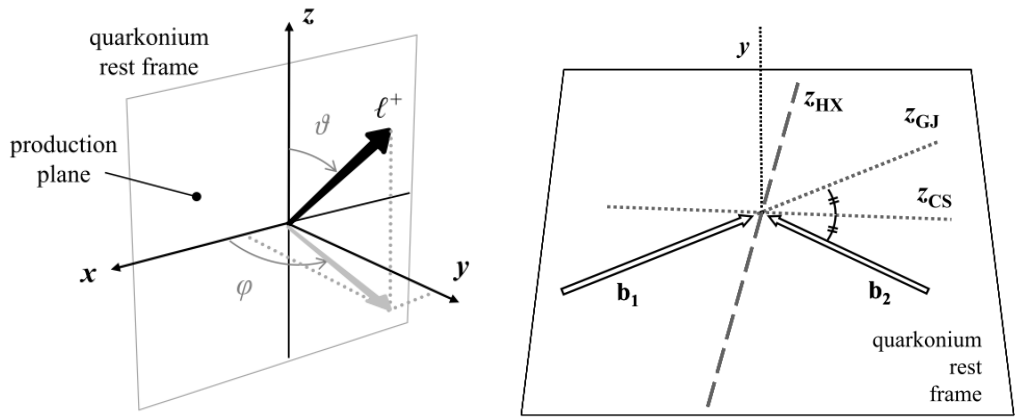

FIGURE 1 – Gauche : définition des axes dans le référentiel du quarkonium et des angles de désintégration en dilepton. Droite : définition des différents axes de référence pour l'étude de la polarisation, avec HX = repère d'Hélicité, CS = repère de Collins-Soper, et GJ = repère de Gottfried-Jackson.

i.e. intégrées sur une variable angulaire :

$$W(\cos\theta) \propto \frac{1}{3+\lambda_\theta}[1+\lambda_\theta \cos^2\theta], \tag{3}$$

$$W(\varphi) \propto 1 + \frac{2\lambda_\varphi}{3+\lambda_\theta}\cos(2\varphi), \tag{4}$$

$$W(\tilde{\varphi}) \propto 1 + \frac{\sqrt{2}\lambda_{\theta\varphi}}{3+\lambda_\theta}\cos\tilde{\varphi}. \tag{5}$$

avec $\tilde{\varphi} = \varphi \quad \frac{3}{4}\pi$ si $\cos\theta < 0$ et $\tilde{\varphi} = \varphi \quad \frac{1}{4}\pi$ si $\cos\theta > 0$. La figure 2 présente les distributions angulaires dans les limites des paramètre λ_i. Les valeurs extrêmes du principal paramètre de polarisation λ_θ correspondent aux cas d'une polarisation entièrement transverse ($\lambda_\theta = 1$) ou longitudinale ($\lambda_\theta = \quad 1$).

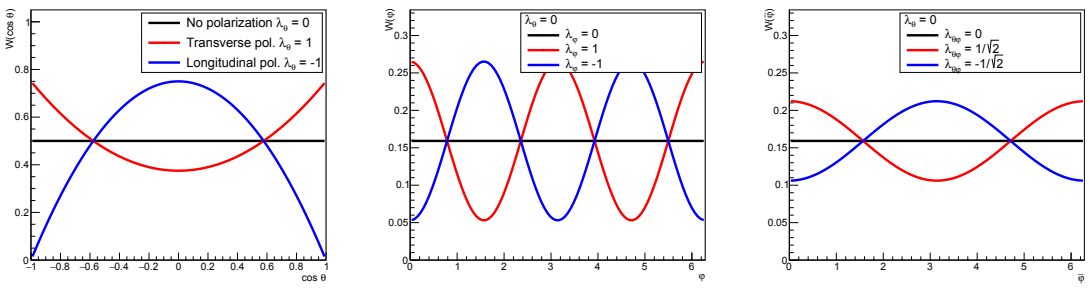

FIGURE 2 – Distributions angulaires théoriques d'une paire de leptons issue de la désintégration d'un quarkonium : $W(\cos\theta)$ pour $\lambda_\theta = \quad 1$, 0 ou 1 (gauche), $W(\varphi)$ pour $\lambda_\theta = 0$ et $\lambda_\varphi = \quad 1$, 0 ou 1 (milieu), et $W(\tilde{\varphi})$ pour $\lambda_\theta = 0$ et $\lambda_{\theta\varphi} = \quad \frac{1}{\sqrt{2}}$, 0 ou $\frac{1}{\sqrt{2}}$ (droite).

Une méthode alternative consiste à étudier des asymétries de comptage de populations entre différentes topologies de désintégrations :

$$\frac{N(|\cos\theta| > 1/2) - N(|\cos\theta| < 1/2)}{N(|\cos\theta| > 1/2) + N(|\cos\theta| < 1/2)} = \frac{3}{4}\frac{\lambda_\theta}{3+\lambda_\theta}, \tag{6}$$

$$\frac{N(\cos(2\varphi) > 0) - N(\cos(2\varphi) < 0)}{N(\cos(2\varphi) > 0) + N(\cos(2\varphi) < 0)} = \frac{2}{\pi}\frac{2\lambda_\varphi}{3+\lambda_\theta}, \tag{7}$$

$$\frac{N(\sin(2\theta)\cos\varphi > 0) - N(\sin(2\theta)\cos\varphi < 0)}{N\sin(2\theta)\cos\varphi > 0) + N(\sin(2\theta)\cos\varphi < 0)} = \frac{2}{\pi}\frac{2\lambda_{\theta\varphi}}{3+\lambda_\theta}. \tag{8}$$

La mesure des paramètres de polarisation d'un quarkonium par rapport à un seul axe de référence n'est pas suffisante pour obtenir une interprétation non ambiguë. Plusieurs axes de référence ont été proposés pour effectuer cette étude, comme représenté sur le figure 1 (droite). Les repères d'Hélicité (HX) et de Collins-Soper (CS) sont les plus "orthogonaux" et donc les plus complémentaires. C'est pourquoi l'analyse des données présentée dans cette thèse porte sur ces deux axes de référence.

De plus, comme les différents axes de référence sont reliés par des rotations, il est possible de former des quantités invariantes par changement de repère. Leur étude systématique contribue à vérifier qu'il n'y a pas de biais d'analyse. Les auteurs de la référence [1] préconisent d'étudier la quantité :

$$\tilde{\lambda} = \frac{\lambda_\theta + 3\lambda_\varphi}{1-\lambda_\varphi}. \tag{9}$$

Notons que la mesure de la polarisation du J/ψ au LHC dans les collisions pp a déjà été reportée à une énergie $\sqrt{s} = 7$ TeV par les expériences ALICE [2], CMS [3] et LHCb [4], mais qu'aucune mesure n'a encore été présentée à $\sqrt{s} = 8$ TeV.

3 Contexte expérimental

ALICE (*A Large Ion Collider Experiment*) [5, 6] est une des quatre grandes expériences qui fonctionnent auprès du LHC au CERN. Le LHC est un accélérateur presque circulaire de 27 km creusé à environ 100 m sous terre à cheval sur la frontière franco-suisse près de Genève. Il permet d'accélérer des faisceaux de proton jusqu'à une énergie de 7 TeV, mais aussi des faisceaux d'ions lourds dans un rapport d'énergie Z/A, où Z est le nombre de charge et A le nombre de masse du noyau.

L'expérience ALICE a été conçue dans le but de caractériser le QGP formé dans les collisions d'ions lourds. La mesure des paramètres thermodynamiques, des effets collectifs, des coefficients de transport dans le QGP... nécessite de reconstruire le maximum des particules produites, jusqu'à 30 000 dans les collisions centrales Pb-Pb, et de les identifier. Pour ce faire, la collaboration ALICE a élaboré et construit un détecteur assez généraliste constitué d'une multitude de sous-détecteurs, comme

illustré sur la figure 3. L'élément central est la chambre à projection temporelle (TPC), complétée par le système de trajectographie interne (ITS), le tout baigné dans un champ magnétique selon l'axe du faisceau produit par un solénoïde. Cette partie centrale est complétée par un spectromètre à muons et de plus petits détecteurs sur l'avant dont le rôle est entre autres de déclencher sur les événements de collision de faisceaux, en particulier les paires de détecteurs T0 et V0.

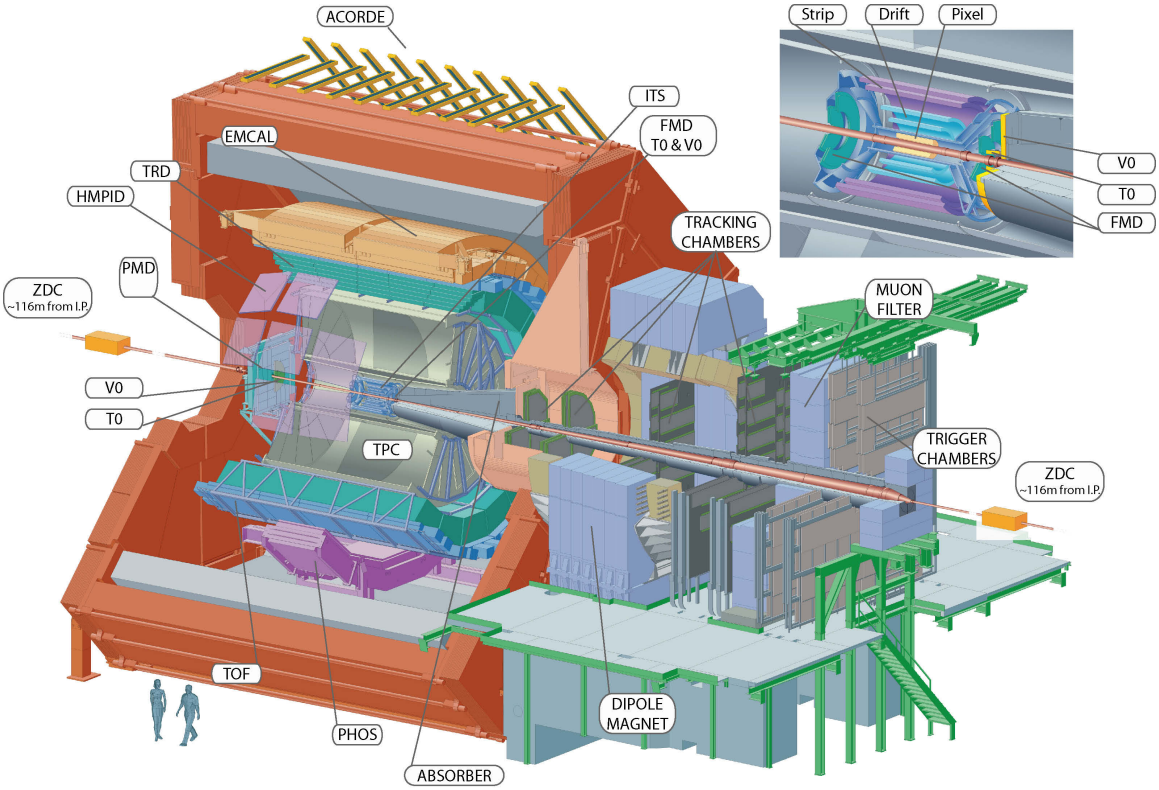

FIGURE 3 – Vue en coupe 3-D du détecteur ALICE.

Le spectromètre à muon, comme indiqué sur la figure 3, est constitué : (i) d'un absorbeur (*absorber*) proche du point d'interaction pour limiter la contamination des muon issus de la désintégration des pions et kaons, (ii) d'un système de trajectographie (*tracking chambers*) composé de cinq stations de deux chambres proportionnelles à cathodes segmentés en damier, la station du milieu étant plongée dans le champ magnétique produit par un dipôle (*dipole magnet*), (iii) un système de déclenchement (*trigger chambers*) basé sur des chambres à plaques résistives (RPCs). Les systèmes de trajectographie et de déclenchement sont séparés par un mur en fer (*muon filter*) pour finir d'atténuer le taux de hadrons au niveau du déclencheur. Enfin, un blindage autour du faisceau court sur la longueur du spectromètre à muons pour limiter la contamination en particules à bas angles et celles issues des interactions entre le faisceau et le gaz résiduel dans le tube à vide.

Chacun des quatre plans de détection du système de déclenchement des muons est

constitué de 18 RPCs (mécaniquement 9 par demi plan), chacune segmentée en bandes de lecture horizontales (dites X, pour une localisation dans le plan de déviation) et verticales (dites Y, pour une localisation dans le plan de non déviation). Ces bandes sont lues par une électronique frontale qui se base sur un ASIC, appelé ADULT (*A DUaL Threshold*) et développé au Laboratoire de Physique Corpusculaire, qui analyse en parallèle huit voies de lecture. Elle a été développée pour un fonctionnement intial des RPCs en mode *streamer*, i.e. sans amplification du signal du détecteur, mais permet un fonctionnement en mode maxi-avalanche. Les 21 000 voies de l'électronique frontale délivrent à une électronique intelligente, appelée locale, un signal logique qui spécifie si la voie a été touchée ou pas. Du point de vue de cette électronique, les plans de détection du système de déclenchement sont segmentés en 234 zones, i.e. 234 cartes locales, homothétiques par rapport au point d'interaction. Chacune des cartes locales reçoit les signaux logiques X et Y des quatre plans de détection, et délivre des décisions de déclenchement avec un seuil en impulsion transverse (p_{T}) en se basant sur la déviation de la trace entre les deux stations, par rapport à une trace d'impulsion infinie, i.e. qui vient droit du point d'interaction.

4 Évaluation de la nouvelle électronique frontale (FEERIC) des RPCs du déclencheur à muons

Pour le run-3 du LHC (à partir de 2020), des améliorations de l'accélérateur sont prévues pour augmenter la luminosité, et en conséquence le potentiel de physique, que ce soit pour l'étude des canaux rares, comme le $\psi(2\mathrm{S})$, ou pour pouvoir augmenter la sensibiliter des mesures à haut p_{T}. Afin de faire face à l'augmentation du taux de collisions, les collaborations ont programmé une mise à jour de leurs détecteurs, et en particulier l'électronique associée.

Au niveau du système de déclenchement à muons, une nouvelle électronique frontale a été mise au point pour permettre un fonctionnement des RPCs en mode avalanche, le but étant de limiter la "taille" des décharges électriques associées aux signaux et donc de limiter leur vieillissement. Pour ce faire un étage d'amplification est nécessaire, et une nouvelle électronique a été développée au Laboratoire de Physique Corpusculaire, le circuit s'appelle FEERIC (*Front-End Electronics Rapid Integrated Circuit*). Cet ASIC a dans un premier temps été testé sur le banc de test des RPCs à Turin. La courbe d'efficacité obtenue sur la figure 4 illustre parfaitement le mode de fonctionnement avalanche, comparé à la version ADULT de l'électronique pour laquelle la haute tension d'alimentation est typiquemement 600 V plus importante, i.e. dans le mode maxi-avalanche.

Durant le long arrêt du LHC entre le run-1 et le run-2 (en 2013-14), une des 72 RPC du système de déclenchement à muons a été équipée avec la nouvelle électronique. Une étude des performances de cette RPC, appelée RPC-FEERIC, a été rélisée en 2015 avec les premiers faisceaux à la nouvelle énergie de 6.5 TeV. Dans un premier

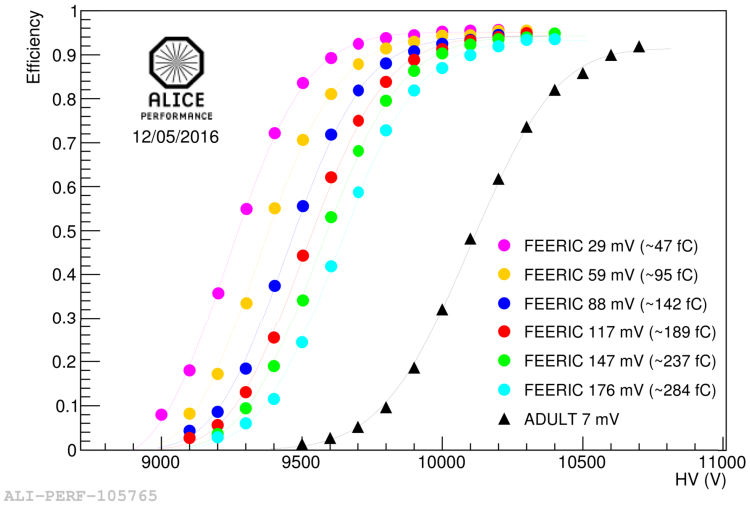

FIGURE 4 – Efficacité d'une RPC en fonction de la tension d'alimentation avec l'ancienne électronique ADULT fonctionnant en mode maxi-avalanche, et avec la nouvelle électronique FEERIC pour différentes valeurs de seuils (les valeurs entre parenthèses donnent la charge correspondante).

temps, un scan de la haute tension pour trois valeurs de seuils de détection (70, 105 et 140 mV) – voir la figure 5 – a permis d'optimiser le point de fonctionnement. La mesure de l'efficacité d'un plan de détection utilise la redondance des 4 plans en sélectionnant les traces qui déclenchent les 3 autres plans (le plan étudié est exclue), puis en comptant le nombre de particules détectées par le plan d'étude i, soit $\epsilon_i = N_{4/4}/N^i_{3/4}$. Comme attendu, plus le seuil de détection est élevé, plus la haute tension de fonctionnement est importante, cette dernière étant définie comme 400 V au-dessus du point à 90% d'efficacité. L'étude en parallèle de la taille des clusters – le nombre de bandes de lectures consécutives touchées par le passage d'une particule – ne montre pas de dégradation notoire lorsqu'on décroit le seuil, du moins pour les valeurs testées. Et comme le but est avant tout de limiter la charge dans la RPC, il a été décidé de fonctionner avec les seuils à 70 mV, en fixant le haute tension d'alimentation à 9375 V.

La quantification du gain en terme de diminution de la charge produite dans la RPC est estimée via le rapport du courant moyen I_{RPC} de l'alimentation haute tension sur un run et du taux de particules f_{part} traversant la RPC, soit $q_{\mathrm{hit}} = I_{\mathrm{RPC}}/f_{\mathrm{part}}$. Le courant est monitoré pendant les prises de données et sa valeur est enregistrée dans une base de données chaque fois qu'elle change ; le courant moyen est donc le courant intégré sur un run divisé par la durée du run. Le nombre de particules qui traversent une RPC est intégré par des échelles de comptage et enregistré dans une base de données avec une périodicité d'environ dix minutes pendant le run. Le taux moyen de particules qui ont traversé la RPC pendant le run s'obtient en divisant les échelles de comptage par leur périodicité de lecture, sous une forme intégrée sur toute

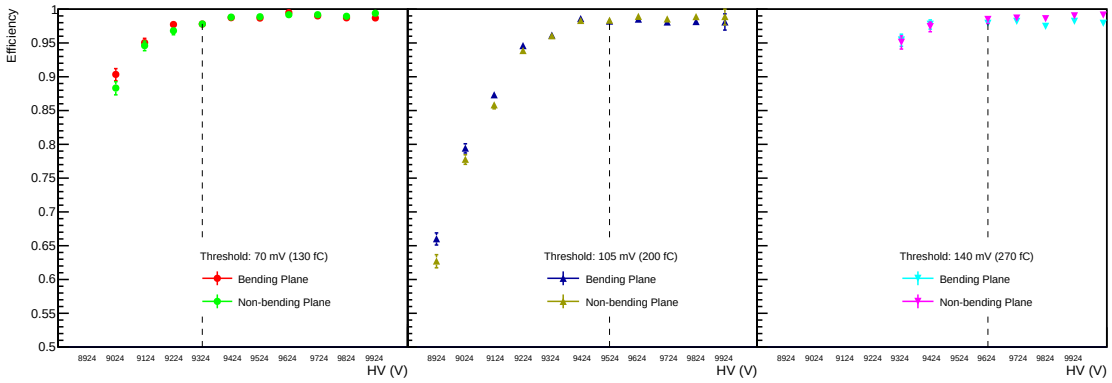

FIGURE 5 – Courbes d'efficacité de la RPC-FEERIC pour chacun des plans (dévition et non déviation) pour trois valeurs de seuil de détection : 70 mV (gauche), 105 mV (milieu) et 140 mV (droite).

la durée du run. La charge moyenne produite par hit q_{hit} obetnue est illustrée sur la figure 6 pour les runs enregistrés en juillet et août 2015. On note que la charge produite par hit est en moyenne environ 5 fois plus faible dans la RPC-FEERIC que dans les RPC-ADULT.

Ce résultat permettra de compenser l'augmentation de la luminosité du LHC à partir du run-3 en terme de viellissement des RPCs du système de déclenchement à muons.

5 Analyse de la polarisation du J/ψ

L'analyse concerne les données enregistrées fin 2012 lors de collisions proton-proton à une énergie dans le centre de masse $\sqrt{s} = 8$ TeV dans un mode de collisions dit faisceau-satellite. Le taux d'interactions était aux alentours de 200 kHz (il décroissait pendant le fill) et le mode de déclenchement des 270 runs analysés était basé sur la présence d'une paire de muons de signes opposés passant le seuil d'impulsion transverse dit low-$p_{\text{T}} \approx 1$ GeV.

L'analyse de la polarisation du J/ψ consiste en la reconstruction des distributions angulaires de désintégration dans le centre de masse du J/ψ – $W(\cos\theta)$, $W(\varphi)$ et $W(\tilde{\varphi})$ – selon un axe de référence : Hélicité (HX) ou Collins-Soper (CS). Ces distributions sont ensuite ajustées par les distributions théoriques des équations 3, 4 et 5. La stratégie d'analyse s'effectue donc selon les étapes suivantes.

1. Comme le canal de désintégration étudié est J/$\psi \to \mu^+\mu^-$, on commence par sélectionner des paires de muons de signes opposés en appliquant une série de coupures qui permettent de conserver autant que faire se peut les muons issues des J/ψ, tout en rejetant les muons des autres sources (mauvaises identification

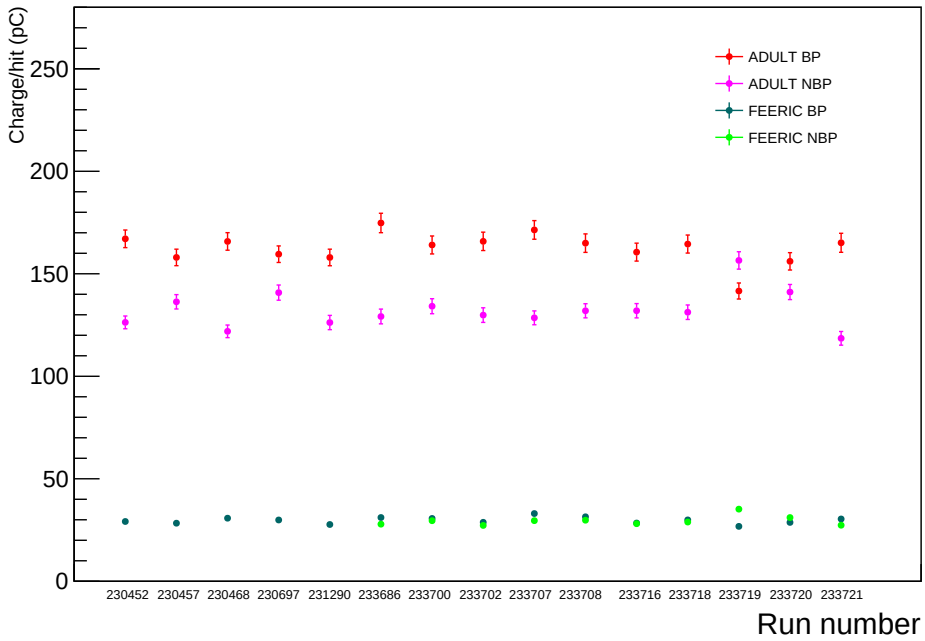

FIGURE 6 – Charge moyenne par hit produite dans les RPC : pour l'ensemble des RPC équipées de l'électronique ADULT, et pour la RPC-FEERIC (les valeurs pour les plans de déviation et de non déviation sont séparées).

de hadrons, muons produits par la désintgration des pions et kaons, ou même du charme et de la beauté ouverte, ...).

2. Le spectre de masse invariante des candidats $\mu^+\mu^-$ est ensuite construit et ajusté par une fonction qui permet de décrire la forme du signal J/ψ, ainsi que l'état excité voisin ψ(2S), mais aussi le bruit de fond. Les fonctions utilisées par défaut sont une Cristal Ball (CB2) étendue pour chacune des deux résonances J/ψ et ψ(2S), et une gaussienne de largeur variable (VWG) pour le bruit de fond. Le nombre de paramètres libres dans l'ajustement (8 au total) est limité en fixant les paramètres des queues de distribution des fonctions CB2 à ce ceux de la simulation du signal, et en fixant la valeur centrale et la largeur de la fonction CB2 qui décrit le ψ(2S) à celles du J/ψ, via un facteur d'échelle de masse. Avec l'échantillon de données analysé, le nombre total de J/ψ reconstruits est $N_{\mathrm{J}/\psi} = 50\,360 \pm 289$. La figure 7 illustre cette procédure avec les deux étapes : ajustement des données de simulation pour fixer les paramètres des queues de distribution, puis ajustement des données réelles.
3. Le nombre de J/ψ ainsi obtenu est corrigé des effets d'acceptance et d'éfficacité de détection. Ces effets sont déterminés à l'aide de simulations Monte Carlo de l'ensemble de la chaîne de détection : (i) génération des événements physiques, (ii) interaction des particules dans le détecteur, (iii) reconstruction des

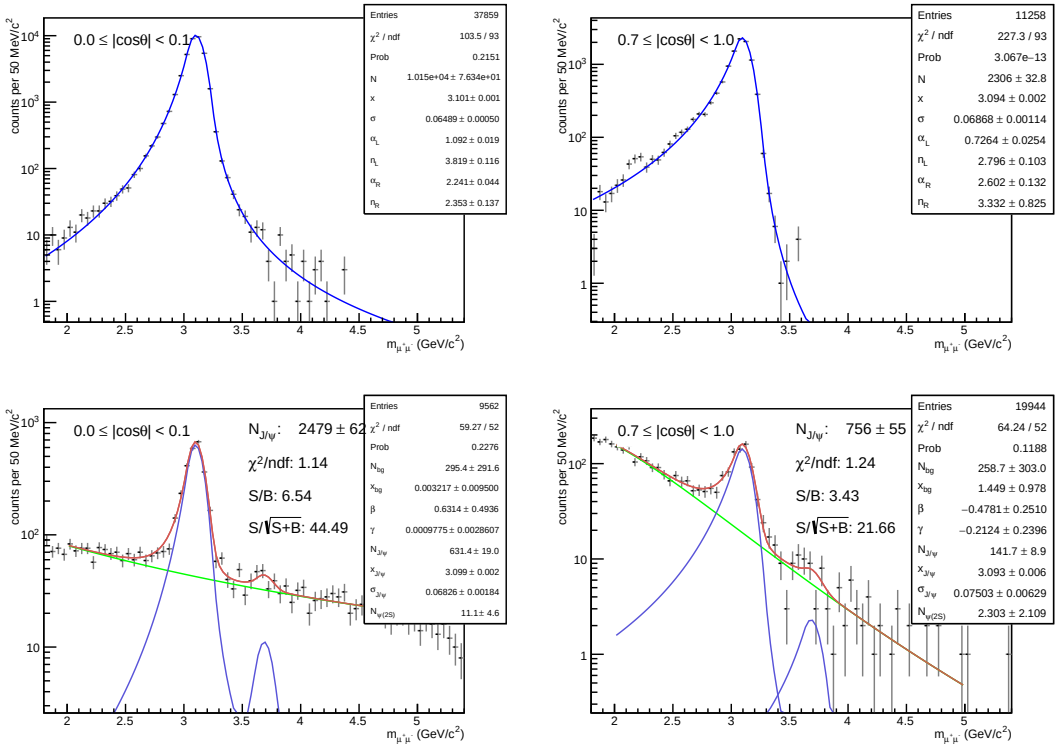

FIGURE 7 – Ajustement de la distribution en masse invariante des paires de muons de signes opposés dans l'intervalle de rapidité $2.5 < y < 4.0$ et d'impulsion transverse $3 < p_{\mathrm{T}} < 4$ GeV/c pour $0 \leq |\cos\theta| < 0.1$ (gauche) et $0.7 \leq |\cos\theta| < 1.0$ (droite) : en haut ajustement de la simulation des J/ψ et en bas ajustement des données. La qualité de l'ajustement, quantifié par le $\chi^2_{/\mathrm{ndf}}$, ainsi que le rapport signal sur bruit (S/B) et la significance ($S/\sqrt{S+B}$) sont indiqués.

traces comme pour des données réelles. Ces simulations sont faites run par run pour prendre en compte la configuration réelle du détecteur pendant les prises de données (éléments de détection off, efficacité des détecteurs, ...). Un total d'environ 3 millions de J/ψ a été simulé pour limiter les fluctuations statistiques dans la détermination de l'acceptance-efficacité ($A \times \epsilon$) qui est calculée comme le rapport du nombre de J/ψ reconstruit après application des coupures de sélection (comme pour les données réelles) et du rapport du nombre de J/ψ généré dans le domaine cinématique d'étude, i.e. dans l'intervalle $2.5 < y < 4.0$.

4. Pour effectuer une étude différentielles en impulsion transverse (p_{T}) de la polarisation du J/ψ, les deux étapes précédentes sont effectuées dans des intervalles de p_{T} prédéfinis et en intervalles de chacune des variables angulaires $\cos\theta$, φ et $\tilde{\varphi}$, et ceci dans les deux référentiels HX et CS. Le choix des différents intervalles est guidés par deux principes : avoir une granularité assez fine en variable angulaire pour être sensible aux effets de polarisation (typiquement 10 inter-

valles), et avoir dans chacun des intervalles une significance de signal de J/ψ supérieure à 5. Ces contraintes imposent de limiter l'étude à l'intervalle en impulsion transverse $2 < p_{\mathrm{T}} < 15$ GeV/c. La limite à 2 GeV/c est imposée par les effets d'acceptance-efficacité qui sont trop faibles en-dessous, tandis que la limite à 15 GeV/c est due à la statistique qui chute à haute impulsion transverse. Pour ces raisons statistiques, le choix a été de 6 intervlles en p_{T} (en GeV/c) : $[2;3)$, $[3;4)$, $[4;5)$, $[5;7)$, $[7;10)$, $[10;15)$.

5. Une fois les différentes distributions angulaires corrigées, elles sont ajustées par les fonctions $W(\cos\theta)$, $W(\varphi)$ et $W(\tilde{\varphi})$ en laissant les paramètres de polarisation du J/ψ libres : λ_θ, λ_φ et $\lambda_{\theta\varphi}$. La figure 8 illustre la correction des nombres bruts de J/ψ obtenus par l'ajustement des spsctre en masse invariante par les facteurs d'acceptance-efficacité, puis de l'ajustement de la distribution angulaire (ici $W(\cos\theta)$) pour obtenir le paramètre de polarisation correspondant (ici λ_θ dans le référentiel CS).

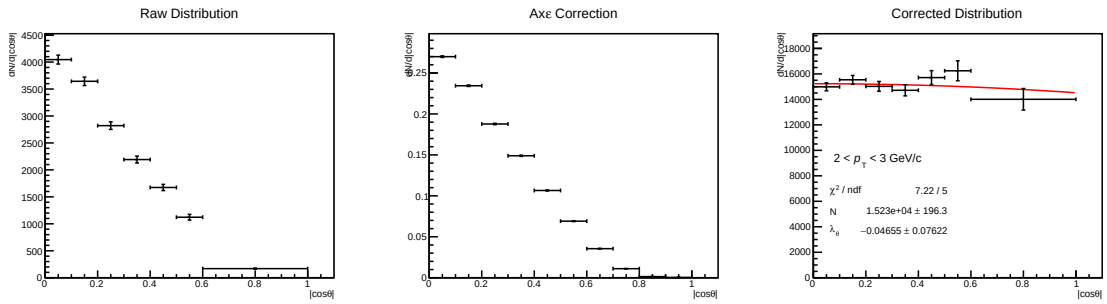

FIGURE 8 – Distribution angulaire $W(|\cos\theta|)$ pour l'intervalle $2 \leq p_{\mathrm{T}} \leq 3$ GeV/c dans le référentiel de Collins-Soper : nombre brut de J/ψ (gauche), facteur $A \times \varepsilon$ (milieu) et nombre corrigé de J/ψ (droite) avec l'ajustement par la fonction 3.

En résumé, la mesure de la polarisation du J/ψ nécessite environ $6_{p_{\mathrm{T}}\mathrm{bins}} \times 6_{\mathrm{variables}} \times 10_{\mathrm{var.bin}} = 360$ ajustements de masses invariantes, suivis de $6_{p_{\mathrm{T}}\mathrm{bins}} \times 6_{\mathrm{variables}} = 36$ ajustements de distributions angulaires.

Les mesures ainsi obtenues doivent être complétées par une étude des effets systématiques potentiels liés aux deux nombres utilisés pour construire les distributions angulaires : le nombre de J/ψ obtenu dans les donnée brutes et le facteur de correction des effets d'acceptance-efficacité.

Le nombre de J/ψ déterminé à partir des données brutes provient de la procédure d'ajustement du spectre de masse invariante des paires de muons de signes opposés. En effet, comme on pré-suppose la fonction qui permet de décrire le spectre de masse invariante, il faut montrer que le nombre de J/ψ obtenu par l'ajustement n'est pas dépendant de ce choix. Pour cela, une fonction alternative pour décrire le signal, la fonction dite NA60, et une autre pour décrire le bruit de fond, le produit d'une gaussienne et d'une exponentielle, ont été utilisées succesivement dans la fonction globale

d'ajustement. Les limites du domaine d'ajustement en masse invariante ont également été variées ; l'intervalle par défaut $[2; 5]$ GeV/c^2 à été soit agrandi $[1.5; 6]$ GeV/c^2, soit restreint $[2.2; 4.5]$ GeV/c^2. À chaque fois, l'analyse est conduite jusqu'au bout, et la moyenne des paramètres de polarisation correspond à la moyenne obtenues par les cinq ajustement, la somme quadratique des écarts à la valeur moyenne est une estimation de l'incertitude systématique associée à cette valeur moyenne. À cela s'ajoute l'incertitude statistique retournée par l'ajustement. La figure 9 (gauche) illustre cet effet systématique, ainsi que l'incertitude statistique dans le cas du paramètre λ_θ dans le référentiel CS.

Le facteur de correction des effets d'acceptance-efficacité est relié à la simulation Monte Carlo utilisée. Dans ce cas, il convient de modifier les paramétrisations à priori utilisées pour décrire la physique de la production et de la désintégration des J/ψ , mais aussi la réponse du détecteur.
Les paramétrisations utilisées reproduisent les spectres en impulsion transverse et en rapidité des J/ψ mesurés par l'expérience ALICE [7], leur polarisation est supposée nulle dans la simulation et leur mode de désintégration en dimuon inclue une fraction de désintégrations radiatives, soit $\mathrm{J}/\psi \to \mu^+\mu^-(\gamma)$, telle que mesurée dans le canal diélectron $\mathrm{J}/\psi \to e^+e^-(\gamma)$ corrigé d'un facteur de masse prédit théoriquement [10]. En pratique, la simulation est changée en appliquant à chacun des événements un poids w défini par le rapport de nouvelle distribution f_{new} et de la distribution par défaut f_{def}, soit $w_i = f_{\mathrm{new}}(i)/f_{\mathrm{def}}(i)$, cette procédure étant mise en œuvre en fonction de la variable cinématique d'intérêt i, par exemple la rapidité y, l'impulsion transverse p_{T} ... La figure 9 (droite) illustre l'effet systématique associé à la variation de la paramétrisation en rapidité et en impulsion transverse des J/ψ dans la simulation (paramétrisation standard pour $\sqrt{s} = 5$ TeV, au lieu de $\sqrt{s} = 8$ TeV par défaut).
L'effet de détecteur dominant pour cette analyse est la façon dont la réponse hardware du déclencheur à muon est simulée, i.e. la coupure en ligne pour la sélection en p_{T} par le système de déclenchement. L'étude de cette efffet systématique a été menée en sélectionnant des muons simples enregistrées durant la même période de prise de données, mais en configuration de déclenchement sans biais, i.e. sans appliquer la coupure low-p_{T}. Ces muons permettent de mesurer la réponse du déclencheur à muon pour la coupure low-p_{T} directement sur les données en construisant le rapport low-p_{T}/all-p_{T} en fonction de l'impulsion transverse des muons (avec all-p_{T} qui représente tous les muons vus par le système de déclenchement). La comparaison de cette distribution à celle de la simulation permet d'estimer l'incertitude associée sur la mesure des paramètres de polarisation du J/ψ.

6 Résultats et discussion

Les mesures des trois paramètres de polarisation – λ_θ, λ_φ et $\lambda_{\theta\varphi}$ – en fonction de l'impulsion transverse du J/ψ dans les deux référentiels (CS et HX) sont présentées sur la figure 10. Les incertitudes systématiques représentées sur cette figure sont

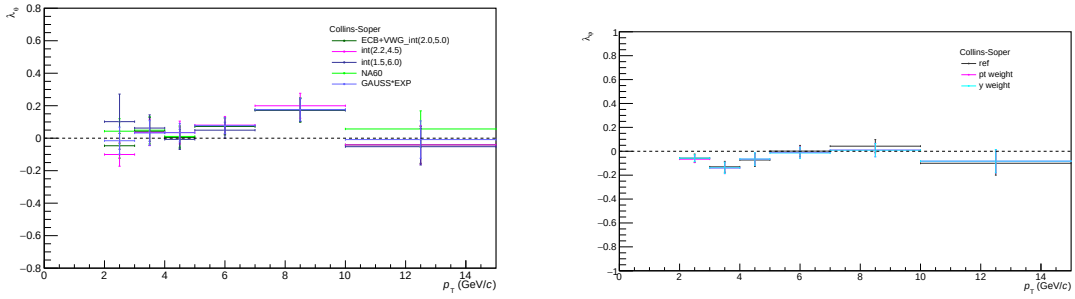

FIGURE 9 – λ_θ dans le référentiel de Collins-Soper en fonction de p_{T} : pour les différents ajustements du spectre en masse (gauche), pour les différentes paramétrisations en rapidité et en impulsion du J/ψ(droite).

une combinaison non corrélées des différents effets. En première approximation, les données n'indiquent aucune polarisation, en tenant compte des incertitudes, sur tout le domaine en impulsion transverse. Seuls les points à haute impulsion transverse ($10 \leq p_{\mathrm{T}} \leq 15$ GeV/c) dans le référentiel d'Hélicité indiquent un écart à zéro de l'ordre de 2 σ. Pour conforter les résultats, l'analyse a été menée avec la méthode du comptage des populations dans les deux configurations topologiques présentée dans les équations 6, 7 et 8 ; et un très bon accord a été trouvé. Ces résultats correspondent à la polarisation des J/ψ produits de façon inclusive dans les collisions pp à $\sqrt{s} = 8$ TeV dans lintervalle de rapidité $2.5 < y < 4.0$. En effet, le spectromètre à muons de l'expérience ALICE ne permet pas de séparer les muons issus du point d'interaction (dits "prompt") de ceux provenant de la désintégration des hadrons beaux (dits "b-hadron" ou "non-prompt"), i.e. associés à un vertex déplacé dans la désintégration $B \to \mathrm{J}/\psi + X$.

Or les modèles théoriques prédisent en premier lieu la composante "prompt". Une correction de la mesure inclusive est donc nécessaire pour que la confrontation aux modèles soit pertinente. Pour ce faire, les mesures effectuées par la collaboration LHCb ont été utilisées. En effet, le détecteur LHCb est capable de séparer les composantes "prompt" et "b-hadron". Leur mesure (différentielle en p_{T}) est en moyenne d'environ 12% de "b-hadron" sur l'ensemble des J/ψ inclusifs [11]. La prise en compte de cette fraction en fonction de l'impulsion transverse du J/ψ se fait au niveau de l'ajustement de la distribution angulaire $\alpha = \cos\theta$ (ou φ ou $\tilde{\varphi}$) en introduisant la fraction f_b de "b-hadron" avec une polarisation λ^b fixe :

$$W(\alpha; N, \lambda) = N \left[W_{\mathrm{prompt}}(\alpha; \lambda) + f_b \, W_{\mathrm{b-hadron}}(\alpha; \lambda^b) \right],$$

où N est un paramètre de normalisation, tandis que les fonctions W_{prompt} et $W_{\mathrm{b-hadron}}$ correspondent aux distributions angulaires théoriques 3, 4 et 5. La polarisation de la composante "b-hadron" est fixée aux valeurs suivantes : $\lambda_\theta^b = 0.0 \pm 0.2$, $\lambda_\varphi = 0$ et $\lambda_{\theta\varphi} = 0$. Ces valeurs sont guidées par deux constatations. D'une part, les effets

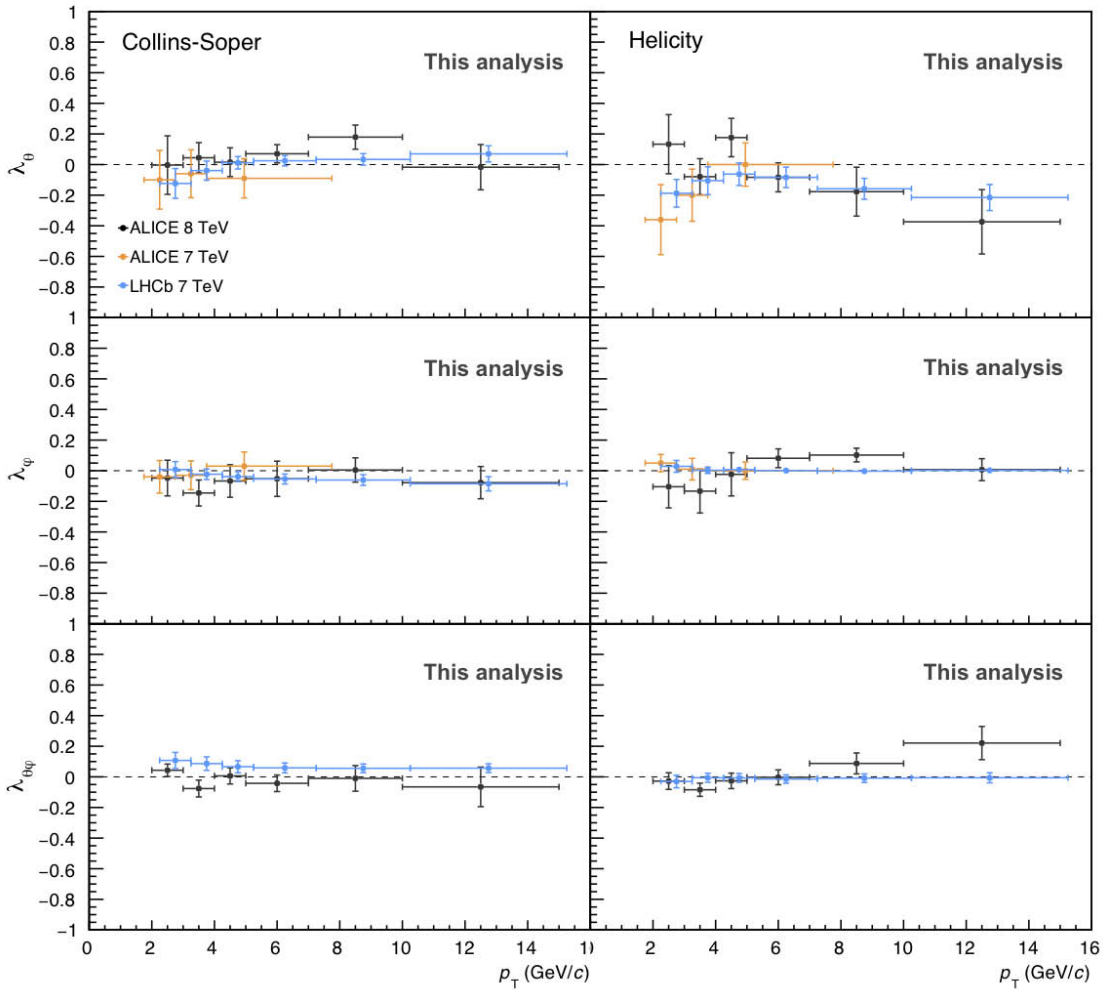

FIGURE 10 – Paramètres de polarisation des J/ψ inclusifs ($2.5 < y < 4.0$) en fonction de leur impulsion transverse : de haut en bas λ_θ, λ_φ et $\lambda_{\theta\varphi}$ mesurés dans le référentiel de Collins-Soper (gauche) et d'Hélicité (droite). Les barres correspondent aux incertitudes statistiques, tandis que les boîtes représentent l'ensemble des incertitudes systematiques.

de polarisation sont dilués dans le processus de désintégration $B \to \mathrm{J}/\psi + X$ car l'axe de référence utilisé n'est pas correct (celui du J/ψ au lieu de celui du hadron beau). D'autre part, la collaboration CDF a mesuré une valeur λ_θ^b compatible avec zéro. L'intervalle de 0.2 autour de zéro a été choisi pour λ_θ^b, car c'est l'intervalle typique indiqué par les données inclusives (figure 10). Les mesures des trois paramètres de polarisation pour les J/ψ "prompt" dans les deux référentiels (CS et HX) sont présentées sur la figure 11. Ces mesures présentent les incertitudes totales (statistiques et systématiques additionnées en quadrature) et sont comparées aux mesures

existantes à une énergie de $\sqrt{s} = 7$ TeV obtenues par ALICE [2] et LHCb [4]. Les prédictions théoriques indiquent qu'une différence mineure est attendue entre les deux énergies $\sqrt{s} = 7$ ou 8 TeV. On note que les résultats obtenus dans cette thèse sont en accord avec les résultats déjà publiés par la collaboration ALICE, mais sont plus complets car ils intègrent le paramètre $\lambda_{\theta\varphi}$ et couvrent un intervalle en impulsion transverse plus important $2 \leq p_{\mathrm{T}} \leq 15$ GeV/c. Par ailleurs, les résultats sont en bon accord avec ceux de l'expérience LHCb, même si on note des tensions de l'ordre de $2\ \sigma$ entre certains points. On remarque également un décalage systématique entre les deux séries de points pour la distribution $\lambda_{\theta\varphi}$ dans le référentiel de Collins-Soper.

La quantité invariante par changement de référentiel $\tilde{\lambda}$ a été calculée en considérant les incertitudes statistiques entre λ_θ et λ_φ comme corrélées et les incertitudes systématiques comme non corrélées. Les résultats sont présentés sur la figure 12 ; il montrent que les données vérifient cette invariance par changement de référentiel dans les incertitudes, ce qui renforce les résultats en montrant qu'il n'y a à priori pas de biais d'analyse.

Les données de cette thèse ont également été comparées aux prédictions théoriques, aussi bien pour chacun des paramètres de polarisation sur la figure 13 que pour la quantité invariante par changement de référentiel sur la figure 12. Les modèles présentés sont le Color Singlet Model (CSM, en bleu) et l'approche NRQCD (en rose) calculés à l'odre NLO [13], et d'une autre prédiction de NRQCD à NLO (en vert) [14] (uniquement pour $5 \leq p_{\mathrm{T}} \leq 15$ GeV/c). La différence entre les deux prédictions NRQCD provient du jeu de données utilisées pour déterminer les éléments de matrice (LDMEs) qui encodent les effets non perturbatifs de QCD.

On note qu'aucun des modèles n'est capable de reproduire l'ensemble des données, i.e. à la fois les trois paramètres de polarisation (λ_θ, λ_φ et $\lambda_{\theta\varphi}$) dans les deux référentiels (CS et HX) et sur tout le domaine en impulsion transverse ($2 \leq p_{\mathrm{T}} \leq 15$ GeV/c). La seule prédiction théorique capable de décrire à peu près les données est celle de NRQCD de la ref. [14], mais cela ne concerne que trois points – il existe uniquement une prédiction pour le paramètre λ_θ, seulement dans le référentiel HX et pour $p_{\mathrm{T}} > 15$ GeV/c. Par ailleurs, on note que les prédictions théoriques, aussi bien du CSM que de NRQCD, sont incapables de reproduire la quantité invariante $\tilde{\lambda}$, même si NRQCD semble être en moins mauvais désaccord.

Enfin, une intégration sur l'intervalle en impulsion transverse permet d'estimer la valeur intégrée des paramètres de polarisation. Pour ce faire, on calcule la moyenne pondérée par la section efficace différentielle en p_{T} pour la composante "prompt". Ce calcul a été fait en utilisant la section efficace inclusive σ^{inc} mesurée par ALICE à $\sqrt{s} = 8$ TeV [7], en la corrigeant de la fraction de "b-hadron" mesurée par LHCb [11] :

$$\langle\lambda\rangle = \frac{1}{\sigma_{\mathrm{tot}}} \sum_j \sigma_j \lambda^j,$$

où σ_j est la section efficace de la composante "prompt" dans le $j^{\text{ème}}$ bin en p_{T}, soit $\sigma_j = (1 - f_b)\sigma_j^{\mathrm{inc}}$ et λ^j le paramètre de polarisation dans le même bin, tandis que $\sigma_{\mathrm{tot}} = \sum_j \sigma_j$, tout cela pour les 6 bins en p_{T} de cette analyse. Les valeurs intégrées

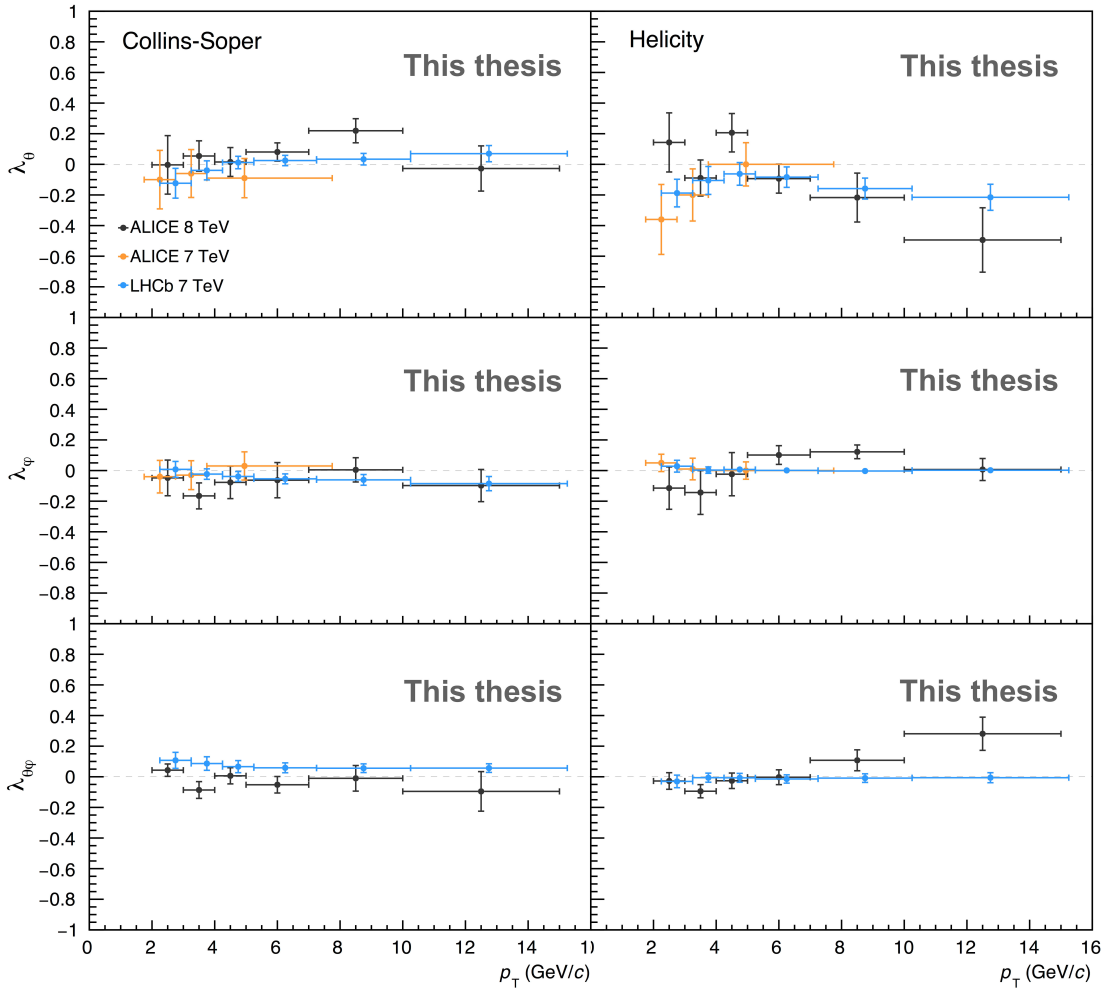

FIGURE 11 – Paramètres de polarisation des J/ψ "prompt" ($2.5 < y < 4.0$) en fonction de leur impulsion transverse : de haut en bas λ_θ, λ_φ et $\lambda_{\theta\varphi}$ mesurés dans le référentiel de Collins-Soper (gauche) et d'Hélicité (droite). Les barres correspondent aux incertitudes totales. Les données à $\sqrt{s} = 8$ TeV de cette thèse (points noirs) sont comparés aux résultats à $\sqrt{s} = 7$ TeV de ALICE [2] (points verts, décalés de -0.25 GeV/c) et de LHCb [4] (points bleus, décalés de $+0.25$ GeV/c).

des paramètres de polarisation des J/ψ "prompt" sur l'intervalle $2 < p_{\mathrm{T}} < 15$ GeV/c et $2.5 < y < 4$ sont :

$$\langle\lambda_\theta^{\mathrm{CS}}\rangle = 0.031 \pm 0.092 \qquad \langle\lambda_\theta^{\mathrm{HX}}\rangle = 0.048 \pm 0.096$$
$$\langle\lambda_\varphi^{\mathrm{CS}}\rangle = -0.083 \pm 0.060 \qquad \langle\lambda_\varphi^{\mathrm{HX}}\rangle = -0.078 \pm 0.075$$
$$\langle\lambda_{\theta\varphi}^{\mathrm{CS}}\rangle = -0.009 \pm 0.025 \qquad \langle\lambda_{\theta\varphi}^{\mathrm{HX}}\rangle = -0.035 \pm 0.028$$

Ces valeurs sont compatibles avec zéro indiquant clairement qu'en moyenne les J/ψ

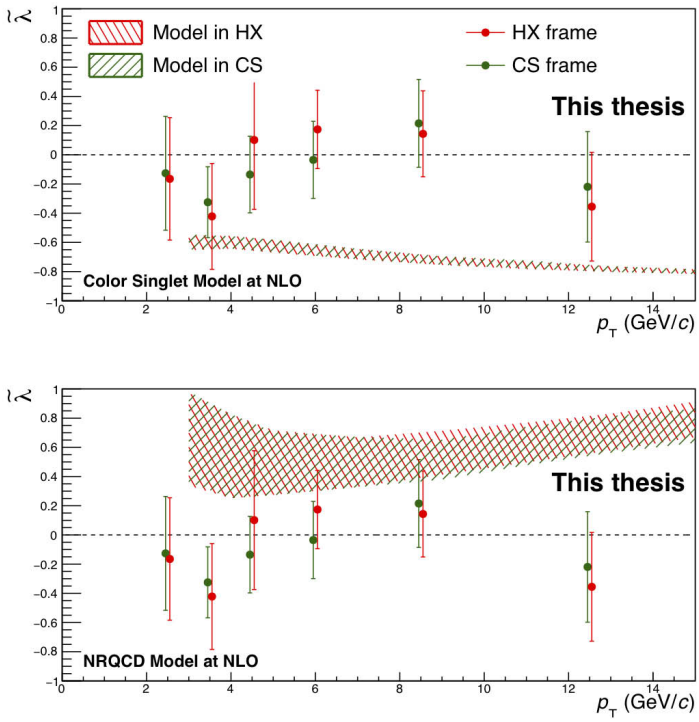

FIGURE 12 – Quantité invariante $\tilde{\lambda}$ en fonction de p_T mesurée dans les référentiels de Collins-Soper (vert) et d'Hélicité (rouge, point décalés de +0.25 GeV/c) : les données sont comparées aux prédictions du CSM (haut) et de NRQCD (bas) [13].

"prompt" ne sont pas polarisés. La figure 14 présente ces résultats dans les plans 2-D des espaces accessibles théoriquement.

Pour conclure, les résultats présentés dans cette thèse sont originaux pour plusieurs raisons. Ils présentent les premières mesures de polarisation du J/ψ dans les collisions proton-proton à une énergie $\sqrt{s} = 8$ TeV et ils montrent pour la première fois une comparaison de la quantité invariante $\tilde{\lambda}$ avec les prédictions théoriques. De façon générale, la confrontation des résultats obtenus avec les prédictions théoriques indique très clairement que le mécanisme de production des quarkonia dans les collisions "basiques" proton-proton n'est pas un problème résolu.

Références

[1] P. Faccioli et al., Eur. Phys. J C (2010) 69 : 657-673.

[2] ALICE Collboration, Phys. Rev. Lett. 108, 082001 (2012).

[3] CMS Collaboration, Phys. Lett. B 727 (2013) 381-402.

[4] LHCb Collaboration, Eur. Phys. J. C (2013) 73 :2631.

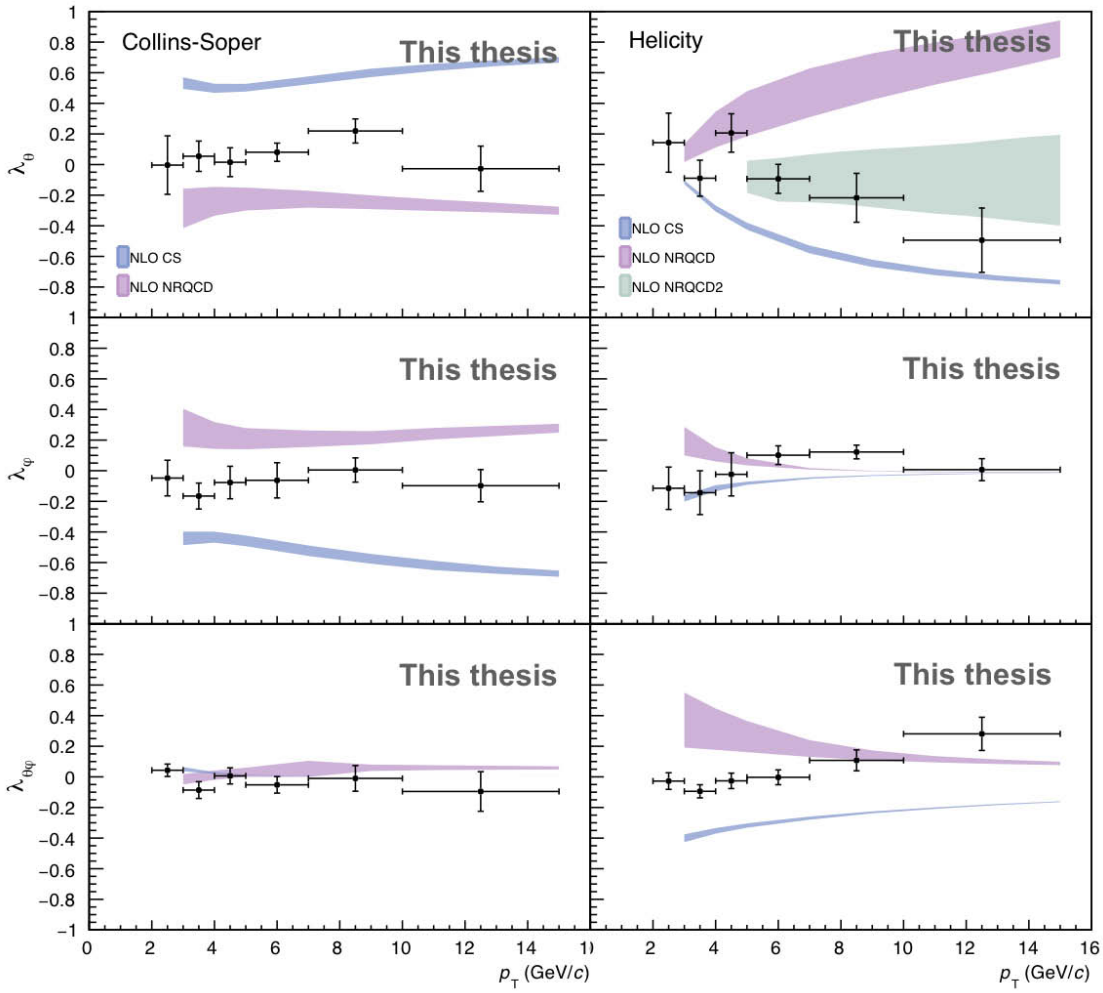

FIGURE 13 – Paramètres de polarisation des J/ψ "prompt" ($2.5 < y < 4.0$) en fonction de leur impulsion transverse : de haut en bas λ_θ, λ_φ et $\lambda_{\theta\varphi}$ mesurés dans le référentiel de Collins-Soper (gauche) et d'Hélicité (droite). Les barres correspondent aux incertitudes totales ; les modèles sont décrits dans le texte.

[5] ALICE Collaboration, JINST, 3 :S08002, 2008.

[6] ALICE Collaboration, Int. J. Mod. Phys. A29 :1430044, 2014.

[7] ALICE Collaboration, Eur. Phys. J. C (2016) 76 :184.

[8] *Measurement of inclusive charmonium production cross section at forward rapidity in pp collision at* $\sqrt{s} = 8$ *TeV*, ALICE-ANA-2015-2400.

[9] *Review of Particle Physics*, K.A. Olive et al. (Particle Data Group), Chin. Phys. C, 38, 090001 (2014).

[10] A. Spiridonov, arXiv :hep-ex/0510076, 28 Oct. 2005.

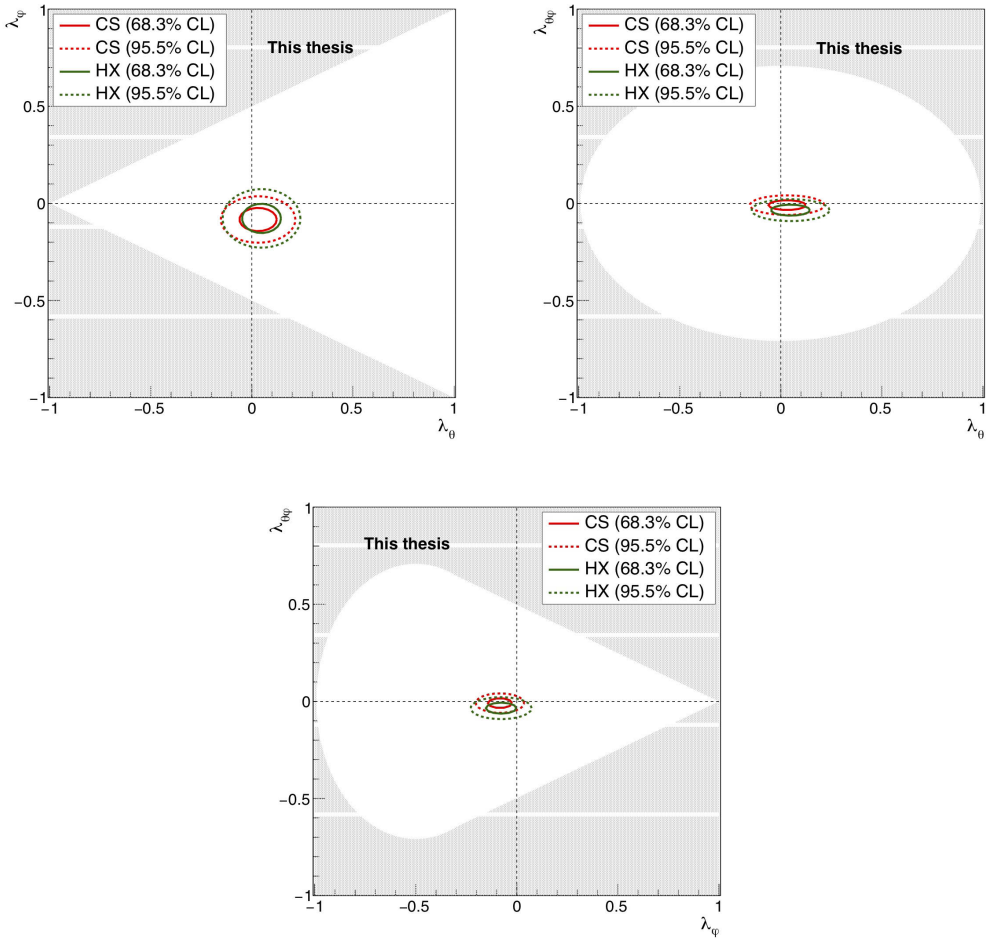

FIGURE 14 – Valeurs intégrées des paramètres de polarisation du J/ψ – $\langle\lambda_\theta\rangle$, $\langle\lambda_\varphi\rangle$ et $\langle\lambda_{\theta\varphi}\rangle$ – sur l'intervalle $2 < p_{\mathrm{T}} < 15$ GeV/c et $2.5 < y < 4$ présentés dans les plans des régions accessibles théoriquement (en blanc) : les ellipses en lignes pleines (tirets) montrent les contours à 1 σ (2 σ) dans le référentiel de Collins-Soper (rouge) et d'Hélicité (vert).

[11] LHCb Collaboration, Eur. Phys. J. C (2011) 71 :1645.

[12] CDF Collaboration, Phys. Rev. Lett. 99, 132001 (2007).

[13] M. Butenschoen and B. A. Kniehl, Phys. Rev. Lett. 108, 172002 (2012).

[14] K.-T. Chao et al., Phys. Rev. Lett. 108, 242004 (2012).

Abstract

The main purpose of the ALICE experiment is the study and characterization of the Quark Gluon Plasma (QGP), a state of nuclear matter in which quarks and gluons are deconfined. Quarkonia (bound states of a heavy quark Q and its anti-quark $\bar{Q}$) constitute one of the most interesting probes of the QGP. Besides this motivation, the study of quarkonium production is very interesting since it can contribute to our understanding of Quantum Chromodynamics, the theory of strong interactions. The formation of quarkonium states in hadronic collisions is not yet completely understood. The two main theoretical approaches to describe the production of quarkonium states, the Color Singlet Model and the Non-Relativistic QCD framework (NRQCD), have historically presented problems to simultaneously describe the production cross section and polarization of such states. On the experimental side, quarkonium polarization measurements have not always been complete and consistent between them. So, neither from the theoretical nor from the experimental point of view the situation was clear.

Improved methods for the measurement of quarkonium polarization have been recently proposed, highlighting the necessity to perform the measurements of all polarization parameters with respect to different reference axes. In this context, new measurements could help to improve and set new constraints to the calculations. ALICE has measured the J/ψ polarization in pp collisions at $\sqrt{s}$= 7 TeV. The higher statistics of the 8 TeV data with respect to the 7 TeV data allows to extend the p_{T} range of the measurements. This thesis presents a complete measurement of J/ψ polarization, i.e. the three polarization parameters, in two polarization frames: the Collins-Soper and Helicity frames. The results show no significant J/ψ polarization in the kinematic domain studied: $2.5 < y < 4.0$ and $2 < p_{\mathrm{T}} < 15$ GeV/c. The measurement of a frame invariant parameter $\tilde{\lambda}$, was also performed to ensure that no bias was present in the analysis procedure. The comparison with different theoretical predictions shows that there is not yet a satisfactory description of quarkonium production. None of the present theoretical approaches is able to describe both, the cross section and polarization measurements.

Keywords: J/ψ, quarkonium polarization, pp collisions, ALICE experiment, LHC

Étude de la polarisation du J/ψ dans les collisions proton-proton avec le détecteur ALICE au LHC

Résumé

L'expérience ALICE a pour principal objectif l'étude et la caractérisation du plasma de quarks et de gluons (QGP), un état de la matière nucléaire dans lequel les quarks et les gluons sont déconfinés. Les quarkonia (des états liés d'un quark lourd Q et de son anti-quark $\bar{Q}$) constituent l'une des plus intéressantes sondes du QGP. De plus, l'étude de la production des quarkonia est très intéressante puisqu'elle peut contribuer à une meilleure compréhension de la Chromodynamique Quantique, la théorie décrivant l'interaction forte. La formation d'états de quarkonia lors de collisions hadroniques n'est pas bien comprise. Les deux principales approches théoriques décrivant la production d'états de quarkonia, le 'Color Singlet Model' (CSM) et la QCD non-relativiste (NRQCD), ont montré des difficultés à décrire simultanément la section efficace de production et la polarisation de tels états. Expérimentalement, les mesures de la polarisation des quarkonia n'ont pas toujours été compatibles entre elles. Ainsi, que ce soit du point de vue expérimental ou théorique, l'étude des quarkonia est restée inachevée.

De nouvelles méthodes récemment proposées ont souligné la nécessité de mesurer tous les paramètres de la polarisation, dans les différents systèmes de référence. Dans ce contexte, de nouvelles mesures peuvent améliorer les constraintes actuelles, voire apporter de nouvelles contraintes sur les prédictions. ALICE a mesuré la polarisation du J/ψ lors de collisions pp à $\sqrt{s}$= 7 TeV. La plus grande statistique des données à 8 TeV par rapport aux données à 7 TeV permet d'étendre les mesures à une gamme de p_{T} plus large. Cette thèse présente une mesure complète de la polarisation de J/ψ, i.e. les trois paramètres de polarisation, dans deux systèmes de référence différents: le système Collins-Soper et le système d'hélicité. Les résultats ne montrent aucune polarisation significative pour le J/ψ dans le domaine cinématique étudié : $2.5 < y < 4.0$ et $2 < p_{\mathrm{T}} < 15$ GeV/c. Le paramètre invariant $\tilde{\lambda}$ a également été mesuré afin d'écarter le risque d'un biais dans la procédure d'analyse. La comparaison de ces résultats avec les prédictions théoriques montre que la production de quarkonia n'est pas encore correctement décrite. Aucun de ces modèles théoriques n'est capable de décrire à la fois les mesures de sections efficaces et de polarisation.

Mots-clés : J/ψ, polarisation de quarkonia, collisions pp, expérience ALICE, LHC